



Kuliková, Adriana (2025) *Data-driven weaker mixed formulation for diffusion problems*. PhD thesis.

<https://theses.gla.ac.uk/85306/>

Copyright and moral rights for this work are retained by the author

A copy can be downloaded for personal non-commercial research or study, without prior permission or charge

This work cannot be reproduced or quoted extensively from without first obtaining permission from the author

The content must not be changed in any way or sold commercially in any format or medium without the formal permission of the author

When referring to this work, full bibliographic details including the author, title, awarding institution and date of the thesis must be given

Enlighten: Theses

<https://theses.gla.ac.uk/>
research-enlighten@glasgow.ac.uk

Data-driven weaker mixed formulation for diffusion problems

Adriana Kuliková

Submitted in fulfilment of the requirements for the
Degree of Doctor of Philosophy

James Watt School of Engineering
College of Science and Engineering
University of Glasgow



University
of Glasgow

December 2024

Abstract

This thesis presents a data-driven mixed finite element framework for solving elliptic equations, i.e. nonlinear diffusion problems, focusing on heat transfer in porous media such as nuclear graphite. Traditional computational approaches rely on phenomenological material models, which contain empirically estimated parameters. However, the models carry uncertainty about the values of these parameters, which we lose by choosing a single value per parameter, which often leads to inaccuracy or overconfidence with complex or inherently stochastic materials. In contrast, the data-driven (DD) approach, as first introduced by Kirchdoerfer and Ortiz [2016], leverages material data directly, avoiding the need for fitted models and allowing uncertainty estimation from data imperfections, such as noise or missing values.

The framework, which employs a weaker DD formulation, is designed to ensure adherence to conservation laws and boundary conditions. The temperature and its gradient are approximated in the L^2 (discontinuous) space while the heat flux is approximated in the $H(\text{div})$ space, which enforces normal flux continuity across internal boundaries and provides *a posteriori* error estimates. An algorithm for adaptive mesh and order refinement is proposed, guided by error indicators and the proximity of the computed fields to the material dataset, assessing the suitability of the material dataset to the problem at hand while minimising computational effort. In contrast to the original “stronger” DD approach, weaker mixed DD formulation results in problems with fewer unknowns and searches through the material dataset while reaching the same accuracy.

The developed framework is applied to a nonlinear problem where heat flux depends on both temperature and its gradient. Uncertainty quantification is performed by perturbing the resulting fields and repeating the iterative process, akin to Monte Carlo simulations, to obtain the standard deviation of the results. Knowing the standard deviation of the results and the distances of the resulting fields from the dataset, the information of the quality of the material dataset for the problem is obtained, suggesting where the material data does not cover the ranges of the fields in the analysis or where the data is too noisy or missing.

The developed framework reformulates the original DD approach and can be further extended to include more complex material datasets and physical phenomena. Allowing for the control and minimisation of FE errors before quantifying the uncertainty of the results propagating from the dataset, the framework can be applied to challenging industrial problems.

This thesis is one of the steps towards the development of a data-driven finite element frame-

work for the analysis of graphite bricks in the advanced gas cooled nuclear reactors (AGRs), which is a complex and evolving environment. The current work introduces and tests the "weaker" DD approach on diffusion problems and provides a foundation for future research and development of the DD framework for more complex problems, such as fracture analysis in nuclear graphite bricks. To this end, a preliminary study is performed on a nuclear graphite brick slice with synthetically generated material datasets.

This thesis is written for engineers, and all of the work is open and reproducible. The implemented framework is an independently developed module [Kulikova, 2024a] in MoFEM, an open-source parallel finite element library, and all examples are collected in another open repository [Kulikova, 2024b] for the reproducibility of the results presented in this thesis.

Contents

Abstract	i
Acknowledgements	xvii
Declaration	xviii
1 Introduction	1
1.1 Structure of the thesis	4
1.2 Literature review	5
1.2.1 Material behaviour and material data acquisition	5
1.2.2 Uncertainty in material behaviour	9
1.2.3 Data-driven approaches	9
1.2.4 Mixed formulations	11
1.2.5 Conclusion of the literature review	13
2 Standard finite element approach to diffusion problems	14
2.1 Boundary value problem for heat diffusion	14
2.2 Linear diffusion problems	15
2.3 Essential boundary conditions for temperature	18
2.3.1 Temperature BC applied <i>a priori</i>	19
2.3.2 Temperature BC applied through the least squares method	19
2.3.3 Convergence to the exact solution	20
2.4 Nonlinear diffusion problems	23
2.4.1 Linearisation of nonlinear diffusion problems	25
2.4.2 Convergence to the exact solution	27
2.5 Summary	30
3 Mixed formulation for diffusion problems	31
3.1 Linear diffusion problems - mixed formulation	31
3.1.1 Boundary conditions in the mixed formulation	34

3.2	Convergence and <i>a priori</i> error estimates	34
3.3	<i>A posteriori</i> error estimators and indicators	41
3.3.1	Error indicator associated with temperature gradient	41
3.3.2	Error indicator associated with flux divergence	42
3.3.3	Jump across the inner boundaries	43
3.3.4	Error estimator	44
3.4	Adaptive refinement	45
3.4.1	Adaptive approximation order refinement	46
3.4.2	Adaptive mesh refinement	49
3.4.3	Adaptive mesh and order refinement algorithm	50
3.5	Summary	52
4	Data-Driven formulation for diffusive problems	53
4.1	Introduction to the data-driven formulation	54
4.1.1	Iterative procedure and convergence of the data-driven approach	58
4.1.2	Scaling the dataset	60
4.2	Working with noisy material datasets	62
4.2.1	Data search averaging	65
4.3	5D material datasets	66
4.3.1	Fully artificial material datasets	68
4.3.2	Material datasets from synthetic experiments	70
4.4	2D brick example with six material datasets	72
4.5	Summary	80
5	Weaker mixed data-driven formulation	82
5.1	Derivation	83
5.1.1	Computational complexity comparison	88
5.1.2	Verification with other formulations	89
5.2	Comparison with the mixed formulation	91
5.2.1	Error indicators associated with temperature gradients	91
5.2.2	Error estimators	91
5.2.3	Adaptive refinement	92
5.3	Results compared to the stronger data-driven formulation	94
5.3.1	Effect of the material dataset quality on the error indicators	97
5.4	Adaptive refinement for weaker data-driven formulation	97
5.4.1	Distance to the material dataset per element	98
5.4.2	Standard deviation of the distance to the material dataset per element	99
5.5	Capturing brick refinement	101
5.6	Summary	103

6	Quantification of nonuniqueness	107
6.1	Uniqueness of the solution	108
6.2	Markov chain Monte-Carlo simulations	109
6.2.1	Effect of noise on the standard deviation of results	112
6.3	Summary of uncertainty measurements on the Brick example	116
7	Conclusions and Perspectives	125
7.1	Conclusions	125
7.1.1	Novelties introduced in this research	126
7.2	Limitations and Future Work	127
7.2.1	Data-driven approach	127
7.2.2	Source of material datasets	128
7.2.3	Uncertainty quantification	128
7.2.4	Adaptive refinements	129
7.2.5	Other applications	129
7.2.6	Matrix structure and scalability	129
A	Functional spaces	130
A.1	L^2 Lebesgue space	130
A.2	H^1 Sobolev space	131
A.3	$H(\text{curl})$ space	132
A.4	$H(\text{div})$ space	133
A.4.1	Functional spaces in 2D	134
B	Finding the closest point on a line	135
C	Example Brick geometry and mesh	136

List of Tables

1.1	Naming convection for the data-driven approaches.	13
2.1	Types of boundary conditions for boundary value problems.	15
2.2	Functional spaces for the standard approach to diffusion problems.	16
2.3	Imposition of boundary conditions in the standard finite element approach.	18
3.1	Functional spaces for the mixed formulation of the diffusion problem.	33
3.2	Finite element basis functions for the mixed formulation of the diffusion problem. T_a , δT_b , $q_{\mathcal{A}}$ and $\delta q_{\mathcal{B}}$ are the coefficients of the approximation. N_a and N_b are the scalar base functions; and $\mathbf{Q}_{\mathcal{A}}$ and $\mathbf{Q}_{\mathcal{B}}$ are the vectorial base functions.	33
3.3	Approximation orders for the mixed formulation of the diffusion problem.	34
3.4	Imposition of boundary conditions in the mixed (weaker) formulation of the heat diffusion problem.	34
4.1	Functional spaces for the data-driven formulation for the diffusion problem. For spaces definitions see appendix A.	56
4.2	Finite element basis functions for the data-driven formulation of the diffusion problem. T_α , δT_β , \mathbf{q}_a , $\delta \mathbf{q}_b$, λ_α and $\delta \lambda_\beta$ are the coefficients of the approximation. N_α , Q_a and L_α are the scalar basis functions.	57
4.3	Approximation orders for the data-driven formulation of the diffusion problem.	57
4.4	Summary of 5D Material Datasets	73
5.1	Functional spaces for the data-driven weaker mixed formulation.	85
5.2	Finite element basis functions for the weaker data-driven formulation of the diffusion problem.	85
5.3	Approximation orders for the weaker mixed data-driven formulation.	86
5.4	Definitions and notations of the error indicators for the weaker data-driven formulation.	92
5.5	Adaptive refinement criteria for the brick example.	101
6.1	Example Brick: Maximum standard deviation of the fields for different material datasets obtained with weaker DD with adaptive refinement , also see Table 4.4.	117

6.2	Summary of findings of analysis with material dataset A.	118
6.3	Summary of findings of analysis with material dataset E.	119
6.4	Summary of findings of analysis with material dataset C and F.	121
6.5	Summary of findings of analysis with material dataset B and D.	122

List of Figures

1.1	Physics based and data-driven approaches. Note: DDCM = Data-Driven Computational Mechanics [Kirchdoerfer and Ortiz, 2016].	2
2.1	A sketch visualising the domain where the conservation of energy is fulfilled and the parts of the boundary where the Dirichlet and Neumann boundary conditions are applied.	15
2.2	Discretisation of the domain Ω with the essential boundary Γ_T for the standard formulation of the heat diffusion problem. The essential boundary is represented by the degrees of freedom B and the rest of the domain by the degrees of freedom D	19
2.3	Example SinCos: Corresponding to the exact solution $\tilde{T} = \cos(2\pi y) \sin(2\pi x)$. The domain is a square with side length $L = 1m$ and the temperature \tilde{T} is prescribed to three sides of the boundary. The source term s and prescribed flux boundary condition \bar{q} , are dependent on the heat conductivity k	21
2.4	Example SinCos: Exact solution, its gradient, flux and source term for the linear diffusion problem with thermal conductivity $k = 1 \text{ W/(m} \cdot \text{ }^\circ\text{C)}$	22
2.5	Example SinCos: Convergence of the finite element solution to the exact one with decreasing element size and increasing approximation order. a) and b) show the L^2 -norm, c) and d) show the H^1 -seminorm, e) and f) show the flux error norm, whereas left column shows the convergence with decreasing element size and right column shows the convergence with increasing number of integration points.	24
2.6	Example SinCos: Nonlinear thermal conductivity $k(T) = 1 + T + T^2$. Note that (b) is for demonstration purposes only and is not an input for the analysis.	27
2.7	Example SinCos (nonlinear): Exact solutions and applied source term for the nonlinear diffusion problem with thermal conductivity $k = 1 + T + T^2$	28

2.8	Example SinCos (nonlinear): Convergence of nonlinear diffusion problem global errors with respect to the exact solution with mesh and approximation order refinement. a) and b) show the L^2 -norm, c) and d) show the H^1 -seminorm, e) and f) show the flux error norm, whereas left column shows the convergence with respect to the element size and right column shows the convergence with respect to the number of integration points.	29
3.1	Discretisation of the domain Ω with the essential boundary Γ_q for the mixed formulation of the heat diffusion problem. The essential boundary is represented by the degrees of freedom B and the rest of the domain by the degrees of freedom D , which are different to the ones presented in Figure 2.2.	35
3.2	Example Exp-Hat: Analysis setup which corresponds to the exact solution $\tilde{T} = e^{-100(x^2+y^2)} \cos \pi x \cos \pi y$	36
3.3	Example Exp-Hat: Exact solutions for the temperature, its gradient and the heat flux, and the source term for the linear heat diffusion problem with thermal conductivity $k = 1$ [W/(m· °C)].	37
3.4	Example Exp-Hat: Temperature field T in L^2 showing jumps across the element boundaries with increasing approximation order p . Element size $h = 0.05$	38
3.5	Example Exp-Hat: Convergence of the finite element solution to the exact one with decreasing element size and increasing approximation order. a) and b) show the L^2 -norm, c) and d) show the H^1 -seminorm, e) and f) show the flux error norm, whereas left column shows the convergence with respect to the element size and right column shows the convergence with respect to the number of integration points.	39
3.6	Example Exp-Hat: Comparison of convergence of the finite element solution obtained by the standard and mixed formulation to the exact one with decreasing element size and increasing approximation order. a) and b) show the L^2 -norm, c) and d) show the H^1 -seminorm, e) and f) show the flux error norm, whereas left column shows the convergence with respect to the element size and right column shows the convergence with respect to the number of integration points.	40
3.7	Example Exp-Hat: Comparison of the magnitudes of the gradient of temperature ∇T and the heat flux \mathbf{q} for approximation order $p = 1$ and element size $h = 0.05$	42
3.8	Example Exp-Hat: Comparison of the error indicator associated with temperature gradient $\eta_e(\nabla T, \mathbf{q})$, see (3.10), and the H^1 -seminorm of temperature error to the exact solution evaluated per finite element.	43
3.9	Example Exp-Hat: Error indicator assessing the conformity of the numerical solution to the conservation of energy equation (3.1a) on element basis.	43
3.10	Example Exp-Hat: Error indicator evaluating the jumps of temperature values, see (3.13), through the inner boundaries, evaluated per element.	44

3.11	Example Exp-Hat: Error estimator calculated according to (3.14) evaluating the temperature gradient, flux divergence, and jumps of temperature values through the inner boundaries, evaluated per element compared to the total mesh dependent error norm.	45
3.12	Example Exp-Hat: Convergence of the finite element solution to the exact one and error indicators with increasing number of Gauss points driven by the global and local h and p refinement.	47
3.13	Example Exp-Hat: Resulting approximation orders of the adaptive refinement with the algorithm described in Algorithm 1.	48
3.14	Example L-shape: Exact solutions and the source term for the linear diffusion problem with thermal conductivity $k = 1$	49
3.15	Example L-shape: Geometry and boundary conditions. Note that \bar{q} is derived from the exact solution (3.18) with linear material behaviour and thermal conductivity $k = 1$	50
3.16	Example L-shape: Convergence of the finite element solution to the exact one and error indicators with increasing number of Gauss points due to global and local mesh and order refinement.	51
4.1	Regular material dataset: Simplest grid material dataset \mathcal{D} with $k = 1$	54
4.2	Regular material dataset & Example SinCos: Path of an integration point finding the closest point in the dataset (Closest data point) and projecting it into a space where conservation laws and boundary conditions are satisfied (Field values).	58
4.3	Example SinCos (Figure 2.3): Global error norms w.r.t. the exact solution and point distance RMS measure (4.8). Convergence with the number of points in the regular material dataset, see Figure 4.1.	59
4.4	Example SinCos: Comparison of Standard FE and data-driven (DD) FE solutions' convergence with element size h and approximation order p if a "saturated" dataset is used (see Appendix B).	60
4.5	Example SinCos: Path of one integration point as the convergence is achieved. Conductivity $k = 0.1 \text{ W}/(\text{m} \cdot ^\circ\text{C})$	61
4.6	Number of iterations with changing conductivity k . The limit for number of iterations is set to 5000.	61
4.7	Example SinCos: Temperature T result with sparse regular material dataset containing 41^4 points with different thermal conductivities without scaling. Note that if scaling is used, (b) will have the same result as (a).	62
4.8	Dataset generation example: (a) Regularly distributed components of temperature gradient; Flux components following linear constitutive law with noise representing (b)-(c) measurement error, (d)-(e) stochastic material behaviour	63

4.9	Example Exp-Hat (Figure 3.2): Influence of noise and number of material data points on global error L^2 -norms for temperature and flux, averaged over 30 realisations (order $p = 2$, element size $h = 0.05$).	64
4.10	Sample of noisy material dataset with 10^6 material datapoints and $\sigma_\eta = 0.1$. . .	65
4.11	Example Exp-Hat (Figure 3.2): Using an average of 30 closest material datapoints instead of the closest point only in material data search (4.1) for the same analysis as Figure 4.9.	65
4.12	Nonlinear thermal conductivity k dependence on temperature T used for the synthetic material dataset generation.	67
4.13	Material dataset A created by Algorithm 3 with $count_T = 50$, $count_G = 50$. The temperature range is $[400, 1100]$, and the gradient range is $[-40 \times 10^3, 40 \times 10^3]$. Material dataset B is similar but with $count_T = 100$, $count_G = 100$, making it denser.	69
4.14	Material dataset C created by Algorithm 4 with 10^6 material datapoints. The temperature range is $[400, 1100]$, the gradient range is $[-40 \times 10^3, 40 \times 10^3]$, and the noise is applied in the range $[10 \times 10^3, 15 \times 10^3]$ with standard deviation $\sigma_\eta = 1.0$	70
4.15	Example Synthetic experiment: Geometry and mesh used for the synthetic experiment setup with \bar{T}_{in} and \bar{T}_{out} as temperature boundary conditions.	71
4.16	Material dataset D created by synthetic experiments.	71
4.17	Material dataset E created by synthetic experiments with missing data.	72
4.18	Material dataset F created by synthetic experiments with intentionally added noise around to values with magnitude of gradient of temperature smaller than 2 [$^\circ\text{C}/\text{m}$].	72
4.19	Example Brick: Geometry and mesh of a nuclear graphite brick with a testing boundary conditions of $\bar{T}_{in} = 1000^\circ\text{C}$ and $\bar{T}_{out} = 500^\circ\text{C}$ and $\bar{q} = 0$ on the symmetry lines and the small inner holes, also see Appendix C	74
4.20	Example Brick: results of the analysis with a dense material dataset with no noise present (dataset B).	74
4.21	Example Brick: Average distance from the dataset per element upon solution of the problem using datasets A-F.	75
4.22	Example Brick: Distance for each integration point between the resulting temperature field T and the temperature component T^* of the closest points in the material dataset upon solution of the problem using datasets A-F. For the resulting values of temperature see Figure 4.20a.	77

4.23	Example Brick: Distance for each integration point between the resulting flux field in y direction q_y and the y flux component q_y^* of the closest points in the material dataset upon solution of the problem using datasets A-F. For the resulting values of flux magnitude see Figure 4.20b.	78
4.24	Example Brick: Standard deviation of the distance from the dataset per element upon solution of the problem using datasets A-F.	79
5.1	Example SinCos (Figure 2.3): Global error norms w.r.t. exact solution and point distance RMS measure (4.8). Convergence with the number of points in the Uniform material dataset, see Figure 4.1.	88
5.2	Example Exp-Hat: Comparison of weaker DD, mixed formulation (chapter 3) and stronger DD formulation (chapter 4). Convergence of the finite element solution w.r.t. the exact one with fully saturated dataset (Appendix B).	90
5.3	Example Exp-Hat: Comparison of weaker DD and mixed formulation with adaptive order refinement.	93
5.4	Example Exp-Hat: Resulting approximation orders of the adaptive refinement with the algorithm described in Algorithm 1.	94
5.5	Example Exp-Hat tweaked dataset: dataset is created with uniform random distribution for temperature gradients in ranges $[-9, 9]$ and flux is afterwards calculated by $\mathbf{q} = -\mathbf{g}$. 10^5 material datapoints are generated and a range of datapoints containing values of $[-6, -5]$ in temperature gradient in x -direction is removed for testing purposes.	95
5.6	Example Exp-Hat: Comparison of data-driven and weaker data-driven formulation and with adaptive order refinement.	96
5.7	Example Exp-Hat: Error estimator and approximation order per element for the weaker data-driven formulation with missing data after adaptive order refinement.	97
5.8	Example Exp-Hat: Using the standard deviation of the distance to the material dataset to refine the mesh and identify the problematic areas w.r.t. the distance to the material dataset.	100
5.9	Example Exp-Hat: Adaptive refinement with the algorithm described in Algorithm 5.	102
5.10	Example Brick: Effect of adaptive refinement on (a-b) error estimator (c-d) average distance to the dataset per element, see subsection 5.4.1, and (e-f) standard deviation of the distance to the dataset per element, see subsection 5.4.2. Analysis with material dataset E, see Figure 4.17.	104
5.11	Example Brick: Effect of adaptive refinement on (a-b) average distance to the dataset per element, see subsection 5.4.1, and (c-d) standard deviation of the distance to the dataset per element, see subsection 5.4.2. Analysis with material dataset C, see Figure 4.14.	105

5.12	Example Brick: Effect of adaptive refinement on (a-b) average distance to the dataset per element, see subsection 5.4.1, and (c-d) standard deviation of the distance to the dataset per element, see subsection 5.4.2. Analysis with material dataset A.	106
6.1	Example L: Temperature field for different initial values of the fields and the material dataset, with 10^4 material datapoints and $\sigma_\eta = 0.02$, used for both analyses. Note the different maximum values of the temperature field in the domain's top right corner.	108
6.2	Example L: Error estimator for different initial values of the fields.	110
6.3	Example L: Influence of standard deviation of perturbation κ on the maximum standard deviation of the resulting fields: σ_T^{\max} , $\sigma_{g_x}^{\max}$, $\sigma_{g_y}^{\max}$, and $\sigma_{q_x}^{\max}$	111
6.4	Example L: Material datasets with various standard deviation of noise σ_η applied to the thermal conductivity in the x -direction. There is no noise present for the values in y -direction and the number of material datapoints is 10^6	112
6.5	Example L: Maximum standard deviation convergence of the fields for standard deviation of noise $\sigma_{\eta_x} = 0.02$ and $\sigma_{\eta_y} = 0$ in the material dataset.	113
6.6	Example L: Standard deviation of the temperature field for standard deviation of noise $\sigma_{\eta_x} = 0.02$ in the material dataset using the stronger and weaker mixed formulation. Note that w/ AR stands for "with adaptive refinement".	113
6.7	Example L: Standard deviation of the flux field for standard deviation of noise $\sigma_{\eta_x} = 0.02$ in the material dataset using the stronger and weaker mixed formulation. Note that w/ AR stands for "with adaptive refinement".	114
6.8	Example L: Standard deviation of the flux field for standard deviation of noise $\sigma_{\eta_x} = 0.02$ in the material dataset using the weaker DD formulation with adaptive refinement.	115
6.9	Example L: Maximum standard deviation of the fields for different standard deviations of noise in the material dataset.	115
6.10	Example Brick: Resulting fields with material dataset D. Note that D is the most accurate dataset, and these resulting fields are therefore chosen for comparison to all of the further results to avoid repeating the figures.	117
6.11	Example Brick: Distance to the material dataset and standard deviation of the results for material dataset A (regular sparse) after Monte-Carlo analysis. . . .	118
6.12	Example Brick: Distance to the material dataset and standard deviation of the results for material dataset E (experiment missing) after Monte-Carlo analysis. .	118
6.13	Example Brick: Distance to the material dataset and standard deviation of the results for material dataset F (experiment noisy) after Monte-Carlo analysis. . .	120
6.14	Example Brick: Distance to the material dataset and standard deviation of the results for material dataset C (random noisy) after Monte-Carlo analysis.	120

6.15	Example Brick: Distance to the material dataset and standard deviation of the results for material dataset B (regular dense) after Monte-Carlo analysis.	121
6.16	Example Brick: Distance to the material dataset and standard deviation of the results for material dataset D (artificial experiment) after Monte-Carlo analysis.	122
6.17	Example Brick: Extract of material datasets used for the Brick example analysis. More information in section 4.3 and Table 4.4.	123
A.1	Hierarchical shape functions of $L^2(\Omega)$ space, up to the third order.	131
A.2	Hierarchical shape functions of $H^1(\Omega)$ space, up to the third order.	132
A.3	Conservation of tangential component in $H(\text{curl})$ space between elements.	133
A.4	Hierarchical shape functions of $H(\text{curl})$ space (Nédélec (second kind)), up to the third order.	133
A.5	Conservation of normal component in $H(\text{div})$ space between elements.	134
A.6	Hierarchical shape functions of $H(\text{div})$ space (Brezzi-Douglas-Marini), up to the third order. Note that for 2D problems, $H(\text{div})$ space is constructed from $H(\text{curl})$ space by (A.9). See the similarity to Figure A.4.	134

List of Symbols

- \mathbf{q} heat flux [W/m^2]; a field of heat flux .
- λ field of scalar Lagrange multiplier.
- $\boldsymbol{\tau}$ field of vector Lagrange multiplier.
- T temperature [$^{\circ}\text{C}$]; a field of temperature .
- k thermal conductivity [$\text{W}/(\text{m}\cdot^{\circ}\text{C})$].
- α trial function basis indices for H^1 space.
- \mathcal{A} trial function basis indices for $H(\text{div})$ space.
- \mathbf{a} trial function basis indices for L^2 space.
- β test function basis indices for H^1 space.
- \mathcal{B} test function basis indices for $H(\text{div})$ space.
- \mathbf{b} test function basis indices for L^2 space.
- \bar{q} function of normal heat flux on boundary Γ_q .
- \bar{T} function of temperature on boundary Γ_T .
- h element size [m].
- γ change trial function basis indices for H^1 space.
- p approximation order for temperature field.
- t_h tolerance for the mesh refinement according to the value of average error estimator.
- t_p tolerance for the order increase according to the value of average error estimator.
- μ error estimator per element (face).
- σ_{η} standard deviation of the noise.

η noise applied to the material dataset.

ξ comparative value for data-driven refinement.

t_{ave} tolerance for the average distances to the material dataset.

d_{ave} average distance to the material dataset.

t_{std}^{ave} tolerance for the standard deviation of the distances to the material dataset compared to the average distances in element.

t_{std} tolerance for the standard deviation of the distances to the material dataset.

d_{std} standard deviation of the distances to the material dataset.

ψ perturbation value.

σ_q standard deviation of the heat flux result.

κ standard deviation of the perturbation value.

σ_T standard deviation of the temperature result.

Acknowledgements

First of all, I would like to thank my supervisors, Andrei Shvarts, Łukasz Kaczmarcyk and Chris Pearce. Without them, this project and its completion would certainly not have been possible. Additionally, the whole of the MoFEM team and all of its members, past and present, form a great community.

I am grateful for the opportunities to go to nice places for conferences that also lifted my spirits throughout this journey: Nottingham (UKACM 2022), Oslo (ECCOMAS 2022), Warwick (UKACM 2023), Porto (YIC 2023), Eidhoven (CMCS 2023), Lisbon (ECCOMAS 2024), Durham (UKACM 2024), and also the summer school in Udine (CISM 2023).

Ďakujem aj rodinke, ktorá pri mne stále stála, obzvlášť mamke a ockovi. Vďačná som aj mojej babke, ktorá sa o mňa trápila snád' viac ako ja. Som rada, že vás všetkých mám, že ste to so mnou vydržali, povzbudzovali ma a dopriali mi radostnú pauzu, keď som prišla.

I would also like to thank my partner Henning, who stuck with me through it all, and my friends Domina, Claire, and Jude, who have made my life full of joy through the good and bad times.

The emotional support I received from everyone around me at the end of this journey was amazing, and being able to travel and visit beautiful places soothed my mind during the writing stage. It was difficult for me, but you made it all better, so thank you, mamka (Turkey); Claire (Dundee); Claire and Jude (Manchester); ocko, Zarka a rodinka (Tatry); Elsa (Ålesund); Domina (Havířov, Vienna); L'udka and Gery (Malta).

These are years I am going to remember forever, and I am grateful for everyone I have had by my side along this amazing journey.

Declaration

This work was supported by EDF and EPSRC. The views expressed in this thesis are those of the author and not necessarily those of EDF.

All work in this thesis has been carried out by the author unless otherwise explicitly stated.

The author confirms that the following thesis has been composed by herself without undue assistance. All references have been clearly stated in accordance with departmental requirements, in both the text and the bibliography. All data and findings herein belong to the author and have not been falsified or embellished.

This work has not been previously, or concurrently, submitted for other courses or within any other exam processes.

Chapter 1

Introduction

Classical computational approaches to engineering problems, such as solid and fluid mechanics, as well as diffusion and transport phenomena, require two components: equations of conservation laws (complemented by appropriate boundary conditions) and constitutive behaviour of the material. While conservation law is a physical law which all systems must obey, any constitutive behaviour is an approximation of reality, often represented by material models obtained by fitting to the experimental data. Material models can vary from simple ones with one or two parameters (e.g. Darcy’s law for fully saturated flow, linear diffusion/heat flow, isotropic linear elasticity) to more complex ones (unsaturated flow [Vogel et al., 2000], nonlinear heat transfer [Matsuo, 1980], hyperelasticity [Bonet and Wood, 1997] and plasticity [Ibrahimbegovic, 2009], among many others).

Fitting material models to experimental data allows for relatively fast and accurate solutions to boundary value problems using physics-based methods, depending on both the complexity of the model and the conformity of the fit. Some examples of the physics-based methods include the finite element method (FEM) [Zienkiewicz and Taylor, 2000], finite difference method (FDM) [Smith, 1985], finite volume method (FVM) [Versteeg, 2007], boundary element method (BEM) [Katsikadelis, 2002], meshfree methods [Liu and Liu, 2003], spectral methods [Boyd, 2001], see Figure 1.1. The material models used in physics-based methods are often constructed and improved by phenomenological laws, with existing models reused for materials of similar types, allowing for extrapolation into states not included in the original experiments (e.g., applying unsaturated flow models developed for soil to microfluidic flow in filter paper [Gerlero et al., 2022]). However, certain materials may not directly fit any established model if underlying phenomenon is unknown [Singh et al., 2022], exhibit changing properties over time due to usage conditions (such as irradiated graphite [Tzelepi et al., 2018; Jordan et al., 2018]), or display inherent variance in their responses [Jones et al., 2019]. Moreover, the fit of material models to actual material behaviour observed in experiments is often poorly understood, particularly regarding the conditions under which these constitutive relations apply [Edition and Bauld, 1986; Belytschko et al., 2014]. Some materials may also exhibit stochastic behaviour, which

Physics-based

Data-driven (no physics)

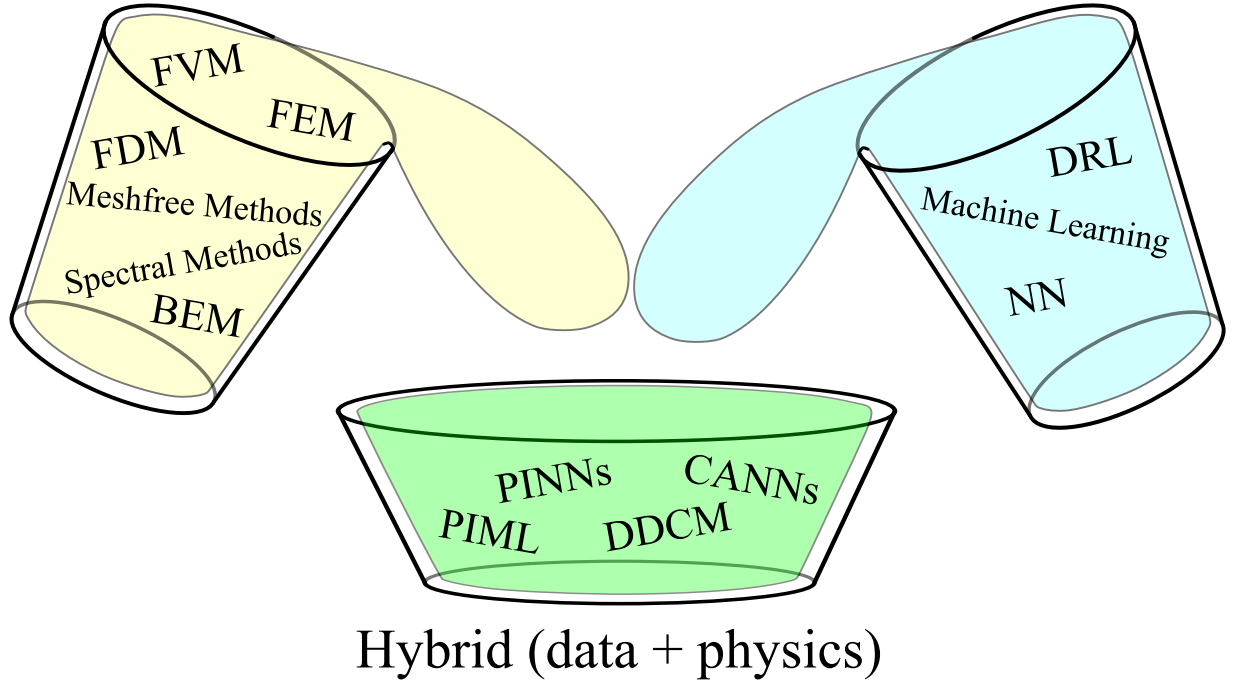


Figure 1.1: Physics based and data-driven approaches.

Note: DDCM = Data-Driven Computational Mechanics [Kirchdoerfer and Ortiz, 2016].

is generally averaged out during model fitting, leading subsequent research to seek methods to reincorporate stochasticity into numerical analyses [Rao, 2013; Bensoussan, 1991].

Comparatively to the past, advances in data acquisition have enabled the collection of larger datasets from experimental studies on materials nowadays [Agarwal and Dhar, 2014; Baesens, 2014]. The variability of this data, along with the different experimental setups and data collection methodologies, impacts how the data is incorporated into numerical simulations. Alternatives to traditional material models include machine learning (ML) [Bishop and Nasrabadi, 2006], neural networks (NN) [Bishop, 1995], and deep reinforcement learning (DRL) [Arulkumar et al., 2017], which can either identify material behaviour for future use or find solutions to entire problems. However, machine learning approaches which are used on their own are often considered "black boxes", providing solutions that may not adhere to established physical laws [Pateras et al., 2023]. Progress in this research area has led to the development of physics-informed machine learning (PIML) [Pateras et al., 2023], constitutive artificial neural networks (CANNs) [Linka et al., 2021], and physics-informed neural networks (PINNs) [Raissi et al., 2019], bringing the solution back to obeying conservation laws [Grossmann et al., 2023]. For visual representation of the difference between the physics-based and data-driven approaches, see Figure 1.1.

Recently, a new approach has emerged in computational mechanics, which provides an alternative to creating material models and allows the use of the data directly in numerical simulations while satisfying conservation laws by means of the finite element method [Kirchdoerfer

and Ortiz, 2016]. This method requires the dataset to define relationships between key variables that would typically be represented in a material model, e.g. stress and strain; heat flux and gradient of temperature; heat flux, temperature and its gradient; etc. These relationships are captured as points within a multidimensional dataset, which can be searched, and where each variable represents a dimension.

Data-driven computational mechanics [Kirchdoerfer and Ortiz, 2016] enables the use of material datasets directly instead of constitutive models and does not infer any material models in the process or try to fit or average the data in any way. This allows the inherent imperfections of the material datasets to influence the results and, therefore, provides future means of quantifying uncertainty related to the material behaviour. The data-driven approach was initially developed for elastic stress-strain problems and has, since its first introduction, been expanding [Kirchdoerfer and Ortiz, 2017; Ayensa-Jiménez et al., 2018]. The applications now include diffusion [Nguyen et al., 2020], elasticity [Conti et al., 2018], nonlinear elasticity [Nguyen and Keip, 2018], inelasticity [Eggersmann et al., 2019], plasticity, and fracture [Carrara et al., 2020]. Other research areas also include retrieving material datasets through data-driven identification [Stainier et al., 2019], multiscale analyses using data-driven approaches in one or multiple scales [Mora-Macías et al., 2020; Karapiperis et al., 2021], methods for completing incomplete datasets [Ayensa-Jiménez et al., 2019], etc.

This thesis is one of the steps towards the development of a data-driven finite element framework for the analysis of graphite bricks in the advanced gas cooled nuclear reactors (AGRs), which is a complex and evolving environment. To verify and assess the implications of using the developed data-driven approach, this thesis uses synthetic material datasets and focuses on nonlinear heat transfer through porous media, such as graphite used in nuclear reactors [Matsuo, 1980] or fibrous and foamed insulating materials used in thermal insulation [Larkin and Churchill, 1959]. When dealing with porous media, radiation through the pores might have a significant impact on the thermal conductivity relative to the temperature the body is experiencing [Larkin and Churchill, 1959]. Therefore, the constitutive relationship for heat is expressed by Fourier's/Fick's law, where the dependence of thermal conductivity on temperature can introduce nonlinearity to the system.

As a main novelty in this thesis, a "weaker" data-driven formulation is formulated by deriving the data-driven approach [Kirchdoerfer and Ortiz, 2016] with the mixed finite element formulation [Boffi et al., 2013]. The fields of temperature and its gradient are approximated in the L^2 (discontinuous) space, allowing for discontinuities between the elements, while the heat flux is approximated in the $H(\text{div})$ (Brezzi-Douglas-Marini) space, which enforces the continuity of the normal flux component across any inner boundaries.

The mixed formulation naturally provides error indicators and estimators [Braess and Verfürth, 1996], which can be used for adaptive mesh and approximation order refinement [Zander et al., 2022]. In the proposed framework, the adaptive refinement is guided by the error indica-

tors and improved by considering the proximity of the computed fields to the material dataset, ensuring only the elements whose refinement might impact the solution are refined. This approach minimises the computational effort required to reach a desired accuracy.

Nevertheless, using a material dataset instead of a material model in the finite element analysis introduces uncertainty related to the material dataset to the results. The material dataset can be sparse, not cover all the required material states, contain noise or outliers, which can impact the solution accuracy. In industrial applications, it is important to not only obtain the results of the analysis but also quantify the certainty of their results. The errors/uncertainty have two sources, the finite element approximation errors and the material dataset quality. Since the finite element approximation errors can be controlled by adaptive refinement, these errors should be reduced first to ensure the material dataset quality is the main source of uncertainty.

If the material dataset contains noisy material datapoints, the solution of the data-driven approach is not unique and the result can vary depending on the initial field values when using the same material dataset [Kirchdoerfer and Ortiz, 2017], the solution can be perturbed and the analysis repeated to quantify the uncertainty in the results. This allows for the quantification of uncertainty in the results, akin to Monte Carlo simulations, which obtain the standard deviation of the results. Since this requires repeating the simulation multiple times, and search through the material dataset happens at every integration point, the adaptive refinement is needed to reduce the number of integration points for a given accuracy, which allows for the uncertainty quantification to be performed in a reasonable time frame.

The aim of this thesis is to build a base for the "weaker" data-driven finite element formulation, which considers nonlinear diffusion problem and the developed techniques can be extended to other problems in further research. This includes the derivation, implementation and testing of the new formulation, adaptive refinement, influence of the material dataset quality, and gaining knowledge of uncertainty through quantifying of the nonuniqueness of the results.

All of the numerical analysis in this work (or thesis) has been performed using specifically developed data-driven module [Kulikova, 2024a] in an open-source finite element software MoFEM [Kaczmarczyk et al., 2020].

1.1 Structure of the thesis

This thesis is organised into the following chapters, each building upon the previous to explore progressively more complex formulations and approaches to solving nonlinear diffusion problems.

- Remainder of chapter 1 addresses the literature review of material behaviour and data acquisition, related uncertainty, data-driven approaches, mixed formulations, and their applications in computational mechanics.

- Chapter 2 provides a review of the standard finite element (FE) formulation for diffusion problems, setting the groundwork for the work presented in the subsequent chapters.
- Chapter 3 presents the mixed FE formulation for diffusion problems, in which the primary variable (e.g. temperature) and auxiliary variable (e.g. heat flux) are approximated separately using distinct functional spaces. This chapter explores techniques for error estimation and adaptive *hp*-refinement, with numerical examples demonstrating the convergence of the solutions.
- Chapter 4 addresses a "stronger" data-driven approach to solving diffusion problems. Instead of relying on predefined material models, this approach uses experimental material datasets directly. The chapter also discusses the effects of dataset noise and sparsity on convergence and solution accuracy. A graphite brick example and six independent material datasets are introduced, which are used to demonstrate how each subsequent chapter adds a new layer to the brick analysis solution and the certainty with which the result is obtained.
- Chapter 5 introduces a "weaker" data-driven approach that combines the data-driven method with the mixed FE formulation, providing error estimation and adaptive refinement capabilities while using material datasets instead of material models.
- Chapter 6 focuses on uncertainty quantification of the formulations developed in the previous chapters, introducing Monte Carlo simulations to assess the impact of noisy or incomplete datasets on solution accuracy. This chapter also explores the variability of results due to dataset imperfections and discusses strategies to mitigate these uncertainties.
- Chapter 7 concludes the thesis by summarising the key findings and contributions of the research. The chapter also outlines potential avenues for future work.

1.2 Literature review

This section presents a literature review of modern data-driven computational methods for modelling material response and advances in finite-element approaches. Starting with the material behaviour and data acquisition, the position of the data-driven approach in the bigger picture of the computational analysis and overview of the current data-driven research, finishing with the overview of the mixed formulation.

1.2.1 Material behaviour and material data acquisition

Understanding material behaviour is crucial in the development and application of predictive models. These models are typically derived from experimental data, with the material properties

of interest characterised by parameters that are fitted to the data. However, the accuracy of these models can be limited by the complexity of the material behaviour, the experimental conditions, and the assumptions made during model development [Singh et al., 2022].

The field of material informatics [Rajan, 2005] has emerged as a means of addressing these challenges. It combines materials science, data science, and informatics to process and interpret vast amounts of data related to materials properties, behaviours, and applications. This approach aligns with the broader field of Data Science, which focuses on extracting knowledge from large volumes of unstructured data [Agarwal and Dhar, 2014; Baesens, 2014].

Sources of material data

An important question in adopting data-driven approaches is: "Where can the necessary data be sourced?" Existing experimental measurement equipment can obtain data for various materials under specific physical conditions [Franck et al., 2007; Mettas, 2010]. However, existing experimental measurement equipment may not be universally applicable as constraints such as high costs, extreme environmental conditions, or the lack of suitable devices for specific material systems can limit data availability.

To address these challenges, innovative techniques for material dataset acquisition are being explored. One promising method is data-driven identification (DDI), which combines digital image correlation with numerical analysis to generate material datasets. This technique builds upon the data-driven paradigm [Kirchdoerfer and Ortiz, 2016], where strain is derived from measured displacements, and stress is determined through finite element analysis, ensuring consistency with experimental boundary conditions [Stainier et al., 2019; Leygue et al., 2018; Valdés-Alonzo et al., 2022].

Originally developed to identify the mechanical response of truss structures [Leygue et al., 2018], DDI can be adapted to other domains such as heat transfer. Consider a large database of measurements, obtained for example using a thermal camera, on a material subjected to varying thermal conditions. For each experiment or data item, indexed by X , the following quantities are available:

- Nodal temperature T^X from the measurements;
- Domain geometry and connectivity, allowing the computation of the temperature gradient ∇T^X via finite element mesh setup;
- Prescribed heat source term s in the domain Ω ;
- Prescribed heat flux $\mathbf{q} \cdot \mathbf{n} = \bar{q}$ on the boundary Γ_q ;
- Prescribed temperature $T = \bar{T}$ on the boundary Γ_T ;
- Conservation law: $\nabla \cdot \mathbf{q} = s$ in Ω .

The solution involves an iterative process that computes and maps between the mechanical and material states of the temperature gradient and heat flux. The output of the DDI process is a

set of material states $\{\mathbf{g}_i^*, \mathbf{q}_i^*\}$, where \mathbf{g}_i^* represents the temperature gradient and \mathbf{q}_i^* the heat flux, for $i \in 1 : N^*$, with N^* denoting the number of material states.

DDI can produce a substantial number of material states, resulting in sufficiently large datasets without assuming any material model. However, it relies heavily on the quality of the equipment and the experimental setup, including full control over boundary conditions.

Another approach involves multiscale computational methods. Simulations on representative volume elements (RVEs) or unit cells can populate the database with relevant material states [Karapiperis et al., 2021; Gorgogianni et al., 2023]. These datasets can be created either beforehand or *in situ* during data-driven analysis, where material states are computed on the fly and stored for future use. While this approach is flexible and can capture a wide range of material behaviors and conditions, it requires detailed knowledge of lower-scale material properties.

This thesis does not focus on the data acquisition process but rather on how to use the data once it is obtained, therefore, synthetic datasets are used to demonstrate the capabilities of the developed data-driven approach. The material datasets used throughout this work are synthetic with various number of material states (material datapoints), which can could theoretically be obtained by the DDI process or multiscale computational methods described above.

Material modelling approaches

Historically, various material models were applied to capture heat transfer behaviour using experimental data [Larkin and Churchill, 1959], machine learning techniques [Tamaddon-Jahromi et al., 2020], and homogenisation methods [Rooney et al., 2021; Liu and Zhang, 2006; Le et al., 2022; Luo et al., 2022]. Furthermore, multiscale modelling and homogenisation techniques have been employed, even in scenarios without data-driven methods [Smit et al., 1998; Miehe et al., 1999; Feyel and Chaboche, 2000; Kaczmarczyk et al., 2008; Kochmann and Bertoldi, 2017].

While these methods have been successful in many applications, they may not fully capture the complexity of material behaviour, particularly in cases where the material response is stochastic or exhibits significant variability. One such example is the behaviour of graphite bricks within nuclear reactors, an example used in this thesis.

Case study: graphite bricks in nuclear reactors

The primary application of the framework developed in this thesis is the heat flow through graphite bricks used in advanced gas-cooled reactors (AGR) in the UK. Graphite bricks form the core of the reactor, providing structural support, and graphite also serves as a neutron moderator, slowing down fast neutrons during the operation. Graphite bricks experience changes in material properties over time, including a decrease in thermal conductivity, an increase in porosity, and density loss due to radiation exposure inside the nuclear reactor's core [Kelly, 1982].

The principles discussed herein regarding nonlinear heat transfer in graphite bricks can also apply to other reactor components, such as boilers, or to entirely different contexts, such as

building insulation or the diffusion of substances like algae in aquatic environments. The properties of graphite bricks, influenced by porosity, depend on factors including weight loss and microstructural changes resulting from irradiation duration and intensity, as well as the specific location within the reactor.

Synthetic datasets for demonstration

While this thesis does not employ real experimental data for the properties of the graphite bricks, it will utilise synthetic datasets to demonstrate the capabilities of the developed data-driven approach. These synthetic datasets are generated through various synthetic experiments, for more details see Section 4.3.2, using one of multiple possible material models for heat transfer in graphite:

$$k(T) = 134.0 - 0.1074T + 3.719 \times 10^{-5}T^2, \quad (1.1)$$

where k [W/mK] represents the thermal conductivity of the graphite brick, and T is the temperature in $^{\circ}C$. This model is derived from work conducted for high-temperature gas-cooled reactors, encompassing temperature ranges from room temperature to $1000^{\circ}C$, where measurements of thermal diffusivity, mass, volume and thermal expansion were converted to thermal conductivity [McEligot et al., 2016].

Note that the material model chosen is for the demonstration purposes only and is not the only possible model for the heat transfer in graphite. The data-driven approach developed in this thesis can be applied to any material dataset, regardless of the underlying material model.

Variability in material properties

The variability in the material properties of irradiated graphite has been a subject of extensive research [Price, 1973]. Previous studies provide insights into the material properties of graphite, highlighting the presence of molecular-level defects due to radiation [Marsden et al., 2005], which can lead to changes in thermal conductivity over time [Snead, 2008; Marsden et al., 2008]. Increased porosity further influences thermal conductivity in nuclear graphite [Babout et al., 2007]. Moreover, heat transfer problem solutions are essential for stress and fracture analyses of the graphite brick [Hashim et al., 2017; Tzelepi et al., 2018; Jordan et al., 2018].

Graphite is not the only material subject to such changes and varying responses in material behaviour. Other materials, such as concrete, polymers, metals, etc., exhibit similar complexities in their responses to external factors [Jones et al., 2019; Edition and Bauld, 1986], requiring the development of advanced computational methods to model their behaviour accurately. The data-driven approach enables skipping of the material modelling process and allows for the direct use of experimental data, which can be particularly beneficial in cases where the material behaviour is not well understood or is subject to significant variability.

1.2.2 Uncertainty in material behaviour

Computational mechanics can be described as an art of controlling errors and uncertainties in the numerical analysis. The finite element approximation errors can be controlled by refining the mesh, increasing the order of the finite element approximation, or using adaptive refinement. Nevertheless, the choice of how the material behaviour is represented is nearly always an approximation of reality regardless of whether a material model or a material dataset is used for the analysis. The choice of material behaviour representation introduces uncertainty that should be carefully evaluated when interpreting results of numerical analysis concerning sensitive usage cases, such as nuclear reactors, as each model inherently simplifies the complexity of real-world material responses.

When using set material models and the material behaviour is stochastic, the stochasticity is averaged out by the material model. The stochasticity can be brought back to the numerical analysis [Ghanem and Spanos, 2003; Rao, 2013; Bensoussan, 1991] or random uncertainty can be introduced to the stiffness matrix [Soize, 2000] or uncertainty can also be embedded in the FEM framework [Jones et al., 2019].

Alternatively, if sensor data is available, the data can be integrated with the finite element models. Statistical finite element methods account for uncertainties in sensor measurements, loading conditions, and model specifications [Febrianto et al., 2022; Herath et al., 2022; Girolami et al., 2021], offering a robust framework for uncertainty quantification in complex, data-rich environments.

In data-driven approaches, where material datasets are used directly without imposing a predefined model structure, the inherent uncertainties within the dataset can propagate into the analysis results. This propagation of uncertainty offers opportunities for uncertainty quantification, allowing for an understanding of the variability in the analysis predictions. The next section describes the current state of the data-driven approaches and their applications in computational mechanics.

1.2.3 Data-driven approaches

Using data instead of traditional material models is not a new concept. Rather than relying solely on constitutive equations, material behaviour can be identified directly from experimental data using machine learning or neural networks [Bishop and Nasrabadi, 2006; Bishop, 1995]. In this context, approaches such as Constitutive Artificial Neural Networks (CANNs)[Linka et al., 2021] aim to construct new material models which can then be used in numerical simulations similarly to conventional ones. Other purely data-driven techniques attempt to bypass the modelling stage entirely by using machine learning to approximate numerical solutions directly. However, when applied without enforcing physical constraints, such methods may act as "black-box" solvers, producing outputs that lack interpretability and may violate fundamental

principles, such as the conservation of energy [Pateras et al., 2023; Grossmann et al., 2023].

To address these shortcomings, hybrid approaches have emerged in which physical laws are embedded directly into the learning process. For example, physics-informed neural networks (PINNs) [Raissi et al., 2019] and physics-informed machine learning (PIML) [Pateras et al., 2023] incorporate governing equations as constraints, ensuring adherence to conservation principles and improving the physical reliability of the solutions.

Building on these developments, a new class of data-driven methods was proposed [Kirchdoerfer and Ortiz, 2016], in which experimental data is used directly in the formulation of the governing equations, rather than to construct surrogate models. This formulation eliminates the "black-box" nature of traditional machine learning approaches and maintains consistency with the underlying physics. The present work contributes to this emerging direction by investigating its application to diffusion problems, as a foundation for more complex analyses involving nuclear graphite.

Data-driven computational mechanics: evolution and expansion

The data-driven computational mechanics started with Kirchdoerfer and Ortiz, who introduced a novel data-driven approach to solving elasticity problems [Kirchdoerfer and Ortiz, 2016]. This approach can be presented as an iterative process of searching the material dataset, consisting of stress-strain material datapoints, to find the appropriate material behaviour for different parts of the domain to use in the numerical analysis, which brings the solution back to satisfying conservation laws. This work set the foundation for further developments in the data-driven mechanics [Kirchdoerfer and Ortiz, 2018; Kirchdoerfer, 2018].

The data-driven mechanics' initial methodology was later adapted to handle noisy data, incorporating clustering analysis and simulated annealing as techniques to enhance data reliability [Kirchdoerfer and Ortiz, 2017]. Statistical techniques further advanced the data-driven framework, enabling inferences on material behaviours and facilitating statistical adjustments in data-driven models [Conti et al., 2021; Prume et al., 2023].

Since the data-driven approach searches through material datasets which can be too large to manage by regular data searching algorithms, various methods have been developed to optimise this process, including advanced dataset assembly techniques and optimised search algorithms [Eggersmann et al., 2021; Bahmani and Sun, 2021]. Recent innovations even explore the use of quantum computing to expedite data searching and handling, promising substantial performance gains in computational mechanics [Xu et al., 2024; Liu et al., 2024].

Application of data-driven mechanics to complex scenarios

The data-driven approach was subsequently extended to address finite strain elasticity [Platzer, 2020] and nonlinear elasticity involving large deformations [Nguyen and Keip, 2018]. Other expansions considered factors such as angular momentum [Platzer et al., 2021] and dynamic

behaviours [Kirchdoerfer and Ortiz, 2018], increasing the applicability of data-driven mechanics to more complex material conditions.

If the material behaviour is history-dependent, short-term temporal dependency can be incorporated into the data-driven framework, supporting applications for inelasticity, viscoelasticity, and plasticity [Eggersmann et al., 2019]. The data-driven approach has also been applied in wave propagation studies within viscoelastic solids [Salahshoor and Ortiz, 2023] and in biomedical engineering contexts, such as analysing the mechanical response of the human brain to sonic and ultrasonic stimuli through *in situ* and *in vivo* imaging [Salahshoor and Ortiz, 2022].

In some cases, combining data-driven approaches with traditional model-driven frameworks has yielded promising results. Data-driven methods can be selectively applied in regions of high uncertainty, while model-driven methods address more predictable material behaviours [Yang et al., 2022]. The data-driven approach can also be combined with traditional material models to compute problems represented by multiple constitutive behaviours. For example, in fracture mechanics, the stress-strain relationship can be addressed using the traditional material models, while the data-driven approach can be used to determine how far a crack will propagate in brittle material [Carrara et al., 2020]. This hybrid approach can be extended further by integrating multiple physical phenomena, employing both data-driven and model-driven approaches as appropriate for each phenomenon [Bahmani and Sun, 2021]. Further applications in molecular dynamics allow for data-driven analysis of interatomic interactions, adding molecular-level detail to the computational framework [Bulin et al., 2022].

Furthermore, data-driven mechanics has increasingly been used to bridge the gap between microscale and macroscale material properties. For instance, in cases where material datasets are incomplete, microscale analyses can be performed *ad hoc* to generate necessary data for macroscale applications [Karapiperis et al., 2021]. This multiscale approach has been implemented for composite materials, where datasets are compiled at the microscale prior to conducting larger-scale data-driven analyses [Huang et al., 2021]. In materials with predictable microstructures, such as open-cell foams, a micro-scale analysis provides insights into macro-scale behaviour, especially when considering anisotropic and nonlinear properties influenced by stochastic microstructural variations [Korzeniowski and Weinberg, 2022].

1.2.4 Mixed formulations

Currently, the original formulation of the data-driven computational mechanics for elasticity already utilises a mixed formulation since two different fields are independently approximated: stress and displacement. Functional spaces appropriate for such a formulation are $\mathbf{L}^2(\Omega, \mathbb{R}_{symm}^{(n \times n)})$ for stresses and $H^1(\Omega, \mathbb{R}^n)$ for displacements, described in [Conti et al., 2018; Korzeniowski, 2022; Nguyen et al., 2020]. $\mathbf{L}^2(\Omega, \mathbb{R}_{symm}^{(n \times n)})$ is the space for symmetric matrices with square integrable values and $H^1(\Omega, \mathbb{R}^n)$ is the space for vector fields with square integrable values and derivatives.

The equivalent for the heat transfer data-driven formulation is $\mathbf{L}^2(\Omega, \mathbb{R}^n)$ for the flux and $H^1(\Omega, \mathbb{R})$ for the temperature [Kuliková et al., 2021; Nguyen et al., 2020], where $\mathbf{L}^2(\Omega, \mathbb{R}^n)$ is a space for vector functions with square integrable values and $H^1(\Omega, \mathbb{R})$ is a space for scalar functions with square integrable values and derivatives, also discussed in Chapter 4.

For comparison, functional spaces used for mechanical and heat transport problems in the standard finite element approach are the relevant $H^1(\Omega)$ space for displacement and temperature, and stresses and fluxes are derived with the help of the constitutive laws [Zienkiewicz and Taylor, 2000; Boffi et al., 2013]. The derived/secondary variable (stress, flux) classically depends on the gradients of the primary variable (displacement, temperature) and is therefore approximated in a relevant $\mathbf{L}^2(\Omega)$ space. In comparison, the secondary variable (stress, flux) is solved for directly in the data-driven approaches.

The mixed finite element formulations started with introducing a new field being calculated for, be it the way boundary conditions are applied [Babuška, 1973], contact formulation [Yastrebov, 2013; Wriggers and Laursen, 2006], incompressible flow/elasticity [Boffi et al., 2013], etc.

In addition, combining two or more fields to solve for leads to separating the primary and secondary variables and solving for them separately. This allows for more natural functional spaces to be chosen for each of the fields [Brezzi et al., 2008; Wakeni et al., 2022; Boffi et al., 2013; Arnold, 1990]. For heat diffusion, the primary variable is the temperature, which, after integration by parts, can be approximated in $L^2(\Omega)$ space, which allows for the temperature to be discontinuous across the elements. Although the exact solution for temperature is always in H^1 space, L^2 space better approximates sharp irregularities. The secondary variable is the heat flux, which is approximated in $H(\text{div}; \Omega)$ space, which enforces the continuity of the normal flux component across any inner boundaries. Such spaces can accommodate problems with expected jumps in temperature, such as problems with high jumps in the heat source term, e.g. a checkerboard pattern, or interaction of materials with different properties [Wakeni et al., 2022].

Error estimation and adaptive refinement

Multiple ways to calculate error estimates were proposed in literature [Oden et al., 1989; Repin, 2008; Grätsch and Bathe, 2005]. However, due to the temperature T and flux \mathbf{q} belonging to different functional spaces in the mixed formulation, naturally emerging error indicators and estimators with little extra computational cost are available [Ainsworth, 2008; Braess and Verfürth, 1996; Carstensen, 1997].

Moreover, the error indicators can be utilised for adaptive refinements of mesh and/or finite element approximation order [Zander et al., 2022]. More information about the development and application of such algorithms is presented in Chapter 3.

Data-driven approach	Naming convention
derived with standard formulation	"stronger" DD
derived with mixed formulation	"weaker" DD

Table 1.1: Naming convection for the data-driven approaches.

1.2.5 Conclusion of the literature review

To conclude, in many applications of computational modelling, material behaviour is not certain and using material datasets instead of material models is possible and advantageous in situations where the material models are lacking or the material behaviour is unpredictable. The data-driven mechanics has advanced in the recent years and is applied to a range of scenarios with complex material behaviour.

Nevertheless, the functional spaces of the standard data-driven computational mechanics formulations could be improved by deriving the problems with a mixed formulation. Since the existing data-driven approach [Kirchdoerfer and Ortiz, 2016] is already mixed, i.e., it contains multiple unknown fields for one physical process [Nguyen et al., 2020], to distinguish between the existing data-driven approach and the data-driven approach derived with the mixed formulation, the latter is referred to as the "weaker" data-driven approach, see Table 1.1. The "weaker" mixed data-driven formulation is the topic of this research, and there is a gap in the current literature.

Chapter 2

Standard finite element approach to diffusion problems

2.1 Boundary value problem for heat diffusion

Diffusion problems are fundamental in many fields of science and engineering. These problems analyse the distribution and movement of a quantity, e.g. heat or mass transfer, within a physical system. This chapter introduces the basic concepts and notation that will be used throughout the discussion of these problems. The formulations and examples considered are time independent and are solved using the finite element method. This introductory chapter aims to provide the necessary background and set the stage for the more complex formulations explored in the subsequent chapters.

The conservation of energy law for the heat diffusion problem, neglecting the effect of time, reads:

$$\nabla \cdot \mathbf{q} = s \quad \text{in } \Omega, \quad (2.1)$$

where ∇ is the gradient operator, $\mathbf{q} = \mathbf{q}(\mathbf{x})$ is a field of the heat flux, $T = T(\mathbf{x})$ is a field of the temperature and $s = s(\mathbf{x})$ is a field for the heat source in the domain Ω . For the simplicity of writing the fields will be from now on referred to as temperature T , flux \mathbf{q} and source s respectively. The boundary conditions on $\Gamma = \delta\Omega$ which compliment the conservation law (2.1) are as follows:

$$\begin{cases} T = \bar{T} & \text{on } \Gamma_T, \\ \mathbf{q} \cdot \mathbf{n} = \bar{q} & \text{on } \Gamma_q, \end{cases} \quad (2.2a)$$

$$(2.2b)$$

where \mathbf{n} is the outward normal vector to the boundary Γ , \bar{q} is the function of normal flux on Γ_q , and \bar{T} is the prescribed function of temperature on Γ_T , see Figure 2.1 and Table 2.1 for the types of boundary conditions of boundary value problems in this work.

To be able to solve a heat diffusion boundary value problem [Lienhard and Lienhard, 2020],

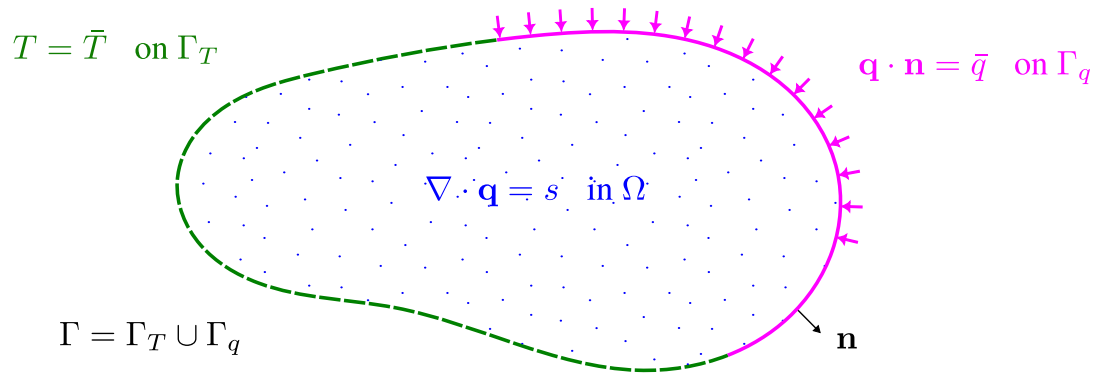


Figure 2.1: A sketch visualising the domain where the conservation of energy is fulfilled and the parts of the boundary where the Dirichlet and Neumann boundary conditions are applied.

BC type	Field on which the condition is applied	Boundary
Dirichlet	Primary variable: temperature T	Γ_T
Neumann	Secondary variable: heat flux \mathbf{q}	Γ_q

Table 2.1: Types of boundary conditions for boundary value problems.

the relation between flux \mathbf{q} and temperature T needs to be introduced. In the simplest (linear) case, this can be done through the phenomenological constitutive equation (Fourier's law):

$$\mathbf{q} = -k\nabla T, \quad (2.3)$$

where k is the heat conductivity [Lienhard and Lienhard, 2020].

However, thermal conductivity k can introduce nonlinearity to the system by the dependence on the unknown temperature T , i.e. $k = k(T)$. Additionally, the thermal conductivity can be dependent on the spatial heterogeneity, such as the porosity of the material, which may evolve in time, e.g. years or months. However, this thesis focuses on a snapshot of the system at a specific point in time, thereby discarding this time dependence. Spatial dependence is also not considered in this work but can be introduced in the future. The resulting constitutive relation could be highly nonlinear and depend on a set of empirical parameters [Lienhard and Lienhard, 2020].

2.2 Linear diffusion problems

Linear diffusion problems assume that the thermal conductivity k is not dependent on the unknown variables, such as temperature, but can be a constant or a function of space representing heat conductivities of different materials present in the domain. The flux can therefore be represented by the Fourier's law (2.3) and the conservation of energy law (2.1) can be rewritten

as:

$$\nabla \cdot (-k\nabla T) = s \quad \text{in } \Omega \quad (2.4)$$

with the boundary conditions (2.2).

Multiplying both sides of (2.4) by a test function δT and integrating over the domain Ω , gives:

$$\int_{\Omega} \delta T \nabla \cdot (-k\nabla T) \, d\Omega = \int_{\Omega} \delta T s \, d\Omega \quad \forall \delta T \in H_0^1(\Omega), \quad (2.5)$$

where $H_0^1(\Omega)$ is a Sobolev space of scalar functions with square-integrable gradient, which have zero values on the boundary Γ_T , see section A.2 for more information.

Integrating the first term in (2.5) by parts gives the weak form:

$$\int_{\Omega} k\nabla \delta T \cdot \nabla T \, d\Omega + \int_{\Gamma} \delta T (-k\nabla T \cdot \mathbf{n}) \, d\Gamma = \int_{\Omega} \delta T s \, d\Omega \quad \forall \delta T \in H_0^1(\Omega). \quad (2.6)$$

The boundary Γ is split into two parts, Γ_q and Γ_T . The test function δT is zero on the boundary Γ_T and the flux boundary condition (2.2b) is applied as follows:

$$\int_{\Omega} k\nabla \delta T \cdot \nabla T \, d\Omega + \int_{\Gamma_T} \delta T (-k\nabla T \cdot \mathbf{n}) \, d\Gamma + \int_{\Gamma_q} \delta T (-k\nabla T \cdot \mathbf{n}) \, d\Gamma = \int_{\Omega} \delta T s \, d\Omega \quad \forall \delta T \in H_0^1(\Omega), \quad (2.7)$$

resulting in the following weak form of the problem (2.6):

Find $T \in \mathcal{T}$ such that:

$$\int_{\Omega} k\nabla \delta T \cdot \nabla T \, d\Omega + \int_{\Gamma_q} \delta T \bar{q} \, d\Gamma = \int_{\Omega} \delta T s \, d\Omega \quad \forall \delta T \in H_0^1(\Omega), \quad (2.8)$$

where the spaces for trial and test functions are defined in Table 2.2.

Field	Space
Temperature T (trial function)	$T \in \mathcal{T} = \{u \in H^1(\Omega) \mid u = \bar{T} \text{ on } \Gamma_T\}$
δT (test function)	$\delta T \in H_0^1(\Omega) = \{v \in H^1(\Omega) \mid v = 0 \text{ on } \Gamma_T\}$

Table 2.2: Functional spaces for the standard approach to diffusion problems.

For definition of Sobolev space $H^1(\Omega)$, see section A.2.

The summation over repeated indices is assumed hereinafter unless stated otherwise. The temperature T and test function δT are approximated by the finite element base functions, $N_\alpha(\mathbf{x})$ and $N_\beta(\mathbf{x})$, respectively:

$$T^h(\mathbf{x}) = T_\alpha N_\alpha(\mathbf{x}) \quad \text{and} \quad \delta T^h(\mathbf{x}) = \delta T_\beta N_\beta(\mathbf{x}), \quad (2.9)$$

where T_α and δT_β are the coefficients of the approximation, and α and β are the indices of the base function for H^1 space, see glossary for indices of other functional spaces. Spatial dependence (\mathbf{x}) is hereinafter omitted for brevity. Since the gradients ∇T^h and $\nabla \delta T^h$ are dependants of T_α and δT_β , their approximation is as follows:

$$\nabla T^h = T_\alpha \nabla N_\alpha \quad \text{and} \quad \nabla \delta T^h = \delta T_\beta \nabla N_\beta. \quad (2.10)$$

The same notations as were introduced in the continuous problem statement are preserved for discretised geometric entities for brevity, i.e. Ω will be used in place of Ω^h .

Substituting the approximations (2.9) and (2.10) into the weak form (2.8) obtains:

$$\delta T_\beta \int_{\Omega} k (\nabla N_\beta \cdot \nabla N_\alpha) d\Omega T_\alpha + \delta T_\beta \int_{\Gamma_q} N_\beta \bar{q} d\Gamma = \delta T_\beta \int_{\Omega} N_\beta s d\Omega \quad \forall \delta T_\beta. \quad (2.11)$$

Since (2.11) holds for any coefficients δT_β , the coefficients of the temperature T_α can be obtained by solving the following matrix form:

$$[\mathbf{K}_{\alpha\beta}] [\mathbf{T}_\alpha] = [\mathbf{F}_\beta], \quad (2.12)$$

where $[\mathbf{T}_\alpha]$ is the vector of unknown coefficients T_α , $[\mathbf{K}_{\alpha\beta}]$ is the diffusivity matrix:

$$[\mathbf{K}_{\alpha\beta}] = \int_{\Omega} k (\nabla N_\beta \cdot \nabla N_\alpha) d\Omega, \quad (2.13)$$

and $[\mathbf{F}_\beta]$ is the external flux vector containing contributions from the heat source s and the Neumann boundary condition \bar{q} ,

$$[\mathbf{F}_\beta] = \int_{\Omega} N_\beta s d\Omega + \int_{\Gamma_q} N_\beta \bar{q} d\Gamma. \quad (2.14)$$

Bilinear (2.13) and linear (2.14) integral forms are evaluated using numerical integration, e.g. the Gauss quadrature. Hierarchical base functions available in MoFEM [Kaczmarczyk et al., 2020] are used for the approximation throughout this thesis. The hierarchical base functions enable a straightforward implementation of p -refinement as increasing of the approximation order adds higher order functions to the existing ones instead of replacing all of the functions in the element, as is the case with Lagrange base functions. The use of hierarchical base functions also allows for multiple fields of different approximation orders and function spaces to be used in the same element. It is important to note that for the case of hierarchical base functions, appropriate integration rules should be chosen to ensure the exact, or sufficiently precise, computations of the integrals of polynomial functions of an arbitrary order.

In the standard finite element approach to the diffusion problems, the Neuman boundary

condition (2.2b) is satisfied as a natural boundary condition and is imposed as a part of the weak form (2.12). The Dirichlet boundary condition (2.2a) is satisfied as an essential boundary condition by either prescribing the value of temperature T *a priori* on the boundary Γ_T or by using the least squares method, see section 2.3 for more details.

BC type	Field on which the condition is applied	Boundary
Essential	satisfied in the strong sense	$\Gamma_{\text{Essential}} = \Gamma_T$
Natural	imposed as a part of the weak form	$\Gamma_{\text{Natural}} = \Gamma_q$

Table 2.3: Imposition of boundary conditions in the standard finite element approach.

Table 2.3 summarises the imposition of boundary conditions for the standard approach. However, these impositions will be reversed when mixed formulation is introduced in chapter 3, where the Neumann boundary condition will be imposed as essential and the Dirichlet boundary condition as natural.

The next section addresses how the Dirichlet boundary condition can be applied in the standard approach.

2.3 Essential boundary conditions for temperature

There are multiple approaches for enforcing the essential boundary conditions in finite element method. This section will discuss two of these approaches for the Dirichlet essential boundary condition, which in this case is for temperature, i.e. $\Gamma_{\text{Essential}} = \Gamma_T$.

The matrix form of the problem, e.g. (2.12), complemented by the essential boundary condition (2.2a) contains parts describing both the domain and the essential boundary. The degrees of freedom corresponding to the essential boundary B and the rest of the domain D are shown in Figure 2.2.

The matrices representing the whole problem are split into the domain D and essential boundary B blocks for visual simplicity:

$$\begin{bmatrix} \mathbf{K}_{DD} & \mathbf{K}_{DB} \\ \mathbf{K}_{BD} & \mathbf{K}_{BB} \end{bmatrix} \begin{bmatrix} \mathbf{T}_D \\ \mathbf{T}_B \end{bmatrix} = \begin{bmatrix} \mathbf{R}_D \\ \mathbf{R}_B \end{bmatrix} \quad (2.15)$$

where $[\mathbf{K}]$ is the stiffness matrix, $[\mathbf{T}]$ is the temperature vector, and $[\mathbf{R}]$ is a vector containing sources and boundary conditions. The subscripts D and B denote the domain and essential boundary parts, respectively, corresponding to Figure 2.2.

Note that for the following derivation, \mathbf{R}_D remains unchanged from the main problem formulation, described by (2.14) in section 2.2, however it does not apply to the degree of freedom indices on the essential boundary.

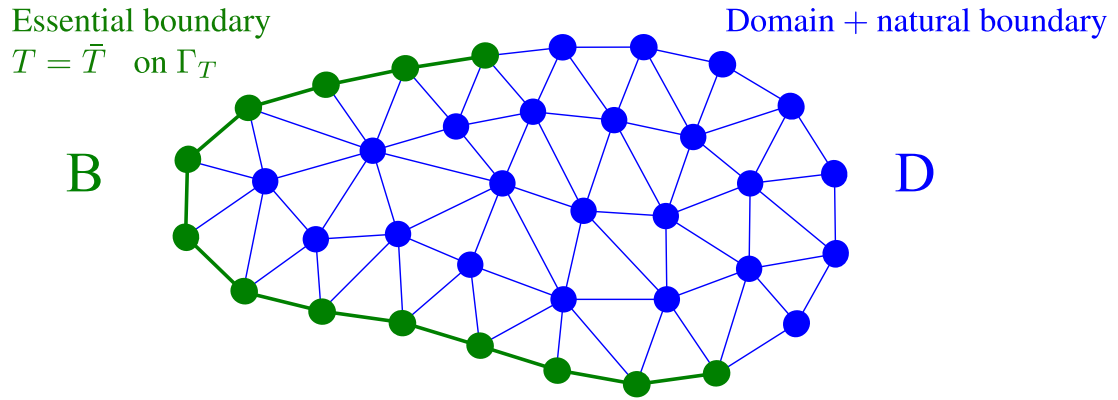


Figure 2.2: Discretisation of the domain Ω with the essential boundary Γ_T for the standard formulation of the heat diffusion problem. The essential boundary is represented by the degrees of freedom B and the rest of the domain by the degrees of freedom D .

2.3.1 Temperature BC applied *a priori*

The temperature T can be set to \bar{T} *a priori* on the boundary Γ_T , i.e. before solving the problem. This can be achieved by setting:

$$\begin{bmatrix} \mathbf{R}_B \end{bmatrix} = \begin{bmatrix} \bar{\mathbf{T}}_B \end{bmatrix}, \quad (2.16)$$

changing \mathbf{K}_{BB} into identity matrix \mathbf{I} and removing \mathbf{K}_{BD} and \mathbf{K}_{DB} from the diffusivity matrix of the problem. The effect of the preset essential boundary condition is reintroduced by calculating the change of the domain through \mathbf{K}_{DB} :

$$\begin{bmatrix} \mathbf{K}_{DD} & 0 \\ 0 & \mathbf{I} \end{bmatrix} \begin{bmatrix} \mathbf{T}_D \\ \mathbf{T}_B \end{bmatrix} = \begin{bmatrix} \mathbf{R}_D - \mathbf{K}_{DB}\mathbf{R}_B \\ \mathbf{R}_B \end{bmatrix}. \quad (2.17)$$

However, applying the essential boundary through this method does not allow for high accuracy when the prescribed value on the boundary is a function of space, as the prescribed temperature $\bar{T}(\mathbf{x})$ might not be interpolated accurately by higher order hierarchical shape functions. The next section describes an alternative to this approach, where the essential boundary condition is enforced through the least squares method.

2.3.2 Temperature BC applied through the least squares method

The aim of this method is to minimise the error between the prescribed boundary condition \bar{T} and the solution T on the boundary Γ_T . Such an error can be defined as:

$$Z(T) = \frac{1}{2} \int_{\Gamma_T} (T - \bar{T})^2 d\Gamma. \quad (2.18)$$

The weak form for the least squares method is derived by minimising the error (2.18) by

taking a variation with respect to T and setting it equal to zero:

$$\int_{\Gamma_T} \delta T T \, d\Gamma = \int_{\Gamma_T} \delta T \bar{T} \, d\Gamma \quad \forall \delta T \in H^{1/2}(\Gamma), \quad (2.19)$$

where $H^{1/2}(\Gamma)$ is the space for traces of functions from $H^1(\Omega)$ on the boundary [Boffi et al., 2013].

Applying shape functions to the variation δT and the solution T in the same way as described by (2.9), the discretised form of the least squares method is as follows:

$$\delta T_\beta \int_{\Gamma_T} (N_\beta N_\alpha) \, d\Gamma T_\alpha = \delta T_\beta \int_{\Gamma_T} N_\beta \bar{T} \, d\Gamma \quad \forall \delta T_\beta. \quad (2.20)$$

Note that δT is set to zero on Γ_T for the diffusion formulation described in this chapter. Therefore, the rows of the stiffness matrix and the force vector corresponding to the essential boundary are zero. However, by using least squares method, the (2.20) is added to the main problem formulation, and the rows of the stiffness matrix and the force vector corresponding to the essential boundary are no longer zero. The amended matrix form (2.20) can then be presented as:

$$\begin{bmatrix} \mathbf{K}_{DD} & \mathbf{K}_{DB} \\ \mathbf{0} & \int_{\Gamma_T} N_\beta N_\alpha \, d\Gamma \end{bmatrix} \begin{bmatrix} \mathbf{T}_D \\ \mathbf{T}_B \end{bmatrix} = \begin{bmatrix} \mathbf{R}_D \\ \int_{\Gamma_T} N_\beta \bar{T} \, d\Gamma \end{bmatrix} \quad (2.21)$$

where \mathbf{K}_{DD} , \mathbf{K}_{DB} and \mathbf{R}_D remain unchanged from the main problem formulation (2.12), and \mathbf{K}_{BB} and \mathbf{F}_B are defined by the least squares method.

In practise, \mathbf{K}_{BB} is not neatly organised in a corner of the global matrix \mathbf{K} , and the matrix \mathbf{K} itself becomes asymmetric, therefore, the use of more advanced solving algorithms is advised. Such matrices could be solved robustly with block solvers, e.g. FieldSplit in PETSc [Sanan et al., 2022].

2.3.3 Convergence to the exact solution

A convergence to the exact solution with mesh and approximation order refinement is expected when solving a problem with a finite element method. This has been demonstrated and confirmed in literature [Zienkiewicz and Taylor, 2000; Lienhard and Lienhard, 2020] but an example is provided here for the sake of completeness and to demonstrate the convergence of the implemented code. The following chapters will use the same approach to demonstrate the convergence of the implemented methods for more complex problems.

To verify the implementation, a heat transfer problem in a square domain with a known analytical solution is studied, see Figure 2.3. This toy example is a two-dimensional heat diffusion

problem with a sinusoidal source term and Dirichlet boundary conditions and contains no high localised gradients or flux singularities. The plotted exact solution, its gradient and source are shown in Figure 2.4 for a linear thermal conductivity $k = 1 \text{ W/(m} \cdot \text{ }^\circ\text{C)}$.

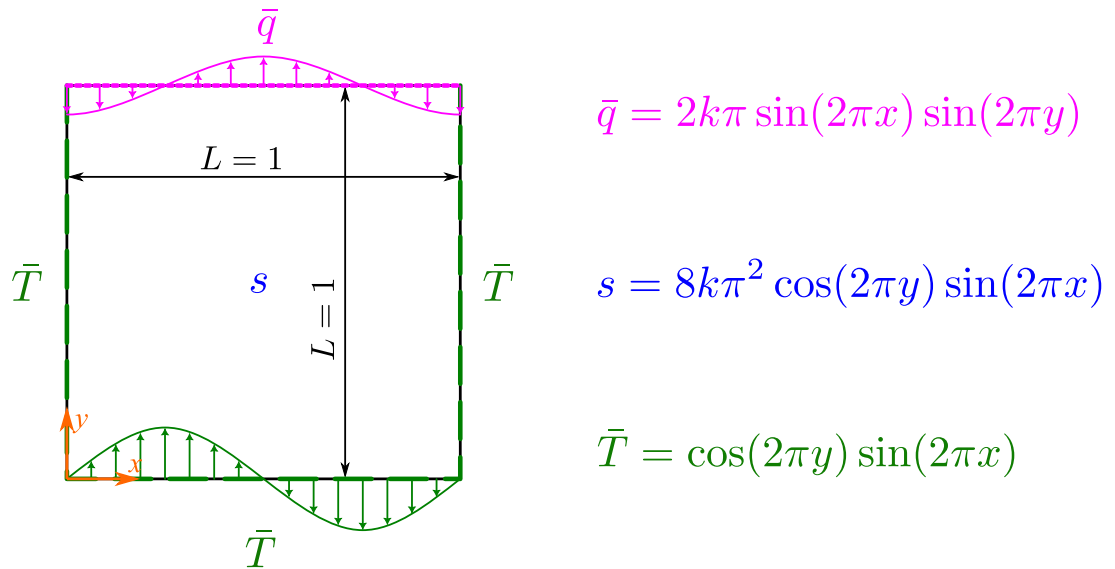


Figure 2.3: Example SinCos: Corresponding to the exact solution $\tilde{T} = \cos(2\pi y) \sin(2\pi x)$. The domain is a square with side length $L = 1 \text{ m}$ and the temperature \bar{T} is prescribed to three sides of the boundary. The source term s and prescribed flux boundary condition \bar{q} , are dependent on the heat conductivity k .

The verification is assessed by calculating the L^2 -norms and H^1 -seminorm of the errors with respect to the exact solutions [Brenner and Scott, 2008; Boffi et al., 2013] of temperature \tilde{T} , temperature gradient $\nabla \tilde{T}$ and flux $\tilde{\mathbf{q}}$, see Figure 2.4 for the plotted exact solutions. The global norms of the errors [Boffi et al., 2013] are calculated as follows:

L^2 -norm of the temperature error:

$$\|T - \tilde{T}\|_{\Omega} = \left(\int_{\Omega} |T - \tilde{T}|^2 d\Omega \right)^{1/2}. \quad (2.22)$$

H^1 -seminorm of the temperature error, equal to the L^2 -norm of the gradient error:

$$|T - \tilde{T}|_{1,\Omega} = \left(\int_{\Omega} |\nabla T - \nabla \tilde{T}|^2 d\Omega \right)^{1/2}. \quad (2.23)$$

L^2 -norm of the flux error:

$$\|\mathbf{q} - \tilde{\mathbf{q}}\|_{\Omega} = \left(\int_{\Omega} |\mathbf{q} - \tilde{\mathbf{q}}|^2 d\Omega \right)^{1/2}. \quad (2.24)$$

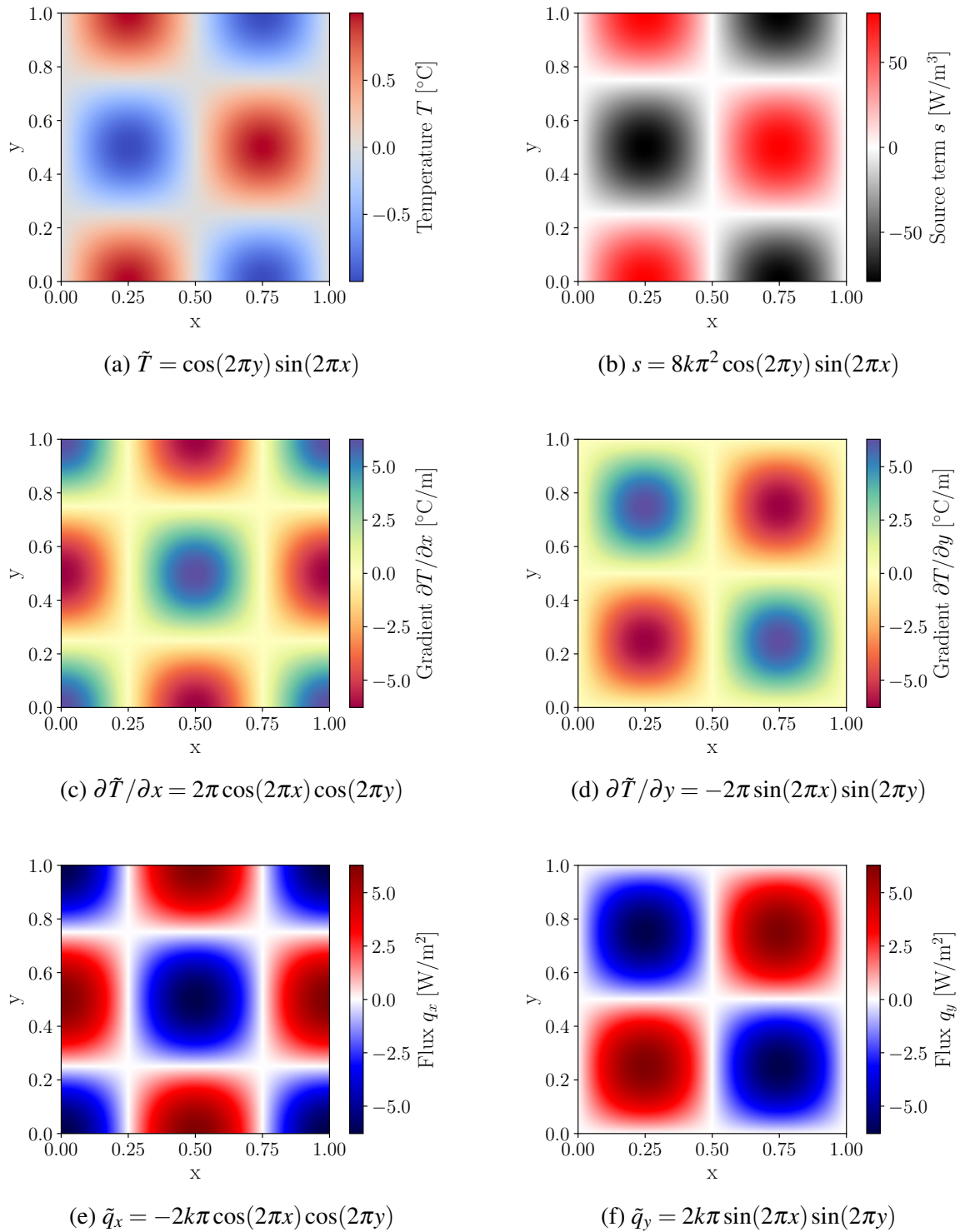


Figure 2.4: Example SinCos: Exact solution, its gradient, flux and source term for the linear diffusion problem with thermal conductivity $k = 1 \text{ W}/(\text{m} \cdot ^{\circ}\text{C})$.

The convergence of the global errors with respect to the exact solution is shown in Figure 2.5. The figure shows the convergence w.r.t. the element size (left) and the number of integration points (right). The reason for showing the number of integration points instead of the number of degrees of freedom is due to the fact that in later chapters, chapters 4 and 5, a data search will take place at every integration point of the domain. The number of integration points is, therefore, a more relevant parameter to show the convergence with respect to and will be used from this point onwards because that will affect the overall time of the calculation.

The global errors decrease with the mesh and approximation order refinement, which confirms the correctness of the implemented code and sets up an example to compare to in the future chapters. In 2D, the total number of Gauss points in a regular mesh is inversely proportional to h^2 , therefore, the slope on the right hand side of Figure 2.5 is 2 times smaller and the trend is in the opposite direction.

Additionally, the slope of the convergence can be checked using the *a priori* error estimators for the standard finite element method [Grätsch and Bathe, 2005]:

$$\begin{aligned} \|\tilde{T} - T^h\|_{\Omega} &\leq Ch^{p+1}, \\ |\tilde{T} - T^h|_{1,\Omega} &\leq Ch^p, \\ \|\tilde{\mathbf{q}} - \mathbf{q}^h\|_{\Omega} &\leq Ch^p, \end{aligned} \tag{2.25}$$

where C is a constant, h is the element size, and p is the approximation order of the temperature T field. The convergence rates of the global errors with respect to the element size and the number of integration points are shown in Figure 2.5 and for the element sizes agree with the *a priori* error estimators (2.25).

Next section will focus on nonlinear diffusion problems and their linearisation with the Newton-Raphson method as another example to refer to in future chapters.

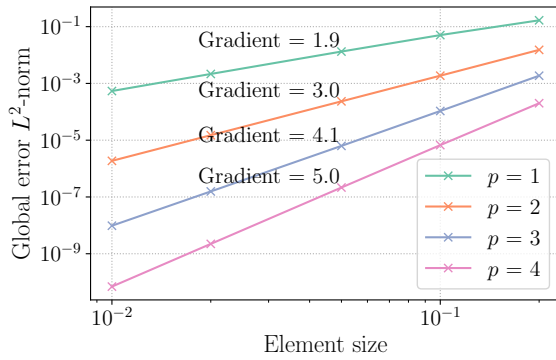
2.4 Nonlinear diffusion problems

Nonlinearity of the problem can be introduced through the thermal conductivity k in the Fourier's law (2.3). The conductivity k can be a function of temperature T , gradient of temperature ∇T , age of the material, its porosity, or any other influential factors. The resulting constitutive relation could be highly nonlinear and depend on a lot of empirical parameters.

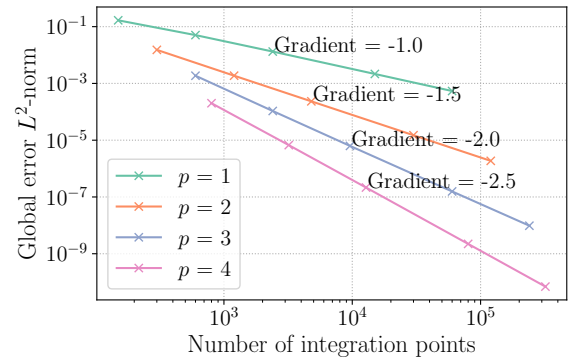
In this thesis, we will focus on the case when the thermal conductivity k is a function of temperature T only, for example:

$$k(T) = a + bT + cT^2, \tag{2.26}$$

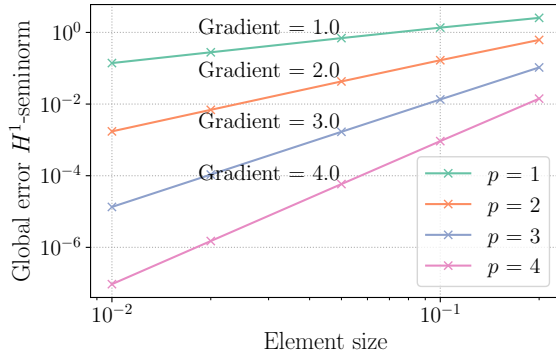
where a , b and c are constants, which corresponds to one of the possible representations of heat transfer thermal conductivity (1.1) in nuclear graphite [McEligot et al., 2016].



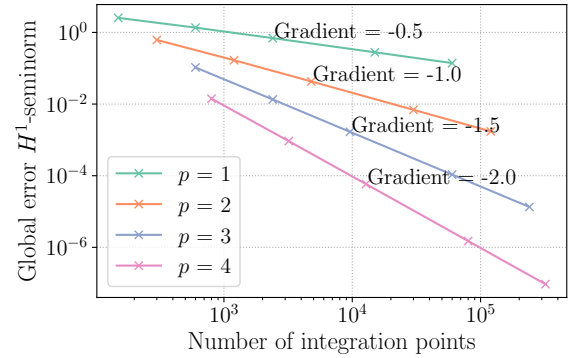
(a)



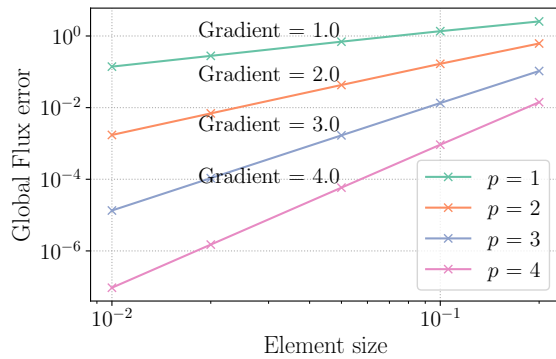
(b)



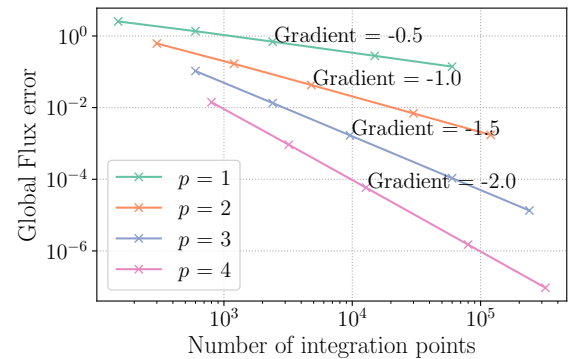
(c)



(d)



(e)



(f)

Figure 2.5: Example SinCos: Convergence of the finite element solution to the exact one with decreasing element size and increasing approximation order. a) and b) show the L^2 -norm, c) and d) show the H^1 -seminorm, e) and f) show the flux error norm, whereas left column shows the convergence with decreasing element size and right column shows the convergence with increasing number of integration points.

When thermal conductivity k is a nonlinear function of T , the conservation of energy law (2.1) can be written as:

$$\nabla \cdot (-k(T)\nabla T) = s \quad \text{in } \Omega. \quad (2.27)$$

The boundary conditions (2.2) remain the same as in the linear case and the nonlinear weak form of the problem (2.27) can be written as:

$$\int_{\Omega} k(T)\nabla\delta T \cdot \nabla T \, d\Omega - \int_{\Gamma_q} \delta T \bar{q} \, d\Gamma = \int_{\Omega} \delta T s \, d\Omega \quad \forall \delta T \in H_0^1(\Omega), \quad (2.28)$$

where the gradients ∇T and $\nabla\delta T$ are considered as dependent variables, which is consistent with the finite element approximation.

However, unlike the linear case, nonlinear problems require linearisation.

2.4.1 Linearisation of nonlinear diffusion problems

There are multiple ways to linearise a nonlinear problem [Zienkiewicz and Taylor, 2000]. This example follows the consistent linearisation using Newton-Raphson method. Starting with definition of the residual, or the "right-hand-side" of the problem:

$$R(T; \delta T) = 0 \quad \forall \delta T \in H_0^1(\Omega) \quad (2.29)$$

which represents (2.28):

$$R(T; \delta T) = \int_{\Omega} k(T)\nabla\delta T \cdot \nabla T \, d\Omega - \int_{\Gamma_q} \delta T \bar{q} \, d\Gamma - \int_{\Omega} \delta T s \, d\Omega. \quad (2.30)$$

Substituting the nonlinear thermal conductivity $k(T)$, see (2.26),

$$R(T; \delta T) = \int_{\Omega} (a + bT + cT^2) \nabla\delta T \cdot \nabla T \, d\Omega - \int_{\Gamma_q} \delta T \bar{q} \, d\Gamma - \int_{\Omega} \delta T s \, d\Omega. \quad (2.31)$$

To find the field T for which the residual $R(T; \delta T)$ is zero (for any δT) or is sufficiently small, the Newton-Raphson method is one of the most common approaches to solving nonlinear equations. Writing the expansion of $R(T; \delta T)$ into Taylor series around T_0 [Bonet and Wood, 1997],

$$R(T_0 + \Delta T; \delta T) = R(T_0; \delta T) + DR(T_0; \delta T) [\Delta T] + O(\Delta T^2), \quad (2.32)$$

where T_0 is the temperature field in the last iteration (or the last converged step), ΔT is the change in the temperature field, and $O(\Delta T^2)$ represent the higher order terms in ΔT which approach zero when ΔT is small and are therefore neglected, see [Zienkiewicz and Taylor, 2000; Bonet and Wood, 1997] for more information. Note that in (2.32), the derivative with respect to ∇T

is not taken, as ∇T is considered to be dependent on T , which will be enforced using the finite element approximation.

$DR(T_0; \delta T) [\Delta T]$ is the Gateaux (directional) derivative of the residual $R(T; \delta T)$ with respect to the change in the temperature field in direction of ΔT at T_0 [Bonet and Wood, 1997]:

$$DR(T_0; \delta T) [\Delta T] = \lim_{\varepsilon \rightarrow 0} \frac{R(T_0 + \varepsilon \Delta T; \delta T) - R(T_0; \delta T)}{\varepsilon}. \quad (2.33)$$

Computing the Gateaux (directional) derivative and using the chain rule, results in the following:

$$DR(T_0; \delta T) [\Delta T] = \int_{\Omega} \nabla \delta T \cdot [(a + bT_0 + cT_0^2) \nabla \Delta T + (b + 2cT_0) \nabla T_0 \Delta T] d\Omega. \quad (2.34)$$

To discretise the residual and its Gateaux derivative, the finite element base functions are used to approximate the test and change functions δT and ΔT respectively:

$$\delta T^h = \delta T_{\beta} N_{\beta} \quad \text{and} \quad \Delta T^h = \Delta T_{\gamma} N_{\gamma} \quad (2.35)$$

where the summation over repeated indices is assumed and gradients are dependants, following the same principles as (2.9) and (2.10). Again, for brevity, we preserve the same notations for discretised entities as were introduced in the continuous problem statement.

When the residual of the current step $R(T_0 + \Delta T, \delta T_{\beta})$ is equated to zero for any coefficients δT_{β} , see (2.32), the coefficients of the change in temperature field ΔT_{γ} can be obtained by solving the system of equations presented in the matrix form:

$$[\mathbf{K}_{\beta\gamma}] [\Delta \mathbf{T}_{\gamma}] = -[\mathbf{R}_{\beta}], \quad (2.36)$$

where $[\Delta \mathbf{T}_{\gamma}]$ is the vector of unknown coefficients, $[\mathbf{K}_{\beta\gamma}]$ is the tangent matrix [Bonet and Wood, 1997] derived from (2.34):

$$[\mathbf{K}_{\beta\gamma}] = \int_{\Omega} (a + bT_0 + cT_0^2) (\nabla N_{\beta} \cdot \nabla N_{\gamma}) + (b + 2cT_0) N_{\gamma} (\nabla N_{\beta} \cdot \nabla T_0) d\Omega, \quad (2.37)$$

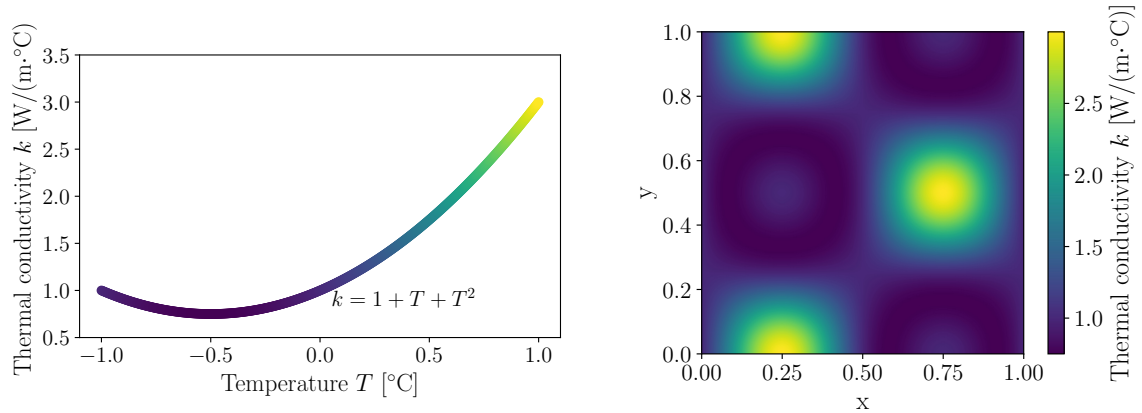
and $[\mathbf{R}_{\beta}]$ is the residual vector derived from (2.31):

$$[\mathbf{R}_{\beta}] = \int_{\Omega} (a + bT_0 + cT_0^2) \nabla N_{\beta} \cdot \nabla T_0 d\Omega - \int_{\Omega} N_{\beta} s d\Omega - \int_{\Gamma_q} N_{\beta} \bar{q} d\Gamma. \quad (2.38)$$

The boundary conditions can be satisfied in a similar way to the the linear case, see section 2.2 and section 2.3 for more information.

2.4.2 Convergence to the exact solution

The same convergence analysis is performed for the nonlinear diffusion problem as for the linear diffusion problem subsection 2.3.3. The problem setup is shown in Figure 2.3, however, the thermal conductivity is now nonlinear with respect to the temperature T , see Figure 2.6 for the plotted thermal conductivity $k(T)$ on the domain considered, for the given exact solution shown in Figure 2.3.



(a) Nonlinear thermal conductivity k in relation to temperature T . (b) Thermal conductivity corresponding to the exact solution, $\tilde{T} = \cos(2\pi y) \sin(2\pi x)$.

Figure 2.6: Example SinCos: Nonlinear thermal conductivity $k(T) = 1 + T + T^2$. Note that (b) is for demonstration purposes only and is not an input for the analysis.

The exact formulas for fluxes and sources for the nonlinear SinCos example also differ from the linear case since they depend on the thermal conductivity $k(T)$, see Figure 2.7 for the plotted exact solutions and sources.

The convergence with respect to the exact solution is shown in Figure 2.8.

The global errors decrease with the mesh and approximation order refinement in the same convergence rate as the linear example, see Figure 2.5. The convergence rate follows the a priori error estimation (2.25), which verifies the implemented code and sets up an example to compare to in future chapters.

The material nonlinearity was introduced through thermal conductivity $k(T)$, which depends on the temperature T . However, the definition of material behaviour varies according to the material and where it is applied, and it often depends on empirical material parameters. Furthermore, most material models are approximations and interpolations of collected material data, and although significantly different material laws may require customised formulations, modern FE codes typically generalise the linearisation process to accommodate a broad class of nonlinear behaviours [Zienkiewicz et al., 2010; Wriggers, 2008]. Nevertheless, an alternative approach to using nonlinear material models is discussed in chapter 4.

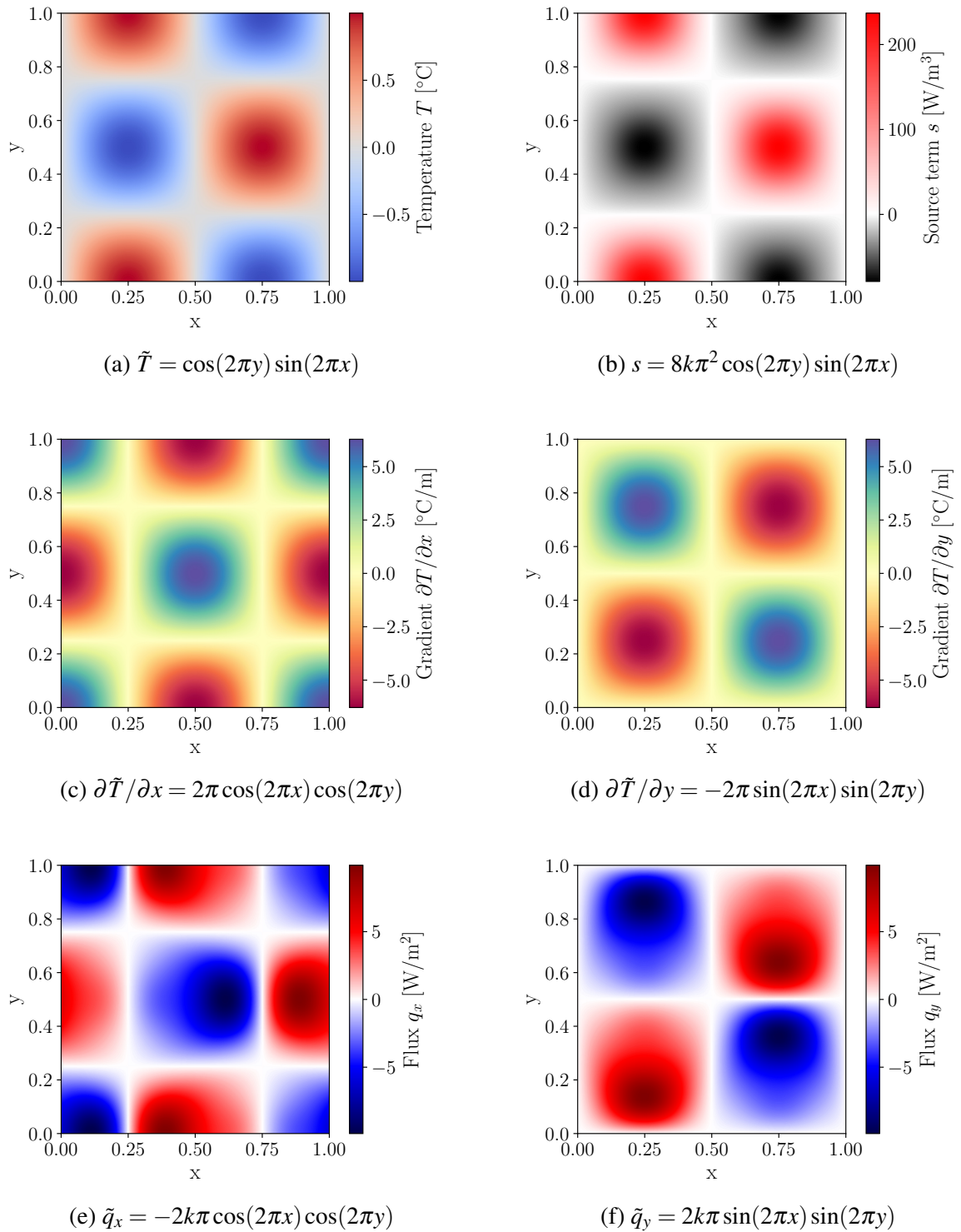
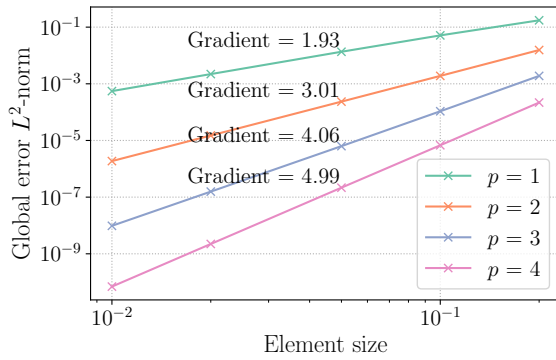
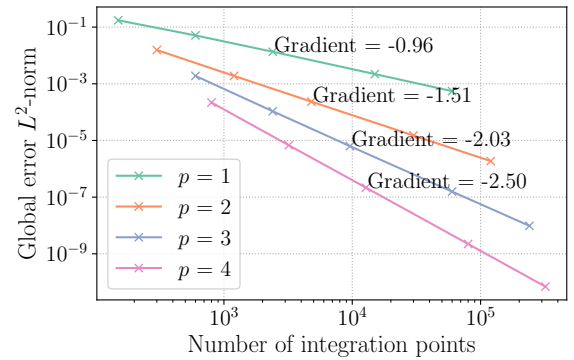


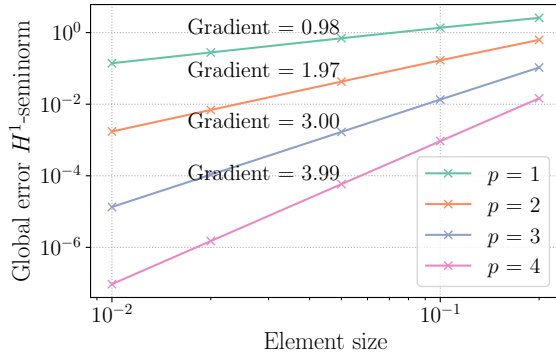
Figure 2.7: Example SinCos (nonlinear): Exact solutions and applied source term for the nonlinear diffusion problem with thermal conductivity $k = 1 + T + T^2$.



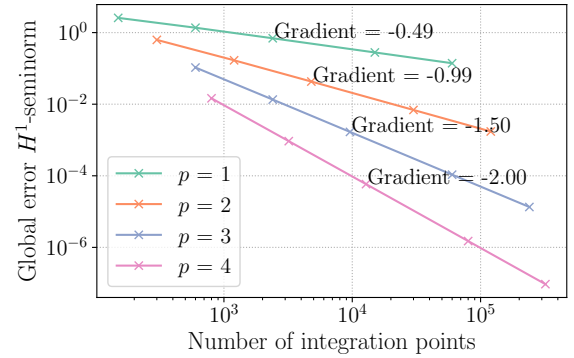
(a)



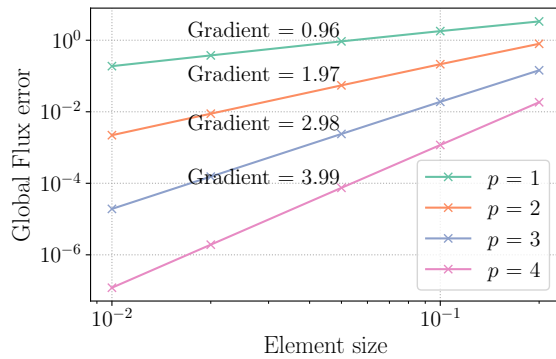
(b)



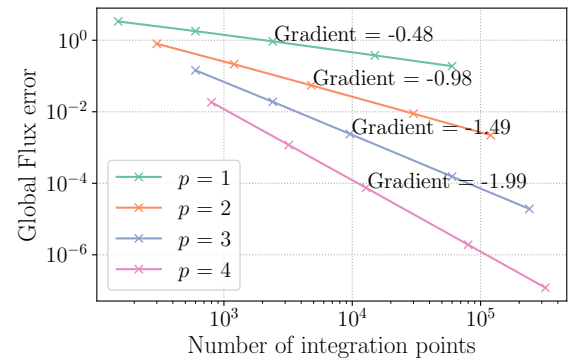
(c)



(d)



(e)



(f)

Figure 2.8: Example SinCos (nonlinear): Convergence of nonlinear diffusion problem global errors with respect to the exact solution with mesh and approximation order refinement. a) and b) show the L^2 -norm, c) and d) show the H^1 -seminorm, e) and f) show the flux error norm, whereas left column shows the convergence with respect to the element size and right column shows the convergence with respect to the number of integration points.

2.5 Summary

In this chapter, the classical finite element approach to solving diffusion problems, both linear and nonlinear, was described. The subsequent chapters will refer to it as a benchmark to compare the results of other formulations and methods. Convergence was achieved with mesh and approximation order refinement as the results were compared to the exact solution. However, the error estimation introduced here is tied to knowing the exact solution and the refinement used is global.

The next chapter will introduce the concept of mixed formulation and its application to diffusion problems. Some of the benefits of this approach include error estimation without the need for knowing the exact solution providing the possibility of a local (adaptive) mesh and approximation order refinement.

Chapter 3

Mixed formulation for diffusion problems

The previous chapter described a more common (standard) approach to solving diffusion problems, including linear and nonlinear heat transfer, with the finite element method. This chapter starts with the same equations of equilibrium, constitutive behaviour and boundary conditions, but the approach to solving the problem is different, as we will use so-called mixed formulation.

One way to introduce the concept of the mixed formulation is by highlighting the similarities and differences between coupled problems and mixed problem formulations. Coupled problems involve the interaction of two or more sub-problems, each governed by distinct physics and described by multiple variables, e.g. thermoelasticity, electroelasticity, fluid-structure interaction, fluid-particle interaction, magnetohydrodynamics, etc. [Boffi et al., 2013; Zienkiewicz et al., 2010]. On the other hand, the mixed problem formulation introduces one or more auxiliary variables in a problem governed by one physical process. In this chapter, two-field solution will be obtained for the heat diffusion problem: temperature T corresponding to the primary variable, and heat flux \mathbf{q} as the auxiliary (secondary) variable.

The variables are assigned functional spaces approximated by relevant finite element basis functions. In particular, the heat flux is approximated in $H(\text{div})$ functional space, which ensures that the flux is continuous across any inner boundaries, which ensures that the conservation law is satisfied *a priori*, and is therefore natural for the diffusion problems. The temperature is approximated in L^2 functional space, which allows for discontinuities across the element boundaries. The chapter will also describe *a posteriori* error estimates provided by the choice of the functional spaces and an example of how they can be utilised for adaptive mesh and/or order refinement for the problem.

3.1 Linear diffusion problems - mixed formulation

The conservation law and boundary conditions for this problem are the same as in the previous chapter and are shown in (2.1) and (2.2) respectively, also see Figure 2.1.

First, to obtain the mixed formulation [Boffi et al., 2013], the constitutive relation (2.3) is

added as a separate equation alongside (2.1) and (2.2). The heat flux becomes an independent variable leading to the problem statement:

Find $T \in L^2$ and $\mathbf{q} \in \mathcal{Q}$ such that:

$$\begin{cases} \nabla \cdot \mathbf{q} = s & \text{in } \Omega & (3.1a) \\ \mathbf{q}/k = -\nabla T & \text{in } \Omega & (3.1b) \\ \mathbf{q} \cdot \mathbf{n} = \bar{q} & \text{on } \Gamma_q & (3.1c) \\ T = \bar{T} & \text{on } \Gamma_T. & (3.1d) \end{cases}$$

To obtain the weak form of the problem, (3.1a) is multiplied by a scalar test function δT and integrated over the domain Ω . Additionally, (3.1b) is multiplied by a vectorial test function $\delta \mathbf{q}$ and integrated over the domain Ω . These steps result in the following equations:

$$\begin{cases} \int_{\Omega} \delta T (\nabla \cdot \mathbf{q}) d\Omega = \int_{\Omega} \delta T s d\Omega & \forall \delta T \in L^2(\Omega) & (3.2a) \\ \int_{\Omega} \frac{1}{k} \delta \mathbf{q} \cdot \mathbf{q} d\Omega = - \int_{\Omega} \delta \mathbf{q} \cdot \nabla T d\Omega & \forall \delta \mathbf{q} \in \mathcal{Q}_0, & (3.2b) \end{cases}$$

where $L^2(\Omega)$ is a space of square-integrable scalar functions and \mathcal{Q}_0 is a space of square-integrable vectorial functions with square integrable divergence and zero normal component on the boundary Γ_q , for more information on functional spaces see Table 3.1 and Appendix A.

The right-hand side term $\int_{\Omega} \delta \mathbf{q} \cdot \nabla T d\Omega$ in (3.2b) is integrated by parts and the temperature boundary condition (3.1d) is applied on the boundary Γ_T , note that $\delta \mathbf{q} \cdot \mathbf{n} = 0$ on Γ_q , resulting in the following weak form of the problem (3.2):

Find $T \in L^2$ and $\mathbf{q} \in \mathcal{Q}$ such that:

$$\begin{cases} \int_{\Omega} \delta T (\nabla \cdot \mathbf{q}) d\Omega = \int_{\Omega} \delta T s d\Omega & \forall \delta T \in L^2(\Omega) & (3.3a) \\ \int_{\Omega} \frac{1}{k} \delta \mathbf{q} \cdot \mathbf{q} d\Omega = \int_{\Omega} (\nabla \cdot \delta \mathbf{q}) T d\Omega - \int_{\Gamma_T} (\delta \mathbf{q} \cdot \mathbf{n}) \bar{T} d\Gamma_T & \forall \delta \mathbf{q} \in \mathcal{Q}_0, & (3.3b) \end{cases}$$

where the spaces for trial and test functions are defined in Table 3.1.

The temperature T , flux \mathbf{q} and test functions δT and $\delta \mathbf{q}$ are approximated by the finite element basis functions N and \mathbf{Q} as shown in Table 3.2.

Substituting the approximations into the weak form (3.3) and multiplying (3.3a) by (-1) to

Field	Space
Temperature T (trial function)	$T \in L^2(\Omega)$
δT (test function)	$\delta T \in L^2(\Omega)$
Flux \mathbf{q} (trial function)	$\mathbf{q} \in \mathcal{Q} = \{\mathbf{u} \in H(\text{div}; \Omega) \mid \mathbf{u} \cdot \mathbf{n} = \bar{q} \text{ on } \Gamma_q\}$
$\delta \mathbf{q}$ (test function)	$\delta \mathbf{q} \in \mathcal{Q}_0 = \{\mathbf{v} \in H(\text{div}; \Omega) \mid \mathbf{v} \cdot \mathbf{n} = 0 \text{ on } \Gamma_q\}$

Table 3.1: Functional spaces for the mixed formulation of the diffusion problem.

	Trial function	Test function
Temperature	$T^h = T_a N_a$	$\delta T^h = \delta T_b N_b$
Flux	$\mathbf{q}^h = q_{\mathcal{A}} \mathbf{Q}_{\mathcal{A}}$	$\delta \mathbf{q}^h = \delta q_{\mathcal{B}} \mathbf{Q}_{\mathcal{B}}$
Divergence of flux	$\nabla \cdot \mathbf{q}^h = q_{\mathcal{A}} (\nabla \cdot \mathbf{Q}_{\mathcal{A}})$	$\nabla \cdot \delta \mathbf{q}^h = \delta q_{\mathcal{B}} (\nabla \cdot \mathbf{Q}_{\mathcal{B}})$

Table 3.2: Finite element basis functions for the mixed formulation of the diffusion problem. T_a , δT_b , $q_{\mathcal{A}}$ and $\delta q_{\mathcal{B}}$ are the coefficients of the approximation. N_a and N_b are the scalar base functions; and $\mathbf{Q}_{\mathcal{A}}$ and $\mathbf{Q}_{\mathcal{B}}$ are the vectorial base functions.

enable the symmetric form of the problem results in:

$$\left\{ \begin{array}{l} - \int_{\Omega} \delta T_b N_b (\nabla \cdot \mathbf{Q}_{\mathcal{A}}) q_{\mathcal{A}} d\Omega = - \int_{\Omega} \delta T_b N_b s d\Omega \quad \forall \delta T_b \\ - \int_{\Omega} \delta q_{\mathcal{B}} (\nabla \cdot \mathbf{Q}_{\mathcal{B}}) N_a T_a d\Omega + \int_{\Omega} \frac{1}{k} \delta q_{\mathcal{B}} (\mathbf{Q}_{\mathcal{B}} \cdot \mathbf{Q}_{\mathcal{A}}) q_{\mathcal{A}} d\Omega \\ = - \int_{\Gamma_T} \delta q_{\mathcal{B}} (\mathbf{Q}_{\mathcal{B}} \cdot \mathbf{n}) \bar{T} d\Gamma_T \quad \forall \delta q_{\mathcal{B}}. \end{array} \right. \quad (3.4)$$

Since (3.4) holds for any δT_b and $\delta q_{\mathcal{B}}$, the following saddle point problem in a matrix form is written as:

$$\begin{bmatrix} 0 & - \int_{\Omega} N_b (\nabla \cdot \mathbf{Q}_{\mathcal{A}}) d\Omega \\ - \int_{\Omega} (\nabla \cdot \mathbf{Q}_{\mathcal{B}}) N_a d\Omega & \int_{\Omega} \frac{1}{k} \mathbf{Q}_{\mathcal{B}} \cdot \mathbf{Q}_{\mathcal{A}} d\Omega \end{bmatrix} \begin{bmatrix} T_a \\ q_{\mathcal{A}} \end{bmatrix} = \begin{bmatrix} - \int_{\Omega} N_b s d\Omega \\ - \int_{\Gamma_T} (\mathbf{Q}_{\mathcal{B}} \cdot \mathbf{n}) \bar{T} d\Gamma_T \end{bmatrix}. \quad (3.5)$$

The mixed formulation can utilise the hierarchical shape functions available in MoFEM [Kaczmarczyk et al., 2020] and applies Gaussian quadrature to compute the integrals. To satisfy the LBB (Ladyzhenskaya-Babuška-Brezzi) stability conditions [Boffi et al., 2013; Gatica, 2014], which ensure the stability and convergence of mixed finite element methods by requiring a proper balance between the approximation spaces of the unknown fields, the approximation orders are assigned accordingly; see Table 3.3.

Field	Approximation order
Temperature T	p
Flux \mathbf{q}	$p + 1$

Table 3.3: Approximation orders for the mixed formulation of the diffusion problem.

Table 3.3 shows the approximation orders relation between the temperature T and the flux \mathbf{q} fields. If the temperature field is approximated by order p , the flux field is approximated by order $p + 1$. Trial and test functions are approximated by the same shape functions and using the same orders, i.e. Galerkin method [Demkowicz, 2024].

3.1.1 Boundary conditions in the mixed formulation

In the mixed formulation, the boundary conditions differ from the standard formulation for diffusion problems described in the previous chapter. The Neumann (flux) boundary condition (3.1c) is applied on the boundary Γ_q and is satisfied as an essential boundary condition, see space description in Table 3.1. The Dirichlet (temperature) boundary condition (3.1d) is applied on the boundary Γ_T , see (3.1d), and is satisfied as a natural boundary condition. The imposition of the boundary conditions in the mixed formulation is summarised in Table 3.4.

BC type	Field on which the condition is applied	Boundary
Essential	satisfied in the strong sense	$\Gamma_{\text{Essential}} = \Gamma_q$
Natural	imposed as a part of the weak form	$\Gamma_{\text{Natural}} = \Gamma_T$

Table 3.4: Imposition of boundary conditions in the mixed (weaker) formulation of the heat diffusion problem.

The essential (flux) boundary condition can be satisfied in a similar way to how it is described in section 2.3.

Figure 3.1 explains how the degrees of freedom are distributed and where the boundary conditions are applied. Note that the temperature and flux boundary conditions are swapped in comparison to the standard diffusion distribution, see Figure 2.2 for reference.

3.2 Convergence and *a priori* error estimates

To verify the implementation of the mixed formulation discussed above and demonstrate the effectiveness of the adaptive refinement driven by the error estimators, a diffusion problem in a square 2D domain with homogeneous Dirichlet boundary conditions prescribed on the whole

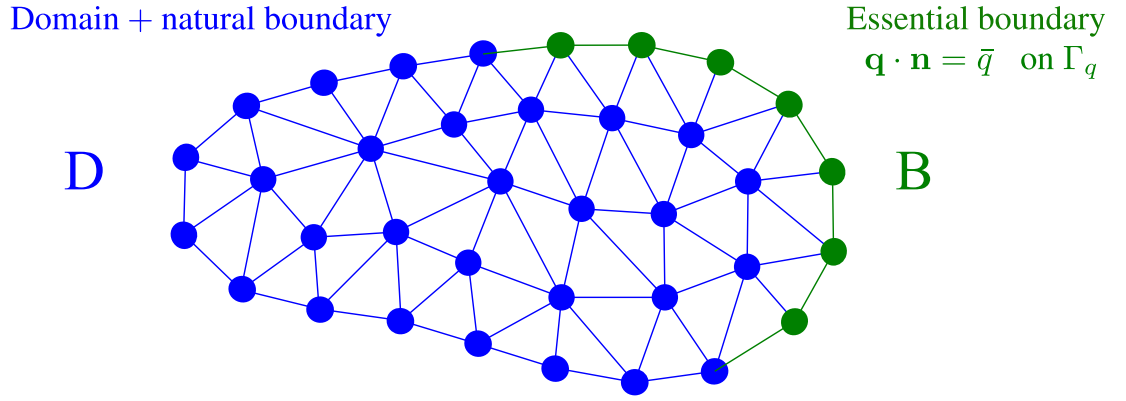


Figure 3.1: Discretisation of the domain Ω with the essential boundary Γ_q for the mixed formulation of the heat diffusion problem. The essential boundary is represented by the degrees of freedom B and the rest of the domain by the degrees of freedom D , which are different to the ones presented in Figure 2.2.

boundary is considered:

$$\begin{cases} \nabla \cdot \mathbf{q} = s & \text{in } \Omega := (-0.5; 0.5) \times (-0.5; 0.5) \\ \mathbf{q}/k = -\nabla T & \text{in } \Omega \\ T = 0 & \text{on } \partial\Omega. \end{cases} \quad (3.6)$$

For testing purposes, we constructed the problem for a given solution of temperature $\tilde{T}(x, y)$:

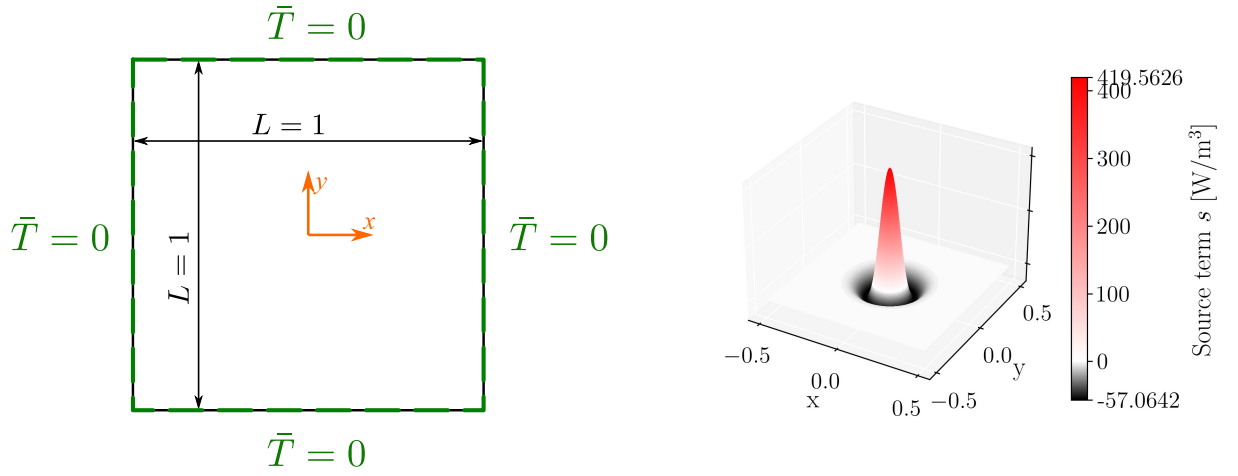
$$\tilde{T}(x, y) = e^{-100(x^2+y^2)} \cos \pi x \cos \pi y. \quad (3.7)$$

The source term $s(x, y)$ applied to the problem is obtained from the temperature $\tilde{T}(x, y)$ and the thermal conductivity k as follows:

$$\begin{aligned} s(x, y) = 2ke^{-100(x^2+y^2)} \{ & -200\pi x \sin(\pi x) \cos(\pi y) \\ & + \cos(\pi x) ((\pi^2 - 200(100x^2 + 100y^2 - 1)) \cos(\pi y) - 200\pi y \sin(\pi y)) \}. \end{aligned} \quad (3.8)$$

The exact solutions to temperature \tilde{T} , its gradient $\nabla \tilde{T}$, the heat flux \tilde{q} , and the source term s are shown in Figure 3.3. The example was chosen due to the localised high gradients which cause numerical difficulties and high finite element approximation errors with low order approximations. For this example, thermal conductivity $k = 1 \text{ W}/(\text{m} \cdot ^\circ\text{C})$ is used and the analysis setup is shown in Figure 3.2.

The resulting temperature field T is shown in Figure 3.4 for different approximation orders p . Due to the temperature field belonging to the L^2 space, the field is allowed to be discontinuous across the element boundaries. The jumps of temperature values between the elements decrease with higher approximation orders when the source term applied to the problem is continuous. Note that the approximation order can be decreased to 0 which corresponds to the values being



(a) Dimensions and boundary conditions.

(b) Source term (3.8) applied to the domain.

Figure 3.2: Example Exp-Hat: Analysis setup which corresponds to the exact solution $\tilde{T} = e^{-100(x^2+y^2)} \cos \pi x \cos \pi y$.

constant within the element.

Any finite element analysis with a unique solution contains *a priori* error estimates that depend on the mesh element size and the approximation order used. Figure 3.5 shows the convergence of the finite element solution to the exact one with decreasing element size and increasing approximation order.

The *a priori* error estimates for mixed formulation [Boffi et al., 2013] are:

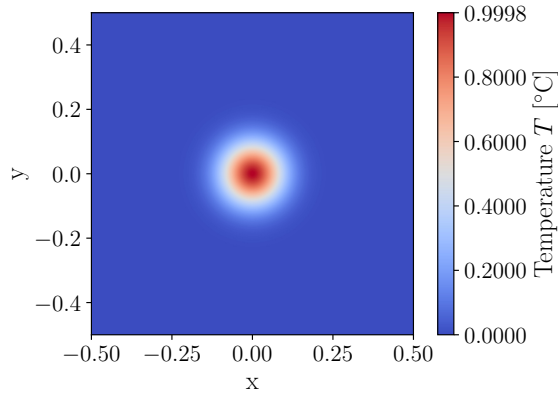
$$\begin{aligned}
 \|\tilde{T} - T^h\|_{\Omega} &\leq Ch^{p+1}, \\
 |\tilde{T} - T^h|_{1,\Omega} &\leq Ch^p, \\
 \|\tilde{\mathbf{q}} - \mathbf{q}^h\|_{\Omega} &\leq Ch^{p+2},
 \end{aligned} \tag{3.9}$$

where C is a constant which does not depend on the mesh, h is the element size, p is the approximation order of temperature field, note that the approximation order for flux is $p + 1$. The norms of the errors, see (2.22) (2.23) (2.24), are shown in Figure 3.5, and the convergence agrees with the error estimates (3.9).

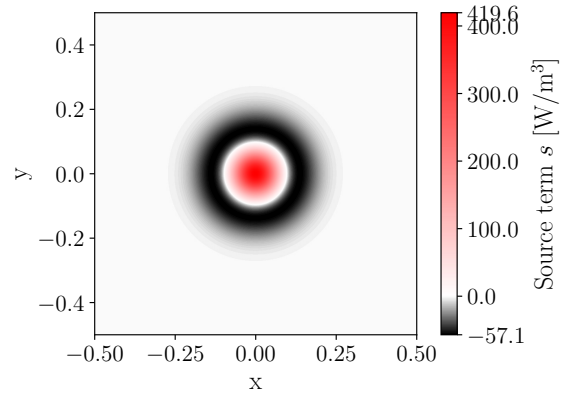
Furthermore, a comparison between the standard formulation described in the chapter 2 and the mixed formulation \tilde{T} is shown in Figure 3.6.

From Figure 3.6 (a-d) it can be seen that the L^2 -norm and H^1 -seminorm of the temperature error converge with the same order as the standard formulation. This is also confirmed with the same *a priori* estimates for the temperature field in (3.9). However, the flux error norm converges with a higher order than the standard formulation, as shown in Figure 3.6 (e-f). This is due to the higher approximation order of the flux field in the mixed formulation.

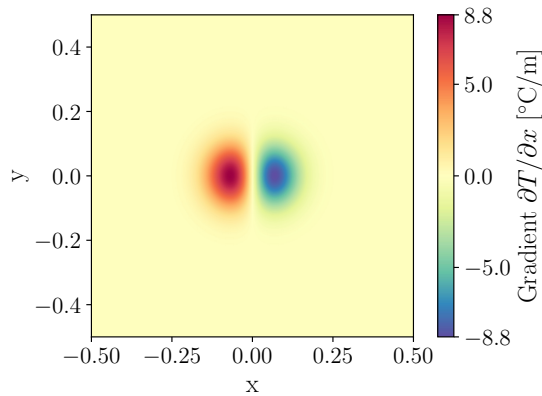
In the standard formulation, the flux is computed *a posteriori* by applying the conservation law to the gradient of the temperature field, resulting in the flux approximation equivalent of order $p - 1$, when the approximation of the temperature is of order p . On the other hand, if



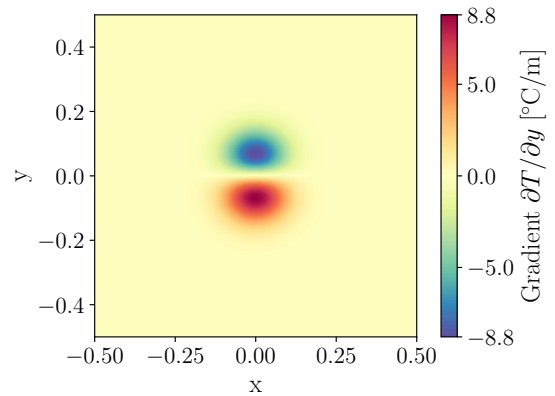
(a) $\tilde{T} = e^{-100(x^2+y^2)} \cos \pi x \cos \pi y$



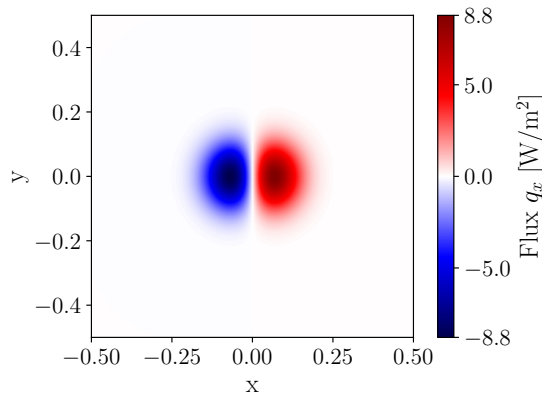
(b) Source s expressed in (3.8)



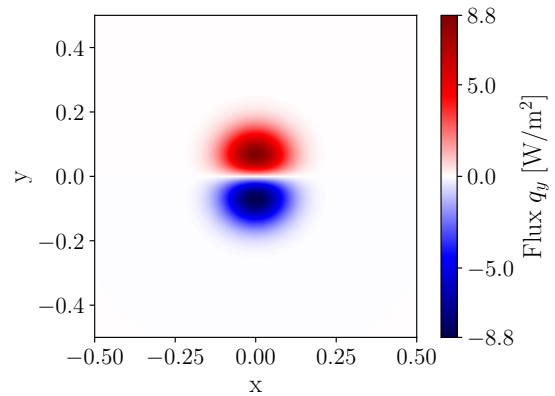
(c) $\frac{\partial \tilde{T}}{\partial x} = -e^{(-100(x^2+y^2))} \cos(\pi y) (200x \cos(\pi x) + \pi \sin(\pi x))$



(d) $\frac{\partial \tilde{T}}{\partial y} = -e^{(-100(x^2+y^2))} \cos(\pi x) (200y \cos(\pi y) + \pi \sin(\pi y))$



(e) $\tilde{q}_x = ke^{(-100(x^2+y^2))} \cos(\pi y) (200x \cos(\pi x) + \pi \sin(\pi x))$



(f) $\tilde{q}_y = ke^{(-100(x^2+y^2))} \cos(\pi x) (200y \cos(\pi y) + \pi \sin(\pi y))$

Figure 3.3: Example Exp-Hat: Exact solutions for the temperature, its gradient and the heat flux, and the source term for the linear heat diffusion problem with thermal conductivity $k = 1$ [W/(m· °C)].

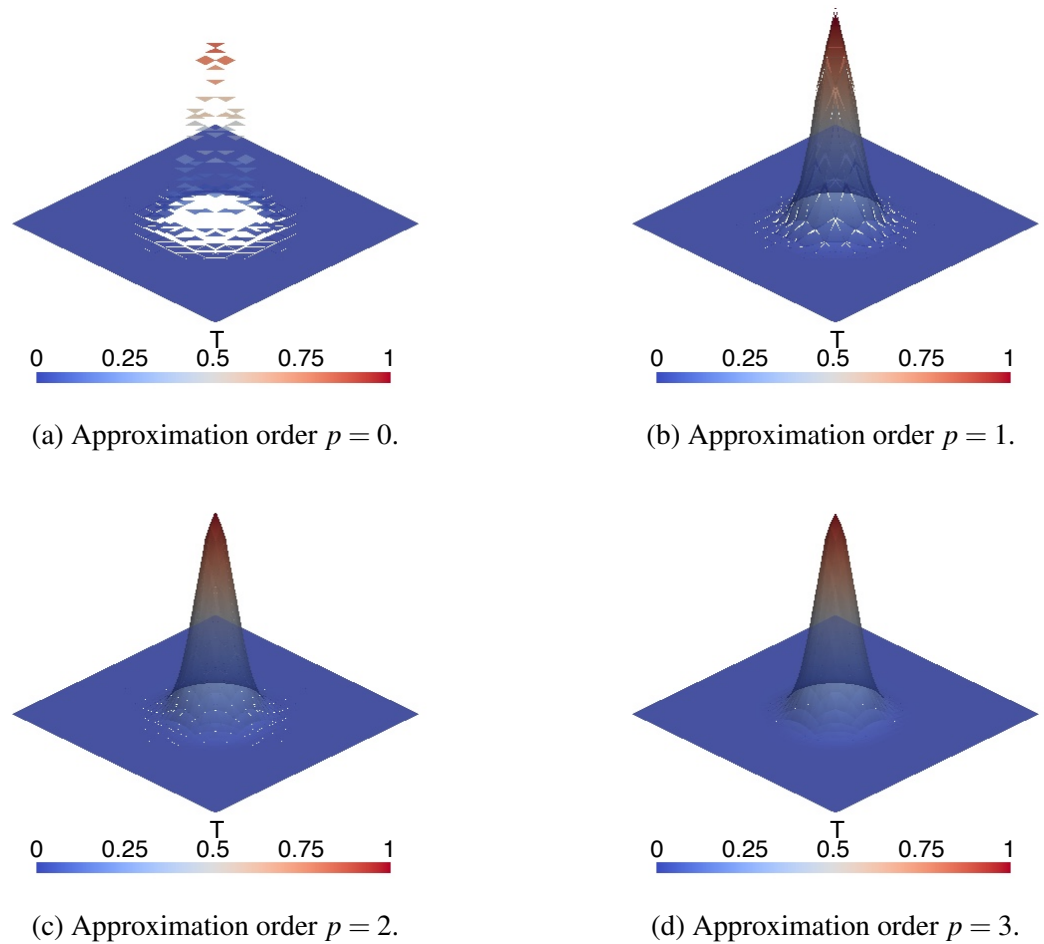
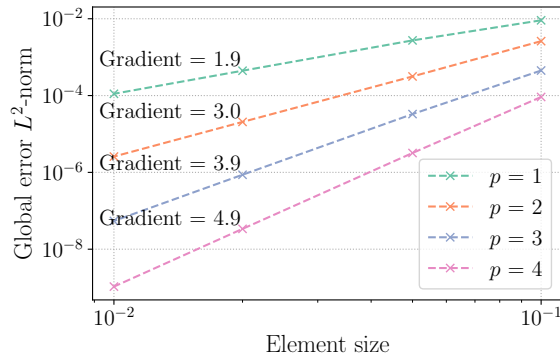
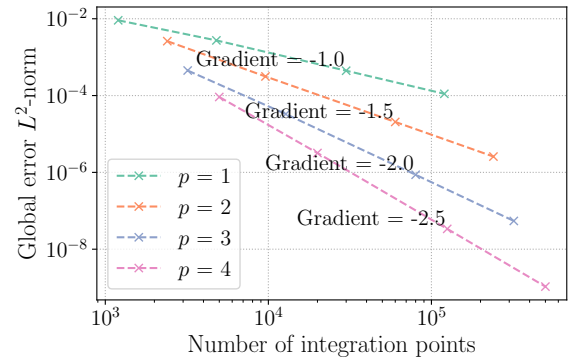


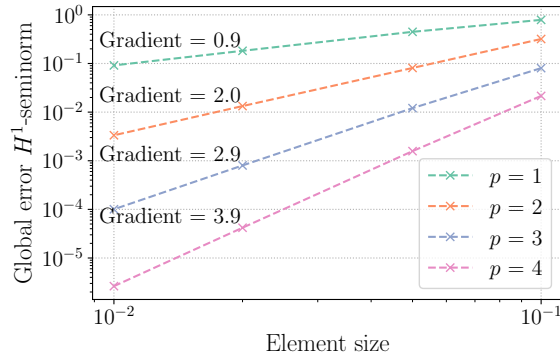
Figure 3.4: Example Exp-Hat: Temperature field T in L^2 showing jumps across the element boundaries with increasing approximation order p . Element size $h = 0.05$.



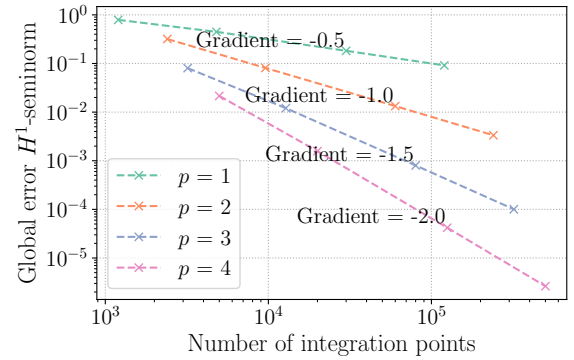
(a)



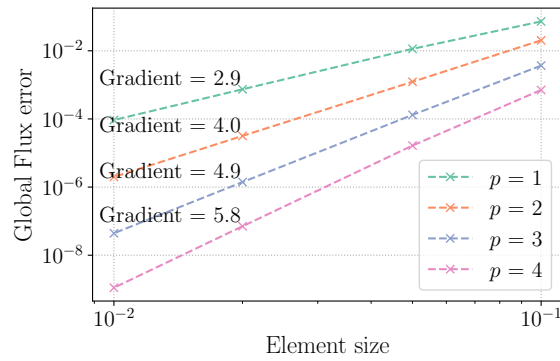
(b)



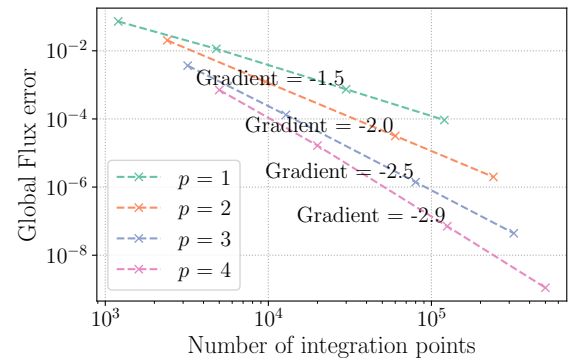
(c)



(d)



(e)



(f)

Figure 3.5: Example Exp-Hat: Convergence of the finite element solution to the exact one with decreasing element size and increasing approximation order. a) and b) show the L^2 -norm, c) and d) show the H^1 -seminorm, e) and f) show the flux error norm, whereas left column shows the convergence with respect to the element size and right column shows the convergence with respect to the number of integration points.

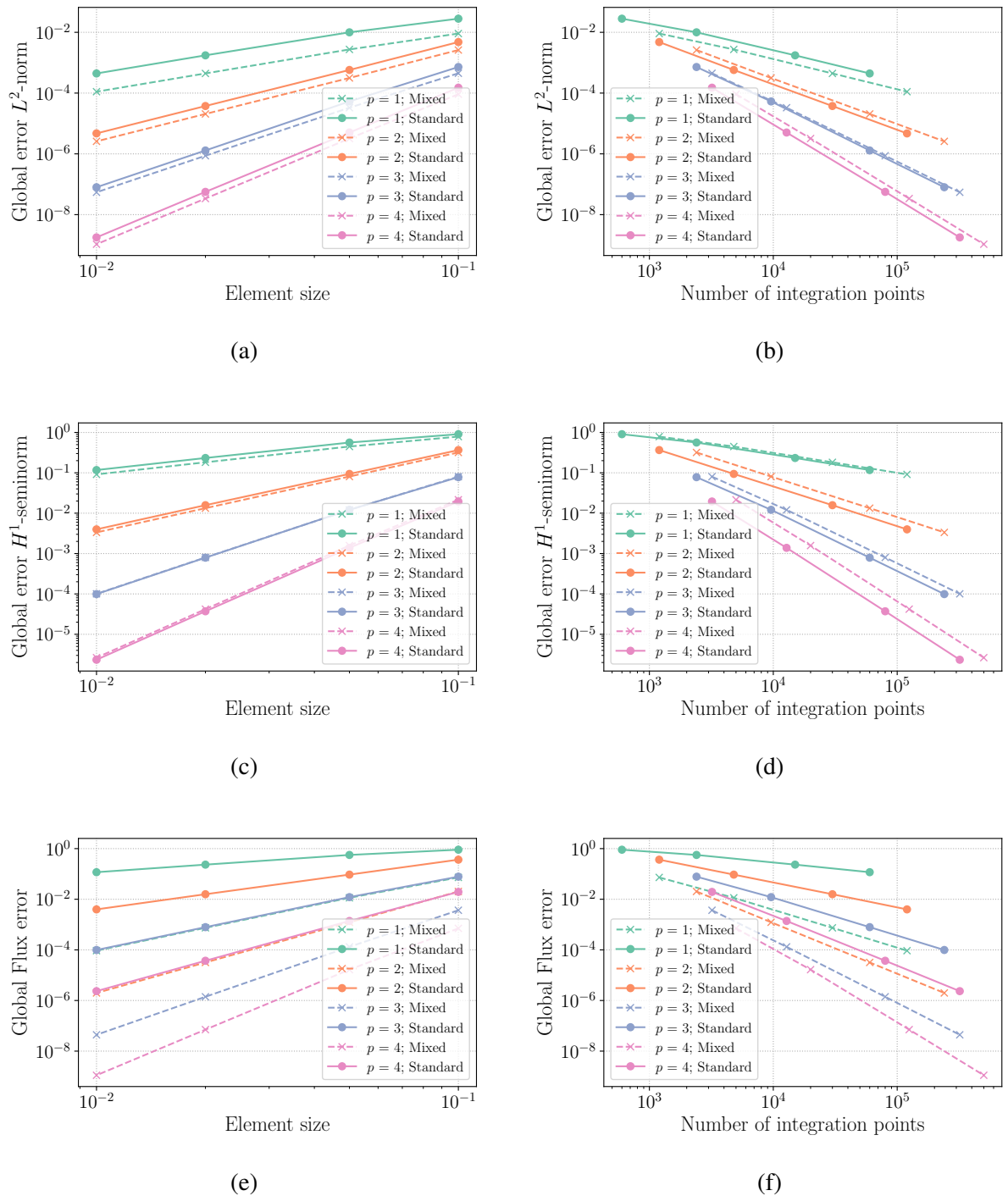


Figure 3.6: Example Exp-Hat: Comparison of convergence of the finite element solution obtained by the standard and mixed formulation to the exact one with decreasing element size and increasing approximation order. a) and b) show the L^2 -norm, c) and d) show the H^1 -seminorm, e) and f) show the flux error norm, whereas left column shows the convergence with respect to the element size and right column shows the convergence with respect to the number of integration points.

order p is chosen for the temperature field in the mixed formulation, the flux is approximated directly by the basis functions of order $p + 1$. This results in a higher convergence rate of the flux error norm compared to the standard formulation.

Nevertheless, these *a priori* error estimates describe global quantities and cannot be used for adaptive refinement in the presented formulation. Error indicators made for the standard approach that can be used for adaptive refinement exist [Oden et al., 1989], however, the mixed formulation allows for different embedded error indicators which are more straightforward to calculate. The following section will describe *a posteriori* error estimates and indicators that can be used for adaptive refinements with the mixed formulation described in this chapter.

3.3 *A posteriori* error estimators and indicators

Numerical solution obtained with the finite element method contains finite element approximation errors. Error estimators can be used to estimate the error of the numerical solution, for a given element size and approximation order.

Multiple ways to calculate error estimates were proposed in literature [Oden et al., 1989; Repin, 2008; Grätsch and Bathe, 2005]. Nevertheless, due to the temperature T and flux \mathbf{q} belonging to different functional spaces in the mixed formulation, error indicators and estimators with little extra computational cost are available [Ainsworth, 2008; Braess and Verfürth, 1996; Carstensen, 1997]. The particular *a posteriori* error indicators and error estimate calculated in this thesis follow [Braess and Verfürth, 1996].

Error indicators indicate where the approximation errors discoverable by that particular indicator are the highest, however, any one error indicator might not capture all of the finite element approximation errors on its own. Therefore, the error estimate introduced in this section is composed of error indicators associated with temperature gradient, flux divergence, and jumps of values across the inner boundaries between elements, described in the following subsections. The error estimate can be used as a whole or parts of it can be used as error indicators for adaptive refinements.

3.3.1 Error indicator associated with temperature gradient

The first error indicator is associated with the temperature gradient ∇T . Since temperature T is approximated by L^2 space, the field is not forced to be continuous, see Figure 3.4, and therefore does not allow to compute temperature gradient. Nevertheless, given that in the finite-element approach the fields are approximated using polynomial base functions, even if the temperature field is not continuous between elements, the gradient of the corresponding polynomial approximation T^h can be readily computed at each element's integration points independently *a posteriori*. This temperature gradient is compared to the flux \mathbf{q} , which is related through the

constitutive relationship (3.1c). Since the flux field is approximated directly with higher approximation order, $p + 1$, the resulting field is much smoother than the computed gradient of temperature ∇T , see Figure 3.7. The error indicator $\eta_e(\nabla T, \mathbf{q})$ is computed over a finite element Ω_e as follows:

$$\eta_e(\nabla T, \mathbf{q}) = \|k\nabla T + \mathbf{q}\|_{\Omega_e}^2. \quad (3.10)$$

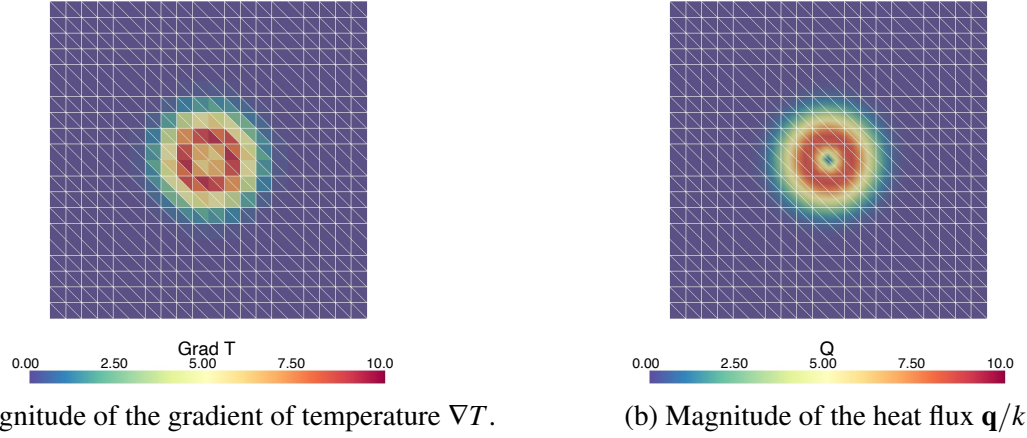


Figure 3.7: Example Exp-Hat: Comparison of the magnitudes of the gradient of temperature ∇T and the heat flux \mathbf{q} for approximation order $p = 1$ and element size $h = 0.05$.

The magnitudes of the fields shown in Figure 3.7 should theoretically have the same values since the thermal conductivity chosen for the Exp-Hat example is $k = 1$ and $\mathbf{q}/k = -\nabla T$, therefore $\mathbf{q} = -\nabla T$ and $|\mathbf{q}| = |\nabla T|$. However, due to the finite element approximation and satisfying the constitutive equation in a weak sense, the results shown in Figure 3.7 differ. The error indicator $\eta_e(\nabla T, \mathbf{q})$ computed for Exp-Hat example is shown in Figure 3.8a. The error indicator can be used to identify elements where the temperature gradient are not well approximated, and where the refinement is needed.

This error indicator alone is sufficient to indicate where the temperature gradient is not well approximated, and where the refinement is needed. The gradient error indicator (3.10) can be compared to the H^1 -seminorm of the temperature error to the exact solution and, as shown in Figure 3.8b, the same elements are identified as problematic.

3.3.2 Error indicator associated with flux divergence

The second error indicator is associated with the flux divergence $\nabla \cdot \mathbf{q}$. The error indicator measures the difference between the source term s and the divergence of the flux $\nabla \cdot \mathbf{q}$, which corresponds to the conservation of energy (3.1a). The divergence error indicator $v_e(\mathbf{q})$ is computed over a finite element Ω_e as follows:

$$v_e(\mathbf{q}) = h \|s - \nabla \cdot \mathbf{q}\|_{\Omega_e}^2 \quad (3.11)$$

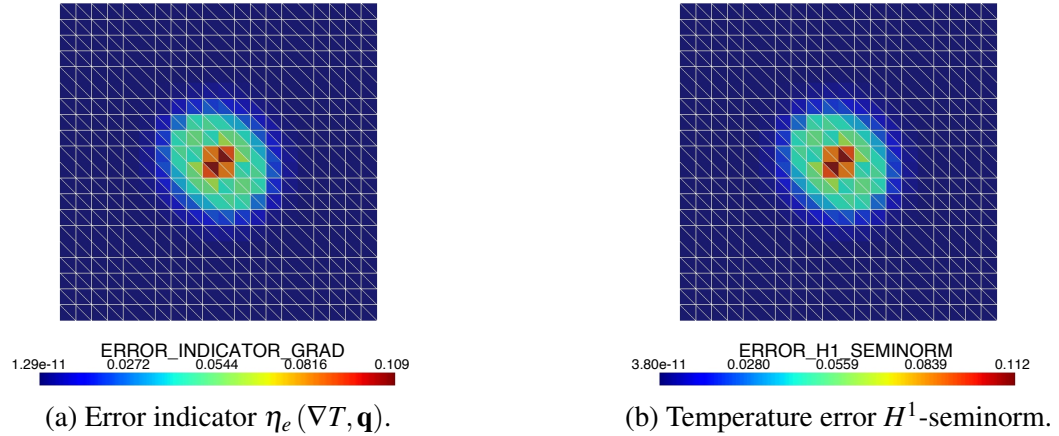


Figure 3.8: Example Exp-Hat: Comparison of the error indicator associated with temperature gradient $\eta_e(\nabla T, \mathbf{q})$, see (3.10), and the H^1 -seminorm of temperature error to the exact solution evaluated per finite element.

where h is the representative size of the element Ω_e ; $h = \sqrt{|\Omega_e|}$, where $|\Omega_e|$ is the area of the element Ω_e .

The error indicator $v_e(\nabla \cdot \mathbf{q})$ computed for Exp-Hat example is shown in Figure 3.9. The error indicator can be used to identify elements where the source term s and the divergence of the flux $\nabla \cdot \mathbf{q}$ are not conforming, see Figure 3.9.

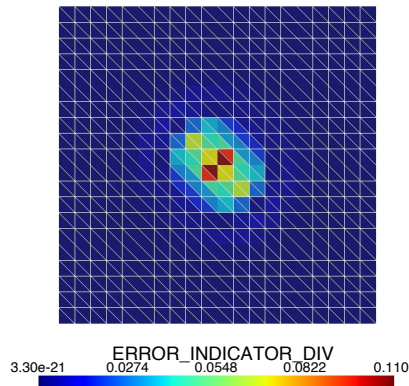


Figure 3.9: Example Exp-Hat: Error indicator assessing the conformity of the numerical solution to the conservation of energy equation (3.1a) on element basis.

3.3.3 Jump across the inner boundaries

Since the temperature field is in L^2 functional space, the finite element solution is not continuous and jump of the field values across the inner boundaries can be calculated, for visual representation of the temperature field values and the jumps between elements see Figure 3.4. A part of

the jump error indicator, $\gamma_l(T)$, is computed over any inner boundary Γ_l as follows:

$$\gamma_l(T) = h^{-1/2} \|J(T)\|_{0,l} \quad (3.12)$$

where $J(T)$ is the jump of the temperature field T across one of the inner boundaries Γ_l belonging to an element Ω_e and h is the representative size of the element Ω_e ; $h = \frac{\sqrt{|\Omega_{e1}|} + \sqrt{|\Omega_{e2}|}}{2}$, where $|\Omega_{e1}|$ and $|\Omega_{e2}|$ are the areas of the elements Ω_{e1} and Ω_{e2} sharing the inner boundary Γ_l .

The jump error indicator $\gamma_e(T)$ for the element is computed by summation of the jumps $\gamma_l(T)$ across all boundaries associated with that element:

$$\gamma_e(T) = \sum_{l=1}^{n_{\Gamma_e}} \gamma_l(T) \quad (3.13)$$

The jump error indicator for Exp-Hat example is shown in Figure 3.10, highlighting where the jump of temperature values between elements is the highest, see Figure 3.4b for the temperature field visualisation.

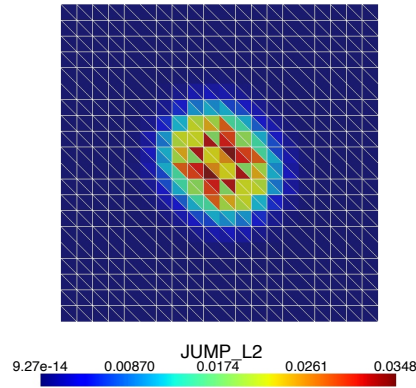


Figure 3.10: Example Exp-Hat: Error indicator evaluating the jumps of temperature values, see (3.13), through the inner boundaries, evaluated per element.

3.3.4 Error estimator

The complete error estimator [Braess and Verfürth, 1996] is a combination of the error indicators associated with temperature gradient (3.10), flux divergence (3.11), and jumps across the inner boundaries (3.13):

$$\mu_e = (\eta_e^2 + v_e^2 + \gamma_e^2)^{1/2}. \quad (3.14)$$

The global error estimator can be computed as:

$$\mu_g = \left(\sum_{e \in \Omega} [\eta_e^2 + v_e^2] + \sum_{l \in \Gamma} \gamma_l^2 \right)^{1/2}, \quad (3.15)$$

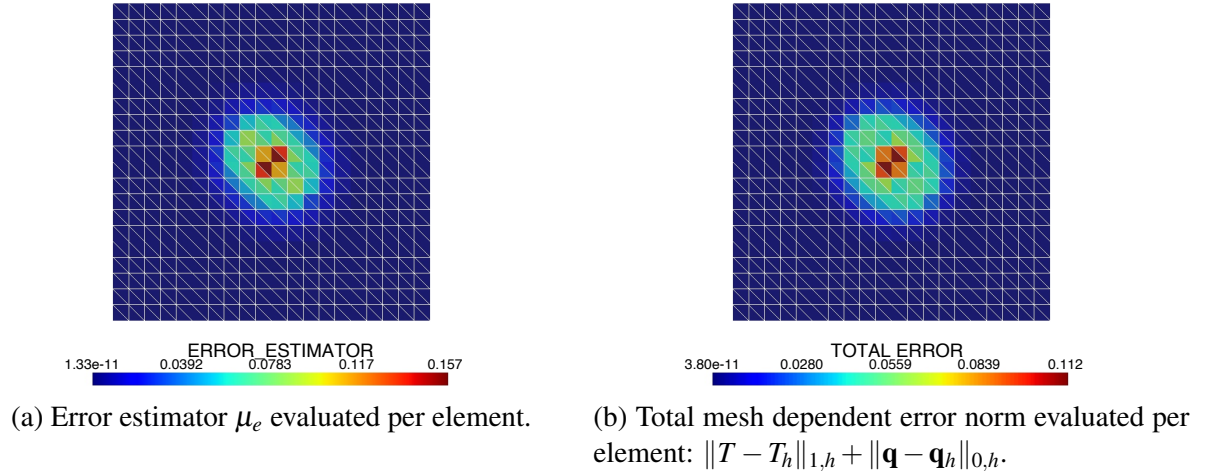


Figure 3.11: Example Exp-Hat: Error estimator calculated according to (3.14) evaluating the temperature gradient, flux divergence, and jumps of temperature values through the inner boundaries, evaluated per element compared to the total mesh dependent error norm.

where Γ refers to the inner boundaries.

The error estimator, or its parts, can be used as error indicators for adaptive refinement, and the complete error estimator can also be extended to calculate the lower and upper bounds of the numerical error [Braess and Verfürth, 1996].

The resulting error estimator for the Example Exp-Hat with approximation order $p = 1$ and element size $h = 0.05$ is shown in Figure 3.11. The estimation of upper and lower bounds of the numerical error for the mixed formulation is not in the scope of this thesis, however, the error estimator can be used to identify elements where the solution is not well approximated and where the refinement is needed.

3.4 Adaptive refinement

Adaptive refinement aims to achieve higher accuracy with adding as few new degrees of freedom as possible. The error indicators described in the previous section can guide the adaptive refinement by identifying elements where the solution is not approximated well and a refinement is recommended.

The choice of elements to be refined according to a given error estimator or indicator vary and can include one or more of the following criteria for the choice of which elements should be refined:

- the highest error indicators.
- the error indicators higher than a certain threshold.
- a certain percentage of elements with the highest error indicators.

- the error indicators higher than the average value of the error indicators.
- the error indicators higher than a fraction of the maximum value of the error indicators.
- a combination of the above approaches and more.

The error indicators can be used to refine the mesh, increase the approximation order, or both, using one or more criteria from the list above. This section will address the adaptive refinements based on the error indicators and estimators described in the previous section.

3.4.1 Adaptive approximation order refinement

For the Example Exp-Hat, Figure 3.2, there are no singularities in any of the fields but there is a high localised temperature gradient present inside of the domain. Intuitively, to capture higher gradients, approximation order refinement (p -refinement) is preferable over a mesh refinement (h -refinement).

To illustrate this approach, on the elements where the errors estimator is higher than the average, the approximation orders for T and \mathbf{q} fields are increased by one, i.e.:

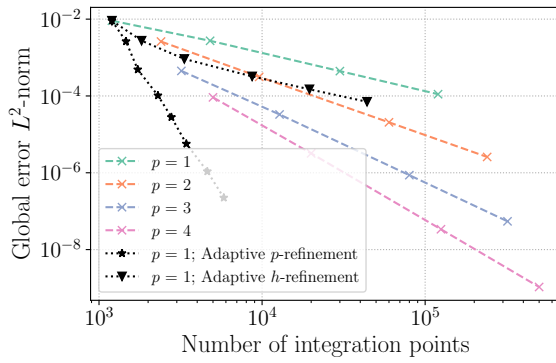
$$p_e := \begin{cases} p_e + 1 & \text{if } \mu_e > \mu_{\text{avg}} \\ p_e & \text{otherwise.} \end{cases} \quad (3.16)$$

For this algorithm, it is necessary to set the number of refinements as it can continue infinitely many times as a new average is calculated after every solution.

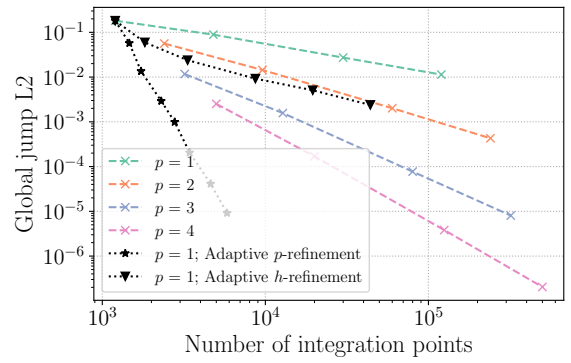
The convergence to the exact solution with global mesh and approximation order refinement is compared to the adaptive order refinement error norms in Figure 3.12. For all of the error norms, p -refinement achieves high accuracy with orders of magnitude smaller number of integration points than the global refinement, although the chosen algorithm does not reach the error norms as small as the global refinement with around 100 times the number of integration points. Figure 3.12 also shows the results of an adaptive h -refinement, which is described in the next subsection 3.4.2 of this thesis, which in this case does not achieve the same improvement in accuracy as p -refinement.

The convergence with the adaptive refinement is considerably faster than that of the global refinement with respect to the number of integration points. The choice of the criterion for refinement will also affect the convergence rate, and the choice of the algorithm should be based on the problem at hand.

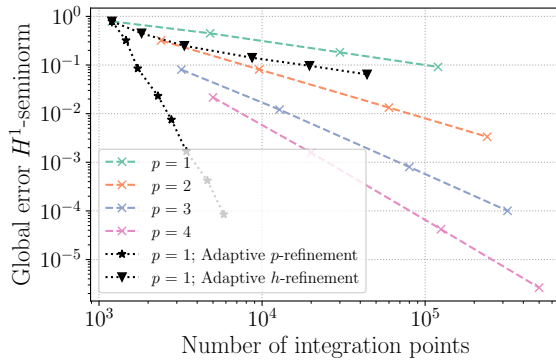
It is important to note that increasing of the approximation order does not alter the mesh and is possible when hierarchical shape functions are utilised Zienkiewicz et al. [2010], for example, using MoFEM [Kaczmarczyk et al., 2020], see Appendix A.



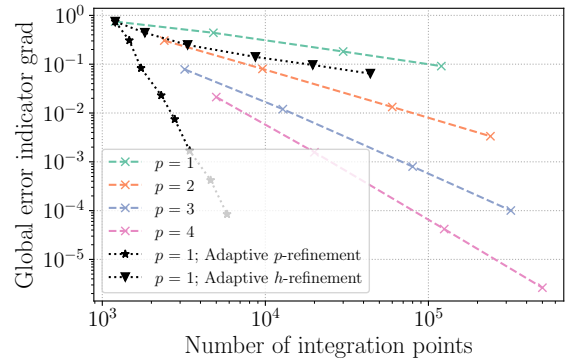
(a) Global temperature error L^2 -norm.



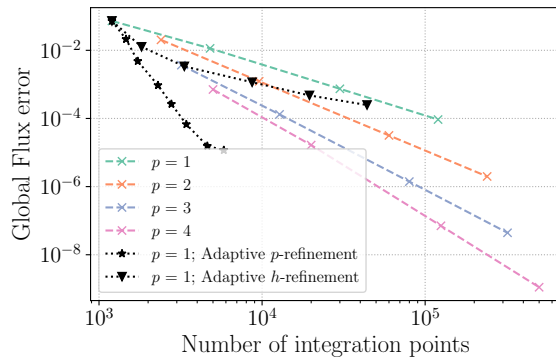
(b) Global L^2 -norm of temperature jumps across inner boundaries.



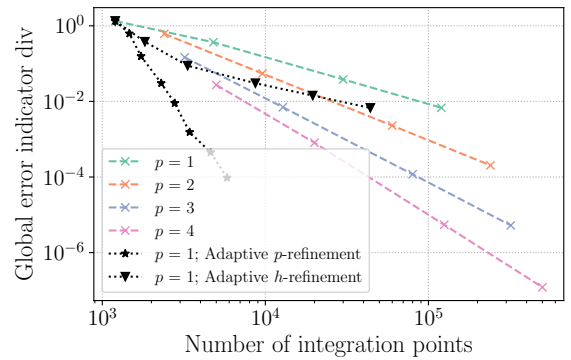
(c) Global temperature error H^1 -seminorm.



(d) Global L^2 -norm of the gradient error indicator.



(e) Global flux error L^2 -norm.



(f) Global L^2 -norm of the divergence error indicator.

Figure 3.12: Example Exp-Hat: Convergence of the finite element solution to the exact one and error indicators with increasing number of Gauss points driven by the global and local h and p refinement.

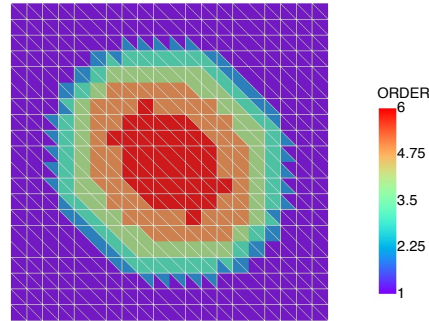


Figure 3.13: Example Exp-Hat: Resulting approximation orders of the adaptive refinement with the algorithm described in Algorithm 1.

Furthermore, the algorithm should not allow for two elements next to each other to have the difference between the approximation orders more than two. Hence, an additional algorithm is introduced to prevent this from happening, see Algorithm 1.

Algorithm 1 Adjusting approximation order for mixed formulation

- 1: Initialise W as the highest p in the mesh
 - 2: **while** $W > p_{\min} + 2$ **do**
 - 3: Identify all elements with the current approximation order W as E_W
 - 4: **for each** E_W **do**
 - 4: Find neighbouring elements connected by an edge to E_W
 - 5: **for each** neighbouring element **do**
 - 5: Get approximation order of the element W_e
 - 5: $W_e = \max(W - 1, W_e)$
 - 6: **end for**
 - 7: **end for**
 - 8: $W = W - 1$
 - 9: **end while**
-

In other words, the algorithm will increase the approximation order of the neighbouring element (connected by an edge) if the difference between the approximation orders is more than one. The increase of the order of neighbouring elements will typically take place in the area where the order refinement has taken place several times.

In the Example Exp-Hat, the area with the high gradient will be refined multiple times, e.g. the approximation order increased to 5, and the neighbouring elements would have the approximation order 1. This would result in the high gradient area being approximated with a much higher order than the neighbouring elements, which is not desired as it potentially introduces other approximation issues. The algorithm will prevent this from happening by adjusting the approximation orders of the neighbouring elements, see Figure 3.13.

The algorithm is applied to the Example Exp-Hat and the convergence is shown in Fig-

ure 3.12. The convergence is significantly improved compared to the global refinement.

3.4.2 Adaptive mesh refinement

Adaptive mesh refinement (h -refinement) uses a similar algorithm as the adaptive p -refinement (refine if $\mu_e > \mu_{\text{avg}}$), however, it is the most required when singularities are present in the problem. When applied to the Example Exp-Hat, the convergence was not improved as significantly as with the order refinement and the error norms were reduced more by a global p -refinement, see Figure 3.12.

To study the possible cases when the mesh refinement is more effective than the order refinement, a new example is introduced which was created based on an exact solution with a singularity following [Demkowicz and Gopalakrishnan, 2011]. The exact solution is shown in Figure 3.14 and is defined in polar coordinates as follows:

$$\tilde{T}(r, \theta) = r^{\frac{2}{3}} \sin\left(\frac{2}{3}\left(\theta + \frac{\pi}{2}\right)\right). \quad (3.17)$$

However, as we usually work in Cartesian coordinates, the exact solution is transformed to Cartesian coordinates as follows:

$$T(x, y) = (x^2 + y^2)^{\frac{1}{3}} \sin\left(\frac{2}{3}\left(\arctan(y/x) + \frac{\pi}{2}\right)\right). \quad (3.18)$$

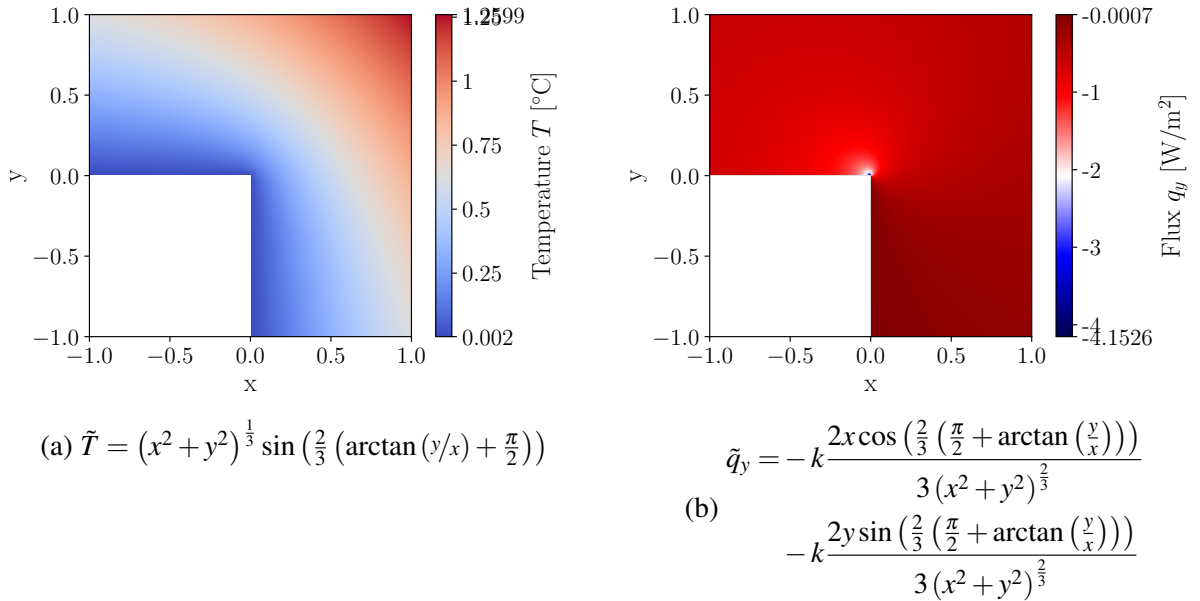


Figure 3.14: Example L-shape: Exact solutions and the source term for the linear diffusion problem with thermal conductivity $k = 1$.

The geometry and boundary conditions are shown in Figure 3.15 and the analysis is done with global and adaptive refinements. The resulting error norms are shown in Figure 3.16 and

hp -refinement is described in the next subsection 3.4.3.

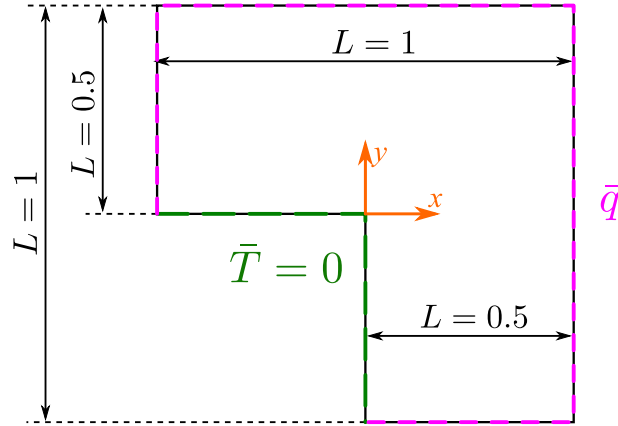


Figure 3.15: Example L-shape: Geometry and boundary conditions. Note that \bar{q} is derived from the exact solution (3.18) with linear material behaviour and thermal conductivity $k = 1$.

The solution to the problem does not improve with the increase of the approximation order, as the singularity is not well approximated.

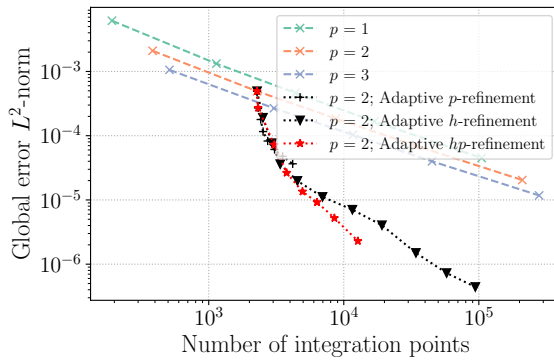
The adaptive mesh refinement is more suitable for problems with singularities, and the adaptive order refinement is more suitable for problems with high gradients of unknown fields. The choice of the algorithm should be based on the problem at hand. Nevertheless, the adaptive refinement can be a combination of the two algorithms, and the choice of the algorithm should be based on the problem at hand.

3.4.3 Adaptive mesh and order refinement algorithm

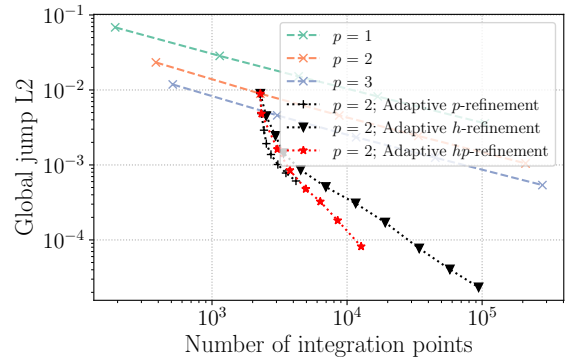
The mesh and order refinement algorithm, also known as hp -refinement is a combination of the previously mentioned approximation order and mesh refinements. The algorithm can have various implementations, and the following algorithm has been implemented in this thesis:

Algorithm 2 Adaptive Refinement and Order Adjustment

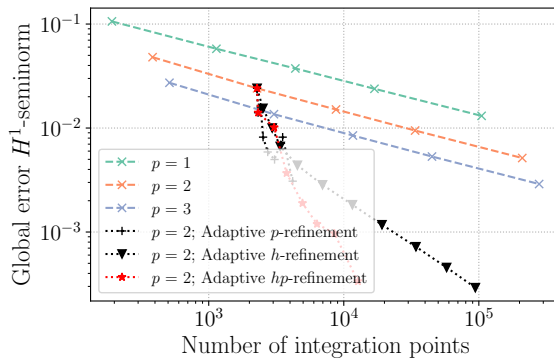
- 1: Initialize with the lowest approximation order $p = 1$ and the coarsest mesh.
 - 2: **repeat**
 - 3: Solve the problem (3.5).
 - 4: Calculate the error indicators and estimator (3.14).
 - 5: **if** an element's error estimator is higher than the average error estimator **then**
 - 6: Increase the approximation order, ensuring that the difference between the approximation orders of neighbouring elements is not more than one, following Algorithm 1.
 - 7: **if** an element is adjacent to the boundary Γ **then**
 - 8: Refine mesh of this element.
 - 9: **end if**
 - 10: **end if**
 - 11: **until** a specified number of iterations is reached or the error estimator is below a specified threshold
-



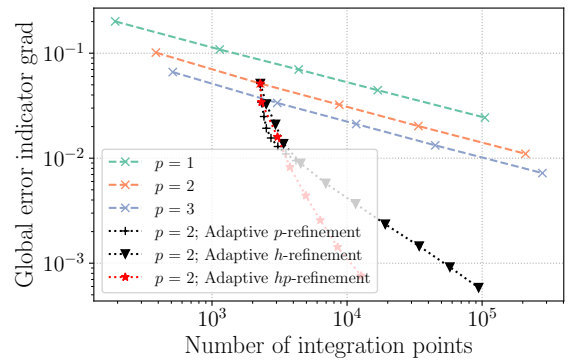
(a) Global temperature error L^2 -norm.



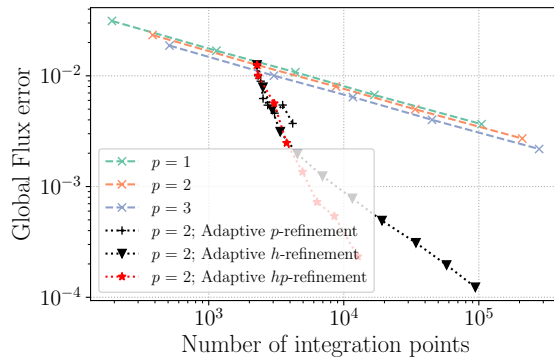
(b) Global L^2 -norm of temperature jumps across inner boundaries.



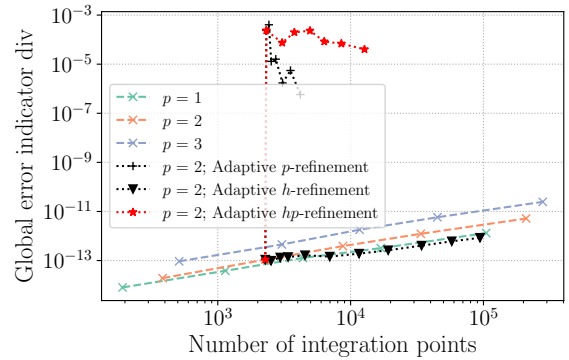
(c) Global temperature error H^1 -seminorm.



(d) Global L^2 -norm of the gradient error indicator.



(e) Global flux error L^2 -norm.



(f) Global L^2 -norm of the divergence error indicator.

Figure 3.16: Example L-shape: Convergence of the finite element solution to the exact one and error indicators with increasing number of Gauss points due to global and local mesh and order refinement.

The convergence to the exact solution and errors with the adaptive mesh and order refinement is shown in Figure 3.16. The convergence is significantly improved compared to the global refinement, however the algorithm can be further adjusted to improve the convergence. The refinement algorithms used later in this thesis use parts of the algorithm described above combined with other inputs, some of which are described later in this thesis, indicating where the mesh refinement should or should not take place and where the approximation order should be increased or decreased.

3.5 Summary

As introduced in the chapter, high finite element approximation errors can be located and reduced with the use of the mixed formulation and associated error indicators/estimators. Once the problematic elements are identified, the adaptive refinements can be applied to reduce the error. The adaptive refinements can be based on the error indicators and estimators associated with temperature gradients, flux divergence, and jumps across the inner boundaries. The adaptive refinements can be applied in terms of the mesh refinement, approximation order refinement, or a combination of the two. The choice of the algorithm should be based on the problem at hand, and the adaptive refinement can be a combination of the two algorithms. The choice of the algorithm should be based on the problem at hand.

The next chapter will introduce a different concept, data-driven approach, not related to the mixed formulation described in this chapter. The principles and concepts introduced in this section will reappear in chapter 5 in combination with the data-driven approach.

Chapter 4

Data-Driven formulation for diffusive problems

In this chapter, data-driven approach for diffusion problems is presented. This work follows and builds on the previous work, see [Kirchdoerfer and Ortiz, 2016], where the idea and implementation of using "model-free" numerical analysis started to thrive. This approach also uses no machine learning or neural networks, but instead relies on the data directly, without any fitting to a model.

The topic has been explored in multiple directions since its establishment in 2016, including elasticity [Kirchdoerfer and Ortiz, 2016], inelasticity [Kirchdoerfer and Ortiz, 2017], fracture [Carrara et al., 2020], etc. with more details on the current state of the topic presented in the literature review in section 1.2.

To introduce the concept of the data-driven approach, this thesis focuses on the scalar problem of heat diffusion, which is introduced and solved using the standard FE approach in chapter 2. The main difference from the standard approach is that the relation between the flux and the gradient of temperature is introduced through the material dataset instead of a constitutive model, meaning that the Fourier's law (2.3) is not used in the formulation nor numerical analysis.

The origin of the constitutive relationships comes from experimentation. In the past, the collection of the material data after experiments produced smaller and often less accurate material datasets. However, with the development of software and technology, such as digital volume correlation or thermal cameras, the data collection has become more efficient and the datasets are larger and more accurate, although there are no out of the box solutions to collect the heat transfer material datasets required at this point. Nevertheless, some material models are still difficult to represent by a model, even when the data has been collected, such as unsaturated flow [Vogel et al., 2000], hyper elasticity, Griffith energy for fracture analysis in nuclear graphite [Tzelepi et al., 2018], etc., requiring fitting of multiple parameters which are often empirical. This has led to the idea of using the data directly in the numerical analysis, without fitting to a model.

The next section introduces the data-driven formulation after a definition of an example material dataset. The following sections present the results of the data-driven approach for the heat transfer problem, including the convergence analysis, effects of noise in the material dataset, and the choice of numerical integration scheme.

4.1 Introduction to the data-driven formulation

The simplest material behaviour for heat diffusion is a linear Fourier's law, where the flux \mathbf{q} is proportional to the gradient of temperature ∇T , $\mathbf{q} = -k\nabla T$ as introduced in (2.3), where, in this case, k is the heat conductivity constant.

For the purpose of introduction to the data-driven method, an example dataset is created as follows: the gradient of temperature ∇T are generated in the range $[-A, A]$ for $\partial T/\partial x$ and $\partial T/\partial y$ independently using a uniform distribution. The flux is then determined from the constitutive equation, (2.3) with a constant thermal conductivity, creating a grid of material datapoints, see Figure 4.1.

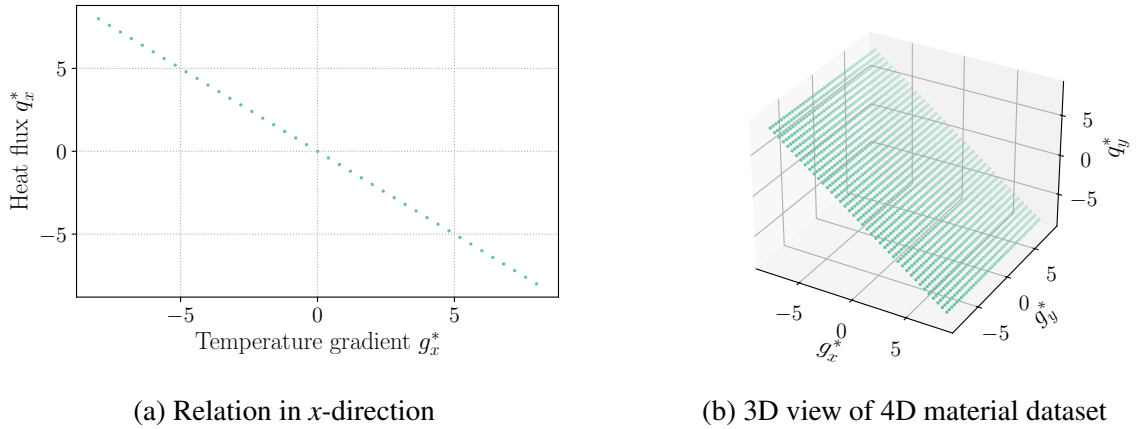


Figure 4.1: Regular material dataset: Simplest grid material dataset \mathcal{D} with $k = 1$.

Any data coming from any kind of material dataset will be denoted with a star, e.g. $\{\mathbf{g}^*, \mathbf{q}^*\}$, where \mathbf{g}^* is the material dataset dimension for the gradient of temperature. In this case the dataset \mathcal{D} is 4D, $\{g_x^*, g_y^*, q_x^*, q_y^*\}_{4D}$. Similarly, the corresponding unknown fields' values at a single integration point result in a point $\{\partial T/\partial x, \partial T/\partial y, q_x, q_y\}_{4D}$.

The data-driven approach [Kirchdoerfer and Ortiz, 2016] is essentially an iterative 2-step procedure, where at each iteration the closest points in the dataset to the previous solution are found and the distance of the unknown fields to the subset of closest datapoints is minimised while satisfying the conservation law and boundary conditions.

For every point (x, y) in the domain Ω , we can define the distance of the values of the tem-

perature gradient and heat flux to the dataset \mathcal{D} as follows:

$$\text{dist}(\{\nabla T, \mathbf{q}\}, \mathcal{D}) = \min_{\{\mathbf{g}^*, \mathbf{q}^*\} \in \mathcal{D}} \sqrt{S_g (\nabla T - \mathbf{g}^*)^2 + S_q (\mathbf{q} - \mathbf{q}^*)^2}, \quad (4.1)$$

where S_g and S_q are stabilisation/scaling parameters that depend on a numerical scheme and, in our case, make the distance unitless. Additionally, if no noise is present and the dataset includes a sufficient number of points, S_g and S_q would affect the speed of convergence and not the result. For this section, S_g and S_q are set to one and scaling will be discussed in subsection 4.1.2. Furthermore, a shorthand notation is used for the dot product between two vectors, such as the following in (4.1):

$$(\nabla T - \mathbf{g}^*)^2 = (\nabla T - \mathbf{g}^*) \cdot (\nabla T - \mathbf{g}^*). \quad (4.2)$$

The closest material datapoint is found as a minimiser of (4.1), which can be found for any point in the domain. To achieve that, C++ boost library [Boost, 2024] allows for efficient search through the dataset using the R-tree data structure [Guttman, 1984].

Depending on the number of data points, the creation of the R-tree can take a significant amount of time, however, the search through the dataset is very efficient. Nevertheless, the search will be executed at every integration point which will take a significant time when the problem has a large number of integration points.

Therefore, in this work, the packing algorithm with the fastest data search offered by the chosen library, R*-Tree [Boost, 2024], is chosen for the implementation of the DD method, on the expense of time for creating the R-tree itself.

The functional representing the integrated distance of the unknown fields \mathbf{q} and gradient of T to the dataset \mathcal{D} can be defined:

$$J(\nabla T, \mathbf{q}) = \frac{1}{2} \int_{\Omega} S_g (\nabla T - \mathbf{g}^*)^2 d\Omega + \frac{1}{2} \int_{\Omega} S_q (\mathbf{q} - \mathbf{q}^*)^2 d\Omega, \quad (4.3)$$

where \mathbf{g}^* and \mathbf{q}^* are the closest datapoints to the values of the unknown fields at every point (x, y) in the domain Ω . The solution of the problem can be found upon minimisation of the functional (4.3) with the conservation law (2.1) imposed as a constraint. Therefore, we formulate the Lagrangian:

$$\mathcal{L}(\nabla T, \mathbf{q}, \lambda) = J(\nabla T, \mathbf{q}) - \int_{\Omega} \lambda \nabla \cdot \mathbf{q} d\Omega + \int_{\Omega} \lambda s d\Omega, \quad (4.4)$$

where λ is the field of scalar Lagrange multipliers.

Integration by parts of the term representing the constraint in the Lagrangian (4.4) and imposing $\lambda = 0$ on Γ_T , see [Nguyen et al., 2020], results in:

$$\begin{aligned}
\mathcal{L}(\nabla T, \mathbf{q}, \lambda) &= J(\nabla T, \mathbf{q}) + \int_{\Omega} \nabla \lambda \cdot \mathbf{q} \, d\Omega - \int_{\Gamma_q} \lambda \mathbf{q} \cdot \mathbf{n} \, d\Gamma + \int_{\Omega} \lambda s \, d\Omega \\
&= J(\nabla T, \mathbf{q}) + \int_{\Omega} \nabla \lambda \cdot \mathbf{q} \, d\Omega - \int_{\Gamma_q} \lambda \bar{q} \, d\Gamma + \int_{\Omega} \lambda s \, d\Omega,
\end{aligned} \tag{4.5}$$

where the Neumann boundary condition (2.2b) was taken into account.

The solution is found as a stationary point of the Lagrangian at which its variation vanishes:

$$\begin{cases}
\int_{\Omega} S_g(\nabla T - \mathbf{g}^*) \cdot \nabla \delta T \, d\Omega = 0 & \forall \delta T \in H_0^1(\Omega) \\
\int_{\Omega} S_q(\mathbf{q} - \mathbf{q}^*) \cdot \delta \mathbf{q} \, d\Omega + \int_{\Omega} \nabla \lambda \cdot \delta \mathbf{q} \, d\Omega = 0 & \forall \delta \mathbf{q} \in \mathbf{L}^2(\Omega) \\
\int_{\Omega} \mathbf{q} \cdot \nabla \delta \lambda \, d\Omega - \int_{\Gamma_q} \bar{q} \delta \lambda \, d\Gamma + \int_{\Omega} s \delta \lambda \, d\Omega = 0 & \forall \delta \lambda \in H_0^1(\Omega),
\end{cases} \tag{4.6}$$

where the unknown test and trial functions belong to the spaces shown in Table 4.1. Note that $\lambda = 0$ on Γ_T reflects the enforcement of the Dirichlet boundary condition on the primary field T and ensures the problem is well posed [Nguyen et al., 2020].

Field	Space
Temperature T (trial function)	$T \in \mathcal{T} = \{u \in H^1(\Omega) \mid u = \bar{T} \text{ on } \Gamma_T\}$
δT (test function)	$\delta T \in H_0^1(\Omega)$
Flux \mathbf{q} (trial function)	$\mathbf{q} \in \mathbf{L}^2(\Omega)$
$\delta \mathbf{q}$ (test function)	$\delta \mathbf{q} \in \mathbf{L}^2(\Omega)$
λ (trial function)	$\lambda \in H_0^1(\Omega)$
$\delta \lambda$ (test function)	$\delta \lambda \in H_0^1(\Omega)$

Table 4.1: Functional spaces for the data-driven formulation for the diffusion problem. For spaces definitions see appendix A.

The unknown fields are then approximated by the finite element basis functions, see Table 4.2.

Since (4.6) holds for any δT_β , δq_b , and $\delta \lambda_\beta$ the following saddle point problem in a matrix form is written as (4.7).

	Trial function	Test function
Temperature	$T^h = T_\alpha N_\alpha$	$\delta T^h = \delta T_\beta N_\beta$
Flux	$\mathbf{q}^h = \mathbf{q}_a Q_a$	$\delta \mathbf{q}^h = \delta \mathbf{q}_b Q_b$
Lagrange multiplier	$\lambda^h = \lambda_\alpha L_\alpha$	$\delta \lambda^h = \delta \lambda_\beta L_\beta$
Gradient of temperature	$\nabla T^h = T_\alpha \nabla N_\alpha$	$\nabla \delta T^h = \delta T_\beta \nabla N_\beta$
Gradient of λ	$\nabla \lambda^h = \lambda_\alpha \nabla L_\alpha$	$\nabla \delta \lambda^h = \delta \lambda_\beta \nabla L_\beta$

Table 4.2: Finite element basis functions for the data-driven formulation of the diffusion problem. T_α , δT_β , \mathbf{q}_a , $\delta \mathbf{q}_b$, λ_α and $\delta \lambda_\beta$ are the coefficients of the approximation. N_α , Q_a and L_α are the scalar basis functions.

$$\begin{bmatrix} \int_{\Omega} S_g \nabla N_\beta \cdot \nabla N_\alpha \, d\Omega & 0 & 0 \\ 0 & \int_{\Omega} S_q I Q_b Q_a \, d\Omega & \int_{\Omega} \nabla L_\beta Q_a \, d\Omega \\ 0 & \int_{\Omega} \nabla L_\beta Q_a \, d\Omega & 0 \end{bmatrix} \begin{bmatrix} T_\alpha \\ \mathbf{q}_a \\ \lambda_\alpha \end{bmatrix} = \begin{bmatrix} \int_{\Omega} S_g \mathbf{g}^* \cdot \nabla N_\beta \, d\Omega \\ \int_{\Omega} S_q \mathbf{q}^* Q_b \, d\Omega \\ \int_{\Gamma_T} \bar{q} L_\beta \, d\Gamma_T + \int_{\Omega} s L_\beta \, d\Omega \end{bmatrix}. \quad (4.7)$$

where I is the identity matrix.

For a saddle point problem (4.7), LBB stability conditions need to be satisfied to prevent an ill-conditioned system [Boffi et al., 2013], hence, the approximation orders are assigned to unknown fields as shown in Table 4.3.

Field	Approximation order
Temperature T	p
Lagrange multiplier λ	p
Flux \mathbf{q}	$p - 1$

Table 4.3: Approximation orders for the data-driven formulation of the diffusion problem.

The initial solution obtained by solving (4.7) with $\mathbf{g}^* = \mathbf{q}^* = \mathbf{0}$, satisfies the conservation law (2.1) and the boundary conditions (2.2), however, the result is not correctly informed of the material behaviour. In the standard finite element formulation, it can be compared to using an incorrect material model or model parameters, e.g. $k = 1$ instead of $k = 5000$. The next section addresses the iterative procedure of the data-driven approach, where the closest points in the dataset are found and the solution is updated accordingly.

4.1.1 Iterative procedure and convergence of the data-driven approach

The iterative process therefore consists of two steps:

1. find closest material datapoint $\{\mathbf{g}^*, \mathbf{q}^*\}_{4D}$ for every integration point in the domain using eq. (4.1),
2. solve eq. (4.7) which utilises the found points and enforces the conservation laws and boundary conditions.

The staggered scheme alternates between these two projections until convergence [Kirchdoerfer and Ortiz, 2016; Nguyen et al., 2020]. An example path of an integration point is shown in Figure 4.2, where all unknown fields start with zero values. The figure shows how the iterative process updates values of just one integration point between the point retrieved from the unknown field values $\{\nabla T, \mathbf{q}\}$ (orange cross) after solving eq. (4.7), and the closest point found in the material dataset $\{\mathbf{g}^*, \mathbf{q}^*\}$ (blue star) until convergence is achieved.

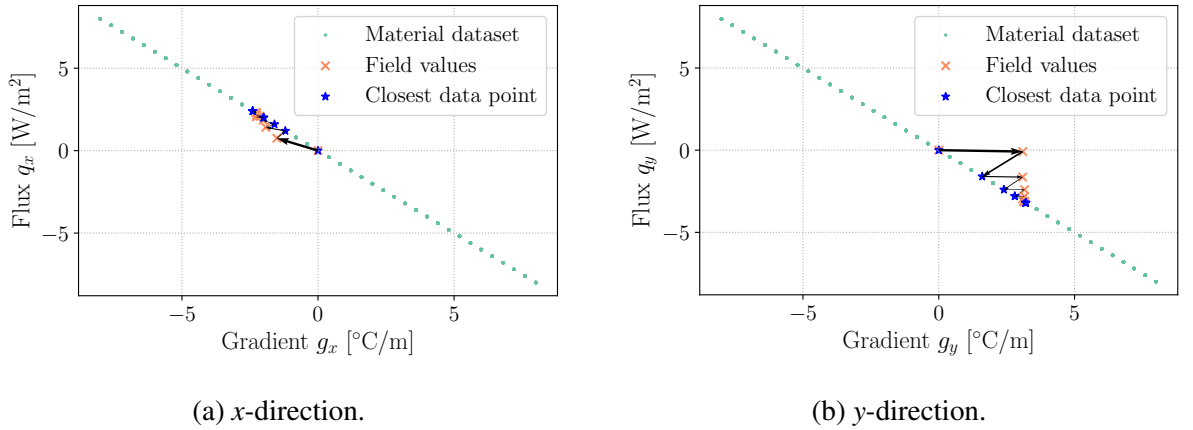


Figure 4.2: Regular material dataset & Example SinCos: Path of an integration point finding the closest point in the dataset (Closest data point) and projecting it into a space where conservation laws and boundary conditions are satisfied (Field values).

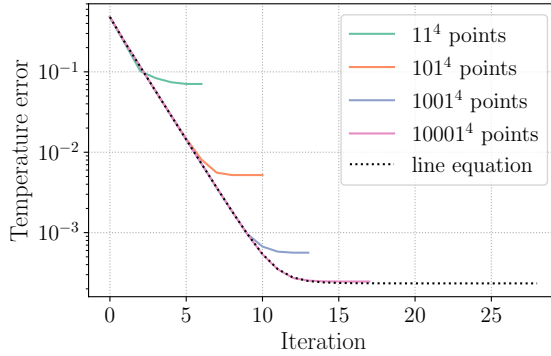
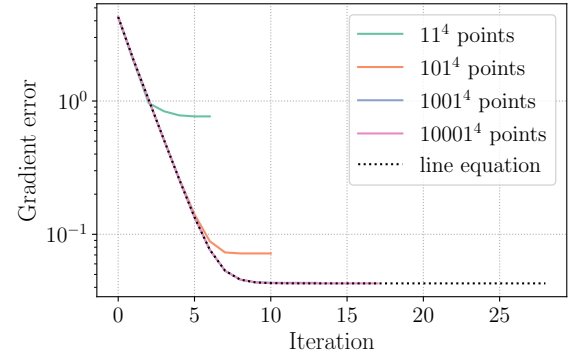
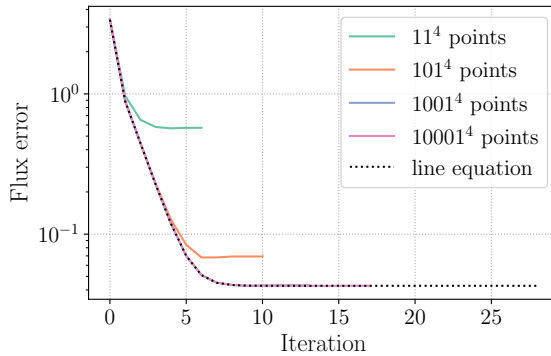
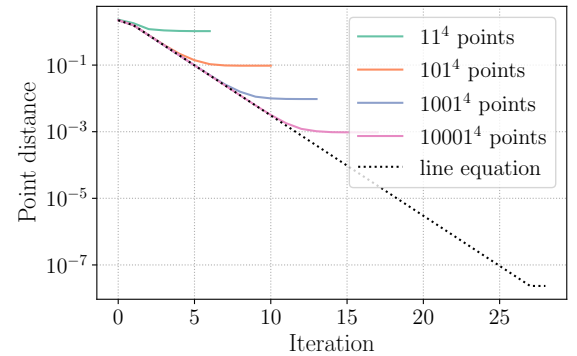
An option for a stopping criterion is comparing RMS measure of the distance between the field values and the dataset between the two iterations with a prior set tolerance:

$$\varepsilon_d(\nabla T, \mathbf{q}) = \sqrt{\frac{1}{\mu(\Omega)} \int_{\Omega} (\text{dist}(\{\nabla T, \mathbf{q}\}, \mathcal{D}))^2 d\Omega}, \quad (4.8)$$

where $\mu(\Omega)$ is the area of the domain Ω in a 2D case, and its volume in a 3D case. Another alternative consists of choosing the same closest points everywhere twice [Kirchdoerfer and Ortiz, 2016; Nguyen et al., 2020], which is equivalent to setting the tolerance $\varepsilon_d(\nabla T, \mathbf{q})$ to zero.

The convergence of the data-driven approach for the SinCos example is shown in Figure 4.3 for the regular datasets with increasing number of data points, as shown in Figure 4.1, and

the "saturated" dataset where the distance calculated by (4.1) is able to reach approximately zero, e.g. the dataset is dense enough that at the end of the iterative procedure, the closest point in the dataset is the same as the field values $\{\nabla T, \mathbf{q}\}$ at every integration point. The dataset search for the "saturated" dataset is replaced with finding the closest point satisfying the constitutive equation, which in this case is a linear relationship between the flux and the gradient of temperature. See Appendix B for the algorithm to find the closest point on the line (B.1) to the field values $\{\nabla T, \mathbf{q}\}_{4D}$ at an integration point.

(a) Temperature error L^2 -norm (2.22).(b) Temperature error H^1 -seminorm (2.23).(c) Flux error L^2 -norm (2.24).

(d) RMS distance (4.8).

Figure 4.3: Example SinCos (Figure 2.3): Global error norms w.r.t. the exact solution and point distance RMS measure (4.8). Convergence with the number of points in the regular material dataset, see Figure 4.1.

As algorithm iterates between the dataset search (4.1) and solving the system of equations (4.7), the global errors w.r.t. the exact solution and the distance RMS measure (4.8) decrease. Regardless to whether the dataset is saturated or not, the RMS measure for all errors reaches a plateau, which can correspond to the element size h and the approximation order p used; the quality of the material dataset used; or a combination of both.

If a "saturated" dataset is used, the convergence with element size and approximation order is achieved similarly to the standard FEM solutions, as shown in Figure 4.4.

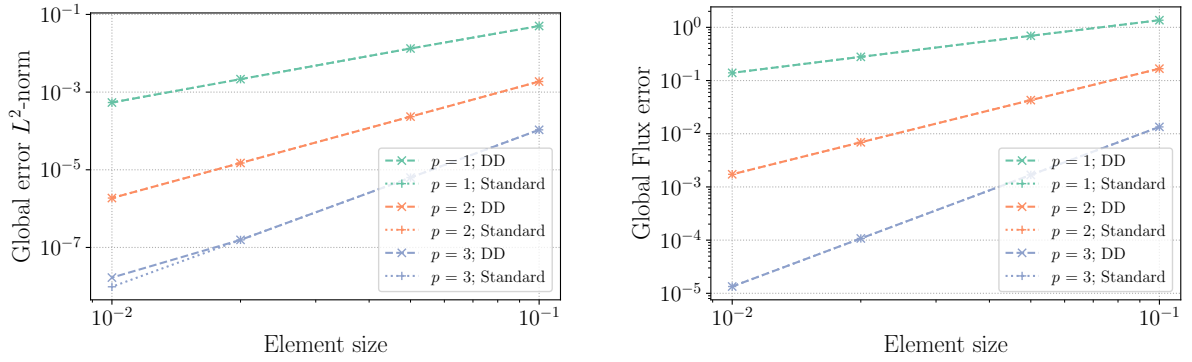
(a) Temperature error L^2 -norm (2.22).(b) Flux error L^2 -norm (2.24).

Figure 4.4: Example SinCos: Comparison of Standard FE and data-driven (DD) FE solutions' convergence with element size h and approximation order p if a "saturated" dataset is used (see Appendix B).

The convergence rate produced by the data-driven formulation shown in Figure 4.4 shows the same slopes as the standard heat transfer formulation introduced in chapter 2 and follows the same *a priori* error estimates (2.25).

4.1.2 Scaling the dataset

Since the data-driven method requires searching through a material dataset, one needs to take into account the difference in magnitudes between the dimensions of the dataset. For example, the magnitudes of the temperature gradient are in tens [$^{\circ}\text{C}/\text{m}$], and the fluxes are in thousands [W/m^2]. The most common search through a dataset is based on minimising the Euclidean distance (4.1) between the point obtained from the field values and the points of the material dataset, which in this case would strongly favour correcting the flux values and almost ignoring the temperature gradient since it would result in a smaller distance (4.1).

To demonstrate this in more detail, we consider a "saturated" dataset again, where the data search is replaced by getting the closest value on the line corresponding to the conservation law (2.3), see Appendix B. Setting the thermal conductivity to $k = 0.1 \text{ W}/(\text{m} \cdot ^{\circ}\text{C})$ and plotting the path of the values of one integration point already shows how a difference in magnitude of the values of the dimensions of the material dataset increases the number of iterations required to converge; see Figure 4.5 in comparison to Figure 4.2.

The comparison of the number of iterations needed to solve a problem for different values of conductivity is presented in Figure 4.6. The fastest convergence is achieved when conductivity is close to one, i.e. heat flux and gradient of temperature have the same order of magnitude, hence a scaling of the dataset is desirable. The thermal conductivity is a good measure for this example but would not be applicable when the conductivity is unknown, a nonlinear dataset is used, or if the dataset extends to more dimensions and starts to depend on temperature, porosity

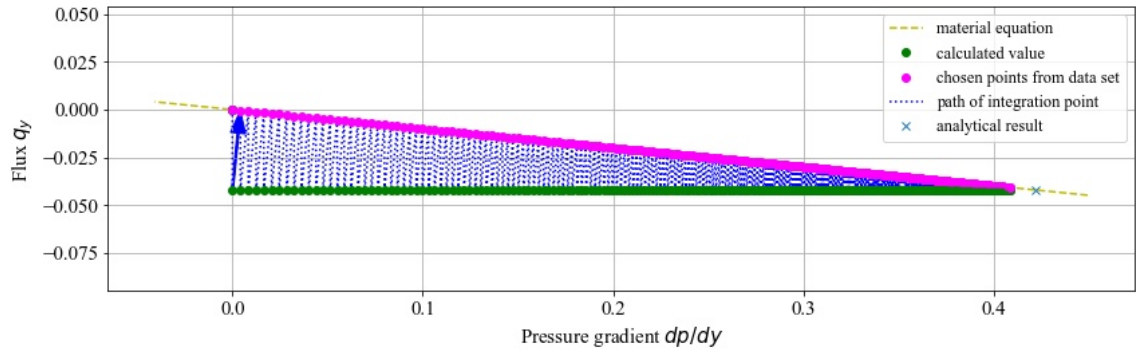


Figure 4.5: Example SinCos: Path of one integration point as the convergence is achieved. Conductivity $k = 0.1 \text{ W/(m}\cdot\text{ }^\circ\text{C)}$.

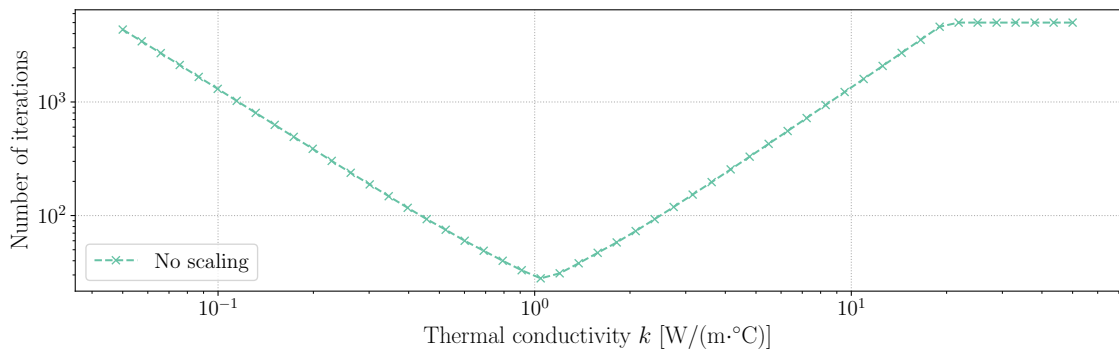


Figure 4.6: Number of iterations with changing conductivity k . The limit for number of iterations is set to 5000.

value, etc.

Choosing the scaling parameters is important when the differences between the dimensions are large, but will only have a noticeable effect on the rate of convergence and not the result when the dataset is saturated. When the material dataset is sparse, and the differences between the dimensions are large, the scaling can have a significant effect on the result, including being able to provide reasonable results, see Figure 4.7.

The scaling strategy chosen for this thesis is to consider temperature gradient as the main dimension and scale all other dimensions to be of a similar order of magnitude, i.e. S_g and S_q become scaling parameters: $S_g = 1$ and S_q is chosen accordingly. For example, if the temperature gradient is in the order of 10^{-2} and the heat flux is in the order of 10^3 , then $S_q = 10^{-5}$ for the whole domain.

The scaling is applied as a preprocessing step to the dataset, the boundary conditions, and the sources. The results are then scaled back in the postprocessing step to regain the correct values. When new dimensions are added to the dataset, e.g. temperature, the same principle applies, and a separate scaling parameter is chosen for each independent dimension to fit the temperature gradient's order of magnitude. Additionally, if any of the dataset dimensions are deemed less

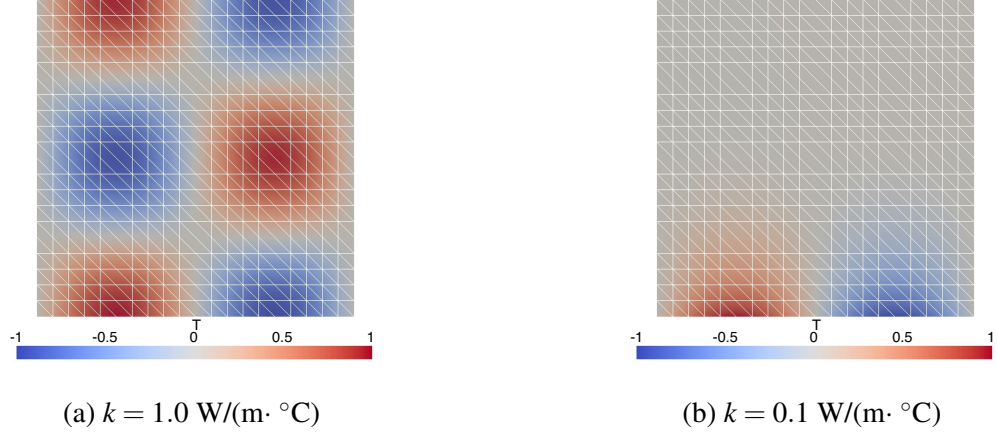


Figure 4.7: Example SinCos: Temperature T result with sparse regular material dataset containing 41^4 points with different thermal conductivities without scaling. Note that if scaling is used, (b) will have the same result as (a).

important than the others, they can be scaled to a smaller order of magnitude to have less effect on the result. For example, if humidity has a small influence on the temperature gradient/heat flux relationship, its values can be an order of magnitude smaller than the other dimensions, so the humidity is taken into consideration, but choosing values close to the temperature gradient and heat flux is prioritised.

Nevertheless, material datasets are rarely as organised and noiseless as in Figure 4.1, and the quality of the dataset affects the result of the numerical analysis. The next section will address the cases when noise is present in the material dataset.

4.2 Working with noisy material datasets

To imitate a slightly more realistic dataset, but still keep control over the input, a new synthetic way of creating datasets is introduced.

First, random values in range $[-A, A]$ for the components of the temperature gradient $\partial T/\partial x$ and $\partial T/\partial y$ are generated independently using uniform distribution, see Figure 4.8(a).

Next, flux is determined from constitutive equation (2.3) plus a noise η value randomly generated with normal distribution with probability density function:

$$f(\eta; \mu, \sigma_\eta) = \frac{1}{\sqrt{2\pi\sigma_\eta^2}} e^{-\frac{(\eta-\mu)^2}{2\sigma_\eta^2}}, \quad (4.9)$$

where mean $\mu = 0$, and the standard deviation σ_η is the input for the noise analysis.

There are multiple options on where to add the noise η and any of them are likely to appear in an experimental material dataset. The first one shown in Figure 4.8(b)-(c) can be used to

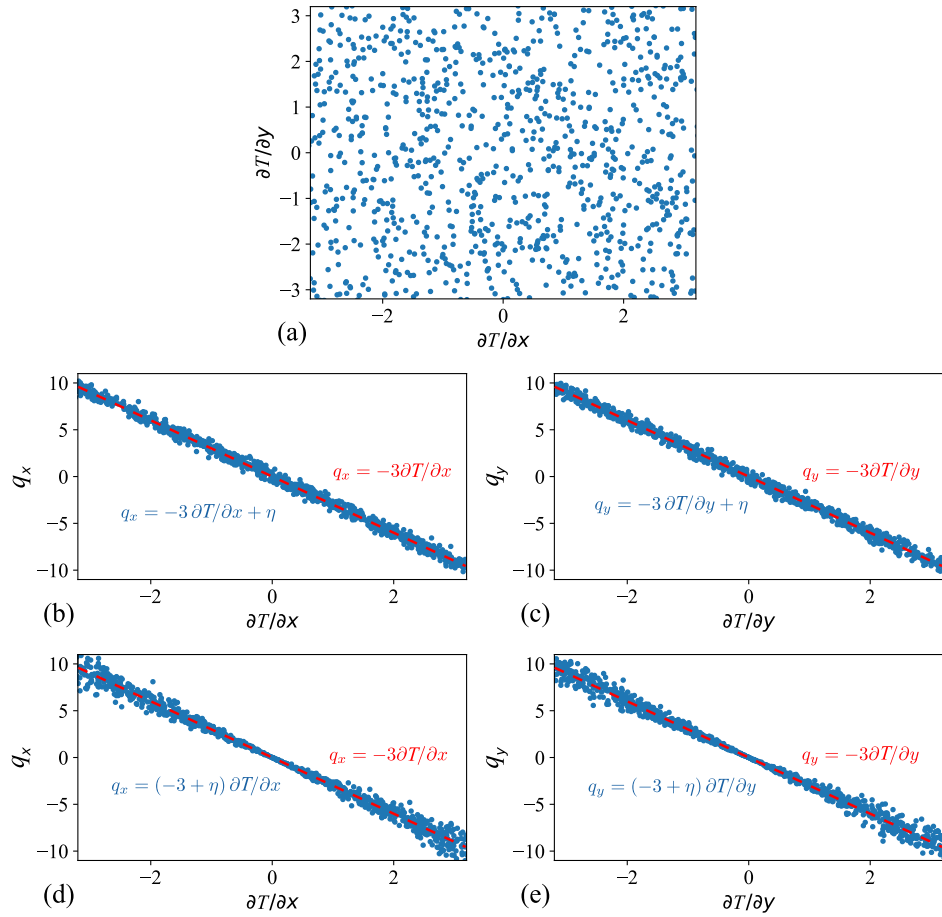


Figure 4.8: Dataset generation example: (a) Regularly distributed components of temperature gradient; Flux components following linear constitutive law with noise representing (b)-(c) measurement error, (d)-(e) stochastic material behaviour

represent measurement errors:

$$\mathbf{q} = -k\nabla T + \boldsymbol{\eta}, \quad (4.10)$$

while the second one shown by Figure 4.8(d)-(e) represents a stochastic material behaviour:

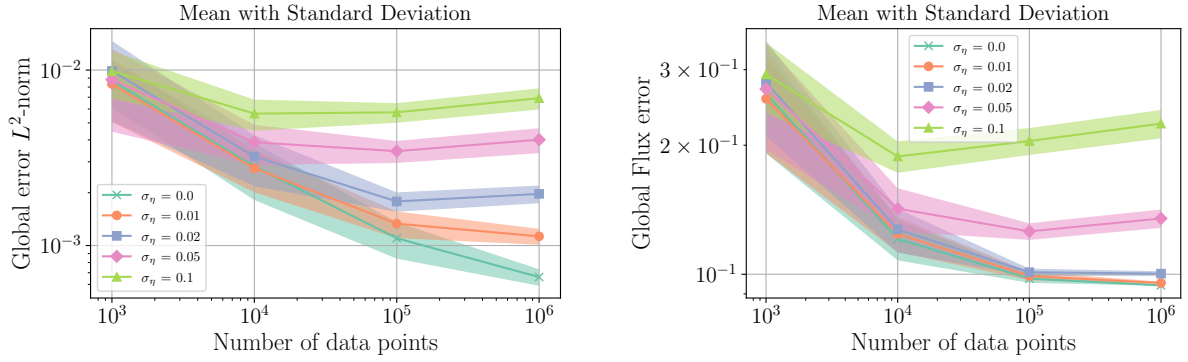
$$\mathbf{q} = -(k + \boldsymbol{\eta})\nabla T. \quad (4.11)$$

All of the points in the generated dataset, examples of which are shown in Figure 4.8,(b) and (c), or (d) and (e), depending on the choice of noise generation.

For the synthetically created material dataset for a 2D problem, one can choose the range A of gradient of temperature ∇T , number of data points generated overall, conductivity k , corresponding to a constitutive relationship (2.3) and the standard deviation of the noise $\boldsymbol{\eta}$ applied to the corresponding flux generation (4.10) or (4.11).

Once noise is present in the dataset, a convergence with an increase in the number of material datapoints (points in dataset \mathcal{D}) is not guaranteed, as it becomes possible for the data search to pick the points affected by the noise (noisy points). To evaluate how much effect the noise

present in the dataset has on the convergence, the L^2 -norm of temperature error (2.22) and flux error (2.24) is calculated after recreating the dataset with the same parameters. The generation of material dataset and numerical analysis are repeated 30 times for each different combination of the number of material datapoints and standard deviation of noise σ_η , and the mean and standard deviation of the calculated error L^2 norms are plotted in Figure 4.9.



(a) Temperature error L^2 -norm (2.22).

(b) Flux error L^2 -norm (2.24).

Figure 4.9: Example Exp-Hat (Figure 3.2): Influence of noise and number of material data points on global error L^2 -norms for temperature and flux, averaged over 30 realisations (order $p = 2$, element size $h = 0.05$).

The results show that the noise in the dataset has a significant effect on the convergence of the data-driven approach, therefore both, the material dataset uncertainties and finite element approximation errors due to mesh size and approximation order, need to be taken into account. The error L^2 norms increase with the standard deviation of the noise σ_η , as expected. However, increasing the number of material datapoints for the same σ_η does not decrease the error norms nor lead to convergence. On the contrary, if the noise is significant, the error norms start to increase with the number of material datapoints.

It can be concluded that once noise is present in the dataset, the basic version of the data-driven approach presented here is not robust enough since the accuracy of the solution cannot be determined without knowing the exact solution beforehand.

The initial assumption was that more data would provide more accurate results, but the results shown in Figure 4.9 indicate that this is not the case. Upon additional consideration, it is important to acknowledge that the noise follows a normal distribution centred around the selected constitutive equation during generation. Why noisy points are likely to be chosen can be better understood by looking at the material dataset sample shown in Figure 4.10. The dataset is created with a range of $[-9,9]$ for temperature gradient, the same as used in the analysis for Figure 4.9, and if the field values at an integration point are far from the material dataset, the closest point is likely to be a noisy point.

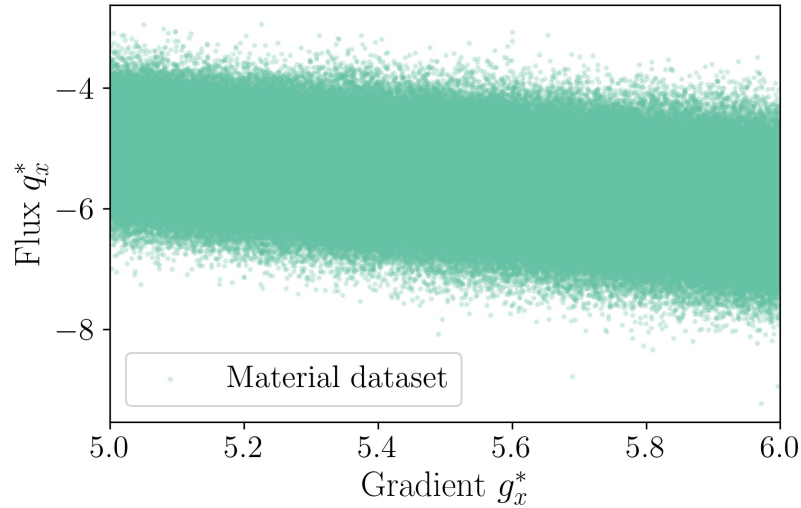
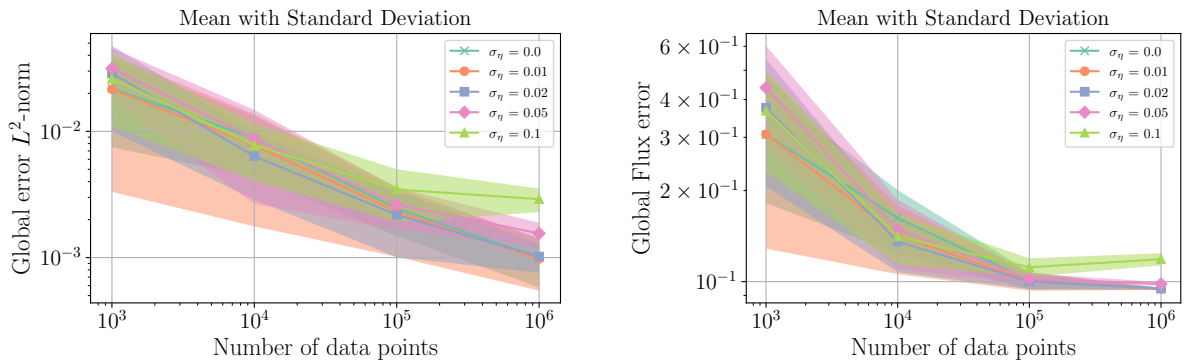


Figure 4.10: Sample of noisy material dataset with 10^6 material datapoints and $\sigma_\eta = 0.1$

4.2.1 Data search averaging

In order to overcome the increase in error with the increasing number of material datapoints, we test the following modification of the procedure described in subsection 4.1.1. Instead of using the closest point $\{\mathbf{g}^*, \mathbf{q}^*\}_{4D}$ found as the minimiser of the distance function (4.1), averaged values of the 30 closest points to the field values are found for each integration point. Figure 4.11 presents the results of this adjustment, highlighting an improvement in the robustness of the method against data noise influence. However, the error norm still shows an increase with the number of material datapoints with $\sigma_\eta = 0.1$. Additionally, the L^2 -norm of the temperature error is higher for less noisy datasets in comparison to the solution without data search averaging shown in Figure 4.9, including the dataset with no noise $\sigma_\eta = 0$: temperature error L^2 -norm increases from 7×10^{-4} to 1×10^{-3} .



(a) Temperature error L^2 -norm (2.22).

(b) Flux error L^2 -norm (2.24).

Figure 4.11: Example Exp-Hat (Figure 3.2): Using an average of 30 closest material datapoints instead of the closest point only in material data search (4.1) for the same analysis as Figure 4.9.

Hence, the number of points for averaging depends on the particular dataset and its influence is not detected without knowing the solution beforehand. Therefore, this solution is not objective, as it depends on an arbitrary choice of the averaging parameters.

The issue of noisy datasets can be mitigated by employing a more advanced data selection method that prioritises points in the centre of the distribution, where data points are more densely clustered and have more neighbours [Kirchdoerfer and Ortiz, 2017]. Alternatively, techniques like Gaussian processes can be applied locally to handle noise independently, as these methods create a smooth model fit that minimises noise impact. However, this approach can inadvertently fulfil the role of a material model, potentially disregarding the effects of noise on the results, which may be an important source of uncertainty in some analyses.

In conclusion, data search averaging will not be used in the rest of this thesis and handling and evaluating uncertainties on the material dataset will be discussed in more detail in chapter 6.

4.3 5D material datasets

The data-driven approach presented in sections 4.1 and 4.2 was limited to 4D material datasets $\{\mathbf{g}^*, \mathbf{q}^*\}_{4D}$, however, the dataset can be extended to include more dimensions, such as temperature, humidity, porosity, etc. To include temperature in a material dataset, as it is a dependency for a graphite constitutive behaviour (section 1.2.1), a 5D material dataset is introduced. The dataset is then defined as $\mathcal{D}_{5D} = (T^*, \mathbf{g}^*, \mathbf{q}^*)$, where T^* is the temperature, \mathbf{g}^* is the temperature gradient and \mathbf{q}^* is the heat flux.

Nevertheless, this is not the only way to extend the dataset, and the dataset can include more dimensions if they are relevant to the material response, such as porosity of the material, which can be prescribed within the domain, hydraulic pressure experienced by the material, which can be solved for by a different part of the numerical analysis, etc. The dimensions of the dataset do not have to correspond to fields that are directly solved for in the numerical problem; instead, they can be any quantities of interest, such as environmental conditions (amount of radiation exposed to, humidity, etc.) or material properties (density, porosity, etc.), that can be spatially assigned within the domain. Alternatively, if there is no information about some of the dimensions of the dataset in the domain, those dimensions can be left out of the dataset and their influence on the dataset can be considered as a source of uncertainty.

When the dataset \mathcal{D} has 5 dimensions, the distance to the dataset (4.1) needs to be updated to include the temperature T as well. The distance to the dataset is then defined as:

$$\text{dist}(\{T, \nabla T, \mathbf{q}\}, \mathcal{D}) = \min_{\{T, \mathbf{g}^*, \mathbf{q}^*\} \in \mathcal{D}} \sqrt{S_T (T - T^*)^2 + S_g (\nabla T - \mathbf{g}^*)^2 + S_q (\mathbf{q} - \mathbf{q}^*)^2}, \quad (4.12)$$

where S_T is the scaling applied to temperature T , in a similar way to S_g and S_q in subsec-

tion 4.1.2.

The integrated distance functional $J(\nabla T, \mathbf{q})$ (4.3) remains unchanged because the relationship between the gradient of temperature and heat flux is dictated by Fourier's law, a fundamental principle in thermodynamics. Fourier's law dictates that heat flows from regions of higher temperature to regions of lower temperature, connecting the heat flux and temperature gradient only. Consequently, temperature T should solely be used to identify the material state of heat flux \mathbf{q} and temperature gradient ∇T through \mathbf{q}^* and \mathbf{g}^* .

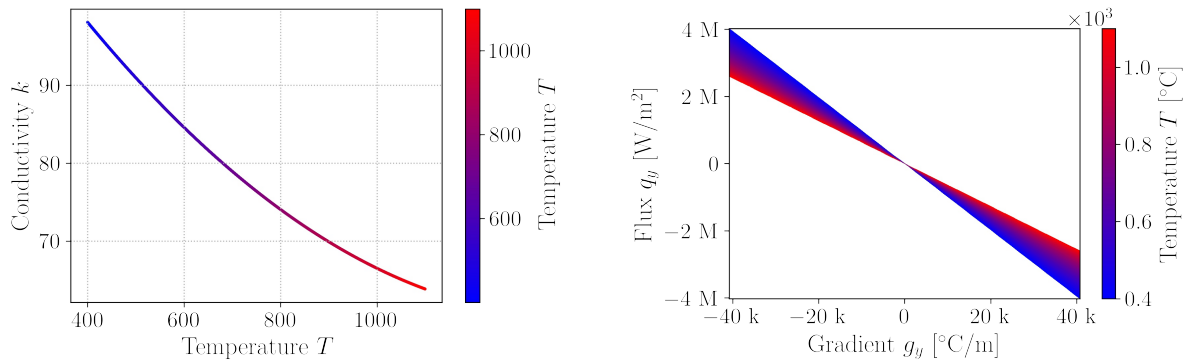
In conclusion, the only change in the formulation of the problem is the search through the dataset (from (4.1) to (4.12)) and not the finite element formulation (4.7). The formulation does not change even when the material behaviour is nonlinear or dependant on multiple additional dimensions, removing the need for linearisation of formulations with complicated material models, an example of which is described in subsection 2.4.1.

The following subsections describe the creation of synthetic material datasets for testing purposes. Ideally, the dataset would be created from a real-life experiment, but this is not always possible and will not be covered in this thesis, the reader is referred to subsection 1.2.1 and the references therein for more information.

The synthetic datasets follow a nonlinear material behaviour of graphite based on [McEligot et al., 2016], see Figure 4.12:

$$k(T) = 134 - 0.1047T + 3.719 * 10^{-5}T^2, \quad (4.13)$$

where the thermal conductivity k is in W/mK and temperature T is in $^{\circ}C$.



(a) Thermal conductivity k dependence on temperature T used for the synthetic experiment, see (4.13).

(b) Impact of the temperature dependant conductivity $k(T)$ on the relationship between temperature gradient and flux.

Figure 4.12: Nonlinear thermal conductivity k dependence on temperature T used for the synthetic material dataset generation.

In this case, in the temperature range $[400, 1000]$, the increase in temperature causes the thermal conductivity to decrease. For more information about the thermal conductivity of graphite,

see section 1.2.1.

4.3.1 Fully artificial material datasets

Starting with a regular material dataset, similar to Figure 4.1, the dataset is extended to include the temperature T as an additional dimension. Based on (4.13) and Figure 4.1, Algorithm 3 is implemented to create a regular 5D material dataset.

Algorithm 3 Creating a regular 5D Material Dataset

- 1: Initialize an empty dataset \mathcal{D}
 - 2: **for** each temperature T in the range $[T_{\min}, T_{\max}]$ with $count_T$ equally spaced intervals **do**
 - 3: **for** each temperature gradient g_x in the range $[G_{\min}, G_{\max}]$ with $count_G$ equally spaced intervals **do**
 - 4: **for** each temperature gradient g_y in the range $[G_{\min}, G_{\max}]$ with $count_G$ equally spaced intervals **do**
 - 5: Calculate the flux component q_x using $q_x = -(134 - 0.1047T + 3.719 * 10^{-5}T^2)g_x$
 - 6: Calculate the flux component q_y using $q_y = -(134 - 0.1047T + 3.719 * 10^{-5}T^2)g_y$
 - 7: Add the point (T, g_x, g_y, q_x, q_y) to the dataset $\mathcal{D}_{5D} = \{T^*, \mathbf{g}^*, \mathbf{q}^*\}$
 - 8: **end for**
 - 9: **end for**
 - 10: **end for**
-

Algorithm 3 creates a regular 5D material dataset, where the temperature T is in the range $[T_{\min}, T_{\max}]$ with $count_T$ equally spaced intervals, and the temperature gradient g_x and g_y are in the range $[G_{\min}, G_{\max}]$ with $count_G$ equally spaced intervals. The flux components q_x and q_y are calculated using the nonlinear relationship (4.13).

Two variants of the regular 5D material dataset are created, one with $count_T = 50$ and $count_G = 50$ for material dataset A, and the other with $count_T = 100$ and $count_G = 100$ for material dataset B. The material dataset A is shown in Figure 4.13 and the material dataset B is similar but denser. The number of material data points was selected arbitrarily, with the intention of evaluating how the developed method responds to different levels of dataset saturation. Datasets such as A and B could, in principle, be generated through microscale simulations, provided that the material behaviour is well characterised at that scale. By prescribing appropriate boundary conditions and source terms, one can run finite element analyses at the microscale to compute the corresponding flux values \mathbf{q}^* , temperature gradients \mathbf{g}^* , and temperatures T^* . This process is conceptually similar to representative volume element (RVE) analysis used in multiscale modelling, where the microscale response is computed directly rather than assumed through a constitutive model. In the data-driven context, these simulation results could be collected beforehand and assembled into a material dataset, which is then used in the macroscopic analysis in place of a fitted model.

Since noise is often present in the material datasets, a controlled way to introduce noise is implemented to evaluate the ability of the implemented tools to capture it and to evaluate the

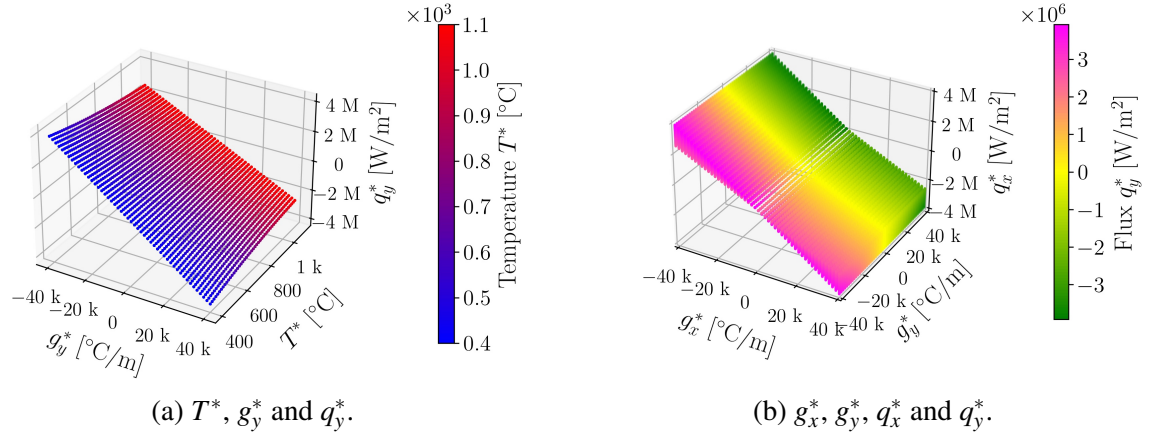


Figure 4.13: Material dataset A created by Algorithm 3 with $count_T = 50$, $count_G = 50$. The temperature range is $[400, 1100]$, and the gradient range is $[-40 \times 10^3, 40 \times 10^3]$. Material dataset B is similar but with $count_T = 100$, $count_G = 100$, making it denser.

uncertainty of the results. The noise is added to the flux values only in certain parts of the dataset to assess its influence on the results throughout the domain and the capabilities of the new features introduced in throughout this thesis. Such noise could correspond to an issue with a measurement equipment or the material experiencing reversible microstructural changes at around the specified range of temperature gradient magnitude, which would affect the material behaviour and the flux values.

The noise is generated using a normal distribution with a standard deviation σ_η and added to the thermal conductivity k when generating flux values \mathbf{q}^* , same as (4.11). Additionally, the values for the temperature T^* and the temperature gradient \mathbf{g}^* are generated using a uniform distribution, instead of being equally spaced in a range. The algorithm for creating a noisy 5D material dataset is shown in Algorithm 4.

Algorithm 4 Creating a 5D Material Dataset with noise and random distribution

- 1: Initialize an empty dataset \mathcal{D}
 - 2: **for** chosen number of material datapoints **do**
 - 3: Generate temperature T in the range $[T_{\min}, T_{\max}]$ with uniform distribution
 - 4: Generate temperature gradient g_x and g_y in the range $[G_{\min}, G_{\max}]$ with uniform distribution
 - 5: Calculate the magnitude of the gradient: $|\mathbf{g}| = \sqrt{g_x^2 + g_y^2}$
 - 6: **if** $|\mathbf{g}|$ is within the range chosen for the noisy datapoints $[B_{\min}, B_{\max}]$ **then**
 - 7: Calculate the flux component q_x using $q_x = -(k(T) + \eta)g_x$
 - 8: Calculate the flux component q_y using $q_y = -(k(T) + \eta)g_y$
 - 9: **else**
 - 10: Calculate the flux component q_x using $q_x = -k(T)g_x$
 - 11: Calculate the flux component q_y using $q_y = -k(T)g_y$
 - 12: **end if**
 - 13: Add the point (T, g_x, g_y, q_x, q_y) to the dataset $\mathcal{D}_{5D} = \{T^*, \mathbf{g}^*, \mathbf{q}^*\}$
 - 14: **end for**
-

The noisy 5D material dataset C is created using Algorithm 4 within the same ranges as the regular dataset A, and the noise is applied in the range $[B_{\min}, B_{\max}] = [10 \times 10^3, 15 \times 10^3]$. The standard deviation of the noise is set to $\sigma_\eta = 1.0$, for reference see (4.11). The resulting material dataset C is shown in Figure 4.14 and since the noise is not visible due to the number of dimensions, the material datapoints which are affected by noise are shown in blue.

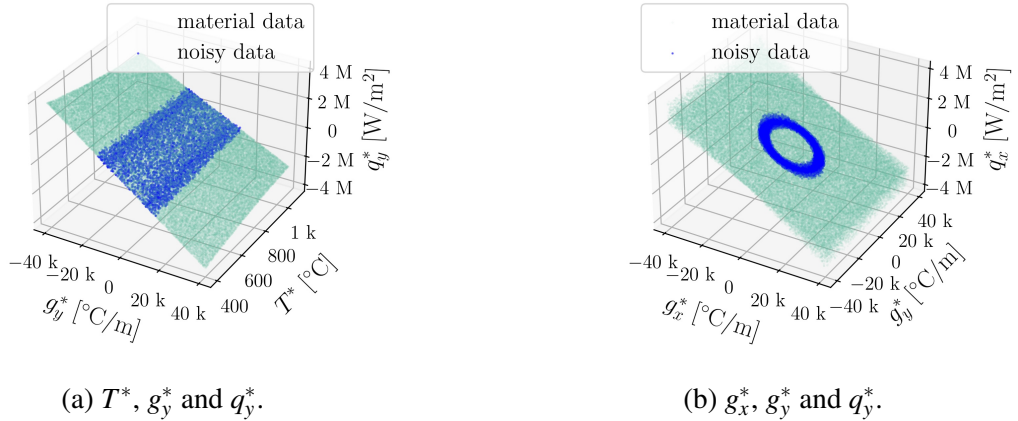


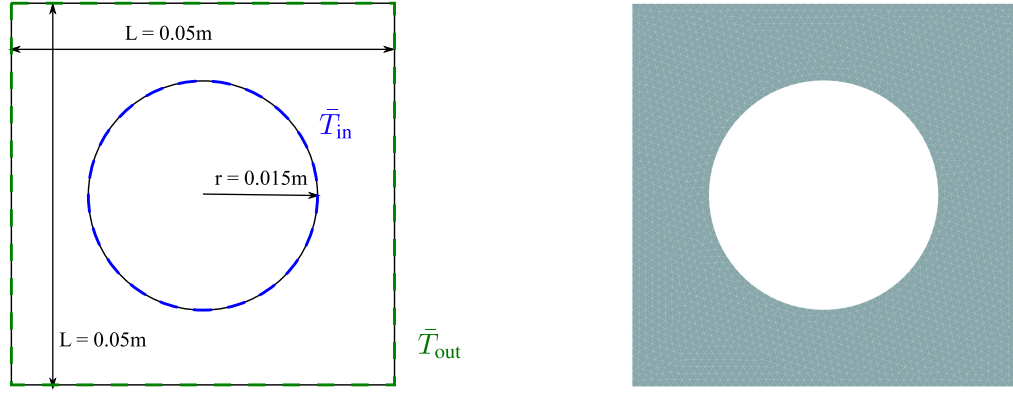
Figure 4.14: Material dataset C created by Algorithm 4 with 10^6 material datapoints. The temperature range is $[400, 1100]$, the gradient range is $[-40 \times 10^3, 40 \times 10^3]$, and the noise is applied in the range $[10 \times 10^3, 15 \times 10^3]$ with standard deviation $\sigma_\eta = 1.0$.

4.3.2 Material datasets from synthetic experiments

Material datasets from real-life experiments are rarely as organised as they were presented in the previous subsection, and noise, scarcity of data and irregularity in dataset density are expected.

In addition to datasets A, B and C created in the previous subsection, we will generate datasets D, E and F using sets of synthetic experiments. A synthetic experiment aims to replicate a real-life experiment on a piece of material considered, such as a piece of graphite used in a nuclear reactor. The geometry and mesh used for the synthetic experiment are shown in Figure 4.15, and the analysis is performed with hierarchical shape functions with approximation order $p = 2$. For an example setup, the temperature on the inner surface is kept at 500°C and on the outer surface at 1100°C for one of the experiments. More experiments are conducted with different inner and outer temperature for each instance of the experiment to cover the possible ranges of temperature, temperature gradient and flux graphite might reach in a nuclear reactor. The temperature, its gradient and flux are recorded at a set of points (integration points of Gauss quadrature), which might be similar to datapoints obtained by a method such as data-driven identification [Leygue et al., 2018; Stainier et al., 2019; Valdés-Alonzo et al., 2022].

The synthetic experiments simulate nonlinear material behaviour (see (4.13)) and apply the nonlinear heat diffusion formulation introduced in section 2.4. These experiments are conducted over a temperature range of $[400, 1100]$ by iterating through 10 equally spaced values for both



(a) Geometry and boundary conditions.

(b) Mesh ($h = 0.0002$).

Figure 4.15: Example Synthetic experiment: Geometry and mesh used for the synthetic experiment setup with \bar{T}_{in} and \bar{T}_{out} as temperature boundary conditions.

\bar{T}_{in} and \bar{T}_{out} within this range. Each combination of \bar{T}_{in} and \bar{T}_{out} values is tested to produce the material dataset D, shown in Figure 4.16.

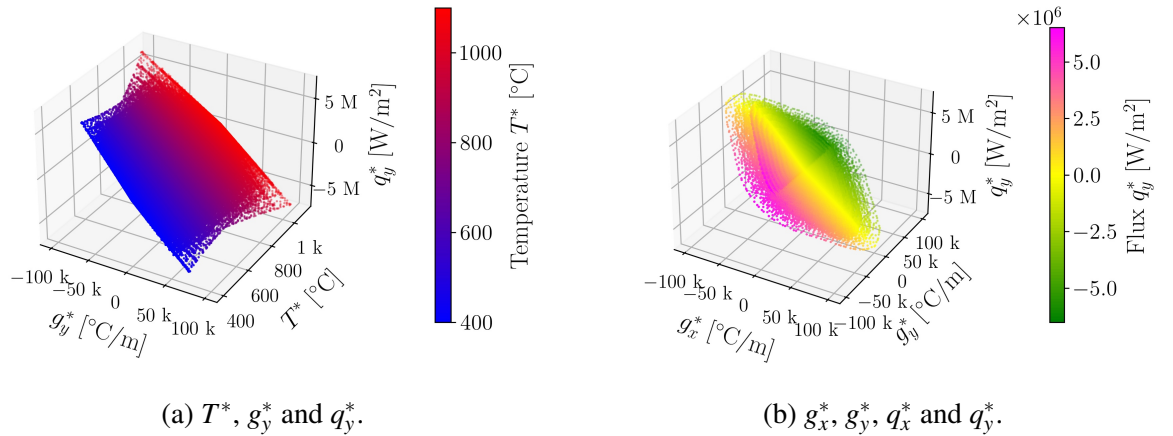
(a) T^* , g_x^* and q_y^* .(b) g_x^* , g_y^* , q_x^* and q_y^* .

Figure 4.16: Material dataset D created by synthetic experiments.

For material dataset E, the same synthetic experiment is conducted with an adjusted temperature range of $[550, 1100]$. In this dataset, shown in Figure 4.17, temperature gradients g_x^* and g_y^* outside the range $[-10 \times 10^3, 10 \times 10^3]$ are intentionally removed. This modified dataset serves to test the robustness of the data-driven approach when the field values of an analysis, introduced in the next section, reach values outside of the material data range, i.e. minimum temperature value in the dataset is 550°C and one of the temperature boundary condition will be 500°C . The missing data in this dataset could correspond to a situation where the experiments simply did not consider the temperature range of $[400, 550]$ or a bulk of the data was removed during preprocessing and only the temperature gradient range of $[-10 \times 10^3, 10 \times 10^3]$ was preserved.

Finally, material dataset F is created by taking the material dataset D and adding noise to the values with a magnitude of the gradient of temperature smaller than $2 [^\circ\text{C}/\text{m}]$ to test the

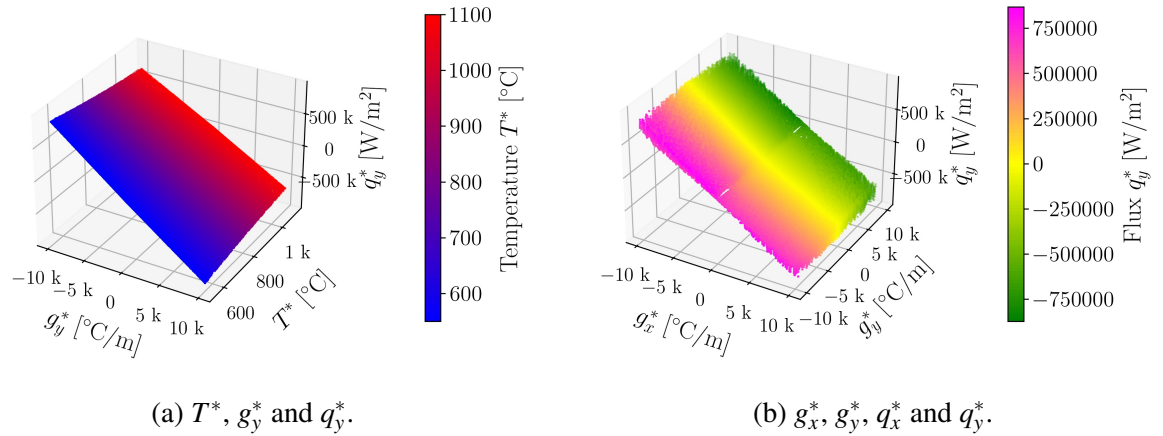


Figure 4.17: Material dataset E created by synthetic experiments with missing data.

robustness of the approach, imitating being unable to measure accurately small values of heat flow. The resulting material dataset F is shown in Figure 4.18.

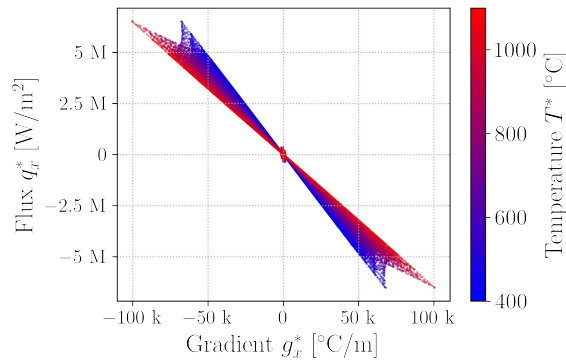


Figure 4.18: Material dataset F created by synthetic experiments with intentionally added noise around to values with magnitude of gradient of temperature smaller than 2 [°C/m].

The datasets introduced in this section are summarised in Table 4.4.

4.4 2D brick example with six material datasets

From this chapter onwards, a graphite brick example, along with the material datasets introduced in section 4.3, is used to evaluate the data-driven approach to diffusion problems. The material datasets A-F (Table 4.4) with the data-driven finite element formulation (4.7) are used to approximate the temperatures and fluxes through the brick. There is no exact solution to compare to; instead, we rely on the uncertainty quantification measures and error estimation introduced in this and the following chapters.

Due to the symmetrical nature of the new example representing a graphite brick in a nuclear reactor and the boundary conditions only a quarter is used in the numerical analysis, as shown in

Dataset	Description	Figure Reference
A (regular sparse)	Created directly from the constitutive relationship (4.13) by prescribing the ranges of temperatures and temperature gradients and calculating the flux values.	Figure 4.13
B (regular dense)	Generated similarly to A, but contains much more datapoints.	Not shown (similar to Figure 4.13)
C (random noisy)	Created directly from the constitutive relationship (4.13) by using uniform random distribution and Gaussian noise (4.11) is added to a part of the dataset.	Figure 4.14
D (synthetic experiment)	Created by running a synthetic experiment (SE).	Figure 4.16
E (SE w/ missing data)	Created by running a synthetic experiment similar to D, but the resulting dataset covers a smaller range of values.	Figure 4.17
F (SE w/ noisy data)	Created by adding noise to a set of datapoints in dataset D.	Figure 4.18

Table 4.4: Summary of 5D Material Datasets

Figure 4.19. The inner boundary is kept at 1000°C to simulate the heat from a nuclear reaction, and the outer boundary is kept at 500°C by the gas when the reactor is operational. These temperatures are chosen for testing purposes only as the temperatures for each of the graphite bricks vary throughout a nuclear reactor. At the same time, it is assumed that there is no heat transfer through the small inner holes, which are filled with methane gas, a poor thermal conductor under reactor operating conditions. The resulting fields of the analysis with material dataset B (regular dense) are shown in Figure 4.20.

Once a solution is obtained, the distance from the dataset can be evaluated at each Gauss point of every finite element. After that, the average distance to material dataset can be computed for each element separately. Additionally, the standard deviation of the distance to the material dataset per element can also be calculated for each element.

The average distance from the dataset per element is shown in Figure 4.21 where the results of simulations with datasets A-F are compared. The results should be interpreted as if there was no prior knowledge of the quality of the datasets, as the aim of this work is to evaluate the capabilities of the introduced approach, not the synthetic material creation. From Figure 4.21 it can be seen that if the dataset is uniformly distributed and covers all of the areas of concern (A, C, D and F), the distance to the dataset depends on the sparsity of the dataset. On the other hand, when more realistic datasets (D-F) are taken into account, the distance to the dataset is more

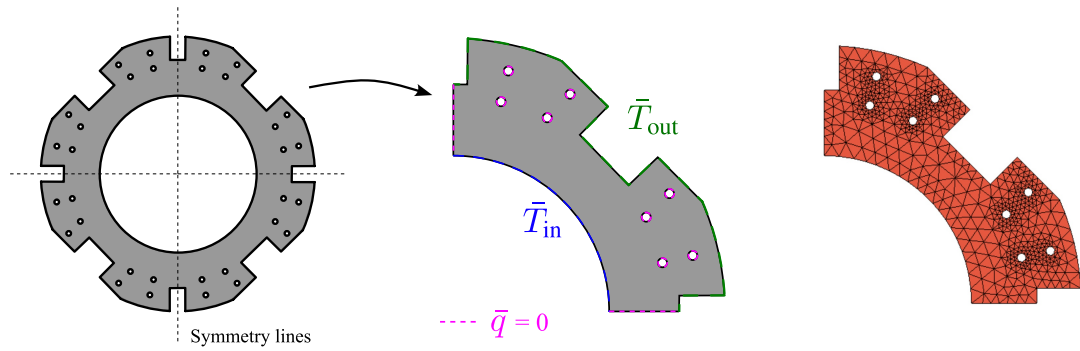


Figure 4.19: Example Brick: Geometry and mesh of a nuclear graphite brick with a testing boundary conditions of $\bar{T}_{in} = 1000^\circ C$ and $\bar{T}_{out} = 500^\circ C$ and $\bar{q} = 0$ on the symmetry lines and the small inner holes, also see Appendix C

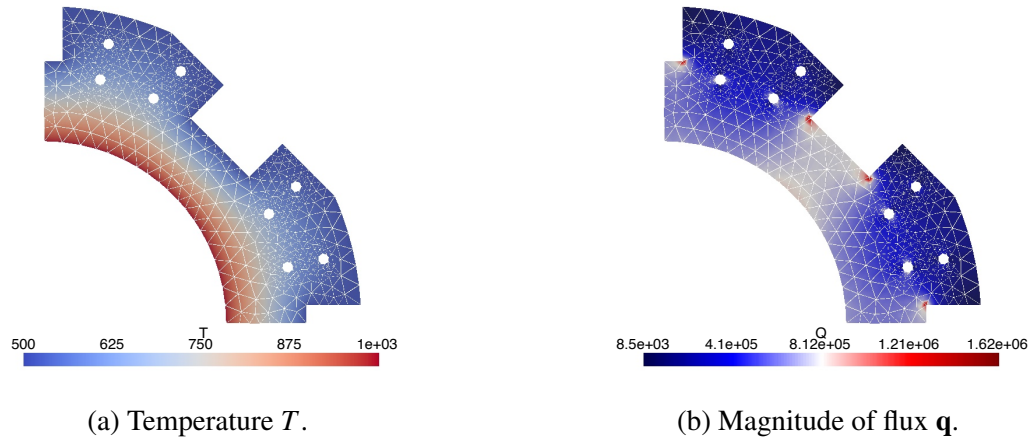
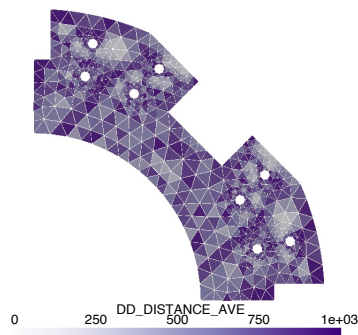


Figure 4.20: Example Brick: results of the analysis with a dense material dataset with no noise present (dataset B).

localised and the areas of concern, which are identifiable areas with potentially less accurate results than the rest of the domain, are more easily identified. Notably, for the analysis with dataset E, the distance to the material dataset per element is the highest in the area where the resulting field values are not covered by the dataset.

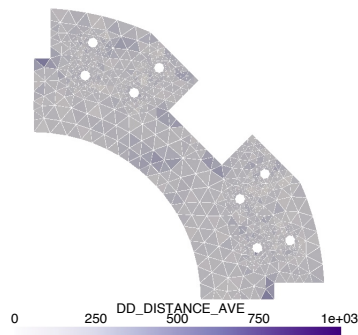
However, the distance to the dataset itself does not carry practical information since the datasets have been scaled *a priori* (see subsection 4.1.2) and the distance is not directly related to the quality of the dataset. The scaling used is $S_q = 0.01$ and $S_T = 10.0$ for all of the datasets to bring the flux values in the material dataset to the same order of magnitude as the temperature gradient considering a comparison of both the maximum and the standard deviation of the values of each of the dimensions g_x^* , g_y^* , q_x^* and q_y^* . The scaling is done to ensure that the distance is not dominated by one of the dimensions. The temperature has been scaled to be an order of magnitude lower than the temperature gradient to inform the material data search choice but not to be the dominating factor. The average distance in Figure 4.21 is rather a measure through a 5D space. Hence, if only one material dataset is present, further investigation is required to



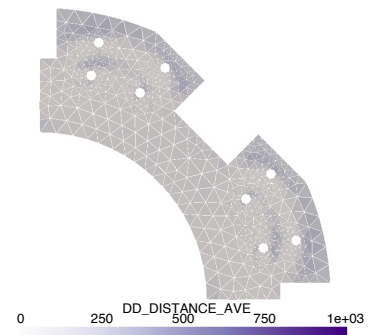
(a) Dataset A (regular sparse): The distance to the dataset is the highest of all datasets but no area is affected more than others.



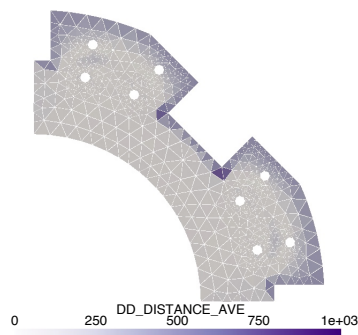
(b) Dataset B (regular dense): Undetermined conclusions.



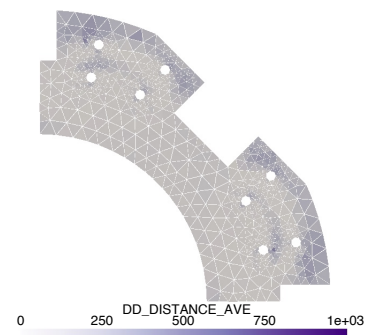
(c) Dataset C (random noisy): Undetermined conclusions.



(d) Dataset D (synthetic experiment): Areas of concern are visible but the distance is low.



(e) Dataset E (SE w/ missing data): The distance to the dataset is high and the areas of concern are localised.



(f) Dataset F (SE w/ noisy data): Undetermined conclusions.

Figure 4.21: Example Brick: Average distance from the dataset per element upon solution of the problem using datasets A-F.

evaluate whether the dataset is sufficient for the analysis and how far the resulting fields are from the dataset. The distance can also be calculated in the relevant dataset dimension, such as the temperature dimension, to evaluate the suitability of the dataset for the analysis considered.

Figure 4.22 and Figure 4.23 show the distances of the resulting fields to the material datasets for temperature and flux in y direction after scaling the relevant components back to the original values. The resulting distances can now be compared directly to the resulting fields in Figure 4.20 for the overall range of values considered. It is up to the user, e.g. an analyst engineer, to decide whether the distance is acceptable or not, and the distance can be used as a measure of the suitability of the dataset for the analysis. From Figure 4.22, it can be seen that the resulting distance between temperature field and temperature component of the closest points for dataset E are ≈ 85 in the area of the domain where the temperature is ≈ 500 . It can also be seen that the flux q_y distance in Figure 4.23 for dataset A is $\approx 70 \times 10^3$ in large part of the domain, including areas where the magnitude of flux reaches as little as $\approx 20 \times 10^3$.

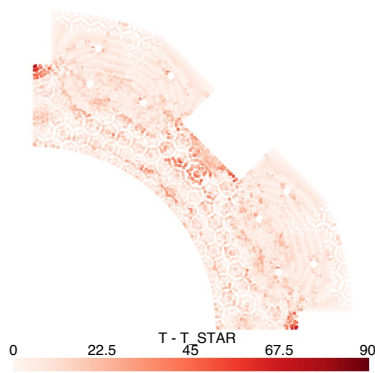
The standard deviation of the distance to the dataset computed separately for each element can be calculated to evaluate the variance of the distance to the dataset. The standard deviation of the distance to the dataset per element is shown in Figure 4.24. If the standard deviation is high on an element, it means that the element considered is partially covered by the dataset and partially not, i.e. field values at some integration points are further from the dataset than at other integration points of the same element. Refining the mesh at these particular elements can help discover the areas where the dataset is far from the values searched for and also isolate and identify the influence of the outliers on the results. Since the datasets B, C, D and F sufficiently cover all of the areas of concern, the standard deviation of the distance is also comparatively low in comparison to the results with datasets A and E. Notably, results with dataset A show no pattern in the standard deviation of the distance, however, results with dataset E show a localised high standard deviation of the distance in some of the corner elements where refinement might have a positive effect on the results. Further discussion about adaptive refinement follows in subsection 5.2.3 after "weaker" data-driven approach is introduced.

The results of the analysis with the data-driven approach introduced in this chapter show that the distance to the material dataset can be used to evaluate the suitability of the dataset and the results obtained and related potential accuracy issues.

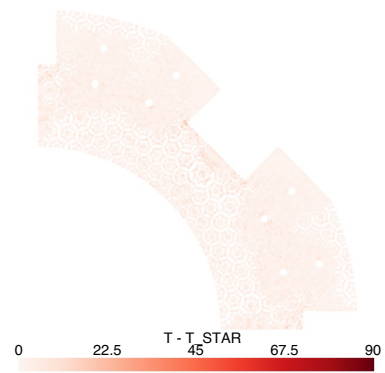
The data-driven formulation introduced relies on finding the closest point in the material dataset at every integration point and then using the found points to satisfy the conservation laws and boundary conditions.

Real-life problems do not have an exact solution to compare the results obtained to, but the steps of this formulation, more specifically the search through the material dataset at every integration point, provide for a sanity check:

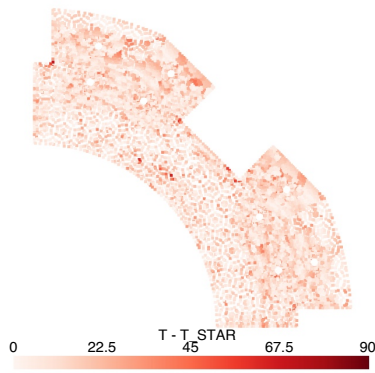
1. How does the average distance between the unknown fields and the material dataset vary across the domain?



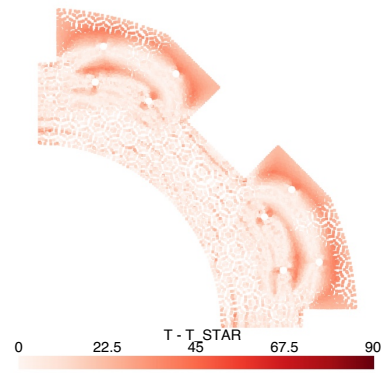
(a) Dataset A.



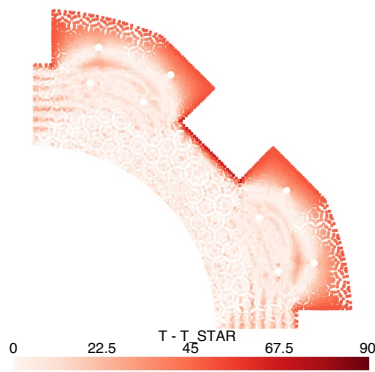
(b) Dataset B.



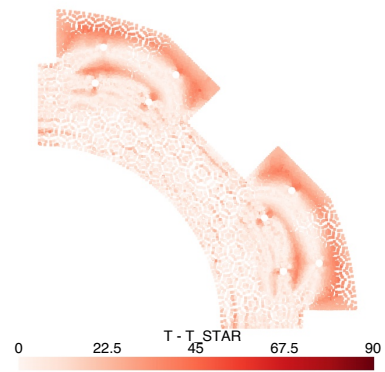
(c) Dataset C.



(d) Dataset D.

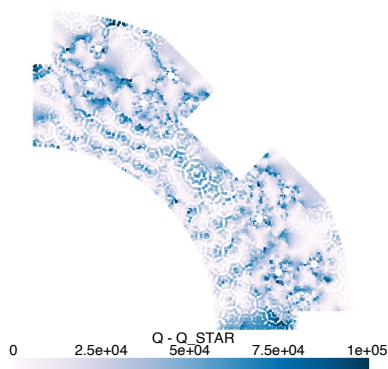


(e) Dataset E.

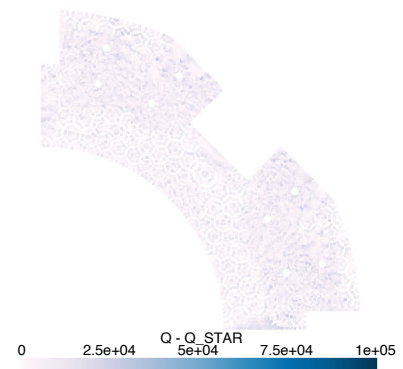


(f) Dataset F.

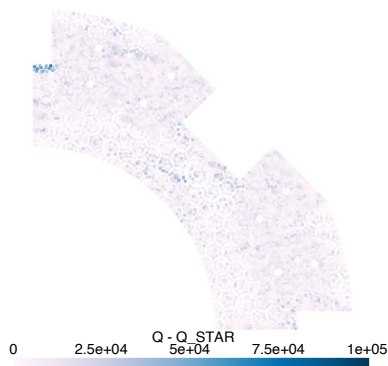
Figure 4.22: Example Brick: Distance for each integration point between the resulting temperature field T and the temperature component T^* of the closest points in the material dataset upon solution of the problem using datasets A-F. For the resulting values of temperature see Figure 4.20a.



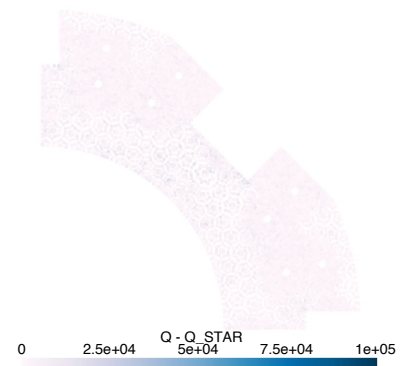
(a) Dataset A.



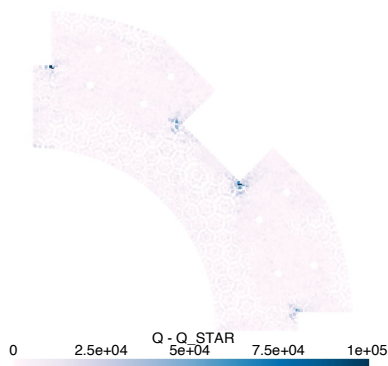
(b) Dataset B.



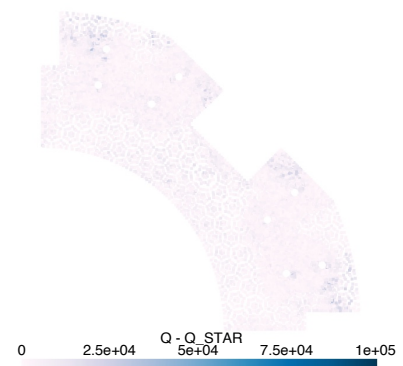
(c) Dataset C.



(d) Dataset D.

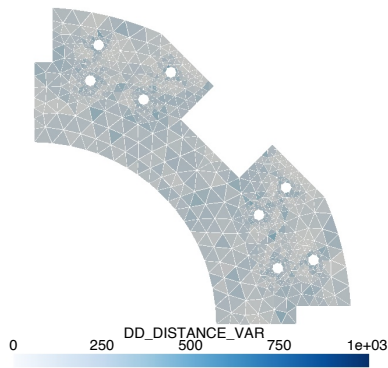


(e) Dataset E.

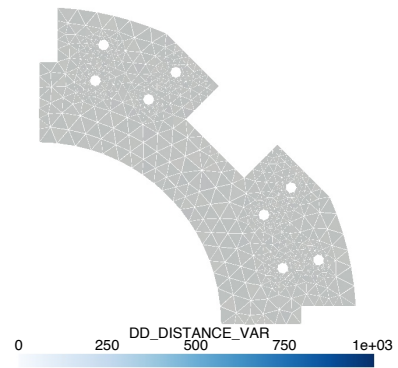


(f) Dataset F.

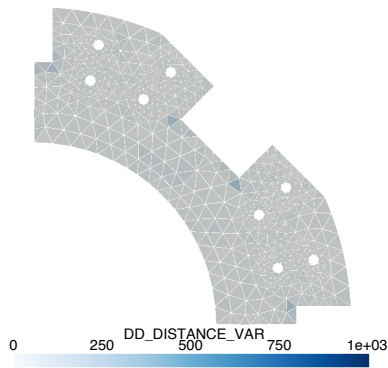
Figure 4.23: Example Brick: Distance for each integration point between the resulting flux field in y direction q_y and the y flux component q_y^* of the closest points in the material dataset upon solution of the problem using datasets A-F. For the resulting values of flux magnitude see Figure 4.20b.



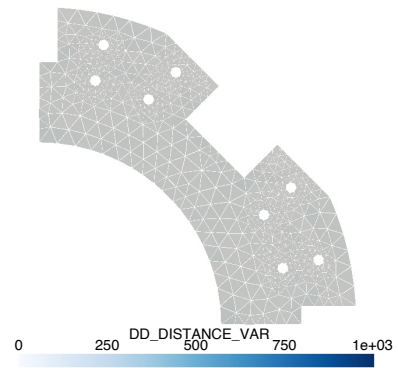
(a) Dataset A. Moderately high variance in distances in elements but with no pattern.



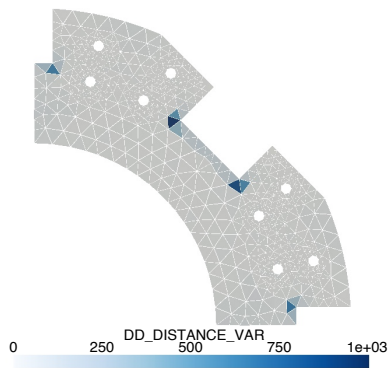
(b) Dataset B.



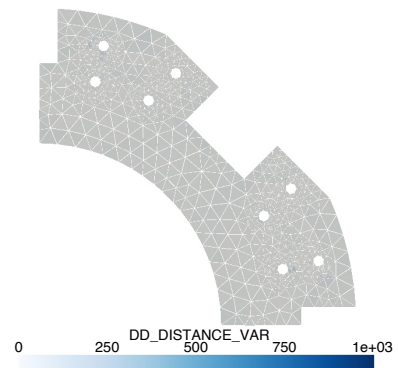
(c) Dataset C.



(d) Dataset D.



(e) Dataset E. High variance in distances within specific elements.



(f) Dataset F.

Figure 4.24: Example Brick: Standard deviation of the distance from the dataset per element upon solution of the problem using datasets A-F.

2. In which dimension of the dataset is the distance high?
3. Is the distance to the material dataset acceptable in the overall range of values considered?
4. Where could the mesh be refined to reduce the uncertainty of the results, i.e. high standard deviation of the distance within an element?

The first point highlights potential problematic areas of the domain where the data from the material dataset is far from the calculated field values, and therefore these areas might not be correctly informed of how the actual material might behave.

The second point identifies which dimensions of the dataset cause the distance to be high in these areas and provides a guide to in which ranges new data could be obtained if possible and necessary.

The third point assesses if the distance is acceptable by comparing the distance in the individual dimensions of the dataset to the resulting field values. This step depends on the requirements of the analysis at hand, for example, there will always be missing data at the singularity (flux field) in the inner corners of the graphite brick where the flux is theoretically infinite.

The last point addresses a potential improvement in accuracy or locating of the problematic areas with a higher number of integration points, i.e. refinement of the element.

However, if the material dataset is dense but noisy, e.g. dataset C and F, a similar scenario to Figure 4.9 is observed and the distances from the material dataset, see Figure 4.21, are small since each noisy point is close to the resulting values of the unknown fields. More on how to address this behaviour is discussed in chapter 6.

Additionally, the data-driven formulation introduced in this chapter does not allow for the *a posteriori* error estimation introduced in chapter 3 and cannot tell where the finite element approximation errors are the highest without further development. The derivation and implementation of robust and accurate finite element error indicators for this formulation are not straightforward and are not covered in this thesis. Instead, the next chapter will introduce a data-driven approach derived with the weaker mixed formulation, which will have access to the uncertainty/error measurements introduced in the present chapter 4 and the previous chapter 3 at the same time.

4.5 Summary

In this chapter, the data-driven approach following [Kirchdoerfer and Ortiz, 2016] is introduced for the heat diffusion problem. The derived formulation is implemented in MoFEM [Kaczmarczyk et al., 2020] and tested with synthetic datasets on examples w.r.t. the analytical solution and the results obtained with the standard FE formulation. The same convergence rate is observed for the data-driven approach as for the standard FE formulation, when the material dataset contains a sufficient number of datapoints ("saturated" dataset) and no noise is present. The same

results are obtained for "saturated" dataset with orders of magnitude difference between the flux and temperature gradient values in the dataset, however, the number of iterations required to converge with the same precision is higher. Moreover, the results obtained with a material dataset with a smaller number of datapoints and orders of magnitude difference between the values of the material dataset dimensions are not satisfactory. Therefore, scaling was introduced to bring the values of the dataset to the same order of magnitude, which is a common practice when searching for a closest point, and improved results were obtained.

This chapter also introduces six 5D synthetic material datasets $\{T^*, g_x^*, g_y^*, q_x^*, q_y^*\}$, which are used for validation of the approach on an example of 2D graphite brick slice. To accommodate the extra dimension T^* , the search through the material dataset is modified to find the closest point in the dataset in 5D space. Some of the material datasets purposefully include noise at specific locations or do not cover the entire range of values to test the robustness of the data-driven approach.

On top of robustness, the aim is to evaluate the ability to determine how certain the user/analyst can be about the results obtained with the data-driven approach. With the formulation introduced in this chapter, the distance to the dataset can be used to evaluate if and where the data does not cover the range of values required for the analysis at hand. The distance can then be further inspected for the individual dimensions. Nevertheless, when noise is present in the material dataset, the results are less accurate and the distance to the dataset can be small and not alert the user to potential issues with the results. The topic of noise and uncertainty is further explored in chapter 6.

The next chapter will combine and expand the data-driven approach introduced in this chapter and the mixed formulation introduced in chapter 3.

Chapter 5

Weaker mixed data-driven formulation

The "stronger" data-driven FE formulation [Kirchdoerfer and Ortiz, 2016; Nguyen et al., 2020] discussed in the previous section is already mixed, i.e., it contains multiple unknown fields for one physical process. However, the choice of spaces in which these unknown fields are approximated is not natural from the functional analysis point of view.

This chapter contains the main novelty of this thesis, deriving the data-driven approach with the mixed formulation resulting in a weaker mixed data-driven formulation (weaker DD). Weaker DD formulation utilises more natural spaces for a diffusion problem, same as the mixed formulation introduced in chapter 3. The heat flux is approximated in $H(\text{div}; \Omega)$ space, which enforces the continuity of the normal flux component across any inner boundaries, further enforcing the conservation of energy *a priori*. The temperature belongs to $L^2(\Omega)$ space, which allows for discontinuous temperature fields across the element boundaries. Furthermore, error indicators from chapter 3 are amended to fit the weaker DD formulation, allowing for adaptive refinement.

The data-driven part of this formulation evolves from the previous chapter, chapter 4, where a material dataset is used instead of a constitutive equation. The search algorithm used for finding the closest points from the material dataset to the unknown field values remains the same as in the previous chapter, as well as the iterative procedure for solving the problem. The distance to the material dataset continues to be used to indicate the quality of the solution, and is additionally used to further improve the adaptive refinement algorithm.

Weaker DD, the main new contribution to the field, is the combination of data-driven approach and mixed formulation concepts, introduced in chapter 4 and chapter 3, respectively, takes advantages and strengths of both and allows for further improvements which would be difficult to achieve with either of them alone.

5.1 Derivation

In chapter 3, the mixed diffusion problem was derived upon introducing a new variable, flux \mathbf{q} , using the constitutive equation, see (3.1). However, since the data-driven approach uses a material dataset, the constitutive equation does not exist in this formulation. Therefore, a new field $\mathbf{g} = \mathbf{g}(\mathbf{x})$ is introduced, representing the gradient of temperature field T :

$$\mathbf{g} = \nabla T \text{ in } \Omega, \quad (5.1)$$

which becomes one of the unknown fields in the finite element analysis. From now on, this field will be referred to as the gradient \mathbf{g} . The problem statement can be summarised as follows:

Find $T \in L^2$ and $\mathbf{q} \in \mathcal{Q}$ such that:

$$\begin{cases} \nabla \cdot \mathbf{q} = s & \text{in } \Omega & (5.2a) \\ \mathbf{g} = \nabla T & \text{in } \Omega & (5.2b) \\ \mathbf{q} \cdot \mathbf{n} = \bar{q} & \text{on } \Gamma_q & (5.2c) \\ T = \bar{T} & \text{on } \Gamma_T & (5.2d) \end{cases}$$

The distance of the fields to the material dataset \mathcal{D} , defined previously in (4.1), which minimisation can find the closest material state $\{\mathbf{g}^*, \mathbf{q}^*\}$ for any point in the domain, is redefined as:

$$\text{dist}(\{\mathbf{g}, \mathbf{q}\}, \mathcal{D}) = \min_{\{\mathbf{g}^*, \mathbf{q}^*\} \in \mathcal{D}} \sqrt{S_g (\mathbf{g} - \mathbf{g}^*)^2 + S_q (\mathbf{q} - \mathbf{q}^*)^2}, \quad (5.3)$$

which uses the new variable, gradient \mathbf{g} , instead of the temperature gradient ∇T , and S_g and S_q remain the same stabilising/scaling parameters.

Similarly, the integrated distance functional (4.3), is redefined as follows:

$$J(\mathbf{g}, \mathbf{q}) = \frac{1}{2} \int_{\Omega} S_g (\mathbf{g} - \mathbf{g}^*)^2 d\Omega + \frac{1}{2} \int_{\Omega} S_q (\mathbf{q} - \mathbf{q}^*)^2 d\Omega, \quad (5.4)$$

Next, the Lagrangian is formulated by minimising the integrated distance functional (5.4), while imposing the energy conservation law (5.2a) and the new variable definition (5.2b) as constraints:

$$\mathcal{L}(\nabla T, \mathbf{g}, \mathbf{q}, \boldsymbol{\tau}, \lambda) = J(\mathbf{g}, \mathbf{q}) + \int_{\Omega} \boldsymbol{\tau} \cdot (\mathbf{g} - \nabla T) d\Omega + \int_{\Omega} \lambda (\nabla \cdot \mathbf{q} - s) d\Omega, \quad (5.5)$$

where λ and $\boldsymbol{\tau}$ are scalar and vector fields of Lagrange multipliers, respectively.

The regularity requirement on temperature is weakened by integrating the component containing the gradient of temperature ∇T by parts, satisfying at the same time the temperature

boundary condition (5.2d) and imposing $\boldsymbol{\tau} \cdot \mathbf{n} = 0$ on Γ_q :

$$\begin{aligned}
\mathcal{L}(T, \mathbf{g}, \mathbf{q}, \boldsymbol{\tau}, \lambda) &= \int_{\Omega} S_g (\mathbf{g} - \mathbf{g}^*)^2 d\Omega + \int_{\Omega} S_q (\mathbf{q} - \mathbf{q}^*)^2 d\Omega \\
&\quad + \int_{\Omega} \boldsymbol{\tau} \cdot \mathbf{g} d\Omega - \int_{\Gamma_T} (\boldsymbol{\tau} \cdot \mathbf{n}) \bar{T} d\Gamma_T + \int_{\Omega} (\nabla \cdot \boldsymbol{\tau}) T d\Omega \\
&\quad + \int_{\Omega} \lambda (\nabla \cdot \mathbf{q}) d\Omega - \int_{\Omega} \lambda s d\Omega.
\end{aligned} \tag{5.6}$$

Note that $\boldsymbol{\tau} \cdot \mathbf{n} = 0$ on Γ_q reflects the enforcement of the Dirichlet boundary condition and ensures the problem is well posed.

The solution is found as a stationary point of the Lagrangian (5.6) at which its variation vanishes:

$$\left\{ \begin{array}{ll}
\int_{\Omega} \delta T (\nabla \cdot \boldsymbol{\tau}) d\Omega = 0 & \forall \delta T \in L^2(\Omega) \\
\int_{\Omega} S_g \delta \mathbf{g} \cdot (\mathbf{g} - \mathbf{g}^*) d\Omega + \int_{\Omega} \delta \mathbf{g} \cdot \boldsymbol{\tau} d\Omega = 0 & \forall \delta \mathbf{g} \in \mathbf{L}^2(\Omega) \\
\int_{\Omega} S_q \delta \mathbf{q} \cdot (\mathbf{q} - \mathbf{q}^*) d\Omega + \int_{\Omega} (\nabla \cdot \delta \mathbf{q}) \lambda d\Omega = 0 & \forall \delta \mathbf{q} \in \mathcal{Q}_0 \\
\int_{\Omega} \delta \lambda (\nabla \cdot \mathbf{q}) d\Omega - \int_{\Omega} \delta \lambda s d\Omega = 0 & \forall \delta \lambda \in L^2(\Omega) \\
\int_{\Omega} (\delta \boldsymbol{\tau} \cdot \mathbf{g} + (\nabla \cdot \delta \boldsymbol{\tau}) T) d\Omega - \int_{\Gamma_T} (\delta \boldsymbol{\tau} \cdot \mathbf{n}) \bar{T} d\Gamma = 0 & \forall \delta \boldsymbol{\tau} \in \mathcal{Q}_0.
\end{array} \right. \tag{5.7}$$

The test and trial functions belong to functional spaces as assigned in Table 5.1, where $L^2(\Omega)$ and $\mathbf{L}^2(\Omega)$ are the Lebesgue spaces for square-integrable scalar and vector functions, respectively, and $H(\text{div}; \Omega)$ is the space for vector functions with square-integrable divergence, also see Appendix A.

The choice of spaces in this weaker mixed formulation results in less requirements on the regularity of the solution, compared with the stronger data-driven formulation presented in chapter 4, since the spaces for T and \mathbf{g} do not require these fields to be smooth across the element boundaries. However, the continuity of the normal flux \mathbf{q} is enforced across any inner boundaries. This choice of spaces is more natural for the transport problems such as heat transfer.

For comparison, the solution of the stronger mixed formulation for the data-driven heat transfer problem would have temperature T in $H^1(\Omega)$ Sobolev space for square-integrable scalar functions, and flux \mathbf{q} in $\mathbf{L}^2(\Omega)$, see Table 4.1, i.e. continuity of flux across element boundaries would not be ensured, which is not natural for the considered transport problem.

The test and trial functions are approximated by the finite element basis functions, see Table 5.2, compare with Table 4.2 and Table 3.2. Note that both the gradient \mathbf{g} and the flux \mathbf{q} are

Field	Space
Temperature T (trial function)	$T \in L^2(\Omega)$
δT (test function)	$\delta T \in L^2(\Omega)$
Gradient \mathbf{g}	$\mathbf{g} \in \mathbf{L}^2(\Omega)$
$\delta \mathbf{g}$	$\delta \mathbf{g} \in \mathbf{L}^2(\Omega)$
Flux \mathbf{q}	$\mathbf{q} \in \mathcal{Q}, \mathcal{Q} = \{\mathbf{u} \in H(\text{div}; \Omega) \mid \mathbf{u} \cdot \mathbf{n} = \bar{q} \text{ on } \Gamma_q\}$
$\delta \mathbf{q}$	$\delta \mathbf{q} \in \mathcal{Q}_0, \mathcal{Q}_0 = \{\mathbf{v} \in H(\text{div}; \Omega) \mid \mathbf{v} \cdot \mathbf{n} = 0 \text{ on } \Gamma_q\}$
Lagrange multiplier λ (scalar)	$\lambda \in L^2(\Omega)$
$\delta \lambda$	$\delta \lambda \in L^2(\Omega)$
Lagrange multiplier $\boldsymbol{\tau}$ (vectorial)	$\boldsymbol{\tau} \in \mathcal{Q}_0$
$\delta \boldsymbol{\tau}$	$\delta \boldsymbol{\tau} \in \mathcal{Q}_0$

Table 5.1: Functional spaces for the data-driven weaker mixed formulation.

vectorial fields, however, the components of gradient are approximated by scalar basis functions G_a , while the flux is approximated by a vectorial basis function $\mathbf{Q}_{\mathcal{A}}$. Indices next to the basis functions N, G, \mathbf{Q}, L and \mathbf{M} indicate the index of the basis function, see glossary for more details. This is due to the fact that the gradient belongs to $\mathbf{L}^2(\Omega)$ space, while the flux belongs to $H(\text{div}; \Omega)$ space.

	Trial function	Test function
Temperature	$T^h = T_a N_a$	$\delta T^h = \delta T_b N_b$
Gradient	$\mathbf{g}^h = \mathbf{g}_a G_a$	$\delta \mathbf{g}^h = \delta \mathbf{g}_b G_b$
Flux	$\mathbf{q}^h = q_{\mathcal{A}} \mathbf{Q}_{\mathcal{A}}$	$\delta \mathbf{q}^h = \delta q_{\mathcal{B}} \mathbf{Q}_{\mathcal{B}}$
Lagrange multiplier (scalar)	$\lambda^h = \lambda_a L_a$	$\delta \lambda^h = \delta \lambda_b L_b$
Lagrange multiplier (vectorial)	$\boldsymbol{\tau}^h = \tau_{\mathcal{A}} \mathbf{M}_{\mathcal{A}}$	$\delta \boldsymbol{\tau}^h = \delta \tau_{\mathcal{B}} \mathbf{M}_{\mathcal{B}}$
Divergence of flux	$\nabla \cdot \mathbf{q}^h = q_{\mathcal{A}} (\nabla \cdot \mathbf{Q}_{\mathcal{A}})$	$\nabla \cdot \delta \mathbf{q}^h = \delta q_{\mathcal{B}} (\nabla \cdot \mathbf{Q}_{\mathcal{B}})$
Divergence of $\boldsymbol{\tau}$	$\nabla \cdot \boldsymbol{\tau}^h = \tau_{\mathcal{A}} (\nabla \cdot \mathbf{M}_{\mathcal{A}})$	$\nabla \cdot \delta \boldsymbol{\tau}^h = \delta \tau_{\mathcal{B}} (\nabla \cdot \mathbf{M}_{\mathcal{B}})$

Table 5.2: Finite element basis functions for the weaker data-driven formulation of the diffusion problem.

Each field can be interpolated using hierarchical shape functions [Kaczmarczyk et al., 2020] and to satisfy LBB stability conditions [Boffi et al., 2013], the approximation orders are assigned to unknown fields as shown in Table 5.3. Note that the approximation order for the gradient field

\mathbf{g} is $p + 1$ as order p is not stable in this formulation.

Field	Approximation order
Temperature T	p
Gradient \mathbf{g}	$p + 1$
Flux \mathbf{q}	$p + 1$
Scalar Lagrange multiplier λ	p
Vectorial Lagrange multiplier $\boldsymbol{\tau}$	$p + 1$

Table 5.3: Approximation orders for the weaker mixed data-driven formulation.

The procedure of deriving the final matrix form of the problem is similar to the one presented in chapter 3, and the final matrix form of the problem is as follows:

$$[\mathbf{K}_{\alpha\beta}][\mathbf{u}_\alpha] = [\mathbf{F}_\beta], \quad (5.8)$$

where $[\mathbf{u}_\alpha]$ is the vector of vectors of unknown coefficients:

$$[\mathbf{u}_\alpha] = \begin{bmatrix} T_a \\ \mathbf{g}_a \\ q_{\mathcal{A}} \\ \lambda_a \\ \boldsymbol{\tau}_{\mathcal{A}} \end{bmatrix}, \quad (5.9)$$

$[\mathbf{K}_{\alpha\beta}]$ is the diffusivity matrix, where $d\Omega$ is dropped in writing the integral for brevity:

$$[\mathbf{K}_{\alpha\beta}] = \begin{bmatrix} 0 & 0 & \mathbf{0} & \mathbf{0} & \int_{\Omega} N_b (\nabla \cdot \mathbf{M}_{\mathcal{A}}) \\ \mathbf{0} & \int_{\Omega} S_g G_b G_a & \mathbf{0} & \mathbf{0} & \int_{\Omega} G_b \mathbf{M}_{\mathcal{A}} \\ \mathbf{0} & \mathbf{0} & \int_{\Omega} S_q (\mathbf{Q}_{\mathcal{B}} \cdot \mathbf{Q}_{\mathcal{A}}) & \int_{\Omega} (\nabla \cdot \mathbf{Q}_{\mathcal{B}}) L_a & \mathbf{0} \\ \mathbf{0} & \mathbf{0} & \int_{\Omega} L_b (\nabla \cdot \mathbf{Q}_{\mathcal{A}}) & \mathbf{0} & \mathbf{0} \\ \int_{\Omega} (\nabla \cdot \mathbf{M}_{\mathcal{B}}) N_a & \int_{\Omega} \mathbf{M}_{\mathcal{B}} G_a & \mathbf{0} & \mathbf{0} & \mathbf{0} \end{bmatrix}, \quad (5.10)$$

and $[\mathbf{F}_\beta]$ is the vector of right-hand side terms, which can be written for the two-step data-driven iterative procedure, see subsection 4.1.1, as follows:

$$[\mathbf{F}_\beta] = \begin{bmatrix} \mathbf{0} \\ \int_{\Omega} S_g G_b \mathbf{g}^* d\Omega \\ \int_{\Omega} S_q \mathbf{Q}_{\mathcal{B}} \cdot \mathbf{q}^* d\Omega \\ \int_{\Omega} L_b s d\Omega \\ \int_{\Gamma_T} (\mathbf{M}_{\mathcal{B}} \cdot \mathbf{n}) \bar{T} d\Gamma \end{bmatrix}. \quad (5.11)$$

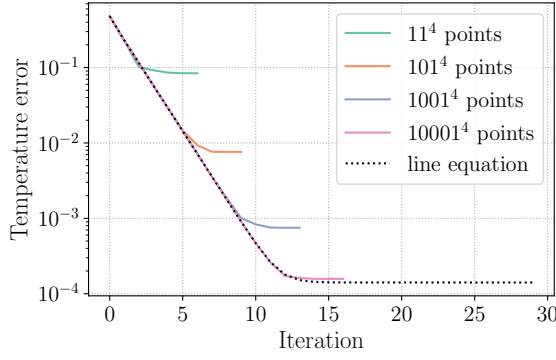
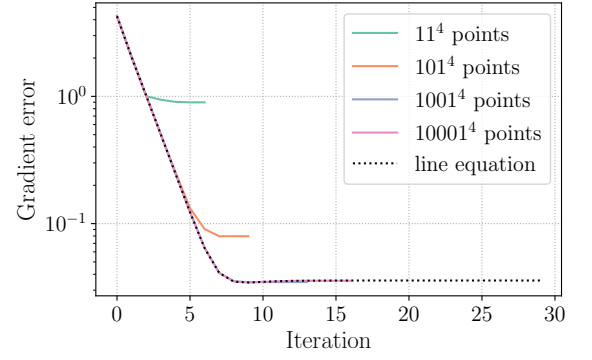
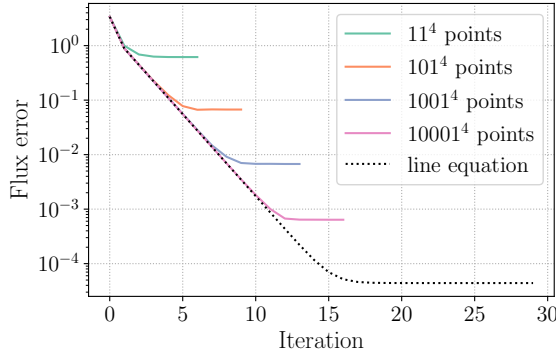
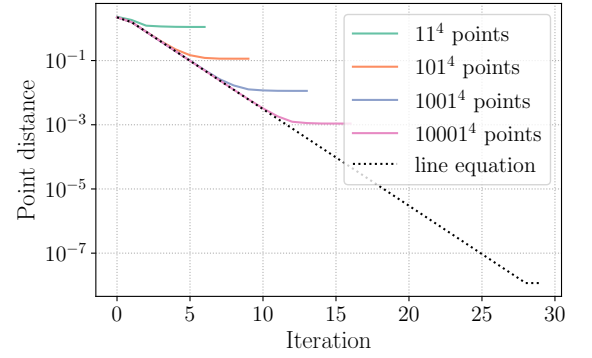
While (5.11) is used for the iterative loop in the two-step data-driven procedure, the procedure can be streamlined by chaining both steps into an iterative solver, similar to what is used for nonlinear problems like the Newton-Raphson method shown in section 2.4. The matrices correspond to (2.36), however, the tangent matrix (5.10) is constant in this case, and the right-hand side residual vector (5.12) is updated at every iteration as follows:

$$[\mathbf{R}_\beta] = \begin{bmatrix} \int_{\Omega} N_b (\nabla \cdot \boldsymbol{\tau}_0) d\Omega \\ \int_{\Omega} S_g G_b (\mathbf{g}_0 - \mathbf{g}^*) d\Omega + \int_{\Omega} G_b \boldsymbol{\tau}_0 d\Omega \\ \int_{\Omega} S_q \mathbf{Q}_{\mathcal{B}} \cdot (\mathbf{q}_0 - \mathbf{q}^*) d\Omega + \int_{\Omega} (\nabla \cdot \mathbf{Q}_{\mathcal{B}}) \lambda_0 d\Omega \\ \int_{\Omega} L_b (\nabla \cdot \mathbf{q}_0) d\Omega - \int_{\Omega} L_b s d\Omega \\ \int_{\Omega} \mathbf{M}_{\mathcal{B}} \cdot \mathbf{g}_0 d\Omega + \int_{\Omega} (\nabla \cdot \mathbf{M}_{\mathcal{B}}) T_0 d\Omega - \int_{\Gamma_T} (\mathbf{M}_{\mathcal{B}} \cdot \mathbf{n}) \bar{T} d\Gamma \end{bmatrix}, \quad (5.12)$$

where the subscript $(\cdot)_0$ denotes the previous iteration values of the unknown fields. This allows for a more straightforward implementation of the data-driven iterative procedure utilising iterative solvers, such as SNES in PETSc [Balay et al., 2023] with custom stopping criteria (same as in subsection 4.1.1).

Applying the same procedure with which Figure 4.3 was obtained, it can be seen that the error norms converge to a plateau with the number of iterations in a similar way with the weaker data-driven formulation, see Figure 5.1. The plateau reached is due to the resulting fields distance to the material dataset, and the finite element approximation errors relating to the quality of the mesh and the approximation orders.

It can be noted that the flux error L^2 -norm, Figure 5.1c, converges to a value which is magnitudes smaller than the one expressed in Figure 4.3c. This is due to the flux field \mathbf{q} belonging to $H(\text{div}; \Omega)$ space which in this case is approximated by a higher approximation order $(p+1)$ than it was in chapter 4 $(p-1)$. The next section compares the computational complexity of the

(a) Temperature error L^2 -norm (2.22).(b) Temperature error H^1 -seminorm (2.23).(c) Flux L^2 -norm (2.24).

(d) RMS distance (4.8).

Figure 5.1: Example SinCos (Figure 2.3): Global error norms w.r.t. exact solution and point distance RMS measure (4.8). Convergence with the number of points in the Uniform material dataset, see Figure 4.1.

standard and data-driven FE formulations.

5.1.1 Computational complexity comparison

For this comparison, the resulting finite element systems, obtained by standard and mixed formulations, are considered to be solved using a Newton-Raphson scheme, where the nonlinearities are solved iteratively. The data-driven formulations are also solved iteratively but require only a single matrix inversion.

Standard nonlinear FE formulation is described in section 2.4. At each iteration, a global system is assembled and solved. Assuming an efficient sparse solver, the matrix inversion scales as $\mathcal{O}(n_{\text{dof}}^{3/2})$, where n_{dof} is the number of degrees of freedom. With N_{NR} Newton iterations, the total complexity becomes:

$$\mathcal{O}(N_{\text{NR}} \cdot n_{\text{dof}}^{3/2}). \quad (5.13)$$

The mixed formulation introduces additional unknowns (e.g., fluxes), increasing the system size but not the order of complexity.

In contrast, the data-driven formulations have a constant diffusivity matrix $[\mathbf{K}_{\alpha\beta}]$, see (4.7) and (5.10), requiring only a single matrix inversion: $\mathcal{O}(n_{\text{dof}}^{3/2})$. However, an iterative process which includes searching for a closest material datapoint for each integration point is performed, see subsection 4.1.1. The cost of searching for the closest point in the dataset is $\mathcal{O}(n_{\text{int}} \cdot n_{\text{mat}})$, where n_{int} is the number of integration points and n_{mat} is the number of material data points. At each iteration, a nearest-neighbour search is carried out at every integration point using an R-tree [Guttman, 1984], yielding a search cost of approximately: $\mathcal{O}(n_{\text{int}} \cdot \log n_{\text{mat}})$, where n_{int} is the number of integration points and n_{mat} the number of material data points. With N_{DD} iterations, the total complexity is:

$$\mathcal{O}(n_{\text{dof}}^{3/2}) + \mathcal{O}(N_{\text{DD}} \cdot n_{\text{int}} \cdot \log n_{\text{mat}}). \quad (5.14)$$

The resulting computational cost difference between the standard and data-driven formulations depends on the size of the problem (n_{dof} and n_{int}), the size of the material dataset (n_{mat}), and the number of iterations required for convergence (N_{NR} or N_{DD}). Larger problems with more degrees of freedom and integration points might perform faster with the data-driven approach, especially if the material dataset is small, as it avoids the need for multiple matrix inversions. On the contrary, small problems with fewer degrees of freedom and integration points will likely perform better with the standard approach, especially if the material dataset is large.

The bottleneck of the data-driven approach is the search through the material dataset, which can be minimised by using efficient data structures (e.g., R-trees) and algorithms, and by keeping the number of integration points to a minimum. For the data-driven approach, the number of degrees of freedom is not the limiting factor, as the diffusivity matrix only needs to be inverted once, and therefore, the increased number of unknowns due to the "weaker" formulation is reasonable. Additionally, to ensure the minimum number of integration points, the error indicators leading to adaptive refinement strategies enabled by the "weaker" formulation are advantageous, see section 3.3.

The next section compares the results obtained by the weaker data-driven FE formulation derived in this chapter to the mixed FE formulation and the stronger data-driven FE formulation, discussed in chapter 3 and chapter 4, respectively.

5.1.2 Verification with other formulations

The weaker data-driven FE formulation builds up on the mixed FE formulation introduced in chapter 3, and the stronger data-driven FE formulation introduced in chapter 4. The comparison of the three formulations in this section is performed using the Example Exp-Hat, see Figure 3.3, and the global norms of errors w.r.t. the exact solution are evaluated. This analysis is done with a "saturated" dataset to confirm the global mesh and approximation convergence properties of the present weaker data-driven FE formulation.

Considering no adaptive refinements, the global error norms are calculated for the tempera-

ture field T , the flux field \mathbf{q} are shown in Figure 5.2. The finite element approximation order is the same for the temperature T field in all formulations, but due to the different formulations, it varies for the flux \mathbf{q} and gradient \mathbf{g} fields, see tables 3.3, 4.3 and 5.3. This is reflected in the convergence observed in the global error norms. The comparison shows that the weaker data-driven FE formulation converges to the exact solution in the same way as the mixed FE formulation, i.e. following the *a priori* error estimates defined in (3.9).

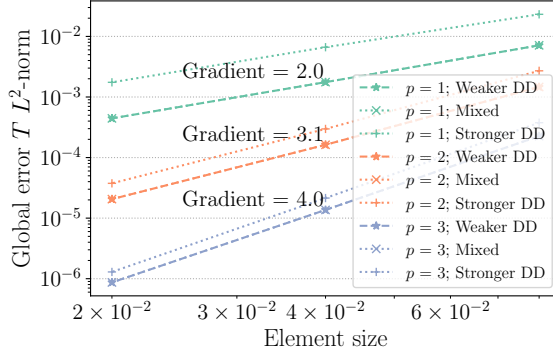
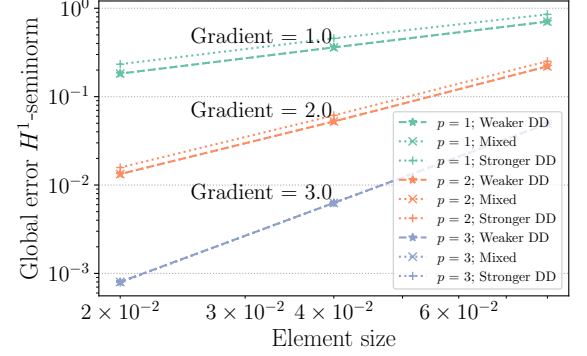
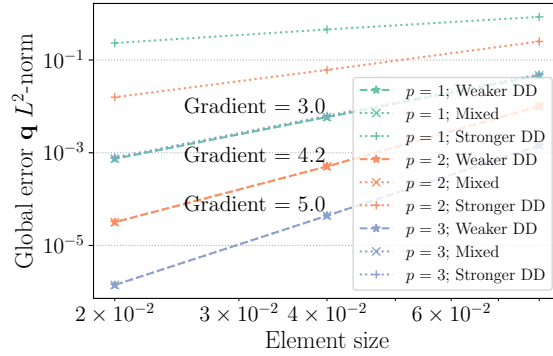
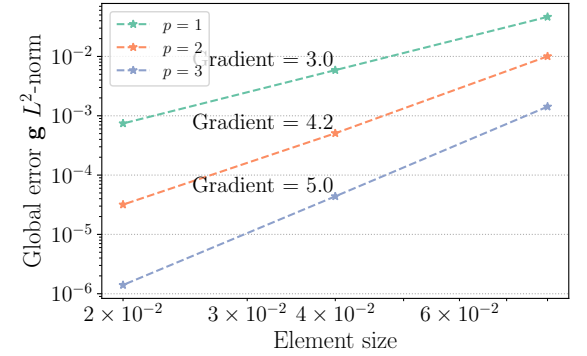
(a) Global temperature error L^2 -norm.(b) Global temperature error H^1 -seminorm.(c) Global flux error L^2 -norm.(d) Global gradient error L^2 -norm (weaker DD).

Figure 5.2: Example Exp-Hat: Comparison of weaker DD, mixed formulation (chapter 3) and stronger DD formulation (chapter 4). Convergence of the finite element solution w.r.t. the exact one with fully saturated dataset (Appendix B).

The temperature L^2 -norm and H^1 -seminorm follow the same convergence for all three formulations, whereas the flux L^2 -norm differs between the formulations due to the finite element approximation order for the flux field. In this case the weaker DD follows the mixed formulation.

The gradient L^2 -norm can only be evaluated for the weaker DD formulation since the other formulations do not contain this field. The gradient L^2 -norm follows the same convergence as the flux L^2 -norm in the weaker DD formulation, which suggests the following:

$$\|\nabla \tilde{T} - \mathbf{g}^h\|_{(\Omega)} \leq Ch^{p+2}, \quad (5.15)$$

where $\nabla\tilde{T}$ is the exact solution of the gradient field, \mathbf{g}^h is the finite element approximation of the gradient field, C is a constant, h is the element size and p is the temperature approximation order.

5.2 Comparison with the mixed formulation

In the previous subsection, it was shown that when a saturated material dataset is used, the weaker data-driven FE formulation (weaker DD) closely follows the mixed FE formulation. However, there is no constitutive equation in the weaker DD and a new field for temperature gradient \mathbf{g} belonging to $\mathbf{L}^2(\Omega)$ space is introduced. This has an effect on the calculation of the error indicators and estimators; for reference, see section 3.3. This section addresses the changes to the *a posteriori* error indicators formulation and investigates the differences between the mixed FE and weaker DD formulations for saturated material dataset before introducing noise and scarcity in the material dataset.

5.2.1 Error indicators associated with temperature gradients

Unlike the mixed FE formulation in chapter 3, constitutive relation (3.1c) is not present as in subsection 3.3.1. Instead, the error indicator associated with the gradient of the temperatures can be defined using the new variable definition (5.2b) of \mathbf{g} as follows:

$$\eta_e(\nabla T, \mathbf{g}) = \|\nabla T - \mathbf{g}\|_{\Omega_e}^2. \quad (5.16)$$

The temperature gradient ∇T is calculated *a posteriori* and it is compared to the gradient field \mathbf{g} , which represents the gradient of temperature. In other words, this indicator checks the conformity to the new variable definition (5.2b), which is one of the constraints in the Lagrangian (5.5). On the elements where the error indicator η_e is high, high finite element approximation error is expected.

5.2.2 Error estimators

The other two error indicators associated with the conservation law,

$$\mathbf{v}_e(\mathbf{q}) = h\|s - \nabla \cdot \mathbf{q}\|_{\Omega_e}^2$$

as in subsection 3.3.2, and temperature jumps across inner boundaries,

$$\gamma_e(T) = \sum_{l=1}^{n_{\Gamma_e}} h^{1/2} \|J(T)\|_{0,l}$$

as in subsection 3.3.3, remain unchanged.

The error estimator [Braess and Verfürth, 1996]

$$\mu_e = (\eta_e^2 + \nu_e^2 + \gamma_e^2)^{1/2}$$

is calculated in the same way as (3.14), however, when noise or scarcity are present in the material dataset, it will not have the same properties as expected from an estimator, i.e. it may not be possible to prove that it can be used to calculate upper or lower bounds of the resulting error on the element. Therefore, the error estimator μ_e presented in this section is not a true error estimator.

However, for notation and consistency the error estimator will continue to be referred to as the error estimator, for summary of the naming and notation of the error indicators see Table 5.4.

Error indicator	Name
$\eta_e(\nabla T, \mathbf{g}) = \ \nabla T - \mathbf{g}\ _{\Omega_e}^2$	Gradient error indicator
$\nu_e(\mathbf{q}) = h \ s - \nabla \cdot \mathbf{q}\ _{\Omega_e}^2$	Divergence error indicator
$\gamma_e(T) = \sum_{l=1}^{m_{r_e}} h^{1/2} \ J(T)\ _{0,l}$	Jump error indicator
$\mu_e = (\eta_e^2 + \nu_e^2 + \gamma_e^2)^{1/2}$	Error estimator

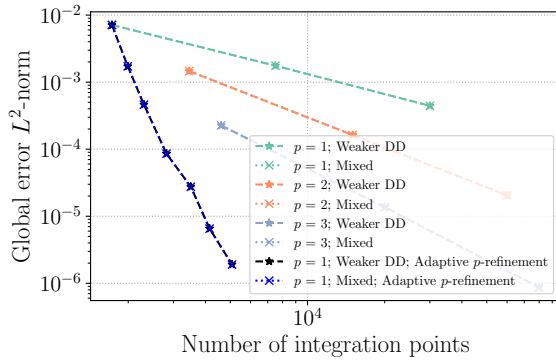
Table 5.4: Definitions and notations of the error indicators for the weaker data-driven formulation.

5.2.3 Adaptive refinement

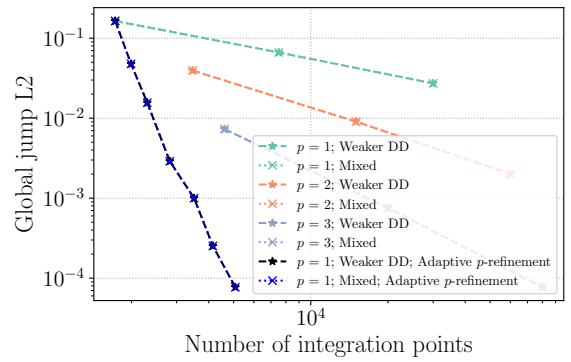
Since error indicators can be computed *a posteriori*, and they still highlight the elements with the worst finite element approximation errors, adaptive refinement can be implemented. For completeness, the same order refinement algorithm is applied to the weaker DD and mixed FE formulations for the Example Exp-Hat, see Figure 3.3. The results with a saturated dataset are shown in Figure 5.3.

The same behaviour is experienced by both the weaker DD and mixed formulations in terms of the number of integration points. Even though the number of degrees of freedom might differ due to the number of fields and the differences in functional spaces of the unknown fields, the search through the material dataset happens at every integration point instead of a degree of freedom, and it is, therefore, more important to consider the number of integration points. The resulting error norms and error indicators follow each other closely and the same elements are highlighted for refinement in both cases, see the resulting approximation orders for both solutions in Figure 5.4.

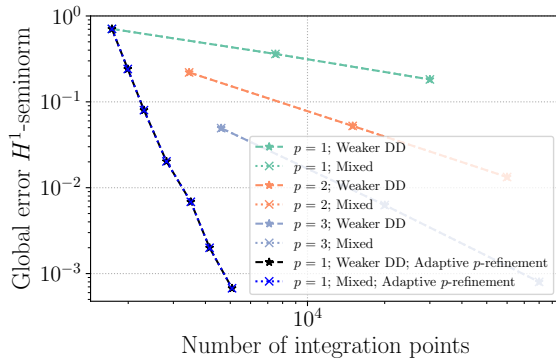
The weaker data-driven formulation solves for more unknown fields than the mixed formulation introduced in chapter 3, however, unlike with the testing in chapter 3, no constitutive



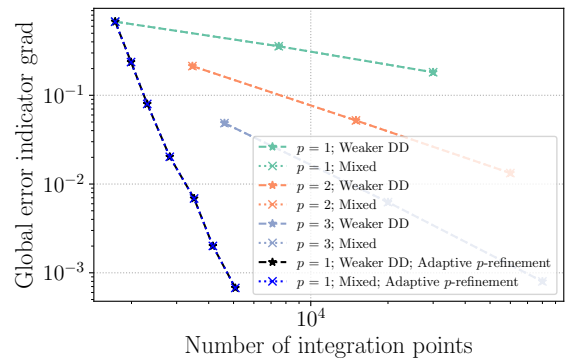
(a) Global temperature error L^2 -norm.



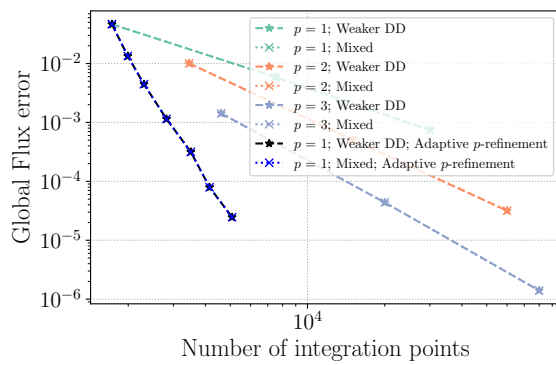
(b) Global L^2 -norm of temperature jumps across inner boundaries.



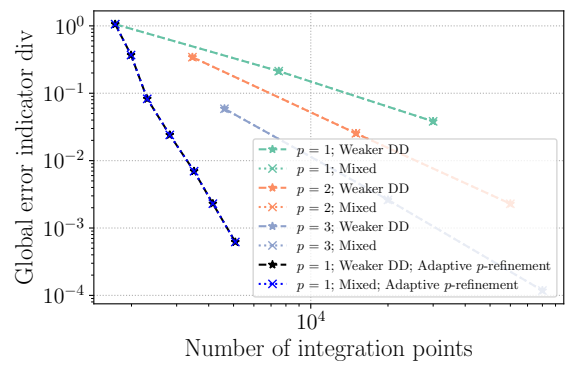
(c) Global temperature error H^1 -seminorm.



(d) Global L^2 -norm of the gradient error indicator.

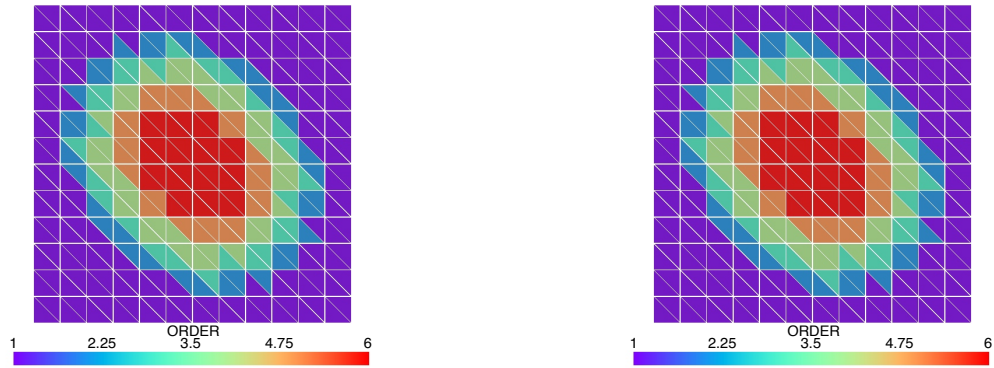


(e) Global flux error L^2 -norm.



(f) Global L^2 -norm of the divergence error indicator.

Figure 5.3: Example Exp-Hat: Comparison of weaker DD and mixed formulation with adaptive order refinement.



(a) Weaker data-driven FE formulation.

(b) Mixed FE formulation.

Figure 5.4: Example Exp-Hat: Resulting approximation orders of the adaptive refinement with the algorithm described in Algorithm 1.

equations are necessary to run the data-driven formulation introduced in this chapter. The material behaviour can be nonlinear, the dataset can be sparse or have data missing and the solution process does not change with nonlinearity as it does when a material model is used, e.g. nonlinear material model in section 2.4. Next, a comparison between the data-driven formulation discussed in chapter 4 and the weaker data-driven formulation derived in this chapter is explored.

5.3 Results compared to the stronger data-driven formulation

The convergence with mesh and approximation order refinement between the weaker and stronger data-driven formulations is shown in Figure 5.2 for a fully saturated dataset. However, in industrial applications, the material dataset is seldom as saturated and noise-free.

Therefore, the comparison in this section is done with noise-free material dataset with 10^5 4D material datapoints created with uniform random distribution, see section 4.2 but without noise η , to confirm the global mesh and approximation convergence properties of the data-driven formulations with the same material dataset. The example used for the comparison is Exp-Hat, Figure 3.3, and the material dataset is created in ranges $[-9, 9]$ for the temperature gradients and datapoints with the gradients of values $[-6, -5]$ in the x -direction are removed, see Figure 5.5.

Figure 5.6 shows the global error norms and error indicators for the weaker data-driven formulation and the standard data-driven formulation. The adaptive refinement is only available for the weaker data-driven formulation, and the error indicators are not calculated for the standard data-driven formulation.

Unlike with the fully saturated dataset (Figure 5.3), the global error norms reach a plateau

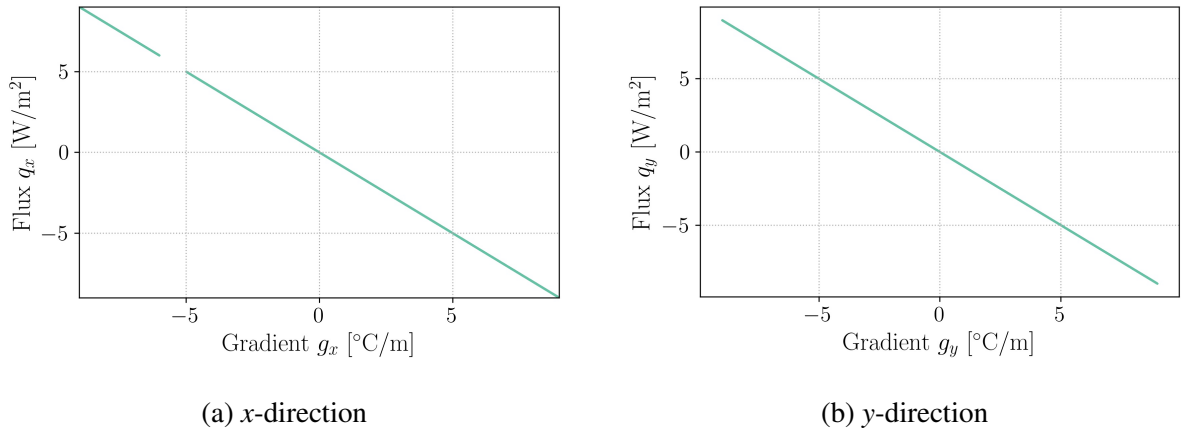


Figure 5.5: Example Exp-Hat tweaked dataset: dataset is created with uniform random distribution for temperature gradients in ranges $[-9, 9]$ and flux is afterwards calculated by $\mathbf{q} = -\mathbf{g}$. 10^5 material datapoints are generated and a range of datapoints containing values of $[-6, -5]$ in temperature gradient in x -direction is removed for testing purposes.

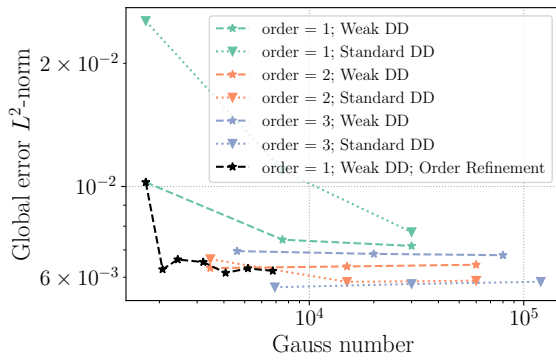
with the order and mesh refinements, see Figure 5.6. This is due to the distance between the resulting fields and the material dataset introducing uncertainty and errors to the numerical solution.

Additionally, it can be observed that the weaker data-driven formulation reaches the plateau faster than the standard data-driven formulation. However, the overall number of degrees of freedom is higher for the weaker data-driven formulation due to the additional fields used in the formulation.

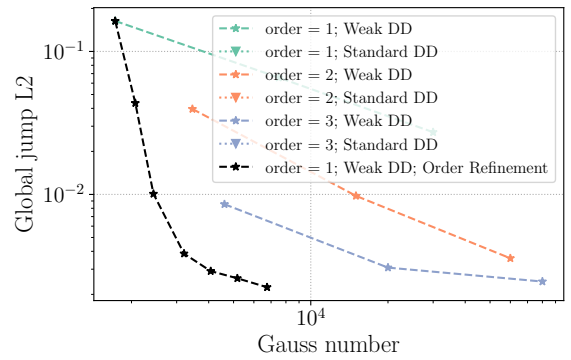
Nevertheless, the availability of the error indicators and estimators still allows for the use of adaptive refinements to improve the results and Figure 5.6 shows that the adaptive refinement is able reach the same plateaus with orders of magnitude smaller number of integration points than the standard data-driven formulation with global refinement. The individual error indicators, shown in figs. 5.6b, 5.6d and 5.6f also reach the plateau slower than the global error norms, figs. 5.6a, 5.6c and 5.6e, ensuring the resulting fields have a sufficient reduction in the finite element approximation errors by the time the adaptive refinement is stopped.

The error indicators/estimators are not calculated in the analysis using the stronger data-driven formulation since they are not introduced there in the same way as in the weaker formulation. Therefore, the adaptive refinement is only available for the data-driven approach with the weaker mixed formulation.

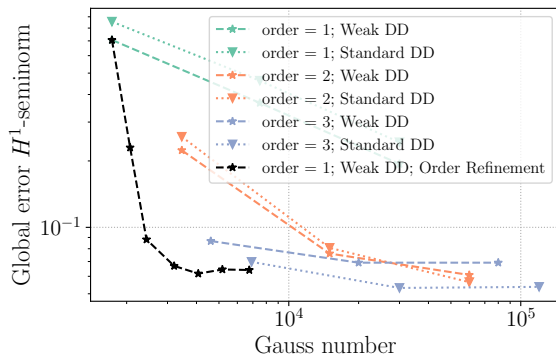
Similarly to the stronger data-driven approach, the increasing noise/sparsity in the material dataset results in more uncertainty of the results. Furthermore, when the quality of the material dataset is decreased, the error indicators are affected by the quality of the material dataset used. Figure 5.7 shows error estimators are high despite the finite element approximation order increase in the area highlighted by the error indicators. Furthermore, the plateaus reached by the error indicators in figs. 5.6b, 5.6d and 5.6f correspond to the error estimator shown in Figure 5.7.



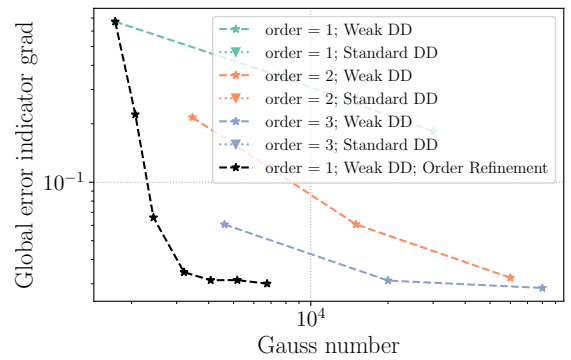
(a) Global temperature error L^2 -norm.



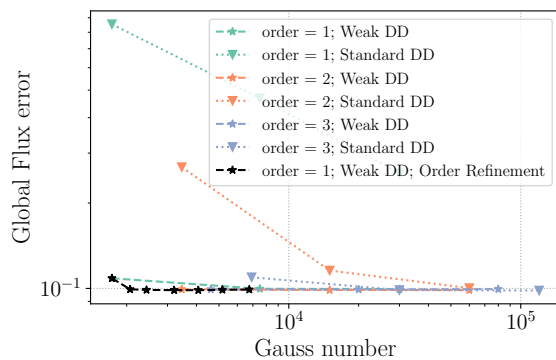
(b) Global L^2 -norm of temperature jumps across inner boundaries.



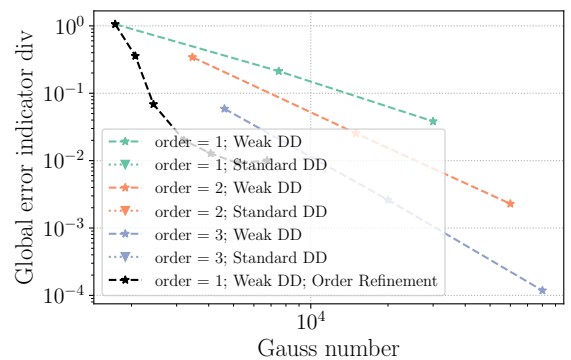
(c) Global temperature error H^1 -seminorm.



(d) Global L^2 -norm of the gradient error indicator.



(e) Global flux error L^2 -norm.



(f) Global L^2 -norm of the divergence error indicator.

Figure 5.6: Example Exp-Hat: Comparison of data-driven and weaker data-driven formulation and with adaptive order refinement.

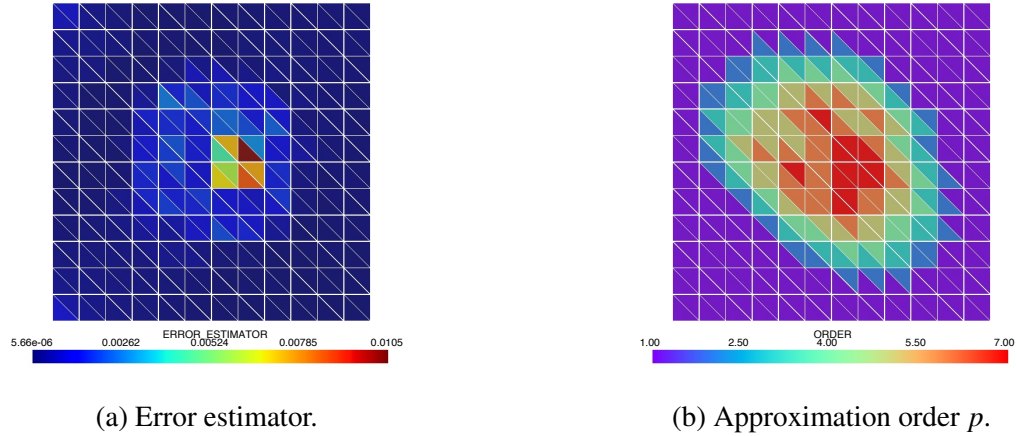


Figure 5.7: Example Exp-Hat: Error estimator and approximation order per element for the weaker data-driven formulation with missing data after adaptive order refinement.

5.3.1 Effect of the material dataset quality on the error indicators

As scarcity of the dataset and noise are introduced to the material dataset, the error indicators can be calculated in the same way as in subsection 5.1.2. The error indicators, similarly to the errors w.r.t. the exact solution, reach a plateau, as shown in Figure 5.6. Upon further inspection of the error indicators plotted on the elements, it is observed that the error indicators are affected by the quality of the material dataset used.

Nevertheless, the error indicators can still be used to identify the elements with the highest finite element approximation errors, and the adaptive refinement can be applied to improve the results and refine the problematic areas of the analysis to pinpoint where the error/uncertainty is the highest, see improvement of the results with the adaptive order refinement in black in Figure 5.6.

Using the adaptive refinement reduces the errors associated with the finite element approximation and it is assumed that the remaining error is associated with the material dataset. This claim is due to the fact that when the material dataset was replaced with a line equation, see (B.3) and Figure 5.1, the errors experienced the expected convergence with the global approximation order and mesh refinement, as shown in Figure 5.2. On the other hand, when a material dataset is used, the resulting global errors eventually reach a plateau which is higher than the predicted error associated with the finite element approximation.

5.4 Adaptive refinement for weaker data-driven formulation

In the data-driven finite element formulations introduced in chapters 4 and 5, the errors and uncertainties have two main sources: finite element approximation errors, and the quality of the material dataset used for the simulation. As it was shown in the previous section, the error

indicators highlight the finite element approximation errors. However, the imperfections in the material dataset sometimes result in high error indicators. When the elements with high error indicators due to the material dataset issues are refined, more accurate result is not guaranteed and can lead to overfitting the result to material behaviour which might not be accurate. This causes an imbalance between the bias and variance.

To prevent overfitting, additional checks and tolerances to the adaptive refinement algorithm, Algorithm 2, are proposed as follows:

- when the result is *too far* from the material dataset for the considered element: do not refine the approximation order
- when the standard deviation of the distance to the dataset is *too high*: consider refining the element to isolate the problematic area.

Taking into account the standard deviation and the average distance to the dataset further refines the adaptive refinement, however, the definition of the values per element being *too high* is ambiguous.

The following subsections provide options for the adaptive refinement considering error indicators and distances to the material dataset per element but a more sophisticated method is a subject of further research.

5.4.1 Distance to the material dataset per element

Distance of the results to the material dataset, which will be denote hereinafter as d , is calculated as a part of finding the closest points in the dataset \mathcal{D} for every integration point using (4.1), (4.12), (5.3) or equivalent.

To identify the problematic elements, average of the distances per element is calculated as follows:

$$d_{ave} = \frac{\sum_{g=1}^G d_g}{G}, \quad (5.17)$$

where G is the number of integration points for the element considered, and g is the integration point.

To address the question of which values are *too high*, a comparative measurement ξ with the same units as d is needed, which represents RMS of the field values relevant for the material data search. ξ can either be calculated locally for each element or globally for the whole domain, representing relative and absolute distance comparison. Since in this case we are interested in high distances globally, a global ξ is defined as follows:

$$\xi = \left(\frac{\int_{\Omega} S_g \mathbf{g}^2 d\Omega + \int_{\Omega} S_q \mathbf{q}^2 d\Omega}{\mu(\Omega)} \right)^{1/2}, \quad (5.18)$$

where $\mu(\Omega)$ is the area of the domain Ω in a 2D case, and its volume in a 3D case. A shorthand notation is used in this section for the dot product between two vectors: $\mathbf{g}^2 = \mathbf{g} \cdot \mathbf{g}$. Note that (5.18) matches the units of $\text{dist}(\{\mathbf{g}, \mathbf{q}\}, \mathcal{D}) = \min_{\{\mathbf{g}^*, \mathbf{q}^*\} \in \mathcal{D}} \sqrt{S_g (\mathbf{g} - \mathbf{g}^*)^2 + S_q (\mathbf{q} - \mathbf{q}^*)^2}$ and new dimensions can be added according to the dataset used.

Alternatively, if the relative distance to the dataset is of importance, ξ can be calculated and compared to on the element basis.

A new tolerance t_{ave} for the ratio of the average distance per element d_{ave} and the equivalent root mean squared measure ξ is introduced to determine which elements should not be taken into account for the adaptive p -refinement as follows:

Do not increase the approximation order of the element if

$$d_{ave} > t_{ave} \xi. \quad (5.19)$$

The relative tolerance t_{ave} is a percentage, therefore, if e.g. $t_{ave} = 2$ the elements which average distance to the dataset is higher than 2% of the root mean square measure of the whole domain, it is deemed to not be properly informed of the material properties, and therefore inaccurate by default and further refinement would be overfitting the result.

5.4.2 Standard deviation of the distance to the material dataset per element

On the other hand, let us consider an element of which one side is well informed of the material properties, and the other side is not. For example Figure 5.8 where there is data missing in a localised area. If the element size is big enough for parts of it to be covered by the dataset and part to be in the middle of the gap, it can sometimes be beneficial to apply mesh refinement to the element.

The standard deviation of the distance to the material dataset on element is calculated as follows:

$$d_{std} = \sqrt{\frac{\sum_{g=1}^G (d_g - d_{ave})^2}{G}}, \quad (5.20)$$

where d_{ave} is defined by (5.17).

In a similar way to subsection 5.4.1, d_{std} can be compared to ξ by taking into consideration the elements which have values higher than a percentage of the relevant root mean square

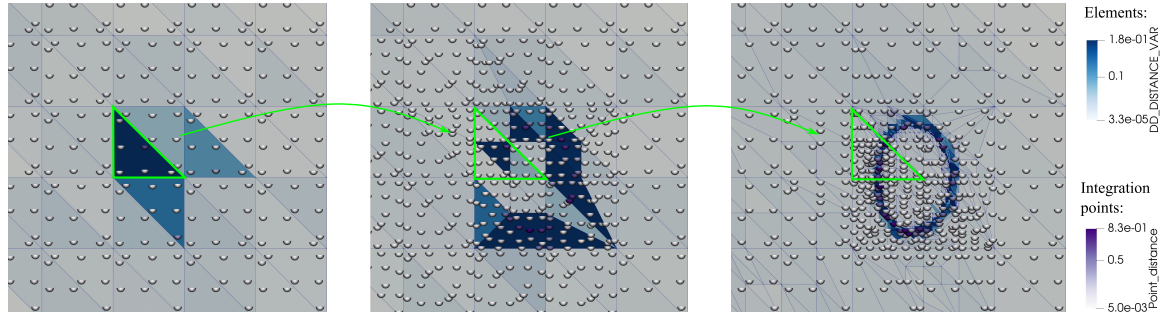


Figure 5.8: Example Exp-Hat: Using the standard deviation of the distance to the material dataset to refine the mesh and identify the problematic areas w.r.t. the distance to the material dataset.

measure:

$$d_{std} > t_{std} \xi, \quad (5.21)$$

where t_{std} is a tolerance related to the standard deviation of the distance and the equivalent RMS measure (5.18).

However, high standard deviation of the distance d within an element does not mean that refining the element mesh yields improved results or provides more information about the problem uncertainty. If an element where all of the values at the integration points are too far from the dataset is considered, i.e. have high distance d , refinement does not provide any advantage.

Therefore, an additional check is proposed which compares the values of the average and standard deviation in the element to evaluate if the refinement should take place:

$$d_{std} > t_{std}^{ave} d_{ave}, \quad (5.22)$$

where t_{std}^{ave} is another user set tolerance. It is advised to set $t_{std}^{ave} \geq 0.5$ if this criteria is considered.

The adjustments to the refinement criteria (5.19, 5.21, 5.22) can be used together or separately from each other. The resulting adaptive hp -refinement algorithm is shown in Algorithm 5. Note that line 12 in Algorithm 5 mentions refinement only in the elements adjacent to the boundary Γ , however, to tackle singularities more efficiently this should be implemented only in the elements adjacent to the corners.

Applying the whole adaptive refinement scheme with $t_{ave} = 4.0$, $t_{std} = 0.5$, $t_{std}^{ave} = 0.5$ and tolerances for order and mesh refinement control set to $t_p = 3.0$ and $t_h = 4.0$, respectively, the results are shown in Figure 5.9. Figure 5.9a shows how the approximation order has not been increased where the distance of the resulting fields to the material dataset is considered *too high*, as shown in Figure 5.9c. Refining the mesh in the areas where the standard deviation of the distance to the dataset is *too high* but satisfies (5.22), see resulting distance standard deviation in Figure 5.9d, also isolates the problematic areas of the analysis while improving the results.

Algorithm 5 Adaptive hp -refinement with error estimator and distance to the material dataset taken into account

- 1: Initialize with the lowest approximation order $p = 1$ and the coarsest mesh.
 - 2: **repeat**
 - 3: Solve the problem (5.7).
 - 4: Calculate the error indicators and estimator, see Table 5.4.
 - 5: Calculate the distance to the material dataset at every integration point using (4.1), (4.12), (5.3) or equivalent.
 - 6: Calculate the average distance d_{ave} with (5.17) per element
 - 7: Calculate the standard deviation of the distance d_{std} with (5.20) per element
 - 8: Calculate the comparative measurement ξ with (5.18)
 - 9: **if** $\mu_e > \mu_{avg} t_p$ **and** $d_{ave} \leq t_{ave} \xi$ **then**
 - 10: $p_e = p_e + 1$
 - 11: **end if**
 - 12: **if** $\mu_e > \mu_{avg} t_h$ **and** element is adjacent to the boundary Γ **then**
 - 13: Refine mesh of this element.
 - 14: **end if**
 - 15: **if** $d_{std} > t_{std} \xi$ **and** $d_{std} > t_{std}^{ave} d_{ave}$ **then**
 - 16: Refine mesh of this element.
 - 17: **end if**
 - 18: Run Algorithm 1 to prevent big jumps in the approximation order between elements.
 - 19: **until** a specified number of iterations is reached
-

5.5 Capturing brick refinement

Before any further uncertainty quantification is considered, The same kind of adaptive refinement is applied to the problem concerning the brick example, see Figure 4.19. The same adaptive refinement with tolerances shown in Table 5.5 was chosen for analysis with all of the material datasets described in Table 4.4.

Refinement criteria name	value
t_p	1.0
t_h	4.0
t_{ave}	1.0
t_{std}	2.0
t_{std}^{ave}	0.5

Table 5.5: Adaptive refinemnt criteria for the brick example.

Starting with the material dataset E, see Figure 4.17, which does not cover all of the required material states, the adaptive refinement is applied. Figure 5.10 shows the error estimators μ and the average d_{ave} and standard deviation d_{std} of the distance to the material dataset per element before and after the adaptive refinement. The measures shown in Figure 5.10 serve as the criteria

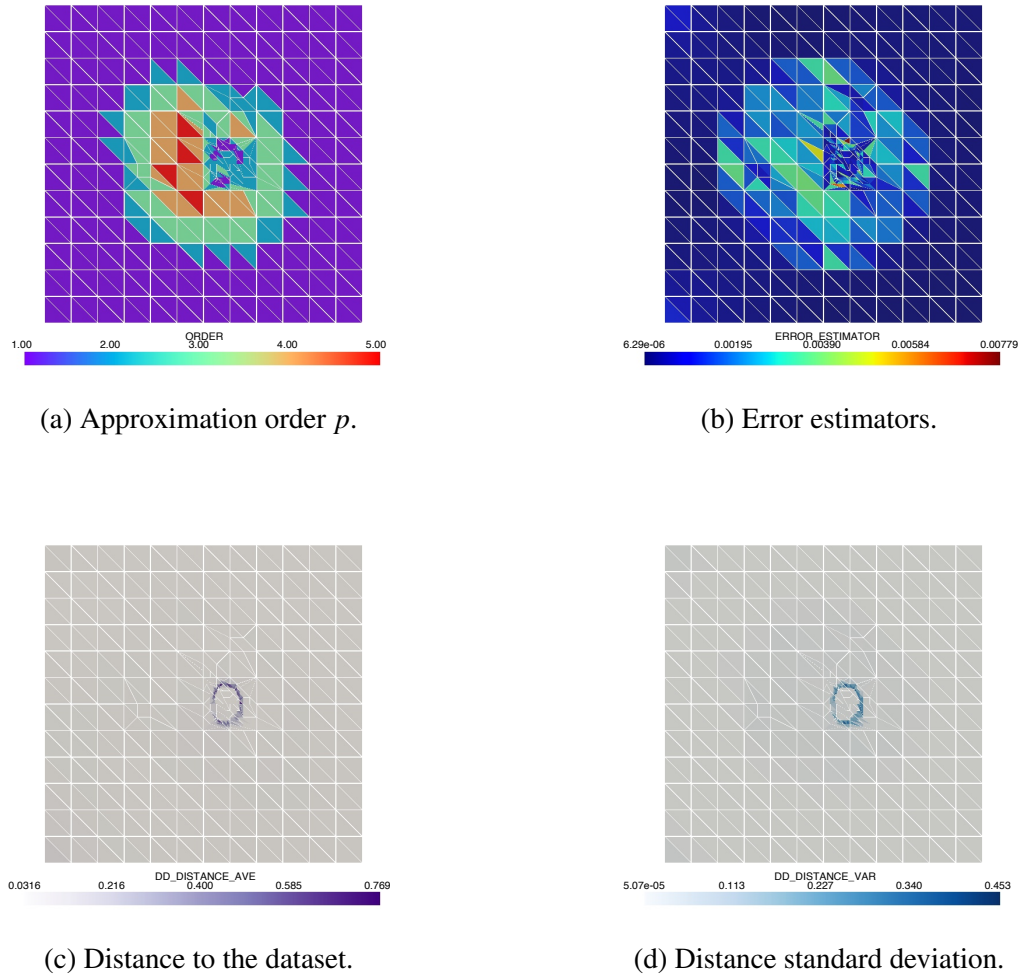


Figure 5.9: Example Exp-Hat: Adaptive refinement with the algorithm described in Algorithm 5.

for the adaptive refinement and measurements of accuracy of the solution at the same time.

Figure 5.10a experiences high error estimators in the corners due to singularities, which are successfully decreased after the refinement, see Figure 5.10b. The average distance to the dataset per element d_{ave} is high and does not decrease with the refinement, however, the area of high distances is now more localised. On the other hand, the standard deviation of the distance to the dataset per element d_{std} is high but the effect of refinement is more pronounced by isolating the problematic areas, see Figure 5.10e and Figure 5.10f. Overall, this process successfully identifies the areas where the material dataset is missing the required material states and the areas where the finite element approximation is less reliable.

On the contrary, when using material dataset C, see Figure 4.14, with noise incorporated to the material dataset, the refinement helps to reduce the finite element approximation errors, see Figure 5.11a and Figure 5.11b, but does not concretely identify the areas of concern and how severely it effects the results.

5.6 Summary

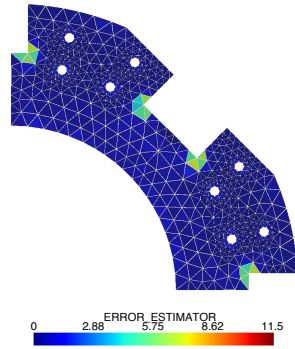
This chapter introduced a data-driven approach derived with the weaker mixed formulation for the heat transfer problem. The approach is compared to the mixed formulation introduced in chapter 3 and the standard data-driven approach introduced in chapter 4.

The approach has access to all the error and uncertainty measurements introduced in the previous chapters as well as the indicators for where the adaptive refinement should take place. To summarise, so far the errors and uncertainties can be identified by:

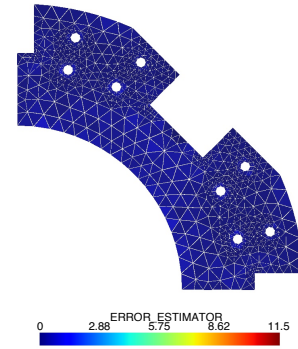
- error indicators associated with the finite element approximation errors, see Table 5.4
 - possible reduction by adaptive refinements
- distance to the material dataset closest point at every integration point
- standard deviation of the distance to the material dataset per element

The error estimation presented in this thesis so far is able to highlight, and possibly improve, some of the problematic areas of the numerical analysis if they are present. However, so far the uncertainty estimation identifies the areas where the material dataset is sufficiently saturated, however, it does not recognise if the material dataset includes a substantial amount of noise and variance. Additionally, the uncertainty is not yet shown in a range of possible outcomes for the resulting fields.

The next chapter addresses the uncertainty quantification in terms of uncertainty of the resulting fields which, as will be shown, in turn capture locations of noise in the dataset. The noise is not removed, instead it is captured and measured to be assessed after the analysis.



(a) Error estimator before refinement.



(b) Error estimator after refinement.

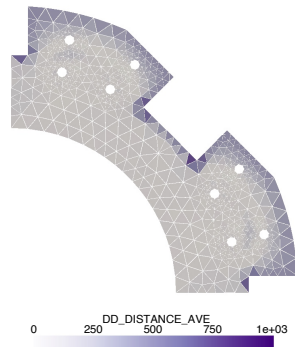
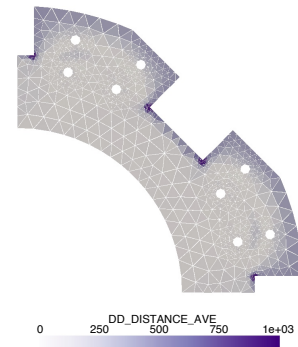
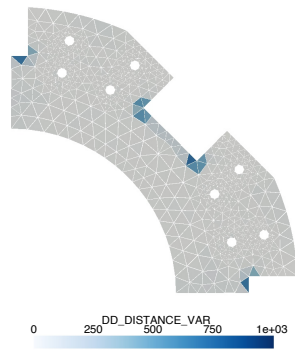
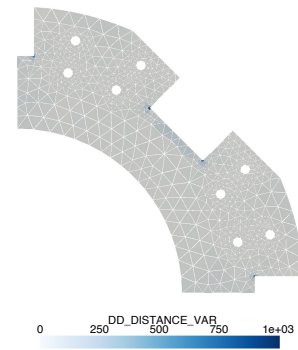
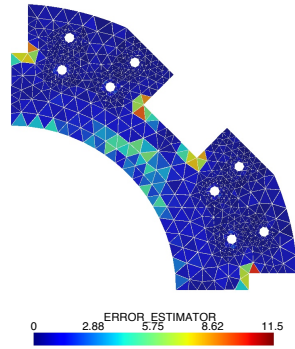
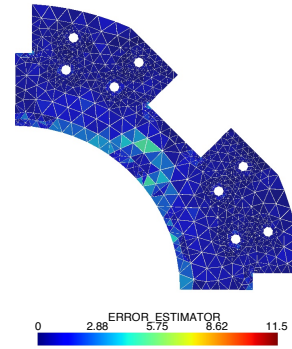
(c) d_{ave} before refinement.(d) d_{ave} after refinement.(e) d_{std} before refinement.(f) d_{std} after refinement.

Figure 5.10: Example Brick: Effect of adaptive refinement on (a-b) error estimator (c-d) average distance to the dataset per element, see subsection 5.4.1, and (e-f) standard deviation of the distance to the dataset per element, see subsection 5.4.2. Analysis with material dataset E, see Figure 4.17.



(a) Error estimator before refinement.



(b) Error estimator after refinement.

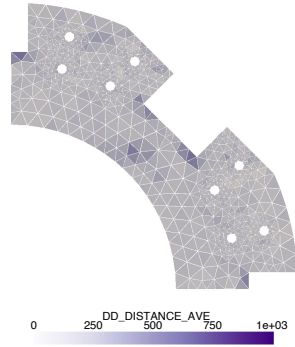
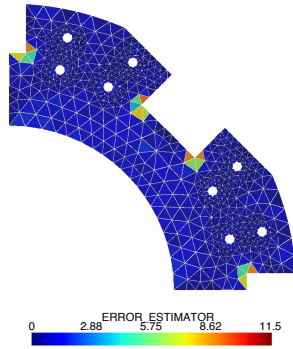
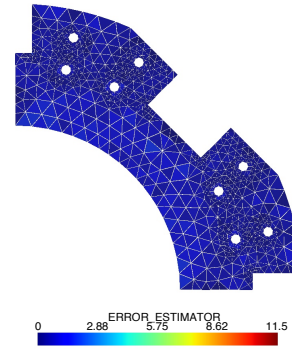
(c) d_{ave} before refinement.(d) d_{ave} after refinement.(e) d_{std} before refinement.(f) d_{std} after refinement.

Figure 5.11: Example Brick: Effect of adaptive refinement on (a-b) average distance to the dataset per element, see subsection 5.4.1, and (c-d) standard deviation of the distance to the dataset per element, see subsection 5.4.2. Analysis with material dataset C, see Figure 4.14.



(a) Error estimator before refinement.



(b) Error estimator after refinement.

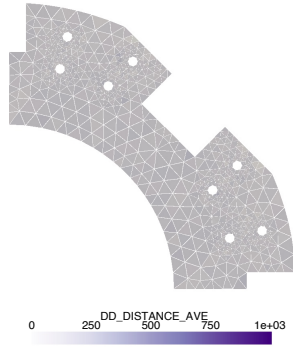
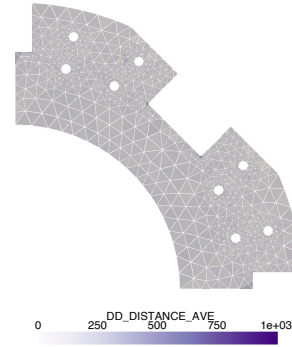
(c) d_{ave} before refinement.(d) d_{ave} after refinement.(e) d_{std} before refinement.(f) d_{std} after refinement.

Figure 5.12: Example Brick: Effect of adaptive refinement on (a-b) average distance to the dataset per element, see subsection 5.4.1, and (c-d) standard deviation of the distance to the dataset per element, see subsection 5.4.2. Analysis with material dataset A.

Chapter 6

Quantification of nonuniqueness

In the previous chapters, a weaker mixed formulation for the data-driven approach was introduced. This formulation incorporates both the minimisation of finite element approximation errors and the evaluation of distances between computed fields and the material dataset.

This chapter investigates the nonuniqueness of the solution obtained using the weaker data-driven formulation and proposes a method to quantify the nonuniqueness, thereby providing insight into the uncertainty of the results. The proposed method is based on Markov chain Monte-Carlo simulations, iterating between solving the problem using the data-driven approach and perturbing the resulting fields to obtain a set of possible solutions.

To keep the finite element approximation errors from polluting the quantification of nonuniqueness, the weaker data-driven formulation's adaptive refinement algorithm is used to reduce the finite element approximation errors while keeping the number of integration points as small as possible for the desired accuracy. The adaptive refinement is based on the error indicators embedded in the mixed formulation and the distances of the field values to the material dataset, as described in section 5.4.

Since the material dataset is used to obtain a solution that more accurately represents a real-life response of the system, such as a graphite brick in a nuclear reactor, the uncertainty related to the material dataset propagates to the numerical prediction. Quantifying the nonuniqueness, helps to gain information about the uncertainty, which is essential from the safety perspective to ensure the numerical prediction is interpreted correctly and can, therefore, be used to make informed decisions for the safety of the system.

In most cases, some areas in the domain require higher safety than others. For example, regions likely to develop cracks or other defects are of higher concern when analysing a graphite brick, similar to how a nuclear reactor core requires higher safety than the cooling system. Additionally, higher uncertainty requires higher safety factors to be applied. Therefore, identifying the uncertainty in high-risk areas and potentially reducing it by conducting further experiments or simulations to obtain more relevant material data could decrease the safety factors necessary to keep the risk low.

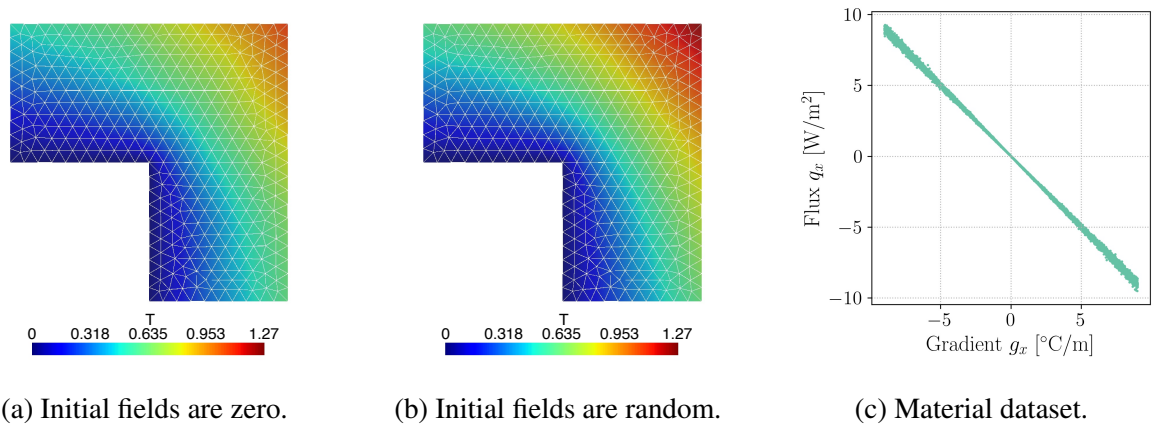


Figure 6.1: Example L: Temperature field for different initial values of the fields and the material dataset, with 10^4 material datapoints and $\sigma_\eta = 0.02$, used for both analyses. Note the different maximum values of the temperature field in the domain's top right corner.

While this chapter proposes a method for quantifying the nonuniqueness and uncertainty arising from the material dataset, it does not aim to define safety factors for specific industrial applications. Rather, the goal is to provide a framework for evaluating uncertainty in data-driven simulations and the conclusions that can be drawn from the various uncertainty indicators introduced in this thesis.

6.1 Uniqueness of the solution

The data-driven approach is based on finding the closest material datapoints to the current values of the unknown fields, using the material states of these datapoints to compute the fields, ensuring the satisfaction of the conservation laws, and repeating the process until the convergence criteria are satisfied; this process is described in more detail in Chapter 4. From mathematical point of view, the problem is well-posed, however, the solution obtained is not unique.

The non-uniqueness emerges through the data-driven algorithm. First, the distance of the resulting field values can be the same for multiple material datapoints. Another non-uniqueness comes from the data-driven algorithm searching for a subset of material datapoints closest to the resulting field values that satisfy the conservation laws and boundary conditions as multiple combinations exist (resulting field and material subset).

Therefore, the result differs depending on the initial values of the fields considered in finding the closest material datapoints, as shown in Figure 6.1. The material dataset used in this example is generated with 10^5 material datapoints with noise added to the thermal conductivity to highlight the non-uniqueness of the solution. The standard deviation of the noise added to the data is $\sigma_\eta = 0.02$; for more information, see section 4.2.

Both of the solutions in Figure 6.1 use the same material dataset and have the same boundary conditions applied, however, Figure 6.1a analysis starts with zero initial fields and Figure 6.1b

starts with random initial fields. The solutions are different; however, they are both valid as they satisfy the conservation laws, boundary conditions, and criteria for stopping the iterations. When no noise is present in a sufficiently saturated material dataset covering all of the required material states, the dependence of the solution on the initial values is less pronounced or completely negligible; see subsection 4.1.1 for the convergence of results with no noise and increased number of material datapoints.

This lack of uniqueness of the solution is a feature of the material dataset being used instead of equations representing the constitutive material behaviour, and this feature can be exploited to evaluate the uncertainty of the solution through quantification of nonuniqueness.

Implemented within the weaker mixed formulation, error indicators highlight the elements with a high error in the finite element approximation of the fields. Adaptive refinement based on the error indicators increases the number of integration points only where it improves the finite element approximation of the fields, or where the material dataset quality is low.

By choosing an appropriate algorithm for the adaptive refinement, the increase of the number of integration points can be minimised for a given accuracy, often saving orders of magnitude of the number of integration points and computational time compared to the global refinement, see section 5.4 for refinement details. This method removes the trial and error method of defining the mesh and approximation orders before running the analysis. Therefore, the time saved preparing the analysis and solving the problem can be used to repeat the analysis and obtain a set of possible solutions with different initial values of the fields. This process can be automated by using Markov chain Monte-Carlo simulations.

6.2 Markov chain Monte-Carlo simulations

Markov chain Monte-Carlo simulations are used to quantify the nonuniqueness and therefore evaluate the uncertainty of the solution, and will hereinafter be referred to as Monte-Carlo. The start of the analysis is the same as in the previous chapters regarding the data-driven approach, regardless of whether a stronger or weaker formulation is used. The resulting fields are saved and perturbed once the data-driven convergence and adaptive refinement criteria are satisfied. The perturbed fields are then used as initial fields for the next Monte-Carlo iteration. The process is repeated several times, and the results are saved. The algorithm for the Monte-Carlo simulations for the data-driven approach is shown in Algorithm 6.

Instruction on line 1 of Algorithm 6 initialises the fields which can be random or zero. Considering the number of repeated runs of the analysis, the choice of the initial fields has little impact on the resulting standard deviation. However, depending on whether adaptive refinement is used, the initial fields can impact how the domain is refined. When noise and sparsity are present in the material dataset, starting with random initial fields can result in noise affecting the error estimator values before the refinement is completed. Figure 6.2 shows that the zero

Algorithm 6 Monte-Carlo Simulations

- 1: Initialize the fields.
- 2: Solve the problem using the data-driven approach and adaptive refinement.
- 3: **repeat**
- 4: Solve the problem.
- 5: Save the fields.
- 6: Perturb the fields.
- 7: Use the perturbed fields as initial fields.
- 8: **until** Monte-Carlo criteria are satisfied
- 9: Calculate the average and standard deviation of the resulting fields.

initial field values result in more localised high error estimator values than the random initial field values. Therefore, for the first initialising of the fields, the zero-valued fields are used in the examples in this chapter to minimise the effect of the noise on the error estimator values before the adaptive refinement is completed.

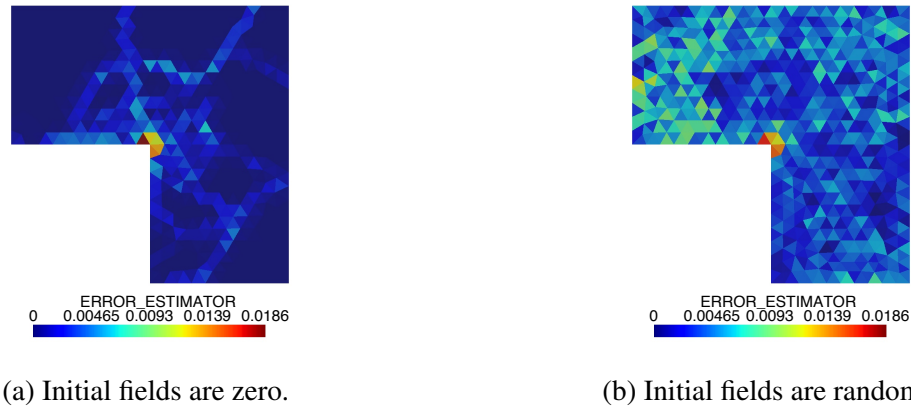


Figure 6.2: Example L: Error estimator for different initial values of the fields.

Instruction on line 2 of Algorithm 6 solves the problem either using the stronger or weaker formulation of the data-driven approach, described in chapter 4 and chapter 5, respectively. If the adaptive refinement is used, the refinement is done before the Monte-Carlo simulations are started. The adaptive refinement is done based on the error indicators imbedded in the mixed formulation and the distances of the field values to the material dataset, described in section 5.4. Once sufficient refinement has been achieved, the resulting fields are saved.

The resulting fields are then perturbed in a random direction by a perturbation value, which is normally distributed as:

$$\psi \sim \mathcal{N}(0, \kappa), \quad (6.1)$$

where κ is a metaparameter corresponding to the standard deviation of the perturbation value. The perturbation metaparameter κ can be chosen based on the average value of the field, the current local standard deviation of the field, the maximum value of the field, or the local or average distance to the material dataset.

Larger perturbation values can result in longer computation times, as more data-driven iterations might be needed to obtain a solution for each of the Monte-Carlo iterations. On the other hand, a small value for the perturbation parameter can result in a slow or a lack of exploration of the solution space. Since exploring the most suitable perturbation parameter is not in the scope of this work, a fixed value of $\kappa = 10$ is used in the example in this section, which is deemed sufficiently large in relation to each of the material datasets used, see Figure 6.3. Figure 6.3a shows that convergence is also reached with values smaller than $\kappa = 10$. Nevertheless, values of κ order of magnitude bigger do not slow the convergence w.r.t. the number of iterations, see Figure 6.3b, therefore, using higher κ , such as $\kappa = 10$, is sufficient.

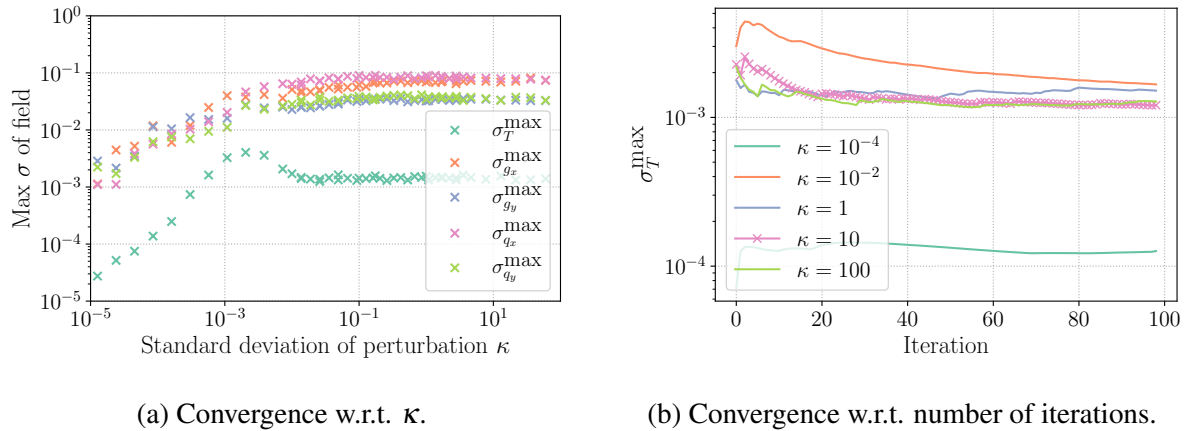


Figure 6.3: Example L: Influence of standard deviation of perturbation κ on the maximum standard deviation of the resulting fields: σ_T^{\max} , $\sigma_{g_x}^{\max}$, $\sigma_{g_y}^{\max}$, and $\sigma_{q_x}^{\max}$.

The fields requiring perturbation are the fields that are being solved for and are at the same time used in the search for the closest material data points, i.e. the flux field \mathbf{q} , the gradient field \mathbf{g} for the weaker formulation or the temperature field T for the stronger formulation or if 5D material dataset is used.

The perturbed fields are then used as initial fields for the next Monte-Carlo iteration of the analysis. Henceforth, iteration refers to a Monte-Carlo iteration unless stated otherwise. The mesh and the approximation order are unchanged between the iterations and remain the same as at the end of the adaptive refinement. After each solution, the resulting fields are saved and the process is repeated a number of times until the Monte-Carlo criteria are satisfied. The stopping criteria can be set to the number of iterations or the difference between the average standard deviation of the fields from the previous and the current iteration.

The integration scheme used for calculating the fields is Gauss quadrature, with standard Gauss points chosen based on the approximation order of the fields. In contrast, the field values used for statistical analysis are evaluated and stored at regularly spaced locations within each element, determined using Newton-Cotes points. These Newton-Cotes points are not used for integration; rather, they serve only as evaluation points to simplify the computation of uncertainty due to nonuniqueness.

The results of the Monte-Carlo simulations are the average and the standard deviation of the fields evaluated on each regular evaluation point. The standard deviation is in the same units as the fields; hence, the interpretation is straightforward and understandable by the naked eye. The standard deviations are furthermore summarised per element for ease of interpretation.

6.2.1 Effect of noise on the standard deviation of results

To consider the effect of noise on the standard deviation of the fields, the Monte-Carlo simulations are run for the material dataset with different standard deviations of noise. The material dataset used in this example is generated with 10^6 material datapoints and the noise is added to the thermal conductivity only in the x -direction. The material datasets used for the Monte-Carlo simulations with standard deviation of noise in x -direction $\sigma_{\eta_x} = 0$, $\sigma_{\eta_x} = 0.02$, and $\sigma_{\eta_x} = 0.05$ are shown in Figure 6.4.

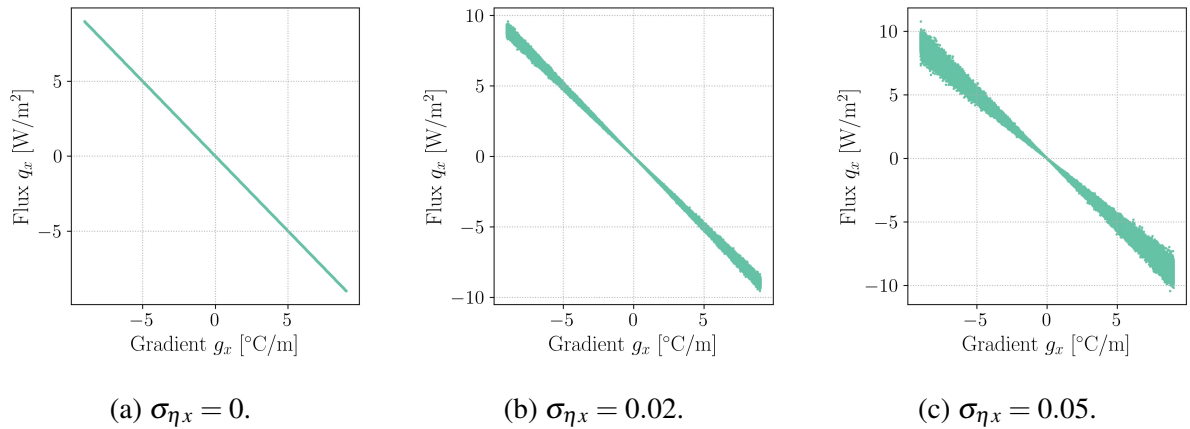


Figure 6.4: Example L: Material datasets with various standard deviation of noise σ_{η} applied to the thermal conductivity in the x -direction. There is no noise present for the values in y -direction and the number of material datapoints is 10^6 .

As the noise is applied only to the x -direction of the material dataset, the standard deviation of the results shows higher values for the x -direction in comparison to y -direction, see Figure 6.5. Nevertheless, even if the dataset only includes noise in the x -direction, the standard deviation of the results of the y -direction is affected. Additionally, the maximum standard deviation of the results obtained with the weaker data-driven formulation is higher than the maximum standard deviation of the results obtained with the stronger data-driven formulation, which might be desirable from a safety point of view, especially in sensitive environments such as nuclear reactors.

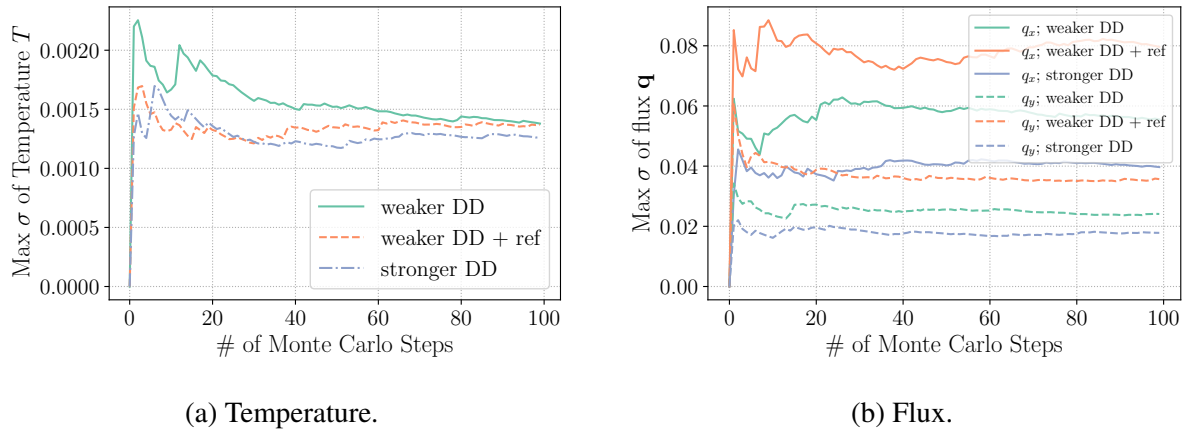


Figure 6.5: Example L: Maximum standard deviation convergence of the fields for standard deviation of noise $\sigma_{\eta_x} = 0.02$ and $\sigma_{\eta_y} = 0$ in the material dataset.

The values of the maximum standard deviation stabilise with the increasing number of the Monte-Carlo steps, as shown in Figure 6.5 for the Example L analysis with $\sigma_{\eta_x} = 0.02$. The resulting standard deviation of the temperature field is also shown in Figure 6.6 for the stronger and weaker mixed formulation and the weaker mixed formulation with adaptive refinement.

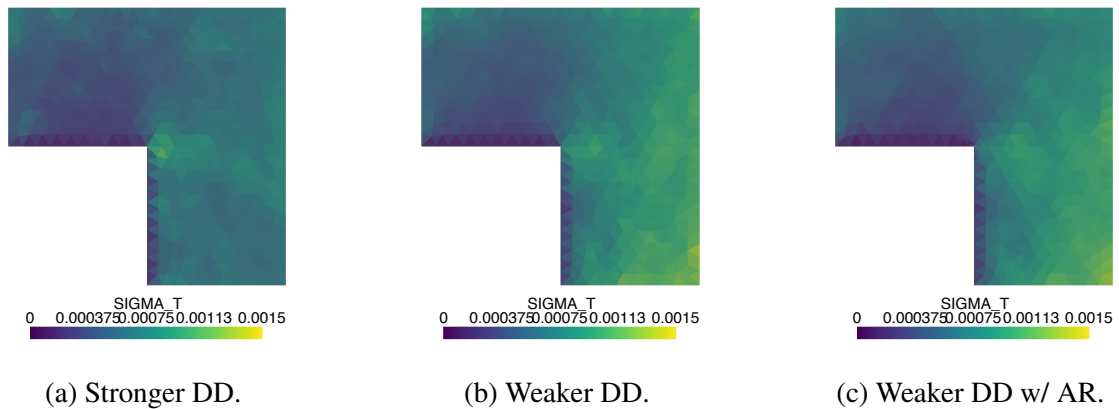


Figure 6.6: Example L: Standard deviation of the temperature field for standard deviation of noise $\sigma_{\eta_x} = 0.02$ in the material dataset using the stronger and weaker mixed formulation. Note that w/ AR stands for "with adaptive refinement".

In this case, the resulting standard deviation of temperature obtained with the stronger DD formulation, Figure 6.6a, is the highest on the right side of the inner corner, which corresponds to the area to which the closest points from the material dataset are in an area with the noisy points (high values of flux in the x -direction, see Figure 6.4b).

On the other hand, the location of the highest resulting standard deviation of temperature obtained with the weaker DD formulation extends further to the right side of the domain. This behaviour is probably associated with the lower regularity of the temperature solution and the ability of the L^2 space to better approximate the jumps caused by the material dataset and, hence,

the variability of the solution.

Nevertheless, the resulting maximum standard deviation of the temperature field for any one regular integration point of the temperature field for both formulations is less than 0.0015 with the average value of the temperature field being around 0.53, see Figure 3.14.

While the standard deviation of the flux field captures the noisy area in both formulations, it is more pronounced with the weaker DD, for magnitudes see Figure 6.7. Refining the mesh further localises the high standard deviation of the flux field and identifies the noisy areas in the material dataset. Unlike with the temperature results, the flux results differ more between the stronger and weaker DD formulations in terms of the maximum standard deviation, see Figure 6.5b.

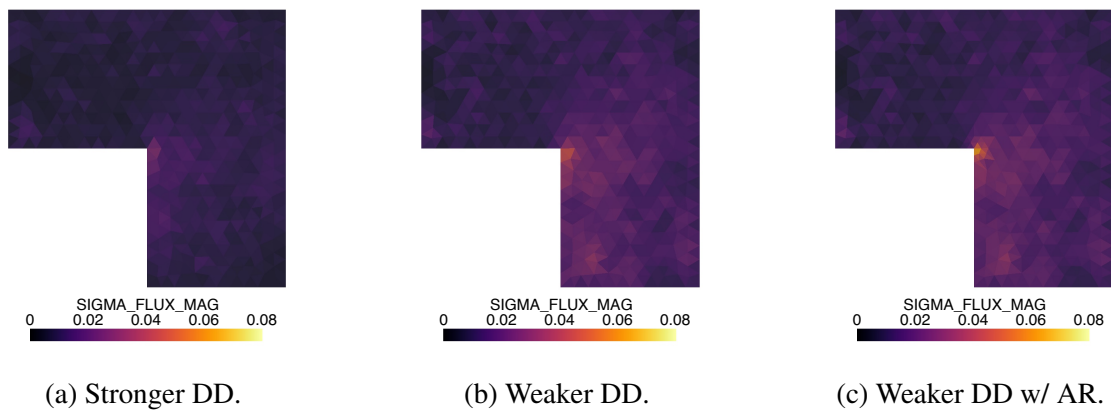


Figure 6.7: Example L: Standard deviation of the flux field for standard deviation of noise $\sigma_{\eta_x} = 0.02$ in the material dataset using the stronger and weaker mixed formulation. Note that w/ AR stands for "with adaptive refinement".

Furthermore, the noise is applied in x -direction only, and the standard deviation of the flux field has its highest values at the location of the highest noise for both the x and y -directions, see Figure 6.8, even though the noise in y -direction is of a smaller magnitude.

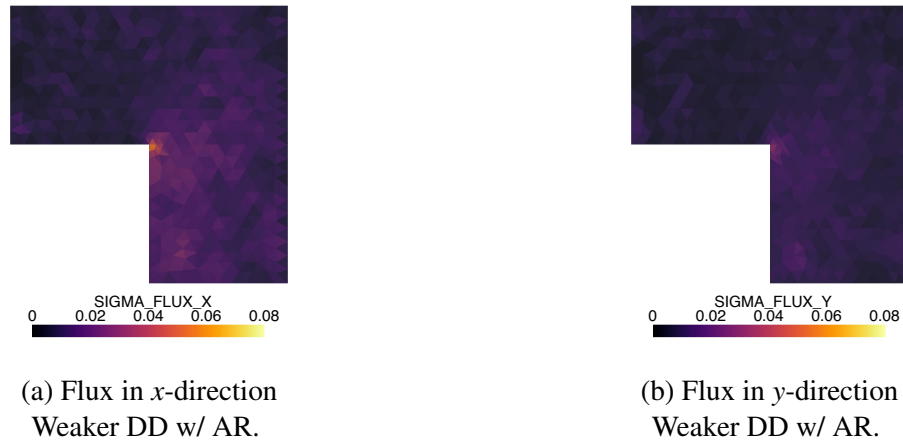


Figure 6.8: Example L: Standard deviation of the flux field for standard deviation of noise $\sigma_{\eta_x} = 0.02$ in the material dataset using the weaker DD formulation with adaptive refinement.

Figure 6.9 shows the maximum standard deviation of the fields for different standard deviations of noise in x -direction of the material dataset. The results show that the standard deviation of the fields increases with the standard deviation of the noise in the material dataset, however, more statistical analysis is needed to confirm the relationship between the noise in the material dataset and the standard deviation of the results, which is out of the scope of this work.

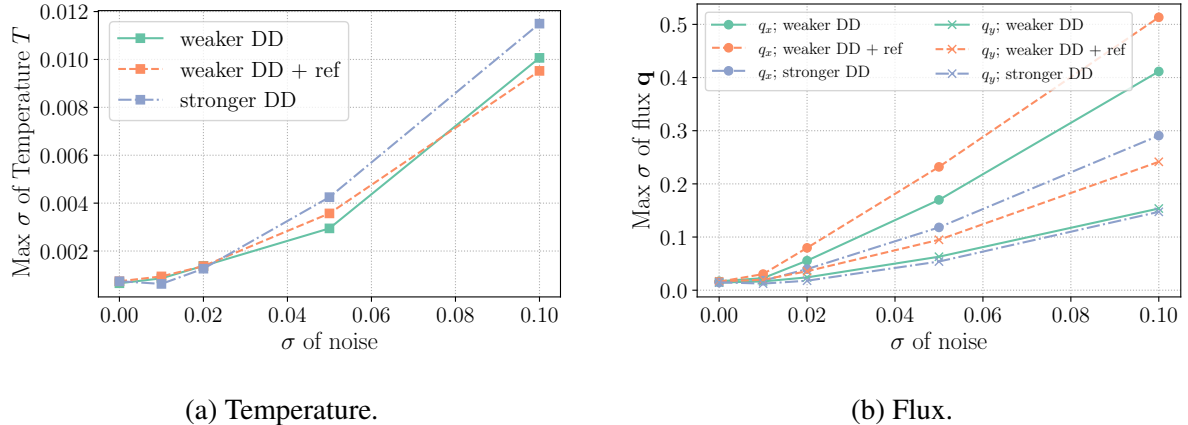


Figure 6.9: Example L: Maximum standard deviation of the fields for different standard deviations of noise in the material dataset.

Additionally, Figure 6.9 shows that using stronger and weaker data-driven formulation with the same mesh produces similar results. Nevertheless, using the weaker DD formulation with the adaptive refinement shows an increase in the resulting fields' standard deviation compared to the analysis without any refinement. This is due to the singularity experiencing higher noise due to the choice of the material dataset generation, see Figure 6.4, and refinement allowing for higher flux values in the singularity area.

These results show that Monte-Carlo simulations can be used to evaluate the uncertainty of

the results produced with material datasets instead of material models. Such an analysis can also broadly identify the potentially problematic areas of the material dataset used. Additionally, in the context of this thesis, reducing the regularity of the approximation spaces enables to better see the discrete nature of the dataset and the uncertainties associated with it. The following section applies the Monte-Carlo simulations with the methods from previous chapters to the Brick example, see Figure 4.19, to summarise the different ways the uncertainty of the results can be evaluated.

6.3 Summary of uncertainty measurements on the Brick example

The Brick example was introduced in the data-driven chapter 4 where the material datasets, summarised in Table 4.4, were used with the stronger data-driven approach. The results contained the temperature field, the flux field, and the distance d of the results to the 5D dataset \mathcal{D} used for the analysis. The distance d and its components are calculated in the same way for the stronger and weaker data-driven approach. They are one of the ways to evaluate how informed the results are by the material dataset, i.e. material dataset A is nearly equally sparse throughout the domain considered and material dataset E does not sufficiently cover a part of the domain.

Next, calculating the error indicators and estimator with the weaker data-driven approach, see chapter 5, allows for checking the conformity to the chosen constraints, i.e. conservation law $\nabla \cdot \mathbf{q} = -s$, equality of the gradient of temperature $\mathbf{g} = \nabla T$, and the continuity of temperature across inner boundaries. The error indicators and estimator are used for the adaptive hp -refinement. The adaptive refinement is used to improve the finite element approximation of the fields and to reduce the numerical errors and decrease bias. Nevertheless, refining the mesh too much can increase the variance significantly and cause overfitting, and hence, the distance of the results to the material dataset is also taken into account.

The error estimators highlight where the finite element approximation is the highest within the domain, but the cause can be the finite element approximation error, which is reducible by hp -refinement, or the material dataset quality. Nevertheless, the error estimator does not provide values that are comprehensive enough to evaluate the magnitude of the uncertainty of the results; it only provides the areas where the finite element approximation error is the highest.

The Monte-Carlo analysis provides a way of quantifying uncertainty in the same units as the results obtained, therefore, it is easily interpretable. Table 6.1 shows the maximum standard deviations of the resulting fields for the 5D material datasets.

Material dataset	$\max \sigma_T$ [$^{\circ}\text{C}$]	$\max \sigma_{\mathbf{g}}$ [$^{\circ}\text{C}/\text{m}$]	$\max \sigma_{\mathbf{q}}$ [W/m^2]
A (regular sparse)	2.52	724	67×10^3
B (regular dense)	0.83	389	25.7×10^3
C (random w/ noise)	4.18	695	124×10^3
D (artificial experiment)	0.387	330	29.4×10^3
E (experiment w/ missing data)	0.3	342	28.6×10^3
F (experiment w/ noise)	4.67	1380	213×10^3

Table 6.1: Example Brick: Maximum standard deviation of the fields for different material datasets obtained with weaker DD with adaptive refinement , also see Table 4.4.

The maximum standard deviations of the results only offer a rough estimate of the overall quality of the results and need to be compared to the values of resulting fields in the relevant areas of the domain. The resulting fields with material dataset D for the Brick example are shown in Figure 6.10.

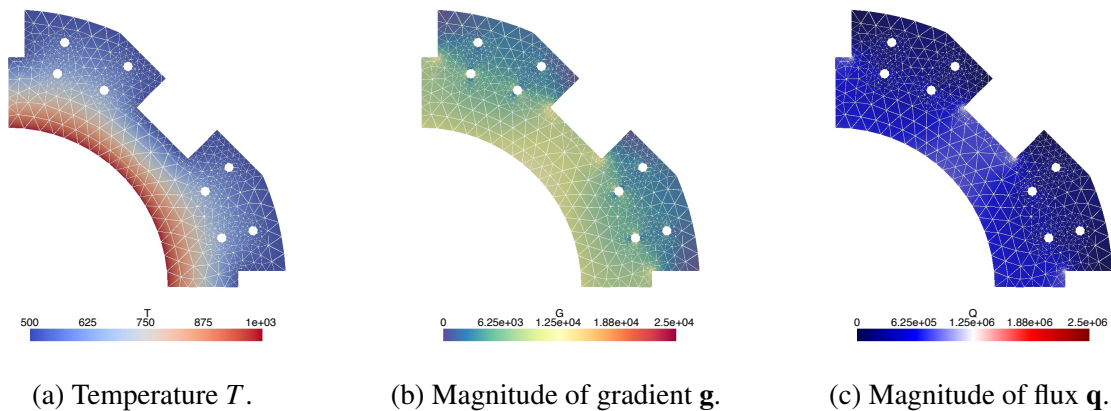


Figure 6.10: Example Brick: Resulting fields with material dataset D. Note that D is the most accurate dataset, and these resulting fields are therefore chosen for comparison to all of the further results to avoid repeating the figures.

Material datasets A and E have already been flagged with issues thanks to the calculation of the distance to the material dataset. The resulting locations of the high standard deviations of the results also correspond to the areas of the high distance to the material dataset, and the uncertainty can propagate to one or multiple of the fields solved for, as shown in Figure 6.11.

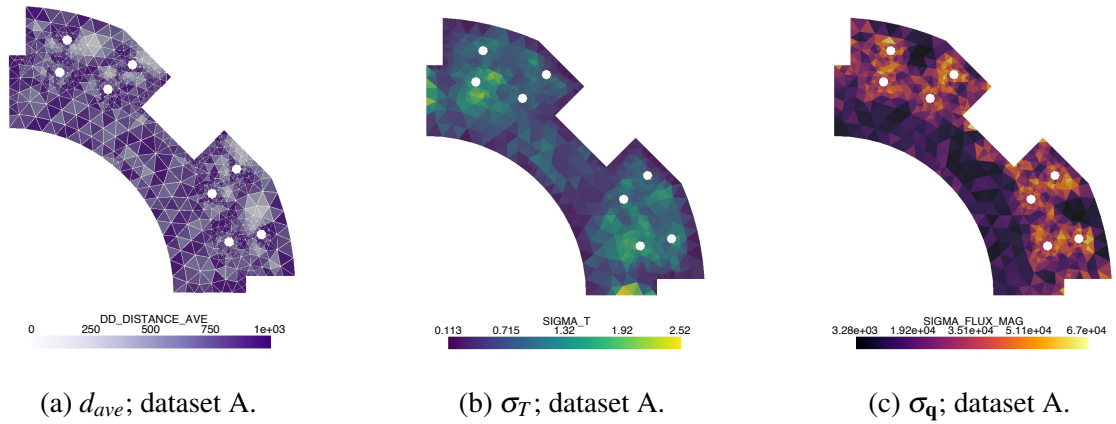


Figure 6.11: Example Brick: Distance to the material dataset and standard deviation of the results for material dataset A (regular sparse) after Monte-Carlo analysis.

The sparsity of dataset A results in a high standard deviation of the results in most of the domain. Comparing the magnitudes of the standard deviation of flux σ_q in Figure 6.11c with the flux q values in Figure 6.10c, values of σ_q around 60×10^3 are observed in areas where the flux is around 0. For the summary of findings of the analysis with material dataset A see Table 6.2.

Observation 1	distance to the material dataset d_{ave} is high in most of the domain
Interpretation 1	the dataset is too sparse or does not cover the ranges required by the analysis sufficiently
Observation 2	standard deviation of the results σ is high in most of the domain
Interpretation 2	it is not confirmed if the dataset includes noise
Recommendation	the results are not reliable, additional experiments are needed to improve the dataset

Table 6.2: Summary of findings of analysis with material dataset A.

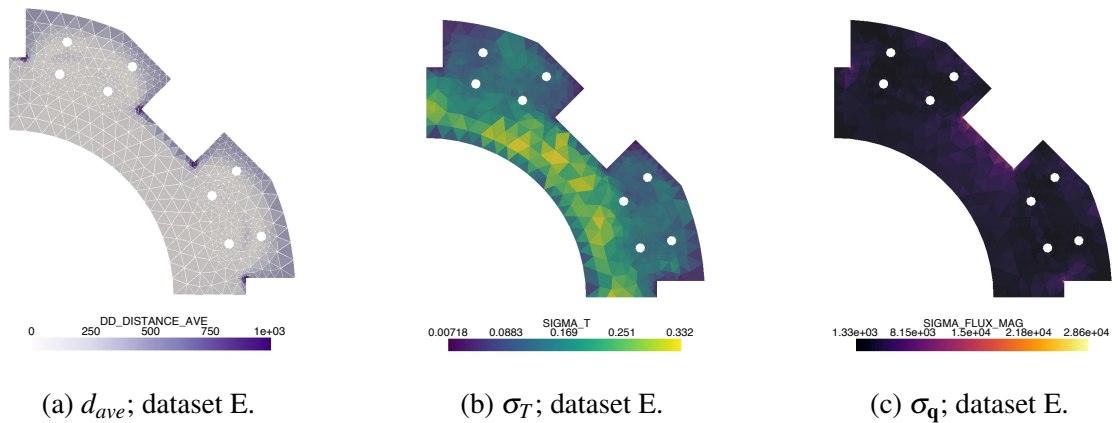


Figure 6.12: Example Brick: Distance to the material dataset and standard deviation of the results for material dataset E (experiment missing) after Monte-Carlo analysis.

On the other hand, due to the boundary conditions of the Brick example, dataset E results have low values of the temperature standard deviation since the highest noise is located at the temperature boundary condition. The flux field, however, has high standard deviations in the areas where the material data is missing, see Figure 6.12 and Table 6.3.

Observation 1	distance to the material dataset d_{ave} is high in specific areas of the domain
Interpretation 1	the dataset is missing information in the areas where the distance to the dataset is high
Observation 2	standard deviation of the results σ is high in the same areas where the distance to the dataset is high
Interpretation 2	the noise is assumed to be low for the points of the dataset used in the analysis where the distance to the dataset and the standard deviation of the results are low
Interpretation 3	the results are not reliable in the areas where the standard deviation is high and the uncertainty there might have affected the results in the rest of the domain if the boundary conditions were different
Recommendation	additional experiments are needed to obtain more data for the values missing in the dataset to improve the dataset and certainty of the results

Table 6.3: Summary of findings of analysis with material dataset E.

The highest standard deviation of the flux field observed in Table 6.1 is performed in the analysis with the material dataset F. Figure 6.13 shows that the highest standard deviation of flux is no longer located where the flux values are the highest, but are located where the noise in the material dataset is the highest. Upon inspection of the result and standard deviation values, it can be determined that the results obtained with the material dataset F for this analysis are not reliable in the area on the outside edge of the brick. Note that $\max \sigma_{\mathbf{q}} = 0.2 \times 10^6$ [W/m²] on the outside of the brick, when $\max \mathbf{q} \approx 2.5 \times 10^6$ [W/m²] is at the singularity.

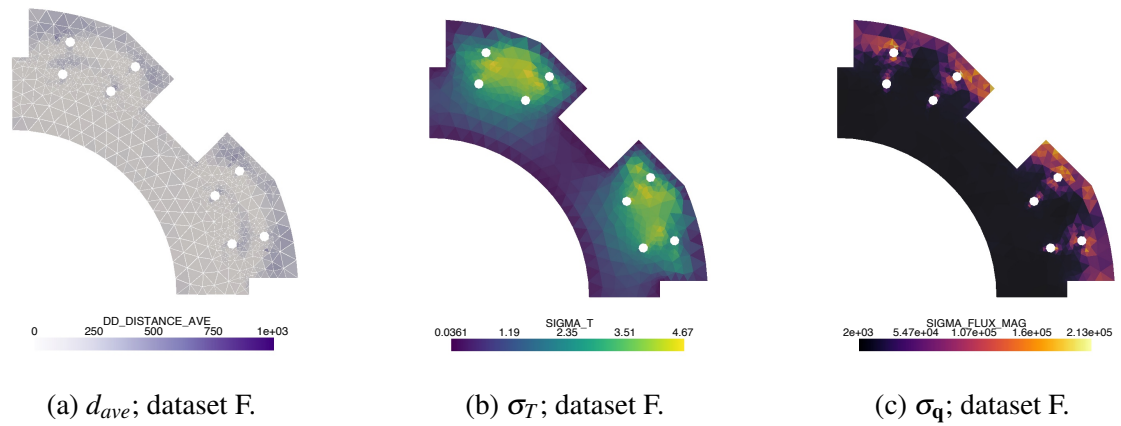


Figure 6.13: Example Brick: Distance to the material dataset and standard deviation of the results for material dataset F (experiment noisy) after Monte-Carlo analysis.

Analysis run with material dataset C (random noisy) also shows increased flux standard deviation in the areas where the noise in the material dataset is the highest, see Figure 6.14. The results show that the standard deviation of the flux field is higher in the areas where the noise in the material dataset is higher. The combined summary of analysis with material datasets C and F is shown in Table 6.4.

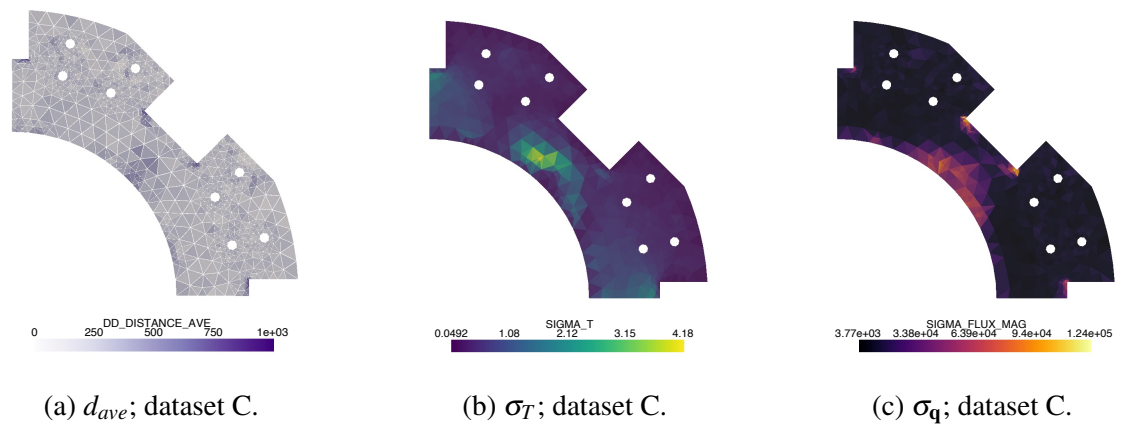


Figure 6.14: Example Brick: Distance to the material dataset and standard deviation of the results for material dataset C (random noisy) after Monte-Carlo analysis.

Observation 1	distance to the material dataset d_{ave} is low in most of the domain with few exceptions
Interpretation 1	the dataset and the results can be slightly improved by conducting more experiments in the areas where the distance to the dataset is high
Observation 2	standard deviation of the results σ is high in particular areas of the domain
Interpretation 2	since d_{ave} is low where the standard deviation of the results is high, the dataset contains noise which affects the results
Recommendation 1	the parts of the distance to the dataset can be checked individually, e.g. $T^h - T^*$, throughout the domain to identify potential areas where the dataset is lacking and conduct more experiments in those areas
Recommendation 2	review of the material dataset is advised to analyse the noise <ul style="list-style-type: none"> • the noise is the stochastic response of the material: the results are likely sound • the noise is an error in the dataset handling/measurements: fix the errors if possible, otherwise accept that the results are affected by the noise • the noise source is unclear: accept the results for what they are or conduct a new set of experiments

Table 6.4: Summary of findings of analysis with material dataset C and F.

On the other hand, material datasets which are denser and do not contain any added noise still do not result in a unique solution, and the resulting standard deviation of the results can be computed. The results for the material dataset B (regular dense) are shown in Figure 6.15.

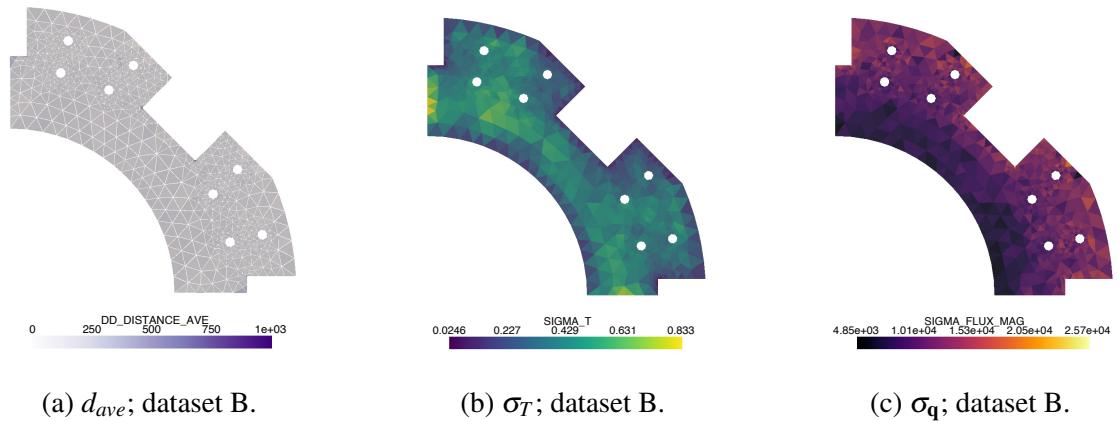


Figure 6.15: Example Brick: Distance to the material dataset and standard deviation of the results for material dataset B (regular dense) after Monte-Carlo analysis.

In comparison to the analysis with dataset B (regular dense), the results for the material dataset D (artificial experiment) show that the standard deviation of the results is lower, see Figure 6.16. The summary of findings of the analysis with material datasets B and D is shown in Table 6.5.

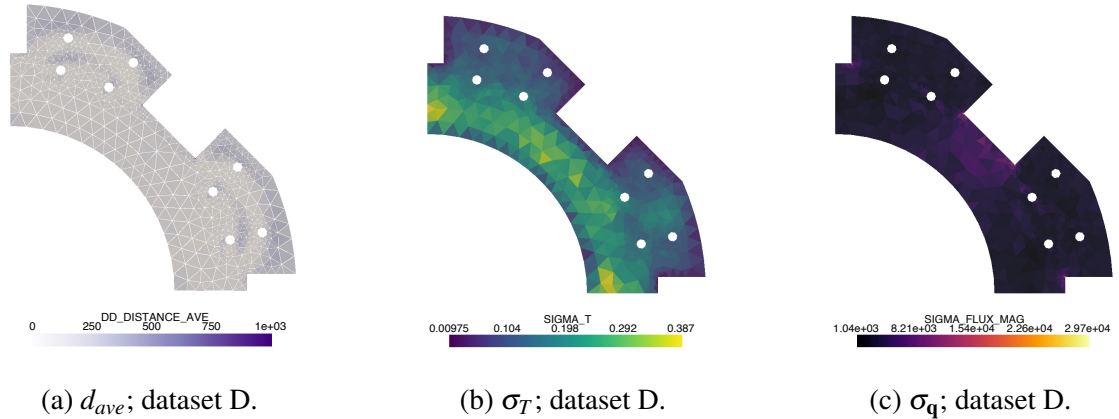


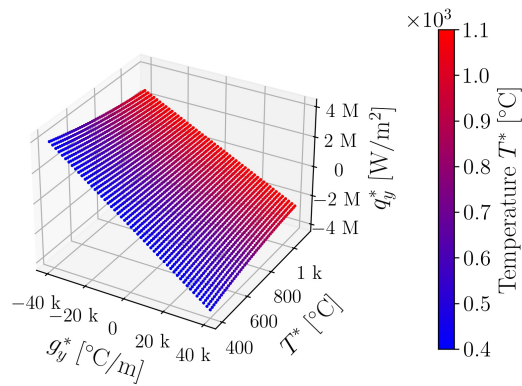
Figure 6.16: Example Brick: Distance to the material dataset and standard deviation of the results for material dataset D (artificial experiment) after Monte-Carlo analysis.

Observation 1	distance to the material dataset d_{ave} is low throughout the domain
Interpretation 1	the dataset is dense and covers the ranges required by the analysis sufficiently
Observation 2	standard deviation of the results σ is low throughout the domain with the highest values at identifiable areas
Interpretation 2	the reliability of the results depends on the requirements of the analysis, i.e. how much distance to the dataset and uncertainty is acceptable
Recommendation	the results are likely sound, however, recommendations from the summary of analysis with material dataset C and F can be used, see Table 6.4

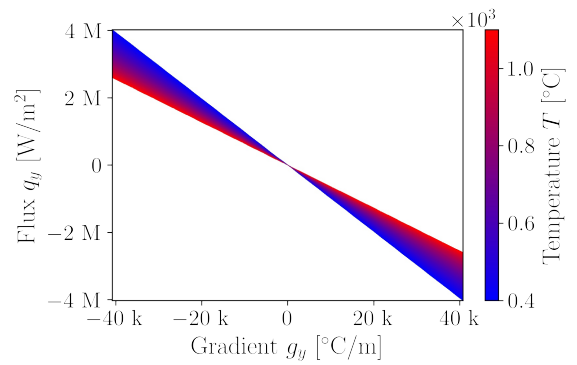
Table 6.5: Summary of findings of analysis with material dataset B and D.

This section could be read without the need to see or analyse the material datasets beforehand, however, glimpses of each material dataset are shown in Figure 6.17 for reference. The summaries of findings of the analysis in this section identify the quality of the material dataset used without prior knowledge of the dataset. All of the results could be used as presented without any further interference, however, the uncertainty needs to be taken into account when interpreting the results.

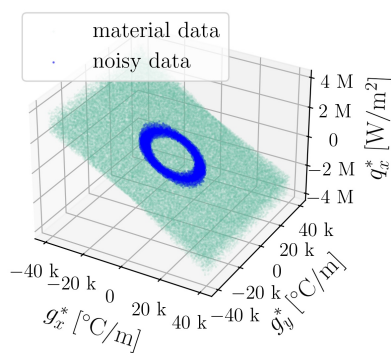
To conclude, the analysis with the data-driven weaker mixed formulation does not provide a unique solution. The nonuniqueness can therefore be quantified and be used to evaluate the



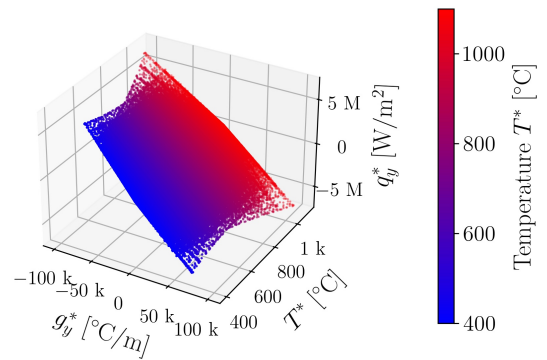
(a) Material dataset A.
Regular sparse



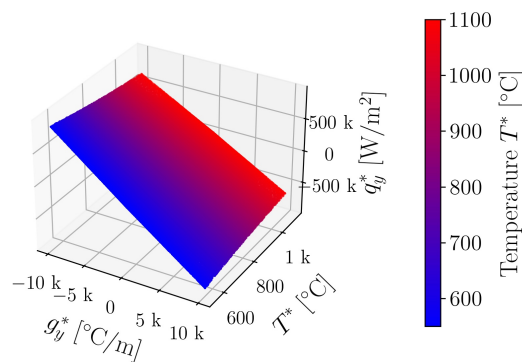
(b) Material dataset B.
Regular dense



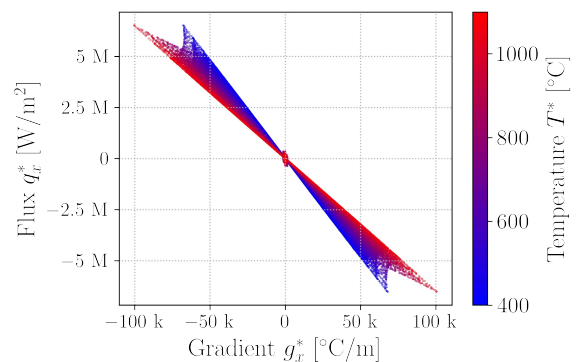
(c) Material dataset C.
Random noise



(d) Material dataset D.
Artificial experiment



(e) Material dataset E.
Experiment trimmed



(f) Material dataset F.
Experiment noisy

Figure 6.17: Example Brick: Extract of material datasets used for the Brick example analysis. More information in section 4.3 and Table 4.4.

uncertainty of the results, which should be viewed together with the distance to the material dataset. The data-driven formulation is able to provide results with a single material datapoint in the material dataset which would show no standard deviation of the resulting fields, however, the information of the material behaviour would be wrong. Therefore, both the distance to the material dataset and the standard deviation of the results should be used to evaluate the certainty with which the results are viewed. On the other hand, it should be noted that the boundary conditions reduce the nonuniqueness of the relevant fields in their vicinity, regardless of the state of the material dataset in that region. Additionally, the boundary conditions are rarely known with as high accuracy as it is assumed in the presented formulation of the data-driven approach and should be taken into consideration.

Chapter 7

Conclusions and Perspectives

7.1 Conclusions

This thesis presented an investigation into diffusion problems, particularly nonlinear heat transfer, through a combination of classical finite element method (FEM), mixed formulation, and a data-driven approach.

The standard FE formulation, described in chapter 2, serves as a foundation for the more advanced methods introduced in subsequent chapters. The study confirmed the reliability of standard FE formulation in solving linear and nonlinear diffusion problems, demonstrating convergence through global mesh and approximation order refinement.

The mixed FE formulation, discussed in chapter 3, consists of a two-field solution for heat diffusion problems, separating the temperature field from the heat flux field. One of the advantages of the mixed formulation is the higher order convergence of heat flux errors compared to standard formulations, enhancing the accuracy of numerical solutions for flux. The formulation also allows for adaptive mesh and order refinements, guided by error indicators associated with temperature gradients, flux divergence, and jumps across inner boundaries. The adaptive refinements were shown to reduce errors and improve convergence to exact solutions, demonstrating the effectiveness of the mixed formulation in managing approximation errors.

The stronger data-driven approach, presented in chapter 4, is based on a novel method for solving diffusion problems by using material datasets instead of constitutive models. The approach is able to use data directly to perform the numerical analysis, providing information on the accuracy of the results in terms of the distance to the dataset. The study found that the stronger data-driven approach permits the identification of whether the results are far from the material dataset, caused by the dataset not covering parts of the domain or being sparse. However, it is not able to detect if the dataset is noisy or if the solution contains finite element approximation errors without knowing the exact solution beforehand.

To address these limitations, chapter 5 introduces a weaker data-driven approach that derives the data-driven approach with the mixed formulation, which is the main novelty of this research.

The weaker data-driven approach combines the advantages of the mixed formulation and data-driven approach, providing more natural spaces for the diffusion problem, *a posteriori* error indicators/estimates, adaptive refinement, and the use of material datasets instead of constitutive equations. The study showed that the error estimates capture problematic areas of the numerical analysis, which includes finite element approximation errors and/or when a significantly problematic part of the dataset is used to evaluate the results. New adaptive refinement algorithm is proposed, which considers the error estimator, the distance of the results to the material dataset, and the variance of this distance within an element. The adaptive refinement is able to reduce the error in the solution in terms of finite element approximation errors and prevent overfitting where the knowledge of the material behaviour is poor. However, the error estimators and the distance of the results to the material dataset cannot capture the resulting uncertainty of the results in easily measurable terms and cannot evaluate if there is a noise present in the material dataset used.

Therefore, repeating the simulations with perturbed initial field values, akin to Monte-Carlo simulations, while keeping the same material dataset is proposed in chapter 6. Since the adaptive refinement can reduce the finite element approximation errors with a much smaller increase to the total number of integration points in comparison to global refinement for similar accuracy, repeating the analysis multiple times becomes feasible. Saving the resulting fields of each iteration of the Monte-Carlo simulation allows for the evaluation of the standard deviation of the results, which has the same units as the fields themselves, making it easier to interpret the overall uncertainty of the solution obtained. The study confirmed that the material dataset's quality affects the solution's uncertainty. The standard deviation of the results is high where there is noise in the dataset and where the dataset has sparse or missing parts of the data required for the analysis. Additionally, depending on the boundary conditions, the uncertainty can propagate to the parts of the domain where the dataset is relatively complete and noise-free. Regardless, it is possible to identify what issues are present in the material dataset and suggest which values are affected if obtaining more data is possible.

Overall, the study showed that the mixed formulation and data-driven approach can be combined and provide a solution with information about the accuracy and uncertainty of the results.

7.1.1 Novelties introduced in this research

The main novelty of this research is the proposed framework combining the mixed formulation and data-driven approach. Mixed formulation uses the natural spaces for the unknown fields, allows for the jump of temperature between elements, and enforces the continuity of the normal flux component across any inner boundaries. The mixed formulation provides naturally arising error indicators and estimator, which are used for adaptive refinement criteria.

The adaptive refinement algorithm was extended by calculating the variance of the distance to the material dataset within an element, which can be used together with the average distance

to the material dataset per element to choose which elements should be refined.

The error indicators introduced through the mixed formulation were adapted to the weaker data-driven approach. The analysis showed that the standard error indicators highlight not only where the finite element approximation is poor, which can be decreased by refinement, but also elements that use a problematic part of a material dataset. By using the proposed criteria for adaptive hp refinement and choosing where h and p refinement takes place independently of each other, the refinement is able to reduce the finite element approximation errors where the material dataset is relatively reliable and isolate areas where the material dataset is missing data.

Having used the adaptive refinement in the areas where it makes an impact on the accuracy, it is feasible to repeat the analysis multiple times with different initial field values to evaluate the uncertainty of the results.

The final novelty is quantifying the uncertainty of the resulting fields values using Monte-Carlo simulations, evaluating the standard deviation of the results, and interpreting the uncertainty in terms of the material dataset used.

Using this approach provides transparent results and it is possible to differentiate between the errors coming from the finite element approximation, uncertainty related to sparse, missing or noisy parts of material dataset.

7.2 Limitations and Future Work

The research presented in this thesis has several limitations that could be addressed in future work. First, even if the formulation is general, the implementation and the problems considered were 2D, and the extension to three-dimensional problems is an obvious next step when tackling real-life problems.

7.2.1 Data-driven approach

There already exist improved versions of the data-driven approach than the formulation used for the weaker DD formulation introduced in this work. The most straightforward formulation was chosen to assess the influence of the mixed formulation on the data-driven approach, but it is not the limit.

Novel algorithms for searching the material dataset, which are more suited for highly nonlinear problems and large number of material datapoints, could be implemented. The dimensions of the material dataset needed for the numerical analysis could also be updated, e.g. instead of gradient of temperature and flux in x and y direction, magnitudes can be used for homogenous and isotropic materials, or magnitudes and information of the local anisotropic behaviour can be used.

The data-driven approach could be extended to include the uncertainty of the material dataset, e.g. by using the Bayesian approach or simulated annealing to estimate the uncertainty of the

material dataset and the results. Additionally, local information about the material behaviour can be extracted as part of the material dataset search and inform the system of equations to accelerate the convergence of the solution.

Research on most of the topics mentioned is already done or ongoing for the stronger data-driven approach, i.e. without the mixed formulation, and could be derived with the mixed formulation.

Additionally, in relation to the nuclear graphite analysis, irradiation or porosity within the brick/reactor can be added as one of the dimensions of the material dataset. The addition of another dimension could follow the same process as the temperature dimension in see section 4.3, however, the irradiation can be prescribed on the domain beforehand or be a result of another analysis. Since the material properties change with time and irradiation dosage within the reactor, the thermal conductivity and other material properties can be updated with the irradiation dosage and porosity without the need for fitting experimental datasets into material models.

7.2.2 Source of material datasets

The material datasets used in this work were synthetic since the focus was on the development of the numerical analysis method and not on obtaining the material dataset itself. One of the main challenges in applying data-driven methods in practice is the limited availability of suitable material datasets. In many cases, the data required to fully capture material behaviour across relevant loading and environmental conditions are either incomplete or simply not available. Often, material data are collected under standardised testing procedures that may not reflect the specific conditions of interest, particularly in complex systems such as components operating in high-temperature or irradiated environments. The data-driven identification [Stainier et al., 2019; Leygue et al., 2018; Valdés-Alonzo et al., 2022] has been proposed and used for obtaining material datasets for solid mechanics problems and the formulation can be amended to fit diffusion problems such as heat transfer, utilising tools such as digital image correlation or infrared thermography. Ongoing research in the acquisition of the material data is being done through the advancements in the experimental equipment and techniques such as data-driven identification or multiscale approaches but the approaches are not yet widely available.

7.2.3 Uncertainty quantification

Advanced statistical methods could be used to evaluate the uncertainty of the results, e.g. the Bayesian approach or the Gaussian processes, at various stages of the analysis. Simulated annealing mentioned in the data-driven section subsection 7.2.1 can also be implemented in the current framework.

7.2.4 Adaptive refinements

The adaptive refinement presented in this work is a proof of concept and has a potential for improvement. Each criterion for refinement at the element can be optimised for the problem at hand, and the combination of the criteria can be adjusted to the problem.

Mesh refinement with hanging nodes was not considered in this work, and it could be implemented in the future to improve the accuracy of the results and enable the possibility of decreasing the refinement in parts of the domain where it is no longer necessary when considering time-dependent problems.

Finally, adaptive refinement with higher-order geometries is lacking in this work and could be implemented to improve the accuracy of the results along curved boundaries.

7.2.5 Other applications

The methods introduced can be expanded to other applications, e.g., a data-driven approach for elasticity derived with the mixed formulation. The data-driven approach also does not have to be limited to replacing all of the constitutive models. The examples include using the data-driven approach for the diffusion calculation and the constitutive model for elasticity for the thermal elastic problems, or using the data-driven approach for the part of the domain where the material dataset is available and using the constitutive model for the rest of the domain.

7.2.6 Matrix structure and scalability

Using the mixed formulation offers a matrix structure that has lower bandwidth and predictable connectivity. This applies to the weaker mixed data-driven formulation as well. A block-diagonal structure may develop in certain situations, such as with L2 fields. This allows for the exact inversion of element matrices in parallel, especially on GPUs. Block preconditioners like the Schur block-solver can be implemented for the developed framework. As a result, the scalability for large-scale problems should be enhanced on high-performance computing (HPC) systems, using both CPUs and GPUs.

Appendix A

Functional spaces

In this section, all of the functional spaces [Boffi et al., 2013] used in this thesis are defined. Some of these appear as an intermediate step for construction of other functional spaces only, but are included here for the sake of completeness.

The figures in this section illustrate the hierarchical shape functions for the functional spaces in 2D, which are used in this thesis. The properties of the functional spaces in 3D are similar, but the figures are omitted for brevity.

A.1 L^2 Lebesgue space

The Lebesgue space $L^2(\Omega)$ is a set of scalar functions with square integrable values on Ω :

$$L^2(\Omega) := \left\{ u(\mathbf{x}) : \Omega \rightarrow R \mid \int_{\Omega} |u|^2 d\Omega = \|u\|_{\Omega}^2 < +\infty \right\}. \quad (\text{A.1})$$

Lebesgue space can be used for both scalar and vectorial functions, denoted by $L^2(\Omega)$ and $\mathbf{L}^2(\Omega)$, respectively. The vectorial Lebesgue space can further be defined by $[L^2(\Omega)]^d$, where d is the dimension of the problem. This thesis only considers two-dimensional problems therefore $\mathbf{L}^2(\Omega)$ refers to $[L^2(\Omega)]^2$ throughout the chapters of this thesis.

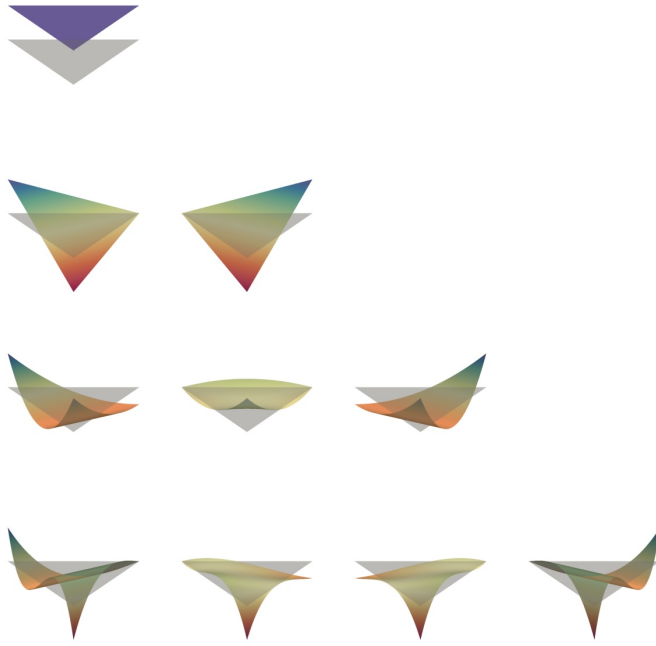


Figure A.1: Hierarchical shape functions of $L^2(\Omega)$ space, up to the third order.

Unlike other spaces introduced in this section, Lebesgue space $L^2(\Omega)$ shape functions can approximate the 0^{th} approximation order scalar field, which is a constant on an element, see first row in Figure A.1. Additionally, $L^2(\Omega)$ shape functions are discontinuous between elements and, therefore, allow for jumps of field values between the elements.

A.2 H^1 Sobolev space

Sobolev space $H^1(\Omega)$ is a set of scalar functions with square-integrable values and square integrable derivatives.

$$H^1(\Omega) := \left\{ u \in L^2(\Omega) \mid \int_{\Omega} |\nabla u|^2 \, d\Omega < +\infty, \text{ i.e. } \nabla u \in \mathbf{L}^2(\Omega) = [L^2(\Omega)]^d \right\}. \quad (\text{A.2})$$

A subset of this space, $H_0^1(\Omega)$, is used throughout this thesis to represent the functions from $H^1(\Omega)$ with prescribed zero values on the boundaries with an essential boundary condition:

$$H_0^1(\Omega) := \{ u_0 \in H^1(\Omega) \mid u_0 = 0 \text{ on } \Gamma_{\text{Essential}} \}, \quad (\text{A.3})$$

where $\Gamma_{\text{Essential}}$ is used for the Dirichlet boundary condition $\Gamma_{\text{Dirichlet}}$, e.g. temperature Γ_T , in the standard finite element approach.

H^1 shape functions are shown in Figure A.2 and are continuous between elements.

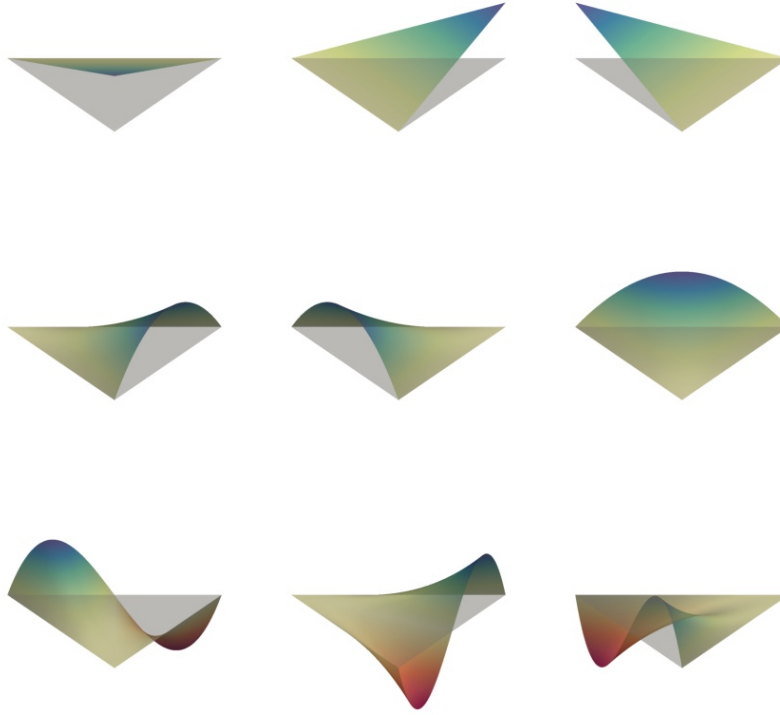


Figure A.2: Hierarchical shape functions of $H^1(\Omega)$ space, up to the third order.

A.3 $H(\text{curl})$ space

Nédélec space is a set of vectorial functions with square-integrable values and square-integrable curl:

$$H(\text{curl}; \Omega) := \left\{ \mathbf{v} \in [L^2(\Omega)]^d \mid \text{curl } \mathbf{v} \in [L^2(\Omega)]^n, \begin{array}{l} n = 1 \text{ if } d = 2 \\ n = 3 \text{ if } d = 3 \end{array} \right\} \quad (\text{A.4})$$

Curl of a vector function \mathbf{v} in 2D is defined as:

$$\text{curl } \mathbf{v} := \frac{\partial v_y}{\partial x} - \frac{\partial v_x}{\partial y} \quad (\text{A.5})$$

A property of $H(\text{curl})$ space is that the tangential component of the function is continuous across any inner boundary in the domain, which is natural for (electro)magnetic problems, see Figure A.3.

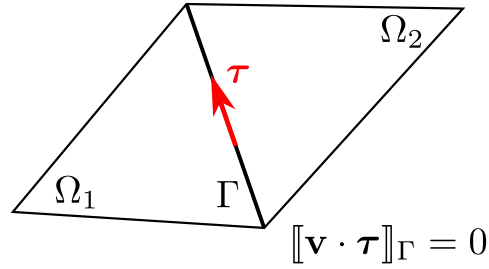


Figure A.3: Conservation of tangential component in $H(\text{curl})$ space between elements.

The hierarchical shape functions of $H(\text{curl})$ space are illustrated in Figure A.4. The $H(\text{curl})$ space is not used in this thesis by itself, however, it is used as an intermediate step to construct the $H(\text{div}; \Omega)$ space in 2D in subsection A.4.1.

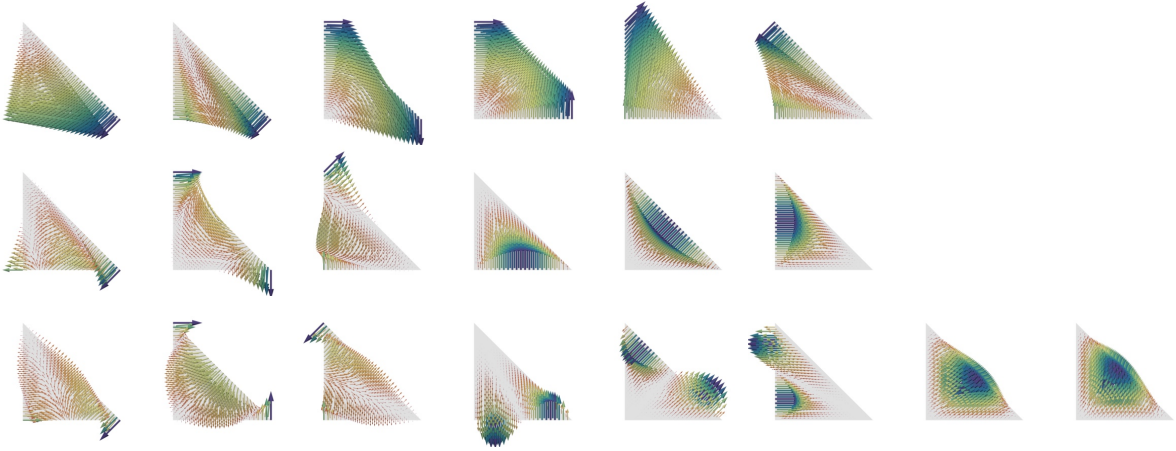


Figure A.4: Hierarchical shape functions of $H(\text{curl})$ space (Nédélec (second kind)), up to the third order.

A.4 $H(\text{div})$ space

Brezzi-Douglas-Marini $H(\text{div})$ space is a set of vectorial functions with square-integrable values and square-integrable divergence:

$$H(\text{div}; \Omega) := \left\{ \mathbf{v} \in [L^2(\Omega)]^d \mid \nabla \cdot \mathbf{v} \in L^2(\Omega) \right\} \quad (\text{A.6})$$

Divergence of a vector function \mathbf{v} is defined as:

$$\nabla \cdot \mathbf{v} = \frac{\partial v_x}{\partial x} + \frac{\partial v_y}{\partial y} \quad (\text{A.7})$$

A property of $H(\text{div})$ space is that the normal component of the function is continuous across any inner boundaries in the domain, which is natural for flow problems, see Figure A.5.

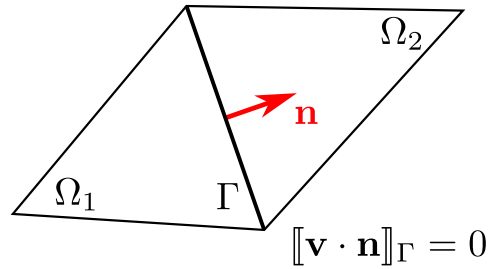


Figure A.5: Conservation of normal component in $H(\text{div})$ space between elements.

A.4.1 Functional spaces in 2D

This thesis considers problems in two dimensions only, and the spaces $H(\text{div})$ and $H(\text{curl})$ are isomorphic in 2D [Boffi et al., 2013]:

$$-\text{div } \mathbf{v}^\perp = \text{curl } v. \quad (\text{A.8})$$

Therefore $H(\text{div})$ space can be constructed from $H(\text{curl})$ space by rotating the vector field by a right angle:

$$(v_x, v_y)^\perp = (-v_y, v_x). \quad (\text{A.9})$$

Two dimensional $H(\text{div})$ space constructed from $H(\text{curl})$ space is used in chapter 3 and for the rest of the thesis thereafter and is referred to as $H(\text{div})$ space only and is visualised in Figure A.6.

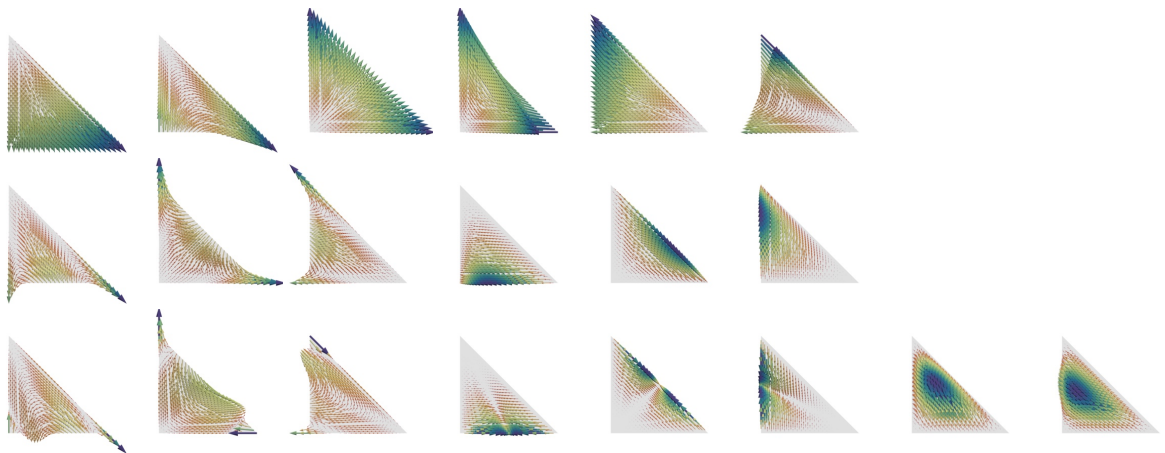


Figure A.6: Hierarchical shape functions of $H(\text{div})$ space (Brezzi-Douglas-Marini), up to the third order. Note that for 2D problems, $H(\text{div})$ space is constructed from $H(\text{curl})$ space by (A.9). See the similarity to Figure A.4.

Appendix B

Finding the closest point on a line

The data search described by (4.1) in chapter 4, in case of "fully saturated" dataset, can be replaced by the search for the closest point on a curve corresponding to the conservation law equation (2.3). For simplicity, $\nabla T = \mathbf{g}$, and $(\cdot)^*$ refers to the value on the line in this section.

To find the closest point $\{\mathbf{g}^*, \mathbf{q}^*\}_{4D}$ on the line

$$\mathbf{q}^* = -k\mathbf{g}^* \quad (\text{B.1})$$

to the field values $\{\mathbf{g}, \mathbf{q}\}_{4D}$ at an integration point, the data search can be replaced by the following algorithm. First the distance of the point $\{\mathbf{g}^*, \mathbf{q}^*\}_{4D}$ to the line (B.1) is defined as:

$$\text{dist}(\{\mathbf{g}, \mathbf{q}\}_{4D}, \mathbf{q}^* + k\mathbf{g}^* = 0) = \frac{|\mathbf{q} + k\mathbf{g}|}{\sqrt{1 + k^2}}. \quad (\text{B.2})$$

Then the closest point on the line to the field values $\{\mathbf{g}, \mathbf{q}\}_{4D}$ is found by:

$$\begin{aligned} \mathbf{q}^* &= \frac{k(k\mathbf{q} - \mathbf{g})}{1 + k^2} \\ \mathbf{g}^* &= \frac{(-k\mathbf{q} + \mathbf{g})}{1 + k^2}, \end{aligned} \quad (\text{B.3})$$

for a linear constitutive relationship.

Appendix C

Example Brick geometry and mesh

The following is a content of a journal file with which the geometry and mesh can be reproduced in Coreform Cubit software.

```
reset
set duplicate block elements on

# GEOMETRY
# main body
create surface circle radius 0.22975 zplane
create surface circle radius 0.131625 zplane
subtract surface 2 from surface 1
# cut straight edges
webcut surface all with plane xplane offset 0.214
webcut surface all with plane xplane offset -0.214
webcut surface all with plane yplane offset 0.214
webcut surface all with plane yplane offset -0.214
delete Surface 7 10 4 9
# rotate
rotate all about z angle -45
# create and subtract rectangles
create surface rectangle width 0.05995 height 0.050 zplane
move surface 12 y -0.205
rotate surface 12 about z angle 45
surface 12 copy rotate 90 about z repeat 3
subtract surface 12 13 14 15 from surface 11
# create and subtract rectangles
create surface rectangle width 0.0267 height 0.050 zplane
move surface 17 y -0.215
surface 17 copy rotate 90 about z repeat 3
subtract surface 17 18 19 20 from surface 16
```

```

# make all quarters separate
webcut surface all with plane xplane
webcut surface all with plane yplane
# delete three quarters of the brick
delete Surface 24 27 26

# methane holes
create surface circle radius {0.00785 / 2} zplane
surface 28 copy move y {0.362 / 2}
move surface 28 y {0.415 / 2}
rotate surface 28 29 about z angle -13
surface 28 copy rotate {-90 + 2 * 13} about z
surface 29 copy rotate {-90 + 2 * 13} about z
create curve arc radius {0.415 / 2} center location 0 0 0 normal 0 0
  1 start angle 0 stop angle 90
create curve arc radius {0.362 / 2} center location 0 0 0 normal 0 0
  1 start angle 0 stop angle 90
create curve location 0 0 0 location 0.300 0 0
curve 123 copy move y 0.059
move curve 123 midpoint y -0.059
rotate curve 124 123 about z angle 45
create vertex atintersection curve 121 123 bounded
create vertex atintersection curve 121 124 bounded
create vertex atintersection curve 122 123 bounded
create vertex atintersection curve 122 124 bounded
delete curve 121 122 123 124
create surface circle radius {0.00785 / 2} zplane
move Surface 32 location vertex 113
create surface circle radius {0.00785 / 2} zplane
move Surface 33 location vertex 112
create surface circle radius {0.00785 / 2} zplane
move Surface 34 location vertex 114
create surface circle radius {0.00785 / 2} zplane
move Surface 35 location vertex 115
delete vertex 112 113 114 115
# remove methane holes from the main body
subtract surface 32 33 34 35 36 28 29 30 31 from surface 25

# ensure normals of edges are pointing outwards
create surface rectangle width 0.500 height 0.500 zplane

```

```
intersect surface all
curve all tangent opposite

#BLOCKSETS
block 1 add curve 162 161 156 157 158 155 159 160
block 1 name "FLUX_UNIFORM_HOLES"
block 1 attribute count 1
block 1 attribute index 1 0

block 4 add curve 153 141
block 4 name "FLUX_UNIFORM_0"
block 4 attribute count 1
block 4 attribute index 1 0

block 2 add curve 154
block 2 name "PRESSURE_UNIFORM_1000"
block 2 attribute count 1
block 2 attribute index 1 1000

block 3 add curve 152 151 150 149 148 147 146 145 144 143 142
block 3 name "PRESSURE_UNIFORM_OUT"
block 3 attribute count 1
block 3 attribute index 1 500

block 5 add surface all
block 5 name "domain"
block 5 attribute count 1
block 5 attribute index 1 0

#mesh
{scale=7}
surf all scheme trimesh
surf all sizing function type skeleton scale {scale}
mesh surf all
```

Bibliography

- T. Kirchdoerfer, M. Ortiz, Data-driven computational mechanics, *Computer Methods in Applied Mechanics and Engineering* 304 (2016) 81–101. doi:[10.1016/j.cma.2016.02.001](https://doi.org/10.1016/j.cma.2016.02.001).
- A. Kulikova, `mofem_data_driven_finite_elements`, 2024a. URL: https://bitbucket.org/AdrianaKul/mofem_data_driven_finite_elements/src/master/, bitbucket repository.
- A. Kulikova, `thesis_ak_analysis`, 2024b. URL: https://github.com/AdrianaKul/thesis_AK_analysis, gitHub repository.
- T. Vogel, M. T. van Genuchten, M. Cislérova, Effect of the shape of the soil hydraulic functions near saturation on variably-saturated flow predictions, *Advances in Water Resources* 24 (2000) 133–144. doi:[10.1016/S0309-1708\(00\)00037-3](https://doi.org/10.1016/S0309-1708(00)00037-3).
- H. Matsuo, The effect of porosity on the thermal conductivity of nuclear graphite, *Journal of Nuclear Materials* 89 (1980) 9–12. doi:[10.1016/0022-3115\(80\)90003-3](https://doi.org/10.1016/0022-3115(80)90003-3).
- J. Bonet, R. D. Wood, *Nonlinear continuum mechanics for finite element analysis*, Cambridge university press, 1997.
- A. Ibrahimbegovic, *Nonlinear solid mechanics: theoretical formulations and finite element solution methods*, volume 160, Springer Science & Business Media, 2009.
- O. C. Zienkiewicz, R. L. Taylor, *The finite element method*, 5th ed ed., Butterworth-Heinemann, 2000.
- G. D. Smith, *Numerical solution of partial differential equations: finite difference methods*, Oxford university press, 1985.
- H. K. Versteeg, *An introduction to computational fluid dynamics the finite volume method*, 2/E, Pearson Education India, 2007.
- J. T. Katsikadelis, *Boundary elements: theory and applications*, Elsevier, 2002.
- G.-R. Liu, M. B. Liu, *Smoothed particle hydrodynamics: a meshfree particle method*, World scientific, 2003.

- J. P. Boyd, *Chebyshev and Fourier spectral methods*, Courier Corporation, 2001.
- G. S. Gerlero, A. R. Valdez, R. Urteaga, P. A. Kler, Validity of capillary imbibition models in paper-based microfluidic applications, *Transport in Porous Media* 141 (2022) 359–378.
- V. Singh, S. Patra, N. A. Murugan, D.-C. Toncu, A. Tiwari, Recent trends in computational tools and data-driven modeling for advanced materials, *Materials Advances* 3 (2022) 4069–4087.
- A. Tzelepi, P. Ramsay, A. G. Steer, J. Dinsdale-Potter, Measuring the fracture properties of irradiated reactor core graphite, *Journal of Nuclear Materials* 509 (2018) 667–678. doi:[10.1016/j.jnucmat.2018.07.024](https://doi.org/10.1016/j.jnucmat.2018.07.024).
- M. S. L. Jordan, P. Ramsay, K. E. Verrall, T. O. van Staveren, M. Brown, B. Davies, A. Tzelepi, M. P. Metcalfe, Determining the electrical and thermal resistivities of radiolytically-oxidised nuclear graphite by small sample characterisation, *Journal of Nuclear Materials* 507 (2018) 68–77. doi:[10.1016/j.jnucmat.2018.04.022](https://doi.org/10.1016/j.jnucmat.2018.04.022).
- R. E. Jones, B. L. Boyce, A. L. Frankel, N. Heckman, M. Khalil, J. T. Ostien, F. Rizzi, K. Tachida, G. H. Teichert, J. A. Templeton, Uncertainty Quantification of Microstructural Material Variability Effects, Technical Report, Sandia National Lab.(SNL-NM), Albuquerque, NM (United States), 2019.
- M.-H. Edition, N. Bauld, *Mechanics of materials*, PWS Publishers, Boston, Mass. • Belmonte, HMS, Mulheron, MJ, and Smith, PA (2009).“Some observations on the strength and fatigue properties of samples extracted from cast iron water mains.” *Fatigue Fracture Eng. Mater. Struct* 32 (1986) 916–925.
- T. Belytschko, W. K. Liu, B. Moran, K. Elkhodary, *Nonlinear finite elements for continua and structures*, John Wiley & sons, 2014.
- M. M. Rao, *Foundations of stochastic analysis*, Courier Corporation, 2013.
- A. Bensoussan, A model of stochastic differential equation in hubert spaces applicable to navier stokes equation in dimension 2, in: E. Mayer-Wolf, E. Merzbach, A. Shwartz (Eds.), *Stochastic Analysis*, Academic Press, 1991, pp. 51–73. doi:<https://doi.org/10.1016/B978-0-12-481005-1.50009-0>.
- R. Agarwal, V. Dhar, *Big data, data science, and analytics: The opportunity and challenge for is research*, 2014.
- B. Baesens, *Analytics in a big data world: The essential guide to data science and its applications*, John Wiley & Sons, 2014.

- C. M. Bishop, N. M. Nasrabadi, Pattern recognition and machine learning, volume 4, Springer, 2006.
- C. M. Bishop, Neural networks for pattern recognition, Oxford university press, 1995.
- K. Arulkumaran, M. P. Deisenroth, M. Brundage, A. A. Bharath, Deep reinforcement learning: A brief survey, *IEEE Signal Processing Magazine* 34 (2017) 26–38.
- J. Pateras, P. Rana, P. Ghosh, A taxonomic survey of physics-informed machine learning, *Applied Sciences* 13 (2023) 6892.
- K. Linka, M. Hillgärtner, K. P. Abdolazizi, R. C. Aydin, M. Itskov, C. J. Cyron, Constitutive artificial neural networks: A fast and general approach to predictive data-driven constitutive modeling by deep learning, *Journal of Computational Physics* 429 (2021) 110010.
- M. Raissi, P. Perdikaris, G. E. Karniadakis, Physics-informed neural networks: A deep learning framework for solving forward and inverse problems involving nonlinear partial differential equations, *Journal of Computational physics* 378 (2019) 686–707.
- T. G. Grossmann, U. J. Komorowska, J. Latz, C.-B. Schönlieb, Can physics-informed neural networks beat the finite element method?, 2023. [arXiv:2302.04107](https://arxiv.org/abs/2302.04107).
- T. Kirchdoerfer, M. Ortiz, Data driven computing with noisy material data sets, *Computer Methods in Applied Mechanics and Engineering* 326 (2017) 622–641. doi:[10.1016/j.cma.2017.07.039](https://doi.org/10.1016/j.cma.2017.07.039).
- J. Ayensa-Jiménez, M. H. Doweidar, J. A. Sanz-Herrera, M. Doblaré, A new reliability-based data-driven approach for noisy experimental data with physical constraints, *Computer Methods in Applied Mechanics and Engineering* 328 (2018) 752 – 774. doi:<https://doi.org/10.1016/j.cma.2017.08.027>.
- L. T. K. Nguyen, M. Rambausek, M.-A. Keip, Variational framework for distance-minimizing method in data-driven computational mechanics, *Computer Methods in Applied Mechanics and Engineering* 365 (2020) 112898.
- S. Conti, S. Müller, M. Ortiz, Data-Driven Problems in Elasticity, *Archive for Rational Mechanics and Analysis* 229 (2018) 79–123. doi:[10.1007/s00205-017-1214-0](https://doi.org/10.1007/s00205-017-1214-0).
- L. T. K. Nguyen, M.-A. Keip, A data-driven approach to nonlinear elasticity, *Computers & Structures* 194 (2018) 97 – 115. doi:<https://doi.org/10.1016/j.compstruc.2017.07.031>.
- R. Eggersmann, T. Kirchdoerfer, S. Reese, L. Stainier, M. Ortiz, Model-free data-driven inelasticity, *Computer Methods in Applied Mechanics and Engineering* 350 (2019) 81 – 99. doi:<https://doi.org/10.1016/j.cma.2019.02.016>.

- P. Carrara, L. De Lorenzis, L. Stainier, M. Ortiz, Data-driven fracture mechanics, *Computer Methods in Applied Mechanics and Engineering* 372 (2020) 113390. doi:[10.1016/j.cma.2020.113390](https://doi.org/10.1016/j.cma.2020.113390).
- L. Stainier, A. Leygue, M. Ortiz, Model-free data-driven methods in mechanics: material data identification and solvers, *Computational Mechanics* 64 (2019) 381–393. doi:[10.1007/s00466-019-01731-1](https://doi.org/10.1007/s00466-019-01731-1).
- J. Mora-Macías, J. Ayensa-Jiménez, E. Reina-Romo, M. H. Doweidar, J. Domínguez, M. Doblaré, J. A. Sanz-Herrera, A multiscale data-driven approach for bone tissue biomechanics, *Computer Methods in Applied Mechanics and Engineering* 368 (2020) 113136.
- K. Karapiperis, L. Stainier, M. Ortiz, J. E. Andrade, Data-driven multiscale modeling in mechanics, *Journal of the Mechanics and Physics of Solids* 147 (2021) 104239.
- J. Ayensa-Jiménez, M. H. Doweidar, J. A. Sanz-Herrera, M. Doblaré, An unsupervised data completion method for physically-based data-driven models, *Computer Methods in Applied Mechanics and Engineering* 344 (2019) 120–143.
- B. K. Larkin, S. W. Churchill, Heat transfer by radiation through porous insulations, *AIChE Journal* 5 (1959) 467–474. doi:[10.1002/aic.690050413](https://doi.org/10.1002/aic.690050413).
- D. Boffi, F. Brezzi, M. Fortin, et al., *Mixed finite element methods and applications*, volume 44, Springer, 2013.
- D. Braess, R. Verfürth, A posteriori error estimators for the raviart–thomas element, *SIAM Journal on Numerical Analysis* 33 (1996) 2431–2444.
- N. Zander, H. Bériot, C. Hoff, P. Kodl, L. Demkowicz, Anisotropic multi-level hp-refinement for quadrilateral and triangular meshes, *Finite Elements in Analysis and Design* 203 (2022) 103700. doi:<https://doi.org/10.1016/j.finel.2021.103700>.
- L. Kaczmarczyk, Z. Ullah, K. Lewandowski, X. Meng, X.-Y. Zhou, I. Athanasiadis, H. Nguyen, C.-A. Chalons-Mouriesse, E. Richardson, E. Miur, A. Shvarts, M. Wakeni, C. Pearce, MoFEM: An open source, parallel finite element library, *Journal of Open Source Software* 5 (2020) 1441. doi:[10.21105/joss.01441](https://doi.org/10.21105/joss.01441).
- K. Rajan, Materials informatics, *Materials Today* 8 (2005) 38–45.
- C. Franck, S. Hong, S. Maskarinec, D. Tirrell, G. Ravichandran, Three-dimensional full-field measurements of large deformations in soft materials using confocal microscopy and digital volume correlation, *Experimental mechanics* 47 (2007) 427–438.

- A. Mettas, Design for reliability: Overview of the process and applicable techniques, *International Journal of Performability Engineering* 6 (2010) 577.
- A. Leygue, M. Coret, J. Réthoré, L. Stainier, E. Verron, Data-based derivation of material response, *Computer Methods in Applied Mechanics and Engineering* 331 (2018) 184–196.
- G. Valdés-Alonzo, C. Binetruy, B. Eck, A. García-González, A. Leygue, Phase distribution and properties identification of heterogeneous materials: A data-driven approach, *Computer Methods in Applied Mechanics and Engineering* 390 (2022) 114354.
- A. Gorgogianni, K. Karapiperis, L. Stainier, M. Ortiz, J. E. Andrade, Adaptive goal-oriented data sampling in data-driven computational mechanics, *Computer Methods in Applied Mechanics and Engineering* 409 (2023) 115949. URL: <https://www.sciencedirect.com/science/article/pii/S0045782523000725>. doi:<https://doi.org/10.1016/j.cma.2023.115949>.
- H. R. Tamaddon-Jahromi, N. K. Chakshu, I. Sazonov, L. M. Evans, H. Thomas, P. Nithiarasu, Data-driven inverse modelling through neural network (deep learning) and computational heat transfer, *Computer Methods in Applied Mechanics and Engineering* 369 (2020) 113217. doi:[10.1016/j.cma.2020.113217](https://doi.org/10.1016/j.cma.2020.113217).
- C. M. Rooney, C. P. Please, S. D. Howison, Homogenisation applied to thermal radiation in porous media, *European Journal of Applied Mathematics* 32 (2021) 784–805. doi:[10.1017/S0956792520000388](https://doi.org/10.1017/S0956792520000388).
- S. Liu, Y. Zhang, Multi-Scale Analysis Method for Thermal Conductivity of Porous Material with Radiation, *Multidiscipline Modeling in Materials and Structures* 2 (2006) 327–344. doi:[10.1163/157361106777641332](https://doi.org/10.1163/157361106777641332).
- T. D. Le, C. Moyne, M. Sans, Homogenized models of conduction-advection-radiation heat transfer in porous media, *International Journal of Heat and Mass Transfer* 194 (2022) 123056. doi:[10.1016/j.ijheatmasstransfer.2022.123056](https://doi.org/10.1016/j.ijheatmasstransfer.2022.123056).
- M. Luo, C. Wang, J. Zhao, L. Liu, Characteristics of effective thermal conductivity of porous materials considering thermal radiation: A pore-level analysis, *International Journal of Heat and Mass Transfer* 188 (2022) 122597. doi:[10.1016/j.ijheatmasstransfer.2022.122597](https://doi.org/10.1016/j.ijheatmasstransfer.2022.122597).
- R. J. Smit, W. M. Brekelmans, H. E. Meijer, Prediction of the mechanical behavior of nonlinear heterogeneous systems by multi-level finite element modeling, *Computer methods in applied mechanics and engineering* 155 (1998) 181–192.

- C. Miehe, J. Schotte, J. Schröder, Computational micro–macro transitions and overall moduli in the analysis of polycrystals at large strains, *Computational Materials Science* 16 (1999) 372–382.
- F. Feyel, J.-L. Chaboche, Fe₂ multiscale approach for modelling the elastoviscoplastic behaviour of long fibre sic/ti composite materials, *Computer methods in applied mechanics and engineering* 183 (2000) 309–330.
- Ł. Kaczmarczyk, C. J. Pearce, N. Bićanić, Scale transition and enforcement of rve boundary conditions in second-order computational homogenization, *International Journal for Numerical Methods in Engineering* 74 (2008) 506–522.
- D. M. Kochmann, K. Bertoldi, Exploiting microstructural instabilities in solids and structures: from metamaterials to structural transitions, *Applied mechanics reviews* 69 (2017).
- B. T. Kelly, Graphite—the most fascinating nuclear material, *Carbon* 20 (1982) 3–11.
- D. McEligot, W. D. Swank, D. L. Cottle, F. I. Valentin, Thermal properties of G-348 graphite, Technical Report, Idaho National Lab.(INL), Idaho Falls, ID (United States), 2016.
- R. Price, Review of the thermal conductivity of nuclear graphite under HTGR conditions, Technical Report, Gulf General Atomic Co., San Diego, Calif.(USA), 1973.
- B. J. Marsden, S.-L. Fok, H. Li, Irradiation behaviour and structural analysis of htr/vhtr graphite core components (2005).
- L. L. Snead, Accumulation of thermal resistance in neutron irradiated graphite materials, *Journal of Nuclear Materials* 381 (2008) 76–82.
- B. J. Marsden, G. N. Hall, O. Wouters, J. Vreeling, J. Van Der Laan, Dimensional and material property changes to irradiated gilsocarbon graphite irradiated between 650 and 750 c, *Journal of Nuclear Materials* 381 (2008) 62–67.
- L. Babout, J. Marrow, P. Mummery, B. Marsden, X-ray tomographic observations applied to porosity models for the thermal properties of oxidised nuclear graphite, *SPECIAL PUBLICATION-ROYAL SOCIETY OF CHEMISTRY* 309 (2007) 116.
- A. Hashim, S. Kyaw, W. Sun, Modelling fracture of aged graphite bricks under radiation and temperature, *Nuclear Materials and Energy* 11 (2017) 3–11.
- R. G. Ghanem, P. D. Spanos, *Stochastic finite elements: a spectral approach*, Courier Corporation, 2003.
- C. Soize, A nonparametric model of random uncertainties for reduced matrix models in structural dynamics, *Probabilistic engineering mechanics* 15 (2000) 277–294.

- E. Febrianto, L. Butler, M. Girolami, F. Cirak, Digital twinning of self-sensing structures using the statistical finite element method, *Data-Centric Engineering* 3 (2022) e31.
- S. Herath, X. Xiao, F. Cirak, Computational modeling and data-driven homogenization of knitted membranes, *International Journal for Numerical Methods in Engineering* 123 (2022) 683–704.
- M. Girolami, E. Febrianto, G. Yin, F. Cirak, The statistical finite element method (statfem) for coherent synthesis of observation data and model predictions, *Computer Methods in Applied Mechanics and Engineering* 375 (2021) 113533.
- T. Kirchdoerfer, M. Ortiz, Data-Driven Computing, in: E. Oñate, D. Peric, E. de Souza Neto, M. Chiumenti (Eds.), *Advances in Computational Plasticity: A Book in Honour of D. Roger J. Owen*, Springer International Publishing, Cham, 2018, pp. 165–183. URL: https://doi.org/10.1007/978-3-319-60885-3_8. doi:10.1007/978-3-319-60885-3_8.
- T. T. Kirchdoerfer, *Data Driven Computing*, phd, California Institute of Technology, 2018. doi:10.7907/Z9Z899MV.
- S. Conti, F. Hoffmann, M. Ortiz, Model-free data-driven inference, *arXiv preprint arXiv:2106.02728* (2021).
- E. Prume, S. Reese, M. Ortiz, Model-free data-driven inference in computational mechanics, *Computer Methods in Applied Mechanics and Engineering* 403 (2023) 115704.
- R. Eggersmann, L. Stainier, M. Ortiz, S. Reese, Efficient data structures for model-free data-driven computational mechanics, *Computer Methods in Applied Mechanics and Engineering* 382 (2021) 113855.
- B. Bahmani, W. Sun, A kd-tree-accelerated hybrid data-driven/model-based approach for poroelasticity problems with multi-fidelity multi-physics data, *Computer Methods in Applied Mechanics and Engineering* 382 (2021) 113868.
- Y. Xu, J. Yang, Z. Kuang, Q. Huang, W. Huang, H. Hu, Quantum computing enhanced distance-minimizing data-driven computational mechanics, *Computer Methods in Applied Mechanics and Engineering* 419 (2024) 116675.
- B. Liu, M. Ortiz, F. Cirak, Towards quantum computational mechanics, *Computer Methods in Applied Mechanics and Engineering* 432 (2024) 117403.
- A. Platzer, *Finite strain data-driven computational mechanics.: From tailored data to adaptive solvers for multiscale simulations*, Ph.D. thesis, École centrale de Nantes, 2020.

- A. Platzer, A. Leygue, L. Stainier, M. Ortiz, Finite element solver for data-driven finite strain elasticity, *Computer Methods in Applied Mechanics and Engineering* 379 (2021) 113756.
- T. Kirchdoerfer, M. Ortiz, Data-driven computing in dynamics, *International Journal for Numerical Methods in Engineering* 113 (2018) 1697–1710.
- H. Salahshoor, M. Ortiz, Model-free data-driven viscoelasticity in the frequency domain, *Computer Methods in Applied Mechanics and Engineering* 403 (2023) 115657.
- H. Salahshoor, M. Ortiz, A model-free data-driven paradigm for in situ patient-specific prediction of human brain response to ultrasound stimulation, *bioRxiv* (2022) 2022–09.
- J. Yang, W. Huang, Q. Huang, H. Hu, An investigation on the coupling of data-driven computing and model-driven computing, *Computer Methods in Applied Mechanics and Engineering* 393 (2022) 114798. doi:<https://doi.org/10.1016/j.cma.2022.114798>.
- J. Bulin, J. Hamaekers, M. Ariza, M. Ortiz, Interatomic-potential-free, data-driven molecular dynamics, *arXiv preprint arXiv:2208.04937* (2022).
- W. Huang, R. Xu, J. Yang, Q. Huang, H. Hu, Data-driven multiscale simulation of frp based on material twins, *Composite Structures* 256 (2021) 113013. doi:<https://doi.org/10.1016/j.compstruct.2020.113013>.
- T. F. Korzeniowski, K. Weinberg, Data-driven finite element computation of open-cell foam structures, *Computer Methods in Applied Mechanics and Engineering* 400 (2022) 115487.
- T. F. Korzeniowski, Data-driven finite element computation with material uncertainty, PhD Thesis, Universität Siegen, 2022. doi:<http://dx.doi.org/10.25819/ubsi/10181>, backup Publisher: Institut für Mechanik und Regelungstechnik - Mechatronik Publication Title: Schriftenreihe der Arbeitsgruppe für Technische Mechanik im Institut für Mechanik und Regelungstechnik - Mechatronik.
- A. Kuliková, A. G. Shvarts, L. Kaczmarczyk, C. J. Pearce, Data-driven finite element method, 2021. doi:[10.17028/rd.lboro.14588577.v1](https://doi.org/10.17028/rd.lboro.14588577.v1).
- I. Babuška, The finite element method with lagrangian multipliers, *Numerische Mathematik* 20 (1973) 179–192.
- V. A. Yastrebov, *Numerical methods in contact mechanics*, John Wiley & Sons, 2013.
- P. Wriggers, T. A. Laursen, *Computational contact mechanics*, volume 2, Springer, 2006.
- F. Brezzi, D. Boffi, L. Demkowicz, R. Durán, R. Falk, M. Fortin, *Mixed finite elements, compatibility conditions, and applications*, Springer 2 (2008) 4–2.

- M. F. Wakeni, A. Aggarwal, Ł. Kaczmarczyk, A. T. McBride, I. Athanasiadis, C. J. Pearce, P. Steinmann, A p-adaptive, implicit-explicit mixed finite element method for diffusion-reaction problems, *International Journal for Numerical Methods in Engineering* 123 (2022) 3237–3263.
- D. N. Arnold, Mixed finite element methods for elliptic problems, *Computer methods in applied mechanics and engineering* 82 (1990) 281–300.
- J. T. Oden, L. Demkowicz, W. Rachowicz, T. A. Westermann, Toward a universal hp adaptive finite element strategy, part 2. a posteriori error estimation, *Computer methods in applied mechanics and engineering* 77 (1989) 113–180.
- S. Repin, A posteriori estimates for partial differential equations, Walter de Gruyter, 2008.
- T. Grätsch, K.-J. Bathe, A posteriori error estimation techniques in practical finite element analysis, *Computers & Structures* 83 (2005) 235–265.
- M. Ainsworth, A posteriori error estimation for lowest order raviart–thomas mixed finite elements, *SIAM Journal on Scientific Computing* 30 (2008) 189–204.
- C. Carstensen, A posteriori error estimate for the mixed finite element method, *Mathematics of Computation* 66 (1997) 465–476.
- J. H. Lienhard, IV, J. H. Lienhard, V, A Heat Transfer Textbook, 5th ed., Phlogiston Press, Cambridge, MA, 2020. Version 5.10.
- P. Sanan, D. A. May, R. T. Mills, et al., Dmstag: staggered, structured grids for petsc, *Journal of Open Source Software* 7 (2022) 4531.
- S. C. Brenner, L. R. Scott, *The Mathematical Theory of Finite Element Methods*, volume 15 of *Texts in Applied Mathematics*, Springer New York, New York, NY, 2008. doi:[10.1007/978-0-387-75934-0](https://doi.org/10.1007/978-0-387-75934-0).
- O. C. Zienkiewicz, R. L. Taylor, J. Z. Zhu, *The finite element method: its basis and fundamentals*, 6. ed., reprint., transferred to digital print ed., Elsevier, Amsterdam Heidelberg, 2010.
- P. Wriggers, *Nonlinear finite element methods*, Springer Science & Business Media, 2008.
- G. N. Gatica, *A simple introduction to the mixed finite element method*, Theory and Applications. Springer Briefs in Mathematics. Springer, London (2014).
- L. Demkowicz, *Mathematical theory of finite elements*, volume 28.;28;, Society for Industrial and Applied Mathematics, Philadelphia, 2024.

- L. Demkowicz, J. Gopalakrishnan, Analysis of the dpg method for the poisson equation, SIAM Journal on Numerical Analysis 49 (2011) 1788–1809.
- Boost, Boost c++ libraries, 2024. URL: <https://www.boost.org/>, accessed: 2024-11-26.
- A. Guttman, R-trees: A dynamic index structure for spatial searching, in: Proceedings of the 1984 ACM SIGMOD international conference on Management of data, 1984, pp. 47–57.
- Boost, Boost.geometry: R*-tree indexing structure, 2024. URL: https://www.boost.org/doc/libs/latest/libs/geometry/doc/html/geometry/reference/algorithms/rstar_tree.html, accessed: 2024-11-26.
- S. Balay, S. Abhyankar, M. F. Adams, J. Brown, P. Brune, K. Buschelman, L. Dalcin, A. Gropp, D. Kaushik, M. G. Knepley, D. A. May, L. C. McInnes, K. Rupp, P. Sanan, B. F. Smith, H. Zhang, SNES: Nonlinear Solvers, PETSc Users Manual, revision 3.18 ed., Argonne National Laboratory, 2023. Available from: <https://petsc.org/release/manual/snes/>.